A Whole-Hearted Journey: Mapping Patterns and Pathways of Cardiac Development, Disease, and Regeneration

By
Rebecca J. Salamon

A dissertation submitted in partial fulfillment of
the requirements for the degree of

Doctor of Philosophy
(Genetics)

at the
UNIVERSITY OF WISCONSIN-MADISON
2023

Date of final oral examination: 07/07/2023

The dissertation is approved by the following members of the Final Oral Committee:
Ahmed Mahmoud, Assistant Professor, Cell and Regenerative Biology
Grace Boekhoff-Falk, Associate Professor, Cell and Regenerative Biology
Rupa Sridharan, Associate Professor, Professor, Cell and Regenerative Biology
Francisco Pelegri, Professor and Chair, Genetics
Akihiro Ikeda, Professor, Genetics

© Copyright by Rebecca J. Salamon

2023

- - - - - - - - - - - - - - - - - -

ALL RIGHTS RESERVED

Dedicated to my grandparents.

They say that great bakers make for great scientists.

All those hours spent in the kitchen together sure paid off.

ACKNOWLEDGMENTS

A lot of life happens over the course of a PhD. My path to completing my PhD was filled with incredible highs and lows. At these points, and all the points in between, I was surrounded by supportive faculty, colleagues, friends, family members, and my fiancée, who were championing for my success. I am filled with immense gratitude for all the people that have and continue to support me along the way. Thank you all for being a part of my journey.

To my mentor, Ahmed Mahmoud, thank you for your support and guidance throughout my PhD. You provided me opportunities to grow as a scientist and gave me the independence I needed to take on this project. You were patient and understanding when the science was not working, and the first one to share in the successes when I overcame those hurdles. In your lab I have grown in more ways than I could have imagined, and I feel well prepared to continue my path as an independent scientist. I will take with me your lessons to be flexible and persistent because nothing in research is a guarantee, c'est la vie.

To my committee members, Grace Boekhoff-Falk, Rupa Sridharan, Francisco Pelegri, and Aki Ikeda, thank you all for your feedback, insight, and encouragement on my thesis work. Your guidance helped shape how I pursued and viewed my thesis. I would like to especially thank Grace. You went above and beyond your role as my committee member to become a mentor and pillar of support for me. I always left your office with a clear direction forward and the confidence to know that I could do it (and with a chocolate fix).

To the current and past members of the Mahmoud Lab, Jiyoung Bae, Poorva Halbe, Timothy Aballo, Wyatt Paltzer, Dakota Nuttall, and Alyssa Schuett, thank you all for your feedback

and encouragement. To Timothy and Wyatt, thank you for being in the trenches with me and always offering your help and support. To Poorva, thank you for joining onto my project with drive and ambition. You undertook the challenge of mastering Imaris, spent hours precisely reconstructing my images, and did it all with genuine enthusiasm. To Jiyoung, I am grateful that I got to spend most of my PhD by your side. You are the most talented scientist that I have worked alongside. From you I learned how to uphold a high standard of rigor, overcome challenges, and follow the data. Beyond being a talented scientist, you are a wonderful person, and I am thankful to have you as a close friend.

To my past research mentors, Katie Mouzakis, Steve Fenster, and Sanjay Jain, thank you all for developing my confidence and skills in pursuing independent research. Your thoughtful mentorship and teaching provided me a solid scientific foundation for me to pursue graduate school and be successful in my scientific endeavors. To Katie, I would not be the scientist I am today without your dedication in providing an intensive and engaging first research experience. You shaped how I approached scientific questions and overcame challenges, all with a smile.

To our collaborators, William Kasberg, Youngsook Lee, and Tim Kamp, thank you all for being willing to share your knowledge and expertise to expand on what any of us could do as individuals. To William, thank you for sharing your talents and knowledge on Imaris. You made a major branch of my project come to fruition, and best of all we had fun doing it. To Youngsook and Tim, I aspire to be inquisitive, engaging, and knowledgeable scientists like you both. Also, thank you, Youngsook, for your revisions on my thesis introduction chapter.

To the Optical Imaging Core and BRMS Mouse Breeding Core & Research Services, thank you all for providing the tools and support need for the completion of my thesis work. To Lance Rodenkirch, thank you for keeping all the scopes up and running, and coming to visit during my scope time. From year one, you provided the support and tools needed for me to become the microscopist I am today. To Conrad Blosch, thank you for your dedication in maintaining and breeding our transgenic mice. Managing several transgenic lines and crosses is no small task, and I am thankful for your communication and efforts to generate the mice needed to complete my thesis work.

To the Department of Cell and Regenerative Biology and the Genetics Training Program, thank you all for providing a wonderful environment to pursue my PhD. The Cell and Regenerative Biology community has been a wonderful place to research, and I thank Deneen Wellik, Barak Blum, and Valentina Lo Sardo, for your feedback and encouragement. I am also thankful for the Genetics community, including Audrey Gasch, Nicole Perna, and Martha Reck, for your clear dedication in creating a supportive environment for all graduate students. Thank you all for making both departments a welcoming, diverse, and inclusive place.

To my therapist, Sarah, thank you for meeting me where I was at and helping me grow into a more insightful person. From you I learned to prioritize myself and my mental health. You helped me navigate through new and difficult roads. Thank you for your guidance, empathy, and support.

To my friends, thank you all for being there for me in all the seasons of graduate school. Thank you to my oldest friends, Ashley Crews, Becca Miller, and Kelli Warmouth for being true

lifelong friends. Even though we all live in different states, we continue to find time to catch up, plan trips, and encourage each other, and I am grateful to have you all in my life. I am lucky to also have made wonderful friends in graduate school. To Megan McKeon, Sierra Love, Muhang Li, and Mel Adams, you all make me feel loved, validated, and supported. Graduate school would not have been nearly as memorable or fun without you all.

To my family, Mom, Dad, Stuart, Andrew, and Matthew, you all have continued to support me as I pursued this long path through higher education. You all have given me the support, encouragement, and motivation to reach my goals and aspirations. It is special to have a family that continues to come together and remain connected, no matter the distance or time past. Thank you all for putting your best effort into understanding my research and for continually asking when I will be able to graduate (I think I am getting close). To my grandma, and grandpa (in heaven), you two have inspired me that I could achieve anything. I could always count on a FaceTime with you to brighten my day. I am grateful to have you all as my family, I love you.

To my husband to be, Aus, thank you for supporting me through all of this and I am lucky to have you by my side. You celebrated in my success, and more importantly, stood unwaveringly through the challenges. We have grown both as individuals and as a couple, and I am proud of all we have done together. You made sure we found time to prioritize us. Next to you is my favorite place to be and I am excited to see where we go on this journey of life. I love you, forever and always.

TABLE OF CONTENTS

ABSTRACT

My thesis highlights important discoveries about the pathways and patterns regulating cardiac development, disease, and regeneration. A central regulator of cardiovascular physiology and pathology is the cardiac nervous system, composed of sympathetic, parasympathetic, and sensory nerves. Yet, our understanding of nerve architecture has been limited by two-dimensional analysis. I utilized innovative technologies, including tissue clearing methods and three-dimensional (3D) analysis, to investigate the intact cardiac nervous system. My 3D approach provides a basis for investigating typical cardiac nerve architecture, as well as nerve remodeling in diseased and regenerative settings. My research identified extensive parasympathetic innervation in the cardiac ventricles and a novel phenotype of intertwined parasympathetic and sympathetic axons. I also discovered differences in axon remodeling between the regenerative and non-regenerative mouse heart, demonstrating that the regenerating neonatal heart undergoes a unique process of physiological reinnervation. This neural plasticity may be harnessed therapeutically to prevent arrhythmias after cardiac injury. Additionally, I explored the role of the cellular metabolic state and specific proteins, such as Leucine-rich repeat containing 10 (LRRC10), in promoting neonatal and adult mammalian cardiac regeneration. These studies have direct clinical implications for promoting endogenous cardiac regeneration for the treatment of heart failure, given that current treatments are limited. Furthermore, these findings provide a framework for identifying novel pathways and molecular targets that could reawaken the regenerative response in the adult heart after injury. Taken together, my research represents a significant step forward in understanding the pathways and

patterns underpinning heart development, disease, and regeneration, highlighting exciting new opportunities for developing therapeutic interventions that promote cardiac repair.

CHAPTER I: INTRODUCTION: A COMPREHENSIVE REVIEW OF INNERVATION IN THE CARDIAC VENTRICLES

Rebecca J. Salamon[1]

[1]Department of Cell and Regenerative Biology, School of Medicine and Public Health, University of Wisconsin-Madison, Madison, Wisconsin, USA

Introduction

The intrinsic cardiac nervous system is rich with afferent (sensory) and efferent (motor) nerves that regulate heart rate, contractility, and conduction. Extensive research has been focused on neuronal regulation of the conduction system by direct atrial innervation at the sinoatrial and atrioventricular nodes. Here, the focus is on the other half of the cardiac nervous system, ventricular innervation. Recent technological advances have begun to bring ventricular nerve patterning and physiology into light. The ventricles are densely innervated by sympathetic (adrenergic), parasympathetic (cholinergic), and sensory (glutaminergic) nerves, with nearly all ventricular cardiomyocytes contacting a nerve fiber[1]. Neurogenic regulation is prevalent in developmental, homeostatic, and disease states. Continued research is required to develop a complete picture of the neurocircuitry that regulates cardiac function under a variety of conditions.

A detailed understanding of the anatomy and physiology of the cardiac nervous systems is essential for preventing neuropathogenesis in cardiac disease. Myocardial infarction is the leading cause of death worldwide and causes severe nerve damage to all nerve subtypes subtypes[2-5]. Therapeutic targeting of innervation by vagal stimulation has been attempted, however, the lack of insight into ventricular nerve patterning and regulation has been a barrier to its clinical success[6]. Nerve dysfunction has also been linked with several other cardiovascular disease such as hypertension, coronary artery disease, and heart failure[7]. As we gain a greater depth in understanding nerve dysfunction in disease, novel targets to promote nerve repair and cardiac regeneration can be revealed.

Development of innervation in the ventricles

The process of cardiac nerve development begins with the migration and differentiation of neural crest and placode cells into neurons. The nerves then undergo a complex process of nerve axon pathfinding, facilitated by a variety of guidance molecules. The result is targeted innervation of a variety of cardiac cells, where formed neuronal connections can influence maturation. This section details the guidance and targets of innervation in the developing ventricles.

Origins of the cardiac nerves from the neural crest

The development of the intrinsic cardiac nervous system begins when neural crest cells migrate from the neural tube towards the mesocardium[8, 9] . During migration, the neural crest cells will undergo an epithelial-to-mesenchymal transition and begin differentiation into neural precursors[8, 9]. Additionally, cells from the neurogenetic placode can contribute to the neuronal progenitor pool [10, 11]. Neurotrophic and signaling factors in the regional secretome, including bone morphogenetic protein, Wnt, and fibroblast growth factor, will push the neural precursors to differentiate into defined neural lineages [8, 12, 13]. Eventually, these neuroblasts will give rise to the parasympathetic (cholinergic) ganglia, and to a lesser extent sympathetic (adrenergic) ganglia, within the cardiac plexus[10, 14-16]. The majority of the sympathetic nerves will arise from the paravertebral stellate ganglion to innervate the ventricles. Intriguingly, despite extensive studies on neural crest cell migration and differentiation [10, 12, 15, 16], it remains unclear when neural crest cells and neuronal precursors make the fate decision to adopt either sympathetic or parasympathetic nerve lineage.

Neurotrophic factors for axon guidance in the ventricles

Targeted cardiac axon extension is guided by the secretion of neurotrophic factors, either providing chemoattractant (attractive) or chemorepellent (repulsive) cues. The main neurotrophic factors identified for ventricular axon guidance are classified into the neurotrophic family or the glial line-derived neurotrophic factor (GDNF) family[17]. The expression of neurotrophic factors allows for targeted epicardial-to-endocardial axon extension during heart development[17, 18]. The result is a complex pattering of nerves that precisely innervate a variety of cardiac cell types[1, 19].

The neurotrophic family, including nerve growth factor (NGF), neurotrophin-3 (NT-3), and others, provide chemoattractant cues. The most predominantly studied chemoattractant in the ventricles is NGF[19-22]. Sympathetic and sensory axons are attracted by NGF secretion and signaling through the tropomyosin-receptor kinase (Trk), TrkA, receptor. In rodent models, inhibition of either NGF or TrkA leads to a nearly complete depletion of sympathetic innervation[21-23]. Inversely, driving NGF overexpression leads to hyperinnervation[24], showcasing the sensitivity of axon outgrowth to NGF. Furthermore, NGF also has the potential to promote parasympathetic nerve growth in the heart[25], however, NGF-induced parasympathetic axon growth has been significantly less studied.

NGF is primarily secreted by coronary vessels to pattern the sympathetic axons in the ventricles[19]. Around embryonic day (E) 13.5 in mice, NGF is secreted by the vascular smooth muscle cells of the coronary veins[19]. This promotes axon extension in posterior (dorsal) subepicardium,

extending from the heart base to the apex. By E15.5, the vascular smooth muscle cells surrounding the coronary arteries will activate NGF[19]. This promotes sympathetic innervation of the endocardium, a process completed around E17.5. The coronary arteries are a final target of innervation, determined by axon depth and proximity[19]; however, it is unknown if this transient NGF expression drives nerve-artery alignment.

NGF and NT-3 share the common receptor TrKA[26]. NT-3 is expressed in the aorta, as well as in smooth muscle cells of peripheral vessels[27]. NT-3 is needed for sympathetic axon projection and vessel alignment in the developing cardiac ventricles, where deletion stunts axon extension without impacting neural precursors in mice[27, 28]. Overall, this suggests that the combination of NT-3 with NGF is needed for proper sympathetic axon targeting to the ventricles.

The GDNF family, including GDNF and neurturin (NTN), among others, uniquely provides chemoattractant cues for parasympathetic axon extension[13, 29]. These molecules target binding to the GDNF family receptor α (GFRα) and RET, a tyrosine kinase receptor[30]. In line with its namesake, GDNF is expressed by glia cells in the heart, along with the cardiomyocytes and endothelial cells[29, 31]. In mice with a knockout of the GDF receptor, GFRα2, parasympathetic innervation is specifically reduced by around 40% in the cardiac ventricles, without a significant impact to sympathetic axons density[29]. The partial reduction of parasympathetic innervation in the ventricles suggests parasympathetic axon recruitment is facilitated by other signaling cues than GDNF alone.

NTN knockout in mice also causes a reduction in peripheral parasympathetic ganglia and axons, again without known impairments in sympathetic innervation[32]. The aberrant parasympathetic innervation in NTN knockout mice occurs in the intestine, lachrymal and salivary glands[32], however, cardiac-specific defects have not been investigated.

Equally important to the attraction of axons is the repulsion signals. Semaphorin 3A (Sema3A) is chemorepellent signal that plays a role during heart development and is expressed in a region specific manner[33]. When axons are being recruited into the endocardial layer at E15, Sema3A is expressed in the subendocardial layer, restricting sympathetic innervation depth. In the postnatal heart, Sema3A expression is restricted to the Purkinje fibers within the ventricular free wall[33]. Although Sema3A has been often associated with sympathetic innervation, it can also impair parasympathetic innervation[34]. In rat pelvic neurons, Sema3A acts to collapse neural growth cones of sympathetic and parasympathetic nerves by targeting specific pathways to each nerve subtype. The question of whether Sema3A can affect parasympathetic cardiac axons remains.

Studies of peripheral axon extension have led to the discovery of several additional neurotrophic factors, such as cell adhesion molecules, Netrins, Ephrins, Slits, Morphogens (Wnts, Hedgehog), and growth factors (brain-derived neurotrophic factor, FGF, artemin, and neuregulin) to name a few[35]. The diverse cassette of axon guidance cues highlights the complexity in pattering the peripheral nerves and introduces the likelihood of a variety of signaling molecules that coordinate axon pathfinding in the ventricles. Moreover, further investigations are warranted to dissect the neurotrophic factors and mechanisms that influence parasympathetic axon growth.

Co-maturation and targeted innervation

Nerve axons run proximal to a variety of cell types in the ventricles, including cardiomyocytes, endothelial cells, vascular smooth muscle cells, and lymphocytes. The development of neural communication is established through a co-maturation system where cell-cell interactions alter the physiology of the neuron and the innervated cell[7, 36]. Once proximity is established, two-way communication promotes axon survival and neuronal regulation. Establishing targeted innervation provides an axis for neurogenic influence in the developing ventricles.

Essential to the neurogenic regulation of cardiomyocyte function is the development of the neurocardiac junction (NCJ), a region of junction-like contact between nerve terminals and cardiomyocytes[37, 38]. At the NCJ, cardiomyocytes secrete neurotrophic factors, including NGF, to promote axon survival and maintenance of innervation[39]. In exchange, the newly established innervation stimulates cardiomyocyte transition from hyperplastic to hypertrophic growth[38, 40, 41]. This results in regional differences in cardiomyocyte size, with larger myocytes in the highly innervated epicardial layer and smaller myocytes in the less innervated subendocardial layer[38]. These findings also coincide with the neurogenic regulation of cardiomyocyte cell cycle arrest, where innervation induces expression of the signal for cell cycle exit gene, *Meis1*[41], and circadian rhythm genes, such as gene homologs *Period1* and *Period2*[40]. Ultimately, this cycle arrest leads to cardiomyocyte hypertrophy[40, 41]. Together, these findings implicate the nerves as a key regulator of ventricular cardiomyocyte size and maturation.

Sympathetic innervation as targets and influences the neurovascular system. The nerves first align in the subepicardium with the coronary veins, acting as a transient target for innervation, before extending into the endocardium to target the coronary arteries[19]. Nerves are aligned at least partially to the coronary arteries[42, 43]; however, the timing and overall degree of association is not defined. In the skin, the precise timing and patterning of arterial innervation led to the discovery of nerves as regulators of arterial differentiation through activation of VEGF signaling[44, 45]. Identifying how initial neuronal contacts influence coronary artery development is key to understanding the formation of the cardiac neurovascular system. Furthermore, expanding our knowledge of innervation targets, and identifying those targeted by the parasympathetic nerves, will provide insight into the role of neuronal function and influences throughout the ventricles.

Neurocircuitry and maintenance of the cardiac nervous system

The neurocircuitry of the autonomic nervous system is becoming recognized for its increasing complexity, largely in part due to the advancements in transgenic mouse models, optogenetics, and viral tracing strategies that allow for probing and mapping of neural afferent (sensory) and efferent (motor) circuits[46-48]. These discoveries highlight the regional arrangements of ganglia and axons that permit intercommunication and regulation of the cardiac nervous system[46].

Extrinsic and intrinsic cardiac ganglia

The cardiac nervous system is composed of sympathetic, parasympathetic, and sensory ganglia which coregulate cardiac function. The ganglia contain the nerve body, including the soma. Most postsynaptic sympathetic ganglia are located within the sympathetic chain, whereas most

postsynaptic parasympathetic ganglia are contained within the cardiac plexus. The distribution and composition of the ganglia reflect their role in the cardiac nervous system.

The canonical view of the ganglia are as follows: Preganglionic sympathetic neurons localize to the upper thoracic region of the spinal cord. The sympathetic preganglionic neurons send projections to postganglionic sympathetic ganglia in the sympathetic trunk. (**Figure 1**). The sympathetic trunk runs adjacent to the spinal cord and is divided into left and right nerve trunks. The cardiac ganglia are dispersed through the cervical and thoracic regions of the sympathetic trunk. The cervical ganglia include the superior, medial, and inferior cervical ganglion. The contributing thoracic ganglion includes the stellate (cervicothoracic) ganglion (SG), and the upper thoracic sympathetic ganglion. The SG references the inferior cervical ganglion and the first thoracic ganglion, which are fused together in most humans[49]; in murine species this is termed middle cervical-stellate ganglia complex. The primary source of sympathetic innervation arises from the SG and contributes towards the innervation in the atrial chambers[50].

Preganglionic parasympathetic neurons are located in the vagal nucleus (nucleus ambiguss) within the medulla oblongotta. The preganglionic parasympathetic neurons send projections via the vagal nerve (**Figure 1**). The vagal nerve has right and left branches, tracking alongside the carotid artery. The receiving postganglionic parasympathetic ganglia are dispersed throughout the cardiac plexus (ganglionated plexus) in the upper cardiac regions. The postganglionic parasympathetic nerves contribute towards atrial and ventricular innervation. Sensory ganglia

are distributed between the upper thoracic dorsal root ganglia and nodose ganglia, following the sympathetic chain or vagal nerve tracks, respectively (**Figure 1**).

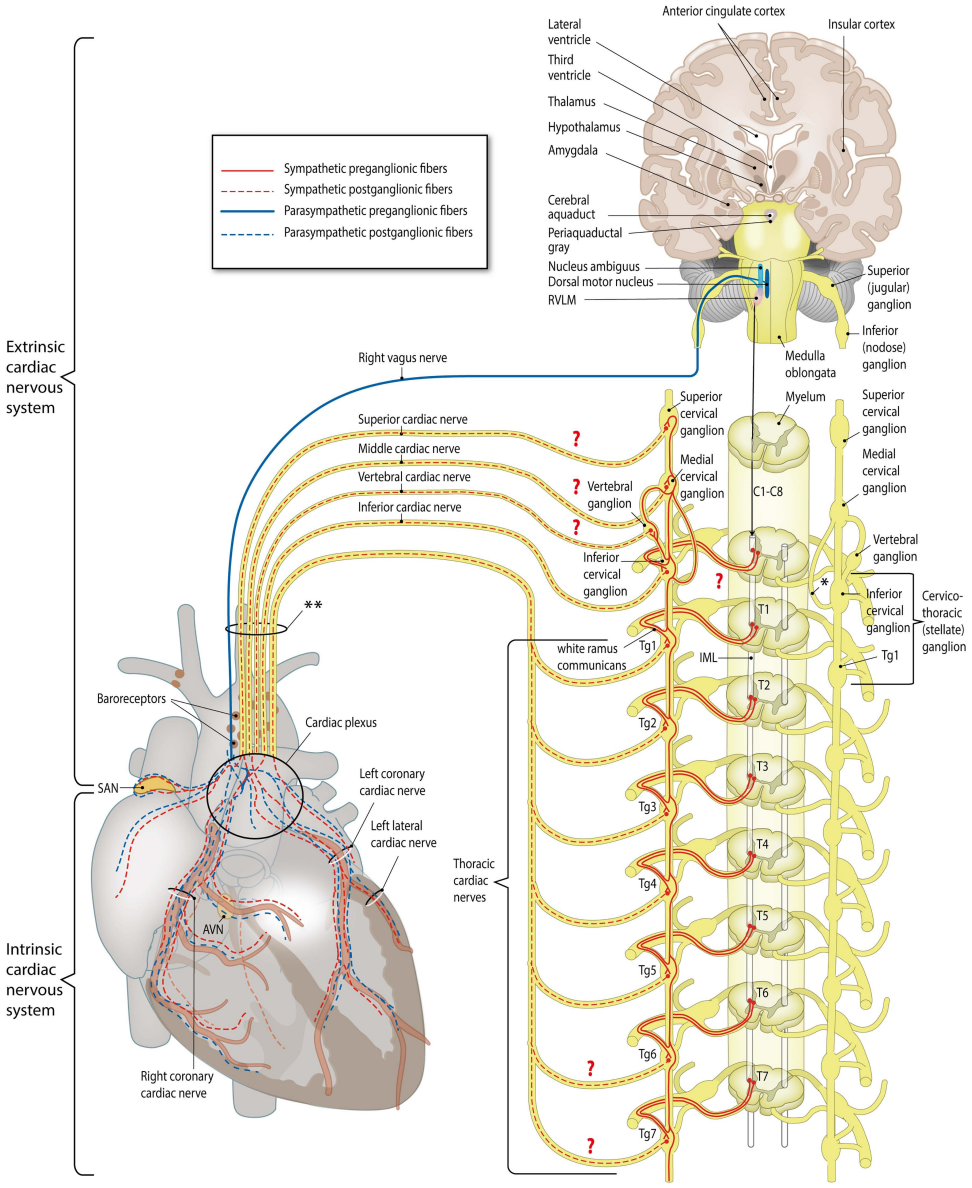

Figure 1: Neurocircuit of the extrinsic and intrinsic cardiac nervous system. Preganglionic parasympathetic nerves (blue) run along the vagus nerve to the cardiac plexus. The cardiac plexus is composed largely of postganglionic parasympathetic ganglia which innervate the atria and ventricles. Preganglionic sympathetic nerves (red) arise from the dorsal root ganglia to the cervical and thoracic sympathetic chain. Postganglionic sympathetic ganglia in the sympathetic chain can directly innerve the atria and ventricles through the superior, middle, vertebral, and inferior cardiac nerves. Filled and dashed lines indicate preganglionic and postganglionic fibers, respectively. Red question marks demonstrate regions where nerve contribution in cardiac innervation of the human heart is unclear. Figure from Wink et al. 2020.

This classical view of these separate and distinct regions of sympathetic and parasympathetic ganglia has recently been challenged[47, 51-54]. Recent studies demonstrate that populations of ganglia can be intermixed[47, 51, 52, 55]. Moreover, subpopulations can have dual neurochemical phenotypes, where ganglia secrete both acetylcholine and norepinephrine[51, 54-57]. Humans show a wide range of variation in the anatomy, distribution, and influence of cardiac ganglia (reviewed by Wink et al. 2020) [47, 58]. Thus, identifying how the composition of diverse ganglia varies across species, especially in humans, is needed to fully uncover neural circuity and function.

Distribution of ventricular cardiac axons

The ventricular cardiac axons create an expansive network where a nerve fiber contacts nearly every ventricular cardiomyocyte[59]. The nerves pattern the ventricles with regions of thick, bundled structures that branch into smaller nerve fibers[59] (**Figure 2**). Nerve fibers have a beaded morphology, with regions of rounded enlargements, or varicosities[1, 59]. These nerves were long thought to be of sympathetic origin, however, parasympathetic[60] and sensory[2] axons have also been demonstrated to contribute towards ventricular innervation.

Herbert H. Woollard was one of the first to detail and illustrate the contribution of innervation in the ventricles nearly a century ago[59, 61]. Yet, the fact that the ventricles are significantly innervated still comes as a surprise to many clinical cardiologists. This is possibly due to outdated diagrams in clinical textbooks[60] and teachings that overemphasizes that cardiac innervation primarily targets the sinoatrial (SA) and atrioventricular (AV) nodes. This is further compounded by the underestimation of ventricular innervation based on gross anatomy, as accurate

identification of nerve subtypes requires nerve-specific labeling techniques and high-resolution microscopes.

Sympathetic axons extensively innervate the epicardial and subendocardial layers of the cardiac ventricles[1, 62]. In contrast, parasympathetic innervation has been less studied for its interactions within the cardiac ventricles, and are commonly noted to have minimal or no contributions to ventricular innervation (reviewed by Coote et al. 2013) [60]. This misconception has been directly countered by evidence from immunohistology studies in mouse, porcine, and human hearts that identified dense ventricular innervation of parasympathetic axons[46, 63, 64]. Additionally, in rodent hearts, sensory nerves extensively innervate the epicardial layer of the ventricles[2, 65, 66].

Regionally, the density and composition of axons varies[46, 63, 64], likely allowing for deferential regulation of cardiac functions. In the human heart, sympathetic axons have a higher density than parasympathetic axons throughout the ventricles[63]. Furthermore, parasympathetic nerves tend to localize more in the subendocardial region, whereas sympathetic nerves have higher density in the subepicardial region[63]. Sensory nerves also have increased density and diameters in the posterior (dorsal) heart, compared to the anterior (ventral) region[2]. To expand on these findings, comparative approaches are needed to precisely annotate the regional neurodiversity of sympathetic (TH-expressing), parasympathetic (ChAT-expressing), and sensory (VGLUT2-expressing) cardiac nerves. The importance of comparative studies cannot be understated, as nerve bundles can include axons of differing origins[2], suggesting complex roles in multi-axon

patterning. Excitingly, our current technology can provide extensive insight into the patterning, density, and distribution of nerve subtypes in ventricular innervation.

Figure 2: Illustration of innervation in the cardiac ventricles. Drawing of large, bundled nerves and smaller, beaded nerve fibers in the left ventricle (dog). Illustration from Woollard et al. 1926.

Neurotransmitter secretion and ventricular responses

The primary mode of neuronal communication is through the synthesis and secretion of neurotransmitters. Neurotransmitters are synthesized through enzymatic processes in neurons, where amino acids are converted into chemical messengers. Secretion of neurotransmitters activate receptors, signaling cascades, and gene transcription in receiving cell types. Two neurotransmitters primarily regulate cardiac function, norepinephrine (NE) and acetylcholine (ACh), which are released from postsynaptic sympathetic and parasympathetic axons, respectively. The release of neurotransmitters onto the pacemakers, the SA and AV nodes, will lead to a cascade that impacts ventricular function, while other effects are the result of direct neurotransmission in ventricular cells. The release of neurotransmitters ultimately dictates the physiological responses of the cardiovascular system.

Activation of the sympathetic "fight or flight" nerves is linked with heightened autonomic responses, such as increased heart rate (chronotropy), contractility (inotropy), and conduction (dromotropy). The presynaptic sympathetic nerves secrete ACh, exciting postganglionic neurons by binding to nicotinic acetylcholine receptors. Postsynaptic sympathetic nerves rely on Tyrosine Hydroxylase (TH) for biosynthesis of catecholamines, the precursors of NE. Secretion of NE targets adrenergic receptors (α_1AR, α_2AR, β_1AR, β_2AR) in the receiving cell type. β_1AR is the predominant receptor subtype expressed in the heart, expressed in SA and AV nodal cells and ventricular cardiomyocytes. In the vascular smooth muscle cells, αAR receptors are expressed, allowing for NE activate vasoconstriction[67].

The parasympathetic “rest and digest” nerves are linked with reduced autonomic activity, antagonizing the chronotropic, inotropic, and dromotropic effects. The presynaptic and postsynaptic parasympathetic nerves both release ACh, which is synthesized by choline acetyltransferase (ChAT). Secretion of ACh will target binding to muscarinic acetylcholine receptors (M_2 and M_3) on innervated cell types. The release of ACh on M_2-expressing atrial and nodal cells will decrease conduction velocity and contractility. The vascular endothelium is also responsive to ACh, where its binding to M_3 receptors stimulates vasodilation[68].

Sensory nerves are responsible for relaying sensations from the heart back to the central nervous system. Sensory nerves utilize the neurotransmitter glutamate. The sensory signals are transmitted from baroreceptors towards the peripheral and central nervous system to provide mechanical and chemical feedback. This creates the baroreceptor reflex, where baroreceptors on the aortic arch relay information on oxygen and nutrient consumption, as well as blood pressure[69]. The feedback from sensory nerves onto receiving ganglia in the central nervous system initiates a feedback response of efferent sympathetic and parasympathetic nerves, closing the cardiac neurocircuit and promoting heart rate regulation and homeostasis[70].

Neurocardiac axis at homeostasis

Nerves are master regulators of cardiovascular physiology. The heart is challenged to respond across a wide gradient of physiological conditions to modulate cardiac output. The neurocardiac axis facilitates rapid communication between nerves and a variety of cells in the ventricles including cardiomyocytes, vascular smooth muscle cells, and endothelial cells. Innervation across

diverse cell types allows for nerves to be an essential mediator of crosstalk and homeostasis in the ventricles.

Nerve and cardiomyocyte crosstalk

In the ventricles, nerve fibers can be found running parallel to the elongated cardiomyocytes[1]. The nerves use these tracks to exchange of information between nerves and cardiomyocytes. Technological advancements in microscopy have led to the anatomical structure of the cardiac nerves terminals in the ventricles to be captured in subcellular resolution[37, 39]. This led to the discovery of the NCJ, a localized and bidirectional signal axis between sympathetic nerves and cardiomyocytes[37, 39]. The NCJ and its junctional-type communication demonstrates the complexity of neural crosstalk in the cardiac ventricles.

Seminal research largely by Marco Mongillo's lab has captured the architecture of the neuro-cardiac junction (NCJ) and further defined its function[1, 37-39, 71]. Anatomically, the group demonstrated that the sympathetic neural network is expansive, creating multiple contacts with nearly all cardiomyocytes in the human and rodent ventricles[1, 37]. It is now estimated that cardiomyocytes are innervated to a similar degree as they are vascularized[1]. The sympathetic nerves communicate in regions with varicosities, where neurotransmission can occur[37]. The varicosities show several contact points per cardiomyocyte from a single neuronal process, and potentially by multiple distinct neuronal contacts[1, 72]. Cellularly, sympathetic nerves stimulate cardiomyocyte contraction via their canonical β-AR-cAMP-PKA signaling pathway[73]. Later studies by the Mongillo group demonstrated that this signaling axis is bidirectional, with retrograde

signaling of cardiomyocyte derived NGF maintaining neuronal contact and health[39] (see Appendix). These findings highlight the role of the NCJ in regulating cardiac function at homeostasis.

Nerve signaling not only regulates cardiomyocyte contractility, but also intercellular processes related to cardiomyocyte size at homeostasis. A variety of studies have linked nerve dysfunction to altered trophic signaling in the heart. In adult mice, increased or decreased sympathetic nerve signaling leads cardiac hypertrophy or atrophy, respectivally[24, 71, 74, 75]. Zaglia et al recently linked the activation of proteolysis during atrophic remodeling as a mechanism for neuronal regulation of cardiomyocyte size[71]. Their results showed that denervated hearts provoked an upregulation of the proteolytic cell machinery, suggesting that constitutive β_2-AR signaling is needed to repress atrophy at homeostasis[1, 71, 76]. These findings demonstrate that a delicate balance of neuronal signaling is required for maintenance of cardiomyocyte size. Further studies are needed to identify the communication between parasympathetic nerves and cardiomyocytes to fully define the neurocardiac axis.

Neurovascular congruence and regulation of the coronary vessels

Neurovascular communication is give-and-take, where neuronal secretion of neurotransmitters and neuropeptides regulates vascular contractility and tension, and the vessels provide oxygen, nutrients, gas, and hormones to the nerves[77-79]. The crosstalk between the nerves and coronary vessels is multi-layered, as the vasculature is also regulated by feedback of heart rate, contractility, blood pressure, and nitric oxide (NO) levels (reviewed by Sheng et al. 2018).

Nerves regulate vasoactivity, either reducing or increasing vascular resistance, to meet the body's demand for oxygenated blood. As a general mechanism, vasoconstriction occurs in response to NE, whereas vasodilation is activated by ACh[78]. Sympathetic and parasympathetic nerves can influence both vasoconstriction and vasorelaxation. Secretion of NE by sympathetic nerves will target α_1AR receptors on smooth muscle cells to promote vasoconstriction[78]. ACh released by parasympathetic nerves can alter vascular resistance by binding to muscarinic receptors. In endothelial cells, ACh binding to M_3 receptors signals for increased NO and vasorelaxation. Conversely, in smooth muscle cells, ACh binds to M_2 or M_3 receptors, decreasing NO and promoting vasoconstriction[80].

Morphologically, peripheral nerves and vessels are patterned in proximity with similar arborization patterning[81], termed as neurovascular congruence. This cellular proximity bridges the nerves and arteries by junction-like connections. Anatomical studies in the heart have long noted the close localization between the nerves and coronary arteries[59]. Surprisingly, even with this knowledge and the established model of nerve-artery regulation, the neurovascular architecture in the heart is not well-defined. Since the cardiac nerves target the coronary arteries for innervation, this presumably builds a structure-function relationship in regulating cardiac blood flow. Yet, the neurovascular congruence of the nerve-artery patterning has only been captured in limited scope[42, 43, 59].

Anatomical studies in the human heart have revealed distinct patterns of nerve association with veins and arteries, strikingly similar to what has been discovered in the mouse heart[82]. Thus, the murine heart is an accessible model to precisely define neurovascular architecture. Identifying nerve-artery patterning under homeostatic conditions is an essential step to elucidating neural influence on coronary arteries in homeostasis and disease.

Nerves in Disease and Regeneration

An array of neurological complications can arise in heart conditions, including coronary artery disease, hypertension, heart failure, and ischemic injury, which have been the subject of many reviews[7, 47, 58, 83-85]. Here the focus is on the nerve pathology after a myocardial infarction (MI), as this has persistently been the leading cause of death worldwide[86] and causes heterogenous remodeling in all nerve subtypes[2-5]. The treatments currently available, such as beta-blockers, can reduce the pathological symptoms post-MI, however the myocardium and nerves remain impaired[83]. Regenerative medicine is a promising strategy on the horizon that could restore cardiac tissue and physiological function post-MI. The regenerated tissue would require proper innervation, performing in synchronicity with the uninjured myocardium to prevent ventricular arrhythmia and sudden cardiac death. Fortunately, adult nerve axons have innate plasticity that may be harnessed therapeutically[87, 88]. Better understanding of nerve pathology post-MI can provide promising avenues to promote nerve repair and tissue regeneration.

Sympathetic nerve pathology in the infarcted myocardium

A myocardial infarction leads to pathological nerve remodeling that creates an arrhythmogenic environment. Increased sympathetic drive, marked by elevated levels of NE, are associated with the pathology after an MI. Beta-blockers have been successful treatments to mitigate increased sympathetic input and aberrant function post-MI. Yet, heterogenous innervation in the myocardium remains, posing serious risk for heart failure and sudden cardiac death[42, 89-91]. An increased understanding of sympathetic nerve pathology post-MI is needed for the development of novel anti-arrhythmogenic treatments.

An MI causes denervation of sympathetic innervation in the left ventricle of dogs and humans[5, 91]. Upregulation of neurotrophic factors at the infarction site can cause sympathetic axon sprouting in canine hearts[90]. This leads to regions of sympathetic denervation and hyperinnervation, which are strongly correlated to ventricular arrythmias in the infarcted myocardium[42, 89-93]. How nerve remodeling contributes to arrhythmic conditions post-MI are still unclear, however, there is increasing evidence for disrupted sympathetic pattering and function as a causal source[83]. After MI, there is a compensatory increase in peripheral sympathetic drive, a hallmark of heart failure[83, 84]. Within the infarcted heart, remodeling of sympathetic innervation will lead to regions that are hypersensitive or desensitized to β-AR signaling[84]. This heterogeneity causes regional differences cardiomyocyte repolarization in response to β-AR activation, increasing arrythmia suseptibility[84].

Disruption of NGF secretion and signaling has also been proposed as a potential link to the arrhythmic landscape after MI[94]. In the healthy heart, NGF secretion maintains nerve contacts[39] and its receptor, TrkA, regulates sympathetic nerve firing patterns[95]. After an MI, NGF levels are increased in the border zone and can stimulate sympathetic hyperinnervation in mouse and canine models[90, 96]. Moreover, inhibition of NGF attenuates sympathetic hyperinnervation and cardiac dysfunction after MI injury in rats[97]. Thus, atypical NGF secretion in combination with altered NGF-TrKA signaling after an MI may lead to disrupted sympathetic nerve patterning and firing, creating a pro-arrhythmic environment. Identifying the cellular pathophysiology in nerve remodeling and arrythmias will be important for the discovery of new therapeutic targets.

The cardioprotective role of the parasympathetic nerves

The parasympathetic nerves are a mediator of cardiac injury and repair, yet their basic influence in the ventricles remains largely unknown. Research continues to suggest that parasympathetic nerves may hold powerful therapeutic potential. Activation of parasympathetic innervation shows cardioprotective effects in preventing ventricular arrhythmias. Vagal nerve stimulation (VNS) has attempted to harness these protective effects; however the clinical success has been limited[6]. The lack of clinical translations with VNS highlights an unmet need to discover mechanisms to restore parasympathetic nerve influence in the infarcted myocardium.

Pathological remodeling occurs in parasympathetic nerves following MI. Parasympathetic nerves begin to degenerate in as little as 5-20 minutes after MI in the canine heart and continue to progress over time[5]. The result is a heterogenous heart with abnormal vagal signaling[5, 98]. Vagal

nerve dysfunction is not well understood. Abnormal vagal activity has been independently linked with both abnormal heart rate variability and baroreceptor sensitivity, increasing the risk for sudden cardiac death[99]. Although the overall vagal tone decreases post-MI, the changes in ACh levels are preserved in non-infarcted and border zone myocardium[3]. Even at 6-8 weeks post-MI, ACh levels appear to be preserved in the infarcted heart[3, 100]. This suggests that restoring parasympathetic nerve patterning and function may be a promising therapeutic option.

Vagal stimulation has been used as a therapy to improve cardiac response after injury, however its application has not been clinically successful[6]. Yet, in a variety of animal models, electrical VNS shows cardioprotective effects after MI injury[3, 101-106]. Specifically, VNS can reduce ventricular arrhythmias by decreasing ventricular excitability post-MI. These effects are a result of reduced ventricular tachyarrhythmia inducibility at the arrhythmogenic boarder zone regions in the porcine heart[3]. VNS also modulates the systemic proinflammatory immune response[107-110]. Thus, promoting parasympathetic reinnervation of the ventricles post-MI may also inherently promote immune resolution and cardiac repair. Further studies are required to elucidate conserved pathways activated by VNS that may be harnessed therapeutically in the human heart.

The ischemic response and cardioprotective role of sensory nerves

Sensory nerves provide life-saving sensory signals of chest pain, or angina, to those suffering an MI. Sensory nerve denervation heightens the risk for an asymptomatic “silent” MI, prevalent in diabetic patients[111, 112]. The sensory nerves not only provide signals for pain, but also mediate cardioprotection[113-115]. After ischemic injury, sensory nerve signaling is essential to mitigate

cardiovascular injury[115]. Yet, the subsequent damages in sensory nerve signaling after MI are not well understood.

Sensory nerves and their related neuropeptides play an important role in mitigating the effects of an MI[113-115]. In rats, treatment with capsaicin was used to induce degeneration of capsaicin-sensitive sensory nerves[113]. Subsequent MI injury demonstrated that rats with sensory nerve degeneration had exacerbated MI injury. Notably, this was correlated with a decrease in neurotrophic factors in rodent and porcine models[113, 116]. The ability of the sensory nerves to ameliorate cardiac injury is related to the capsaicin-sensitive pathway, where capsaicin binds and activates the transient receptor potential vanilloid type 1 (TRPV1) receptor[114]. Genetic knockout of TRPV1 impaired recovery after ischemia-reperfusion injury in mice[117]. Comparably, activation of TRPV1 can promote cardiac repair after ischemia-reperfusion injury[118]. Together, these results highlight that sensory nerve signaling has a cardioprotective role.

Recent work has shown that extensive remodeling of the sensory nerves occurs post-MI. The sensory nerves become hyperinnervated in the border zone and denervated in the infarction zone[2], similar to the remodeling of sympathetic axons[42]. This pathological remodeling of the sensory nerves post-MI serves as a basis for future studies to explore the affected neurocircuit and related pathways. Identifying the pathways underpinning sensory nerve function and cardioprotection will provide therapeutic insights for cardiac injury.

Nerve plasticity and repair in the heart

Neonatal mouse heart regeneration is independently regulated by parasympathetic and sympathetic nerves, where inhibition of either subtype will impair heart regeneration[119, 120]. Moreover, cardiomyocyte proliferation in the neonatal mouse is regulated by neuronal signaling via adrenergic receptors[121] and neurotrophic factors[120]. Our lab along with others have identified that NGF can promote cardiomyocyte proliferation and cardiac regeneration after injury[120, 122, 123]. Thus, the neonatal heart provides a window into understanding the pathways and mechanisms of axon repair and cardiac regeneration in the mammalian heart.

Most strikingly, nerve function appears to be reestablished in the regenerated neonatal heart, where mice regain contractile function and show no signs of arrhythmias[124]. This suggests that the regenerated neonatal heart undergoes physiological reinnervation in the cardiac ventricles. Interestingly, transplanted human hearts can be reinnervated by sympathetic and parasympathetic nerves of the host, which correlates with improved cardiac function[87, 88]. However, the innervation of the transplanted heart is heterogenous, often being described by clinical cardiologists as “patchy,” due to the partial reinnervation phenotype. Ultimately these atypical nerve patterns can contribute to arrhythmogenesis and sudden cardiac death[87]. Nevertheless, this phenotype suggests that adult cardiac nerves may have a degree of plasticity following injury. Elucidating differences between the neonatal and adult heart can provide insights into pathways to elicit physiological, rather than pathological, reinnervation of the infarcted heart.

The development of regenerative therapies for the infarcted heart will require a deep understanding of proper nerve patterning and neurocircuitry in the heathy heart and how this can be reestablished in the regenerated heart. The regenerative response in the neonatal heart provides a unique model for defining the regaining of nerve function post-MI. Thus, the neonatal mouse can serve as a tool to identify the degree, architecture, and function of nerves in the regenerated mammalian heart. This also provides insight into the molecular mechanisms of nerve recruitment during regeneration. Insights into the pathways of neuronal repair will provide the foundational discoveries needed to promote proper reinnervation after MI.

Conclusion

The nerves are a pillar of cardiovascular function, establishing an expansive and complex network within the cardiac ventricles. New discoveries highlight that neuronal regulation stretches beyond its canonical roles in controlling heart rate, contractility, and conduction, to now include non-canonical roles in regulating cardiomyocyte proliferation, hypertrophy, and proteolysis[40, 41, 71]. A myocardial infarction can damage nerve patterning and function, creating arrhythmogenic conditions[83]. Therapeutically, the nerves hold potential for promoting repair after myocardial injury, as nerve signaling provides cardioprotective and regenerative signals. Stimulating nerve repair relies on first detailing normal nerve anatomy and function. Accurately defining the organization and neurocircuitry of the intrinsic cardiac nerves during developmental, homeostatic, regenerative, and disease states will create a path for finding novel therapeutics to stimulate cardiac repair after injury.

REFERENCES

1. Zaglia T and Mongillo M. Cardiac sympathetic innervation, from a different point of (re)view. *J Physiol*. 2017;595:3919-3930.
2. Sahoglu SG, Kazci YE, Karadogan B, Aydin MS, Nebol A, Turhan MU, Ozturk G and Cagavi E. High-resolution mapping of sensory fibers at the healthy and post-myocardial infarct whole transgenic hearts. *Journal of Neuroscience Research*. 2023;101:338-353.
3. Vaseghi M, Salavatian S, Rajendran PS, Yagishita D, Woodward WR, Hamon D, Yamakawa K, Irie T, Habecker BA and Shivkumar K. Parasympathetic dysfunction and antiarrhythmic effect of vagal nerve stimulation following myocardial infarction. *JCI Insight*. 2017;2.
4. Zipes DP and Rubart M. Neural modulation of cardiac arrhythmias and sudden cardiac death. *Heart Rhythm*. 2006;3:108-13.
5. Inoue H and Zipes DP. Time course of denervation of efferent sympathetic and vagal nerves after occlusion of the coronary artery in the canine heart. *Circulation Research*. 1988;62:1111-1120.
6. Gold MR, Van Veldhuisen DJ, Hauptman PJ, Borggrefe M, Kubo SH, Lieberman RA, Milasinovic G, Berman BJ, Djordjevic S, Neelagaru S, Schwartz PJ, Starling RC and Mann DL. Vagus Nerve Stimulation for the Treatment of Heart Failure: The INOVATE-HF Trial. *J Am Coll Cardiol*. 2016;68:149-58.
7. Habecker BA, Anderson ME, Birren SJ, Fukuda K, Herring N, Hoover DB, Kanazawa H, Paterson DJ and Ripplinger CM. Molecular and cellular neurocardiology: development, and cellular and molecular adaptations to heart disease. *J Physiol*. 2016;594:3853-3875.
8. Kirby ML and Hutson MR. Factors controlling cardiac neural crest cell migration. *Cell Adh Migr*. 2010;4:609-621.
9. Butler SJ and Bronner ME. From classical to current: analyzing peripheral nervous system and spinal cord lineage and fate. *Dev Biol*. 2015;398:135-46.
10. Hildreth V, Webb S, Bradshaw L, Brown NA, Anderson RH and Henderson DJ. Cells migrating from the neural crest contribute to the innervation of the venous pole of the heart. *J Anat*. 2008;212:1-11.
11. Kirby ML. Nodose placode contributes autonomic neurons to the heart in the absence of cardiac neural crest. *J Neurosci*. 1988;8:1089-1095.
12. Bhatt S, Diaz R and Trainor PA. Signals and switches in Mammalian neural crest cell differentiation. *Cold Spring Harb Perspect Biol*. 2013;5:a008326.
13. Végh AMD, Duim SN, Smits AM, Poelmann RE, Ten Harkel ADJ, DeRuiter MC, Goumans MJ and Jongbloed MRM. Part and Parcel of the Cardiac Autonomic Nerve System: Unravelling Its Cellular Building Blocks during Development. *Journal of cardiovascular development and disease*. 2016;3:28.
14. Jiang X, Rowitch DH, Soriano P, McMahon AP and Sucov HM. Fate of the mammalian cardiac neural crest. *Development*. 2000;127:1607.
15. White PM, Morrison SJ, Orimoto K, Kubu CJ, Verdi JM and Anderson DJ. Neural Crest Stem Cells Undergo Cell-Intrinsic Developmental Changes in Sensitivity to Instructive Differentiation Signals. *Neuron*. 2001;29:57-71.

16. Tony L. Creazzo, Godt RE, Linda Leatherbury, Simon J. Conway a and Kirby ML. ROLE OF CARDIAC NEURAL CREST CELLS IN CARDIOVASCULAR DEVELOPMENT. *Annual Review of Physiology*. 1998;60:267-286.
17. Kimura K, Ieda M and Fukuda K. Development, maturation, and transdifferentiation of cardiac sympathetic nerves. *Circ Res*. 2012;110:325-36.
18. Tessier-Lavigne M and Goodman CS. The molecular biology of axon guidance. *Science*. 1996;274:1123-33.
19. Nam J, Onitsuka I, Hatch J, Uchida Y, Ray S, Huang S, Li W, Zang H, Ruiz-Lozano P and Mukouyama YS. Coronary veins determine the pattern of sympathetic innervation in the developing heart. *Development*. 2013;140:1475-85.
20. Korsching S and Thoenen H. Developmental changes of nerve growth factor levels in sympathetic ganglia and their target organs. *Dev Biol*. 1988;126:40-6.
21. Ieda M, Fukuda K, Hisaka Y, Kimura K, Kawaguchi H, Fujita J, Shimoda K, Takeshita E, Okano H, Kurihara Y, Kurihara H, Ishida J, Fukamizu A, Federoff HJ and Ogawa S. Endothelin-1 regulates cardiac sympathetic innervation in the rodent heart by controlling nerve growth factor expression. *J Clin Invest*. 2004;113:876-84.
22. Crowley C, Spencer SD, Nishimura MC, Chen KS, Pitts-Meek S, Armaninl MP, Ling LH, McMahon SB, Shelton DL and Levinson AD. Mice lacking nerve growth factor display perinatal loss of sensory and sympathetic neurons yet develop basal forebrain cholinergic neurons. *Cell*. 1994;76:1001-1011.
23. Fagan AM, Zhang H, Landis S, Smeyne RJ, Silos-Santiago I and Barbacid M. TrkA, but not TrkC, receptors are essential for survival of sympathetic neurons in vivo. *Journal of Neuroscience*. 1996;16:6208-6218.
24. Hassankhani A, Steinhelper ME, Soonpaa MH, Katz EB, Taylor DA, Andrade-Rozental A, Factor SM, Steinberg JJ, Field LJ and Federoff HJ. Overexpression of NGF within the heart of transgenic mice causes hyperinnervation, cardiac enlargement, and hyperplasia of ectopic cells. *Developmental biology*. 1995;169:309-321.
25. Rana OR, Saygili E, Gemein C, Zink MD, Buhr A, Saygili E, Mischke K, Nolte KW, Weis J and Weber C. Chronic electrical neuronal stimulation increases cardiac parasympathetic tone by eliciting neurotrophic effects. *Circulation research*. 2011;108:1209-1219.
26. Belliveau DJ, Krivko I, Kohn J, Lachance C, Pozniak C, Rusakov D, Kaplan D and Miller FD. NGF and neurotrophin-3 both activate TrkA on sympathetic neurons but differentially regulate survival and neuritogenesis. *The Journal of cell biology*. 1997;136:375-388.
27. Francis N, Farinas I, Brennan C, Rivas-Plata K, Backus C, Reichardt L and Landis S. NT-3, like NGF, Is Required for Survival of Sympathetic Neurons, but Not Their Precursors. *Developmental Biology*. 1999;210:411-427.
28. Kuruvilla R, Zweifel LS, Glebova NO, Lonze BE, Valdez G, Ye H and Ginty DD. A neurotrophin signaling cascade coordinates sympathetic neuron development through differential control of TrkA trafficking and retrograde signaling. *Cell*. 2004;118:243-55.
29. Hiltunen JO, Laurikainen A, Airaksinen MS and Saarma M. GDNF family receptors in the embryonic and postnatal rat heart and reduced cholinergic innervation in mice hearts lacking Ret or GFRα2. *Developmental Dynamics*. 2000;219:28-39.
30. Baloh RH, Enomoto H, Johnson EM, Jr. and Milbrandt J. The GDNF family ligands and receptors - implications for neural development. *Curr Opin Neurobiol*. 2000;10:103-10.

31. Martinelli PM, Camargos ER, Morel G, Tavares CA, Nagib PR and Machado CR. Rat heart GDNF: effect of chemical sympathectomy. *Histochemistry and Cell Biology*. 2002;118:337-343.
32. Heuckeroth RO, Enomoto H, Grider JR, Golden JP, Hanke JA, Jackman A, Molliver DC, Bardgett ME, Snider WD, Johnson EM, Jr. and Milbrandt J. Gene targeting reveals a critical role for neurturin in the development and maintenance of enteric, sensory, and parasympathetic neurons. *Neuron*. 1999;22:253-63.
33. Ieda M, Kanazawa H, Kimura K, Hattori F, Ieda Y, Taniguchi M, Lee J-K, Matsumura K, Tomita Y, Miyoshi S, Shimoda K, Makino S, Sano M, Kodama I, Ogawa S and Fukuda K. Sema3a maintains normal heart rhythm through sympathetic innervation patterning. *Nature Medicine*. 2007;13:604-612.
34. Nangle MR and Keast JR. Semaphorin 3A inhibits growth of adult sympathetic and parasympathetic neurones via distinct cyclic nucleotide signalling pathways. *Br J Pharmacol*. 2011;162:1083-95.
35. Kolodkin AL and Tessier-Lavigne M. Mechanisms and molecules of neuronal wiring: a primer. *Cold Spring Harb Perspect Biol*. 2011;3.
36. Hildreth V, Anderson R and Henderson D. Autonomic Innervation of the Developing Heart: Origins and Function. *Clinical anatomy (New York, NY)*. 2009;22:36-46.
37. Prando V, Da Broi F, Franzoso M, Plazzo AP, Pianca N, Francolini M, Basso C, Kay MW, Zaglia T and Mongillo M. Dynamics of neuroeffector coupling at cardiac sympathetic synapses. *J Physiol*. 2018;596:2055-2075.
38. Pianca N, Di Bona A, Lazzeri E, Costantini I, Franzoso M, Prando V, Armani A, Rizzo S, Fedrigo M, Angelini A, Basso C, Pavone FS, Rubart M, Sacconi L, Zaglia T and Mongillo M. Cardiac sympathetic innervation network shapes the myocardium by locally controlling cardiomyocyte size through the cellular proteolytic machinery. *J Physiol*. 2019;597:3639-3656.
39. Dokshokova L, Franzoso M, Di Bona A, Moro N, Sanchez Alonso JL, Prando V, Sandre M, Basso C, Faggian G, Abriel H, Marin O, Gorelik J, Zaglia T and Mongillo M. Nerve growth factor transfer from cardiomyocytes to innervating sympathetic neurons activates TrkA receptors at the neuro-cardiac junction. *J Physiol*. 2022;600:2853-2875.
40. Tampakakis E, Gangrade H, Glavaris S, Htet M, Murphy S, Lin BL, Liu T, Saberi A, Miyamoto M, Kowalski W, Mukouyama YS, Lee G, Minichiello L and Kwon C. Heart neurons use clock genes to control myocyte proliferation. *Sci Adv*. 2021;7:eabh4181.
41. Kreipke RE and Birren SJ. Innervating sympathetic neurons regulate heart size and the timing of cardiomyocyte cell cycle withdrawal. *The Journal of Physiology*. 2015;593:5057-5073.
42. Yokoyama T, Lee JK, Miwa K, Opthof T, Tomoyama S, Nakanishi H, Yoshida A, Yasui H, Iida T, Miyagawa S, Okabe S, Sawa Y, Sakata Y and Komuro I. Quantification of sympathetic hyperinnervation and denervation after myocardial infarction by three-dimensional assessment of the cardiac sympathetic network in cleared transparent murine hearts. *PLoS One*. 2017;12:e0182072.
43. Belle M, Godefroy D, Couly G, Malone SA, Collier F, Giacobini P and Chédotal A. Tridimensional Visualization and Analysis of Early Human Development. *Cell*. 2017;169:161-173.e12.
44. Mukouyama YS, Gerber HP, Ferrara N, Gu C and Anderson DJ. Peripheral nerve-derived VEGF promotes arterial differentiation via neuropilin 1-mediated positive feedback. *Development*. 2005;132:941-52.

45. James JM and Mukouyama Y-s. Neuronal action on the developing blood vessel pattern. *Seminars in cell & developmental biology*. 2011;22:1019-1027.
46. Rajendran PS, Challis RC, Fowlkes CC, Hanna P, Tompkins JD, Jordan MC, Hiyari S, Gabris-Weber BA, Greenbaum A, Chan KY, Deverman BE, Münzberg H, Ardell JL, Salama G, Gradinaru V and Shivkumar K. Identification of peripheral neural circuits that regulate heart rate using optogenetic and viral vector strategies. *Nature Communications*. 2019;10:1944.
47. Wink J, van Delft R, Notenboom RGE, Wouters PF, DeRuiter MC, Plevier JWM and Jongbloed MRM. Human adult cardiac autonomic innervation: Controversies in anatomical knowledge and relevance for cardiac neuromodulation. *Auton Neurosci*. 2020;227:102674.
48. Yujuan S, Justinn B, Abigail J, Jinhao X, Jamie MV and Xin S. Mapping the Central and Peripheral Projections of Lung Innervating Sensory Neurons. *bioRxiv*. 2021:2021.05.05.442702.
49. Pather N, Partab P, Singh B and Satyapal KS. Cervico-thoracic ganglion: Its clinical implications. *Clinical Anatomy*. 2006;19:323-326.
50. Pardini BJ, Lund DD and Schmid PG. Innervation patterns of the middle cervical--stellate ganglion complex in the rat. *Neurosci Lett*. 1990;117:300-6.
51. Clyburn C, Andresen MC, Ingram SL and Habecker BA. Untangling Peripheral Sympathetic Neurocircuits. *Front Cardiovasc Med*. 2022;9:842656.
52. Rysevaite K, Saburkina I, Pauziene N, Vaitkevicius R, Noujaim SF, Jalife J and Pauza DH. Immunohistochemical characterization of the intrinsic cardiac neural plexus in whole-mount mouse heart preparations. *Heart Rhythm*. 2011;8:731-8.
53. Kawashima T. The autonomic nervous system of the human heart with special reference to its origin, course, and peripheral distribution. *Anatomy and Embryology*. 2005;209:425-438.
54. Hoard JL, Hoover DB, Mabe AM, Blakely RD, Feng N and Paolocci N. Cholinergic neurons of mouse intrinsic cardiac ganglia contain noradrenergic enzymes, norepinephrine transporters, and the neurotrophin receptors tropomyosin-related kinase A and p75. *Neuroscience*. 2008;156:129-142.
55. Ge Y, van Roon L, van Gils JM, Geestman T, van Munsteren CJ, Smits AM, Goumans M, DeRuiter MC and Jongbloed MRM. Acute myocardial infarction induces remodeling of the murine superior cervical ganglia and the carotid body. *Front Cardiovasc Med*. 2022;9:758265.
56. Bosnjak ZJ and Kampine JP. Electrophysiological and morphological characterization of neurons in stellate ganglion of cats. *American Journal of Physiology-Regulatory, Integrative and Comparative Physiology*. 1985;248:R288-R292.
57. Potter D, Landis S, Matsumoto S and Furshpan E. Synaptic functions in rat sympathetic neurons in microcultures. II. Adrenergic/cholinergic dual status and plasticity. *The Journal of Neuroscience*. 1986;6:1080-1098.
58. Zandstra TE, Notenboom RGE, Wink J, Kiès P, Vliegen HW, Egorova AD, Schalij MJ, De Ruiter MC and Jongbloed MRM. Asymmetry and Heterogeneity: Part and Parcel in Cardiac Autonomic Innervation and Function. *Front Physiol*. 2021;12:665298.
59. Woollard HH. The Innervation of the Heart. *J Anat*. 1926;60:345-73.
60. Coote JH. Myths and realities of the cardiac vagus. *J Physiol*. 2013;591:4073-85.
61. Hirsch E and Borghard-Erdle A. The innervation of the human heart. I. The coronary arteries and the myocardium. *Archives of pathology*. 1961;71:384-407.

62. Vegh AMD, Duim SN, Smits AM, Poelmann RE, Ten Harkel ADJ, DeRuiter MC, Goumans MJ and Jongbloed MRM. Part and Parcel of the Cardiac Autonomic Nerve System: Unravelling Its Cellular Building Blocks during Development. *J Cardiovasc Dev Dis*. 2016;3.
63. Kawano H, Okada R and Yano K. Histological study on the distribution of autonomic nerves in the human heart. *Heart and vessels*. 2003;18:32.
64. Ulphani JS, Cain JH, Inderyas F, Gordon D, Gikas PV, Shade G, Mayor D, Arora R, Kadish AH and Goldberger JJ. Quantitative analysis of parasympathetic innervation of the porcine heart. *Heart rhythm*. 2010;7:1113-1119.
65. Zahner MR, Li DP, Chen SR and Pan HL. Cardiac vanilloid receptor 1-expressing afferent nerves and their role in the cardiogenic sympathetic reflex in rats. *J Physiol*. 2003;551:515-23.
66. Wang T and Miller KE. Characterization of glutamatergic neurons in the rat atrial intrinsic cardiac ganglia that project to the cardiac ventricular wall. *Neuroscience*. 2016;329:134-50.
67. Gordan R, Gwathmey JK and Xie LH. Autonomic and endocrine control of cardiovascular function. *World J Cardiol*. 2015;7:204-14.
68. Brodde OE and Michel MC. Adrenergic and muscarinic receptors in the human heart. *Pharmacol Rev*. 1999;51:651-90.
69. Min S, Chang RB, Prescott SL, Beeler B, Joshi NR, Strochlic DE and Liberles SD. Arterial Baroreceptors Sense Blood Pressure through Decorated Aortic Claws. *Cell Reports*. 2019;29:2192-2201.e3.
70. Coleridge HM and Coleridge JC. Cardiovascular afferents involved in regulation of peripheral vessels. *Annu Rev Physiol*. 1980;42:413-27.
71. Zaglia T, Milan G, Franzoso M, Bertaggia E, Pianca N, Piasentini E, Voltarelli VA, Chiavegato D, Brum PC, Glass DJ, Schiaffino S, Sandri M and Mongillo M. Cardiac sympathetic neurons provide trophic signal to the heart via β2-adrenoceptor-dependent regulation of proteolysis. *Cardiovascular Research*. 2012;97:240-250.
72. Freeman K, Tao W, Sun H, Soonpaa MH and Rubart M. In situ three-dimensional reconstruction of mouse heart sympathetic innervation by two-photon excitation fluorescence imaging. *J Neurosci Methods*. 2014;221:48-61.
73. Sampson KJ and Kass RS. Molecular mechanisms of adrenergic stimulation in the heart. *Heart Rhythm*. 2010;7:1151-1153.
74. Kiriazis H, Du X-J, Feng X, Hotchkin E, Marshall T, Finch S, Gao X-M, Lambert G, Choate JK and Kaye DM. Preserved left ventricular structure and function in mice with cardiac sympathetic hyperinnervation. *American Journal of Physiology-Heart and Circulatory Physiology*. 2005;289:H1359-H1365.
75. Ryall JG, Sillence MN and Lynch GS. Systemic administration of β2-adrenoceptor agonists, formoterol and salmeterol, elicit skeletal muscle hypertrophy in rats at micromolar doses. *British journal of pharmacology*. 2006;147:587-595.
76. Zaglia T, Milan G, Ruhs A, Franzoso M, Bertaggia E, Pianca N, Carpi A, Carullo P, Pesce P, Sacerdoti D, Sarais C, Catalucci D, Krüger M, Mongillo M and Sandri M. Atrogin-1 deficiency promotes cardiomyopathy and premature death via impaired autophagy. *The Journal of Clinical Investigation*. 2014;124:2410-2424.
77. Kingma JG, Simard D and Rouleau JR. Influence of cardiac nerve status on cardiovascular regulation and cardioprotection. *World J Cardiol*. 2017;9:508-520.

78. Sheng Y and Zhu L. The crosstalk between autonomic nervous system and blood vessels. *International journal of physiology, pathophysiology and pharmacology*. 2018;10:17-28.
79. Burnstock G and Ralevic V. New insights into the local regulation of blood flow by perivascular nerves and endothelium. *British Journal of Plastic Surgery*. 1994;47:527-543.
80. Bolton TB and Lim SP. Action of acetylcholine on smooth muscle. *Z Kardiol*. 1991;80 Suppl 7:73-7.
81. Meng B, Pang A and Li M. Principle of relative positioning of structures in the human body. *Neural Regen Res*. 2013;8:853-6.
82. Watanabe Y, Arakawa T, Kageyama I, Aizawa Y, Kumaki K, Miki A and Terashima T. Gross anatomical study on the human myocardial bridges with special reference to the spatial relationship among coronary arteries, cardiac veins, and autonomic nerves. *Clinical Anatomy*. 2016;29:333-341.
83. Zekios KC, Mouchtouri ET, Lekkas P, Nikas DN and Kolettis TM. Sympathetic Activation and Arrhythmogenesis after Myocardial Infarction: Where Do We Stand? *J Cardiovasc Dev Dis*. 2021;8.
84. Gardner RT, Ripplinger CM, Myles RC and Habecker BA. Molecular Mechanisms of Sympathetic Remodeling and Arrhythmias. *Circ Arrhythm Electrophysiol*. 2016;9:e001359.
85. Cao JM, Chen LS, KenKnight BH, Ohara T, Lee MH, Tsai J, Lai WW, Karagueuzian HS, Wolf PL, Fishbein MC and Chen PS. Nerve sprouting and sudden cardiac death. *Circ Res*. 2000;86:816-21.
86. (WHO) WHO. Cause-specific mortality, 2000–2019. 2020;2020.
87. Awad M, Czer LSC, Hou M, Golshani SS, Goltche M, De Robertis M, Kittleson M, Patel J, Azarbal B, Kransdorf E, Esmailian F, Trento A and Kobashigawa JA. Early Denervation and Later Reinnervation of the Heart Following Cardiac Transplantation: A Review. *Journal of the American Heart Association*. 2016;5:e004070.
88. Schwaiblmair M, von Scheidt W, Überfuhr P, Ziegler S, Schwaiger M, Reichart B and Vogelmeier C. Functional significance of cardiac reinnervation in heart transplant recipients. *The Journal of Heart and Lung Transplantation*. 1999;18:838-845.
89. Li W, Knowlton D, Van Winkle DM and Habecker BA. Infarction alters both the distribution and noradrenergic properties of cardiac sympathetic neurons. *American Journal of Physiology-Heart and Circulatory Physiology*. 2004;286:H2229-H2236.
90. Zhou S, Chen LS, Miyauchi Y, Miyauchi M, Kar S, Kangavari S, Fishbein MC, Sharifi B and Chen P-S. Mechanisms of cardiac nerve sprouting after myocardial infarction in dogs. *Circulation research*. 2004;95:76-83.
91. Stanton MS, Tuli MM, Radtke NL, Heger JJ, Miles WM, Mock BH, Burt RW, Wellman HN and Zipes DP. Regional sympathetic denervation after myocardial infarction in humans detected noninvasively using I-123-metaiodobenzylguanidine. *Journal of the American College of Cardiology*. 1989;14:1519-1526.
92. Hartikainen J, Kuikka J, Mäntysaari M, Länsimies E and Pyörälä K. Sympathetic reinnervation after acute myocardial infarction. *The American journal of cardiology*. 1996;77:5-9.
93. Cao J-M, Fishbein MC, Han JB, Lai WW, Lai AC, Wu T-J, Czer L, Wolf PL, Denton TA, Shintaku IP, Chen P-S and Chen LS. Relationship Between Regional Cardiac Hyperinnervation and Ventricular Arrhythmia. *Circulation*. 2000;101:1960-1969.

94. Govoni S, Pascale A, Amadio M, Calvillo L, D'Elia E, Cereda C, Fantucci P, Ceroni M and Vanoli E. NGF and heart: Is there a role in heart disease? *Pharmacological Research*. 2011;63:266-277.
95. Luther JA and Birren SJ. p75 and TrkA signaling regulates sympathetic neuronal firing patterns via differential modulation of voltage-gated currents. *J Neurosci*. 2009;29:5411-24.
96. Oh YS, Jong AY, Kim DT, Li H, Wang C, Zemljic-Harpf A, Ross RS, Fishbein MC, Chen PS and Chen LS. Spatial distribution of nerve sprouting after myocardial infarction in mice. *Heart Rhythm*. 2006;3:728-36.
97. Hu H, Xuan Y, Wang Y, Xue M, Suo F, Li X, Cheng W, Li X, Yin J, Liu J and Yan S. Targeted NGF siRNA delivery attenuates sympathetic nerve sprouting and deteriorates cardiac dysfunction in rats with myocardial infarction. *PLoS One*. 2014;9:e95106.
98. Vaseghi M, Gima J, Kanaan C, Ajijola OA, Marmureanu A, Mahajan A and Shivkumar K. Cardiac sympathetic denervation in patients with refractory ventricular arrhythmias or electrical storm: intermediate and long-term follow-up. *Heart Rhythm*. 2014;11:360-6.
99. Vaseghi M and Shivkumar K. The role of the autonomic nervous system in sudden cardiac death. *Prog Cardiovasc Dis*. 2008;50:404-19.
100. La Rovere MT, Bigger JT, Jr., Marcus FI, Mortara A and Schwartz PJ. Baroreflex sensitivity and heart-rate variability in prediction of total cardiac mortality after myocardial infarction. ATRAMI (Autonomic Tone and Reflexes After Myocardial Infarction) Investigators. *Lancet*. 1998;351:478-84.
101. Rosenshtraukh L, Danilo P, Jr., Anyukhovsky EP, Steinberg SF, Rybin V, Brittain-Valenti K, Molina-Viamonte V and Rosen MR. Mechanisms for vagal modulation of ventricular repolarization and of coronary occlusion-induced lethal arrhythmias in cats. *Circ Res*. 1994;75:722-32.
102. Myers RW, Pearlman AS, Hyman RM, Goldstein RA, Kent KM, Goldstein RE and Epstein SE. Beneficial effects of vagal stimulation and bradycardia during experimental acute myocardial ischemia. *Circulation*. 1974;49:943-7.
103. Kong SS, Liu JJ, Hwang TC, Yu XJ, Zhao M, Zhao M, Yuan BX, Lu Y, Kang YM, Wang B and Zang WJ. Optimizing the parameters of vagus nerve stimulation by uniform design in rats with acute myocardial infarction. *PLoS One*. 2012;7:e42799.
104. Ando M, Katare RG, Kakinuma Y, Zhang D, Yamasaki F, Muramoto K and Sato T. Efferent vagal nerve stimulation protects heart against ischemia-induced arrhythmias by preserving connexin43 protein. *Circulation*. 2005;112:164-70.
105. Shinlapawittayatorn K, Chinda K, Palee S, Surinkaew S, Kumfu S, Kumphune S, Chattipakorn S, KenKnight BH and Chattipakorn N. Vagus nerve stimulation initiated late during ischemia, but not reperfusion, exerts cardioprotection via amelioration of cardiac mitochondrial dysfunction. *Heart Rhythm*. 2014;11:2278-87.
106. Beaumont E, Southerland EM, Hardwick JC, Wright GL, Ryan S, Li Y, KenKnight BH, Armour JA and Ardell JL. Vagus nerve stimulation mitigates intrinsic cardiac neuronal and adverse myocyte remodeling postmyocardial infarction. *Am J Physiol Heart Circ Physiol*. 2015;309:H1198-206.
107. Olofsson PS, Levine YA, Caravaca A, Chavan SS, Pavlov VA, Faltys M and Tracey KJ. Single-pulse and unidirectional electrical activation of the cervical vagus nerve reduces tumor necrosis factor in endotoxemia. *Bioelectronic Medicine*. 2015;2:37-42.

108. Borovikova LV, Ivanova S, Zhang M, Yang H, Botchkina GI, Watkins LR, Wang H, Abumrad N, Eaton JW and Tracey KJ. Vagus nerve stimulation attenuates the systemic inflammatory response to endotoxin. *Nature*. 2000;405:458-62.
109. Pavlov VA, Chavan SS and Tracey KJ. Molecular and Functional Neuroscience in Immunity. *Annu Rev Immunol*. 2018;36:783-812.
110. Olofsson PS, Rosas-Ballina M, Levine YA and Tracey KJ. Rethinking inflammation: neural circuits in the regulation of immunity. *Immunol Rev*. 2012;248:188-204.
111. Elliott MD, Heitner JF, Kim H, Wu E, Parker MA, Lee DC, Kaufman DB, Bonow RO, Judd R and Kim RJ. Prevalence and Prognosis of Unrecognized Myocardial Infarction in Asymptomatic Patients With Diabetes: A Two-Center Study With Up to 5 Years of Follow-up. *Diabetes Care*. 2019;42:1290-1296.
112. Nesto RW and Phillips RT. Asymptomatic myocardial ischemia in diabetic patients. *Am J Med*. 1986;80:40-7.
113. Zhang RL, Guo Z, Wang LL and Wu J. Degeneration of capsaicin sensitive sensory nerves enhances myocardial injury in acute myocardial infarction in rats. *Int J Cardiol*. 2012;160:41-7.
114. Wang Z, Ye D, Ye J, Wang M, Liu J, Jiang H, Xu Y, Zhang J, Chen J and Wan J. The TRPA1 Channel in the Cardiovascular System: Promising Features and Challenges. *Front Pharmacol*. 2019;10:1253.
115. Bencsik P, Gömöri K, Szabados T, Sántha P, Helyes Z, Jancsó G, Ferdinandy P and Görbe A. Myocardial ischaemia reperfusion injury and cardioprotection in the presence of sensory neuropathy: Therapeutic options. *Br J Pharmacol*. 2020;177:5336-5356.
116. Källner G and Franco-Cereceda A. Aggravation of myocardial infarction in the porcine heart by capsaicin-induced depletion of calcitonin gene-related peptide (CGRP). *J Cardiovasc Pharmacol*. 1998;32:500-4.
117. Wang L and Wang DH. TRPV1 gene knockout impairs postischemic recovery in isolated perfused heart in mice. *Circulation*. 2005;112:3617-23.
118. Zhong B and Wang DH. N-oleoyldopamine, a novel endogenous capsaicin-like lipid, protects the heart against ischemia-reperfusion injury via activation of TRPV1. *Am J Physiol Heart Circ Physiol*. 2008;295:H728-35.
119. White IA, Gordon J, Balkan W and Hare JM. Sympathetic Reinnervation Is Required for Mammalian Cardiac Regeneration. *Circulation research*. 2015;117:990-994.
120. Mahmoud AI, O'Meara CC, Gemberling M, Zhao L, Bryant DM, Zheng R, Gannon JB, Cai L, Choi W-Y, Egnaczyk GF, Burns CE, Burns CG, MacRae CA, Poss KD and Lee RT. Nerves Regulate Cardiomyocyte Proliferation and Heart Regeneration. *Dev Cell*. 2015;34:387-399.
121. Sakabe M, Thompson M, Chen N, Verba M, Hassan A, Lu R and Xin M. Inhibition of β1-AR/Gαs signaling promotes cardiomyocyte proliferation in juvenile mice through activation of RhoA-YAP axis. *eLife*. 2022;11:e74576.
122. Meloni M, Caporali A, Graiani G, Lagrasta C, Katare R, Van Linthout S, Spillmann F, Campesi I, Madeddu P, Quaini F and Emanueli C. Nerve growth factor promotes cardiac repair following myocardial infarction. *Circulation research*. 2010;106:1275-1284.
123. Lam NT, Currie PD, Lieschke GJ, Rosenthal NA and Kaye DM. Nerve growth factor stimulates cardiac regeneration via cardiomyocyte proliferation in experimental heart failure. *PLoS One*. 2012;7:e53210-e53210.

124. Porrello ER, Mahmoud AI, Simpson E, Hill JA, Richardson JA, Olson EN and Sadek HA. Transient regenerative potential of the neonatal mouse heart. *Science (New York, NY)*. 2011;331:1078-1080.

CHAPTER II: CAPTURING THE CARDIAC INJURY RESPONSE OF TARGETED CELL POPULATIONS VIA CLEARED HEART THREE-DIMENSIONAL IMAGING

Rebecca J. Salamon[1], Ziheng Zhang[1], Ahmed I. Mahmoud[1]*

[1]Department of Cell and Regenerative Biology, University of Wisconsin-Madison School of Medicine and Public Health

*Corresponding author: Ahmed I. Mahmoud, Ph.D. Email: aimahmoud@wisc.edu

Salamon RJ, Zhang Z, Mahmoud AI. Capturing the Cardiac Injury Response of Targeted Cell Populations via Cleared Heart Three-Dimensional Imaging. J Vis Exp. 2020 Mar 17;(157):10.3791/60482. doi: 10.3791/60482. PMID: 32250361; PMCID: PMC7530371.

AUTHOR CONTRIBUTIONS

R.J.S. designed and developed the methods and performed the experiments. R.J.S., Z.Z. and A.I.M. contributed to the preparation of the manuscript. A.I.M. conceived the approach.

SUMMARY

Cardiomyocyte proliferation following injury is a dynamic process that requires a symphony of extracellular cues from non-myocyte cell populations. Utilizing lineage tracing, passive CLARITY, and three-dimensional whole-mount confocal microscopy techniques, we can analyze the influence of a variety of cell types on cardiac repair and regeneration.

ABSTRACT

Cardiovascular disease outranks all other causes of death and is responsible for a staggering 31% of mortalities worldwide. This disease manifests in cardiac injury, primarily in the form of an acute myocardial infarction. With little resilience following injury, the once healthy cardiac tissue will be replaced by fibrous, non-contractile scar tissue and often be a prelude to heart failure. To identify novel treatment options in regenerative medicine, research has focused on vertebrates with innate regenerative capabilities. One such model organism is the neonatal mouse, which responds to cardiac injury with robust myocardial regeneration. In order to induce an injury in the neonatal mouse that is clinically relevant, we have developed a surgery to occlude the left anterior descending artery (LAD), mirroring a myocardial infarction triggered by atherosclerosis in the human heart. When matched with the technology to track changes both within cardiomyocytes and non-myocyte populations, this model provides us with a platform to identify the mechanisms that guide heart regeneration. Gaining insight into changes in cardiac cell populations following injury once relied heavily on methods such as tissue sectioning and histological examination, which are limited to two-dimensional analysis and often damage the tissue in the process. Moreover, these methods lack the ability to trace changes in cell lineages,

instead providing merely a snapshot of the injury response. Here, we describe how technologically advanced methods in lineage tracing models, whole organ clearing, and three-dimensional (3D) whole-mount microscopy can be used to elucidate mechanisms of cardiac repair. With our protocol for neonatal mouse myocardial infarction surgery, tissue clearing, and 3D whole organ imaging, the complex pathways that induce cardiomyocyte proliferation can be unraveled, revealing novel therapeutic targets for cardiac regeneration.

INTRODUCTION

The heart has long been considered to be a post-mitotic organ, yet recent evidence demonstrates that cardiomyocyte renewal occurs in the adult human heart at about 1% per year[1]. However, these low rates of cardiomyocyte turnover are insufficient to replenish the massive loss of tissue that occurs following injury. A heart that has suffered a myocardial infarction will lose around one billion cardiomyocytes, often serving as a prelude to heart failure and sudden cardiac death[2,3]. With over 26 million people affected by heart failure worldwide, there is an unmet need for therapeutics that can reverse the damages inflicted by heart disease[4].

In order to bridge this gap in therapeutics, scientists have begun investigating evolutionarily conserved mechanisms that underlie endogenous regeneration following injury. One model for studying mammalian cardiac regeneration is the neonatal mouse. Within the week following birth, neonatal mice have a robust regenerative response following cardiac damage[5]. We have previously demonstrated that neonatal mice can regenerate their heart via cardiomyocyte proliferation following an apical resection[5]. Although this technique can evoke cardiac regeneration in the neonates, the surgery lacks clinical relevance to human heart injuries. In order to mimic a human injury in the neonatal mouse model, we have developed a technique to induce a myocardial infarction through a coronary artery occlusion[6]. This technique requires surgical ligation of the left anterior descending artery (LAD), which is responsible for delivering 40%–50% of the blood to the left ventricular myocardium[6,7]. Thus, the surgery results in an infarct that impacts a significant portion of the left ventricular wall. This damage to the myocardium will stimulate cardiomyocyte proliferation and heart regeneration in neonates[5].

The coronary artery occlusion surgery provides a highly reproducible and directly translational method to uncover the inner workings of cardiac regeneration. The neonatal surgery parallels coronary artery atherosclerosis in the human heart, where accumulation of plaque within the inner walls of the arteries can cause an occlusion and subsequent myocardial infarction[8]. Due to a void in therapeutic treatments for heart failure patients, an occlusion in the LAD is associated with mortality rates reaching up to 26% within a year following injury[9], and consequently has been termed the "widow maker." Advancements in therapeutics require a model that accurately reflects the complex physiological and pathological effects of cardiac injury. Our surgical protocol for neonatal mouse cardiac injury provides a platform that allows researchers to investigate the molecular and cellular cues that signal mammalian heart regeneration after injury.

Recent research highlights the dynamic relationship between the extracellular environment and proliferating cardiomyocytes. For example, the postnatal regenerative window can be extended by decreasing the stiffness of the extracellular matrix surrounding the heart[10]. Biomaterials from the neonatal extracellular matrix can also promote heart regeneration in adult mammalian hearts following cardiac injury[11]. Also accompanying cardiomyocyte proliferation is an angiogenic response[12,13]; collateral artery formation unique to the regenerating heart of the neonatal mouse was shown to be essential for stimulating cardiac regeneration[12]. Moreover, our lab has demonstrated that nerve signaling regulates cardiomyocyte proliferation and heart regeneration via modulation of growth factor levels, as well as the inflammatory response following injury[14]. These findings emphasize the need to trace non-myocyte cell populations in response to cardiac

injury. In order to accomplish this goal, we have taken advantage of the Cre-lox recombination system in transgenic mice lines to incorporate constitutive or conditional expression of fluorescent reporter proteins for lineage tracing. Furthermore, we can use advanced methods to determine clonal expansion patterning with the Rainbow mouse line, which relies on stochastic expression of the Cre-dependent, multi-color fluorescent reporters to determine the clonal expansion of targeted cell populations[15]. Employing lineage tracing with the neonatal coronary artery occlusion surgery is a powerful tool for dissecting the intricate cellular mechanisms of cardiac regeneration.

Tracking the lineage of fluorescently labeled cells with three-dimensional (3D) whole organ imaging is difficult to achieve using traditional sectioning and reconstruction technique – especially when cell populations are fragile, such as nerve fibers or blood vessels. While direct whole-mount imaging of the organ by optical sectioning can capture superficial cell populations, structures that reside deep within the tissue remain inaccessible. To circumvent these barriers, tissue clearing techniques have been developed to reduce the opacity of whole organ tissues. Recently, significant advances have been made to Clear Lipid-exchanged Acrylamide-hybridized Rigid Imaging compatible Tissue hYdrogel (CLARITY)–based methods, which clear fixed tissue via lipid extraction[16]. Steps are also taken to homogenize the refractive index and subsequently reduce light scattering while imaging[17]. One such method is active CLARITY, which expedites lipid decomposition by using electrophoresis to penetrate the detergent throughout the tissue[18]. Although effective, this tissue clearing method requires expensive equipment and can cause tissue damage, making the approach incompatible with fragile cell populations such as the

cardiac nerves[19]. Thus, we employ the passive CLARITY approach, which relies on heat to gently facilitate detergent penetration, therefore aiding in the retention of intricate cell structures[20,21].

Passive CLARITY is typically thought to be less efficient than active CLARITY[18], as the technique is often accompanied by two major obstacles: the inability to clear the entire organ depth and the extensive amount of time required to clear adult tissues. Our passive CLARITY approach overcomes both of these barriers with an expeditated clearing process that is capable of fully clearing neonatal and adult heart tissue. Our passive CLARITY tissue clearing technique has reached an efficiency that permits the visualization of a variety of cardiac cell populations, including rare populations distributed throughout the adult heart. When the cleared heart is imaged with confocal microscopy, the architecture of cell-specific patterning during development, disease, and regeneration can be illuminated.

PROTOCOL

All experiments were conducted in accordance with the Guide for the Use and Care of Laboratory Animals and in compliance with the Institutional Animal Care and Use Committee in the School of Medicine and Public Health at the University of Wisconsin–Madison. All methods were performed on wild type C57BL/6J (B6) and transgenic mouse lines obtained from Jackson Laboratories.

1. Coronary Artery Occlusion (Myocardial Infarction) Induced via Ligation of the Left Anterior Descending Artery (LAD) in 1-Day-Old Neonatal Mice

1.1. Separate the 1-day-old neonatal pups from the mother by placing them into a clean cage along with some of the original nesting material.

1.2. Place half of the cage onto a heating pad set to medium heat. The pups should remain on the unheated side of the cage, only being placed onto the heated side after surgery.

1.3. Create a sterile surgical area under an operating microscope. Gather sterilized surgical equipment (**Table 1**).

1.4. Anesthetize the pup via hypothermia: wrap the pup in gauze to avoid direct skin contact with ice and bury it in an ice bed for approximately 3–4 min. Check hypothermia of the mice periodically by performing a toe pinch. Neonates tolerate hypothermia well, however, prolonged exposure to hypothermia may result in frostbite and subsequent mortality.

1.5. Once anesthetized, place the mouse onto the surgical area in the supine position, securing the arms and legs with tape. Sterilize the surgical area of the mouse with an antiseptic solution.

1.6. Locate the lower chest region and make a transverse incision in the skin with small dissecting scissors. To widen the surgical view of the ribs, separate the skin from the muscle by lifting the skin gently with a pair of dressing forceps and gently press against the intercostal muscles with the small scissors in the closed position.

1.7. Locate the fourth intercostal space (**Figure 1A**) and make a small, superficial puncture using sharp forceps, being careful not to puncture any internal organs. Perform a blunt dissection

by widening the area in between the intercostal muscles with dressing forceps. Proper anatomical positioning of the incision is essential for appropriate access to the heart.

1.8. Gently guide the heart out of the chest cavity by placing a finger and applying increasing pressure on the left side of the abdomen while holding the intercostal space open with dressing forceps (**Figure 1B**). Once the heart is outside of the chest, remove the dressing forceps, relieve pressure, and allow the heart to rest on the intercostal muscles.

1.9. Locate the LAD as the area of the heart that has less pooled blood and is in the correct anatomical position (**Figure 1C**). The LAD can be only seen under the microscope if the heart is accessed within a few minutes of beginning surgery.

1.10. Perform LAD ligation by suturing the LAD with a 6-0 suture (**Figure 1D**). Tie a square knot twice to induce myocardial infarction (**Figure 1E**). The depth of the suture into the myocardium may vary, however, proper anatomical positioning of the LAD ligation is crucial for reproducibility. When ligating the LAD, the suture should be pulled tightly but carefully so as not to sever the LAD. Blanching at the apex of the heart will be seen immediately (**Figure 1E**)

1.11. Allow the heart to slip back into the chest cavity; this process can be gently facilitated with dressing forceps. Suture the ribs together with a surgeon's knot followed by a square knot, using blunt forceps to lift the upper set of ribs while passing a 6-0 suture through the upper and lower set of ribs.

1.12. Remove the tape that was used to secure the hind legs of the pup.

1.13. Adhere the skin together by placing a small amount of skin glue on the upper abdomen. Then, grab the skin of the lower abdomen with fine forceps and cover the exposed chest

region. Limit the amount of excess glue that remains on the pups, as this can increase the likelihood of rejection and cannibalism by the mother.

1.14. Immediately facilitate the recovery from anesthesia by placing the pup onto a heating pad set to medium heat. Periodically switch the placement of the neonates to evenly warm all parts of the body.

1.15. Allow the neonate to remain directly on the heating pad for 10–15 min. Typically, movement is regained within 5 min of being placed onto heat.

1.16. Clean the residual blood and glue with an alcohol wipe.

1.17. Cover foreign scents on neonates by rubbing the entire body with bedding from the original cage. Place the pup into the cage on the heated side while other surgeries are being performed.

1.18. Once all surgeries are completed and pups are warm and mobile, transfer the litter along with the original nesting material to the mother's cage.

1.19. Monitor the mice for 30–60 min after surgery and watch for the mother's acceptance of the pups by nesting and/or grooming.

1.20. Check on the mice the morning following surgery. If mother is distressed and has not nested the pups, consider a foster mother for the pups.

2. Clearing the Mouse Heart with Passive CLARITY[21-23]

2.1. Anesthetize the mouse with isoflurane. Remove the animal from the cage and perform a toe pinch to ensure the mouse is fully sedated.

2.2. Place the mouse onto a clean, surgical area in the supine position, securing the arms and legs with tape.

2.3. Maintain isoflurane sedation on the mouse using a nose cone until the heart is extracted.

2.4. Open the lower chest by holding the fur just below the xiphoid process with tissue forceps and make an incision spanning the width of the ribcage using the large dissecting scissors.

2.5. Cut alongside of the distal portions of the rib cage with surgical scissors.

2.6. Expose the diaphragm muscle by grasping the xiphoid process with tissue forceps. Detach the diaphragm using curved forceps.

2.7. While maintaining a grasp of the xiphoid process, pull the tissue cranially until the beating heart is accessible.

2.8. Grasp the heart at the base with curved forceps and dissect the heart from the chest cavity by cutting the aorta and superior vena cava with iridectomy scissors.

2.9. While the heart is still beating, place the heart into a Petri dish filled with PBS so that the heart pumps out the blood inside as it keeps beating. Myocardial infarction can be confirmed by checking that the placement of the suture is in the proper anatomical position for LAD ligation.

2.10. Gently squeeze the heart with forceps to allow the heart to expel the residual blood.

2.11. Transfer the mouse heart into a disposable 2.5 mL glass shell vial with 2 mL of PBS. Wash away residual blood by incubating the heart on a shaker for 10 min at room temperature (RT) several times. Change the PBS solution each time until PBS remains clear.

2.12. Discard the PBS and fill the vial with 2 mL of cold 4% paraformaldehyde (PFA). Incubate for 4 hours at RT (**Figure 2A**).

2.13. After incubation, discard the PFA and the vial with 2 mL of PBS. Wash the heart on a shaker for 10 min at RT. Repeat the washing step twice, draining and filling the vial with new PBS each time to fully wash away excess PFA.

2.14. Discard PBS and fill the vial with 2 mL of 4% acrylamide and 0.5% VA-044 solution. Incubate overnight at 4 °C.

2.15. The next day, perform polymerization by transferring the vial to a heat block set at 37 °C for 3 hours.

2.16. Transfer the heart into a new glass shell vial and repeat step 2.12 (PBS wash cycle).

2.17. Discard PBS and fill the vial with 2 mL of Clearing Solution (**Table 2**). Incubate at 37 °C until the heart is cleared. Change out the solution and refill with fresh Clearing Solution every 2–3 days. The clearing process could take up to several weeks (**Figure 2B,C**).

NOTE: P1 hearts typically take around 3–5 days, whereas P21 hearts can take nearly a month before Clearing Solution incubation is complete.

2.18. Discard PBS and fill the vial with 2 mL of PBS and repeat step 2.12 (PBS wash cycle). Refill the vial with fresh PBS and incubate overnight at 37 °C.

2.19. If immunostaining will be performed, skip steps 2.21–2.22 and proceed to Section 3 for immunostaining. If relying solely on endogenous fluorescence, proceed with steps 2.21–2.22 and skip Section 3.

2.20. Discard PBS and change the solution to Refractive Index Matching Solution (RIMS) (**Table 3**). Incubate overnight at 37 °C .

2.21. After incubation, the cleared tissue can be stored in RIMS solution at RT. Tissue may appear to be white and opaque in the center when first transferred into RIMS; tissue should become transparent after being incubated in RIMS at room temperature for several weeks (**Figure 2D**).

3. Immunohistochemistry Staining of the Whole Mount Mouse Heart

3.1. Remove the cleared heart from the RIMS solution and place into a clean 2.5 mL glass vial with 2 mL of PBST (PBS with 0.1% Triton-X 100)

3.2. Wash the heart in PBST 3 times on an orbital rotator with 30 min incubations at RT.

3.3. Block non-specific antibody binding by immersing the heart in 2 mL of 20% blocking buffer (diluted in PBST) and incubate with rotation for 3 hours at RT, followed by an overnight incubation at 4°C.

NOTE: Blocking buffer is made from normal serum matching the species in which the secondary antibody was raised.

3.4. Wash the heart in PBST 3 times with rotation for 5 min incubations at RT.

3.5. Immerse the heart in primary antibody (diluted in 2% blocking buffer with PBST) and prevent light exposure by wrapping the glass vial in aluminum foil. Incubate with rotation overnight at RT.

3.6. Incubate for an additional 24 hours with rotation at 4°C

3.7. Following primary staining, repeat step 3.2 (long PBST wash cycle) to remove the unbound primary antibody from the tissue. Extend the wash with an overnight incubation with rotation at RT.

3.8. Working in an area with limited lighting to prevent secondary antibody light exposure, immerse the heart in secondary antibody (diluted in 2% blocking buffer with PBST) and incubate with rotation for 3 hours at RT. Transfer to 4 °C to stain with rotation overnight.

NOTE: From this point forward, aluminum foil should be continuously used to protect the antibody staining from light exposure

3.9. On the next day, repeat step 3.2 (long PBST wash cycle) to remove unbound secondary antibody.

3.10. Replace the solution with 2% blocking buffer (diluted in PBST). Remove residual unbound antibody washing overnight with rotation at RT.

3.11. The next day, check that excess secondary antibody has been removed using confocal microscopy. Extend the wash as needed, replacing the 2% blocking buffer solution daily. Proceed once little to no non-specific secondary staining is present.

3.12. Store the immunostained heart in PBS at 4 °C.

3.13. Directly before whole mount microscopy, incubate the heart in RIMS solution overnight at 37 °C. Extend the incubation an additional 24 hours if the tissue is still not fully cleared.

3.14. Store the fully cleared and immunostained heart in RIMS at RT.

4. Visualizing Non-myocyte Populations in 3D with Single-Photon Confocal Microscopy

Imaging of the Cleared Mouse Heart

NOTE: If mouse hearts are harvested embryonically, continue with section 4.1. For mouse hearts harvested postnatally, continue with section 4.2.

4.1. Imaging the Cleared Embryonic Mouse Heart

4.1.1. Fill the microscope depression slide with the PBS solution.

4.1.2. Carefully pick up the cleared heart with curved forceps and place the tissue onto the slide.

4.1.3. Mount the slide with a glass coverslip. The tissue can now be imaged under a confocal microscope.

4.2. Imaging the Cleared Postnatal Mouse Heart

4.2.1. Fill half of the chamber of the depression slide with PBS solution. In order to create a chamber large enough to fit an adult mouse heart, a 3D-printed polypropylene depression slide was custom-made (**Figure 4**).

4.2.2. Carefully pick up the cleared heart with curved forceps and place the tissue into the chamber. Fill the remaining volume of the chamber with PBS.

4.2.3. Fill the chamber with PBS so the surface of the liquid forms a dome above the top of the chamber. Mount the cover slide. The tissue can now be imaged under a confocal microscope.

REPRESENTATIVE RESULTS

Often the two most challenging steps are guiding the heart out of the chest cavity and ligating the LAD. To troubleshoot these steps, adjustments may be made in the placement of the initial puncture between the fourth intercostal muscles; if the puncture and blunt dissection are too close in proximity to the sternum, the heart may not be able to exit the chest cavity (**Figure 1A**).

Additionally, increased pressure on the left abdomen may be needed to facilitate this process (**Figure 1B**). Complications may also occur when resting the heart on the intercostal muscles. We found the heart will remain outside of the cavity without withdrawing when the blunt dissection is kept to a minimal size and performed mainly in the horizontal direction. This orientation also allows for clear visualization and accessibility to the LAD (**Figure 1C**).

When placing the suture needle behind the LAD, it is suggested to penetrate deep into the anterior wall of the left ventricle, as a superficial ligation has less room for adjustment in the final suture placement (**Figure 1D**). Tying the suture around the LAD should be performed with controlled, steady movements, as the LAD is fragile and severing this coronary artery and the anterior wall will cause mortality (**Figure 1E**). Within 5–10 minutes after surgery is complete, the neonate should be lively and breathing normally.

When proceeding to the passive CLARITY protocol, hearts harvested from a mouse line that incorporates an endogenous fluorescent reporter for cell lineage tracing should be protected from light (**Figure 2**), which can be accomplished by wrapping the glass vial in aluminum foil. During the clearing step, the time incubating in Clearing Solution is variable depending on the

age of the mouse when the heart was harvested. This step is complete when the entire tissue is consistently opaque, with no discoloration in the center (**Figure 2B-C**). The hearts will become increasingly transparent after storage in RIMS solution at room temperature for a couple of days (**Figure 2D**). It should be noted that tissue expansion may occur during the clearing process.

Our passive CLARITY protocol permits effective antibody penetration and thus is compatible with immunohistochemistry methods to label protein(s) of interest. This was validated in Actl6b^{Cre};Rosa26^{tdT} transgenic mice, which label mature neurons with the tdTomato (tdT) reporter protein. The cardiac nerves are mainly superficial, with some populations residing in the epicardial layer, therefore we used this cell population as a proof-of-principal model for the reproducibility of endogenous reporter signal (**Figure 3A**), as well as preservation of reporter protein conformation before and after CLARITY (**Figure 3B-C**). Our representative results from Actl6b^{Cre};Rosa26^{tdT} mice show that the endogenous tdT protein signal seen in nerves of an uncleared P7 heart was faithfully recapitulated in nerves of both uncleared and cleared tdT immunolabeled P7 hearts (**Figure 3**). To immunolabel tdT-positive nerves, a Red Fluorescent Protein (RFP) primary antibody (rabbit polyclonal; 1:200 dilution; Rockland #600-401-379) was used along with an Alexa Fluor 488 secondary antibody (goat polyclonal; 1:1000 dilution; Invitrogen #A-11008). To visualize the cleared heart by eye during immunostaining and imaging steps, an ultraviolet flashlight may be briefly used to illuminate the heart.

FIGURES AND TABLES

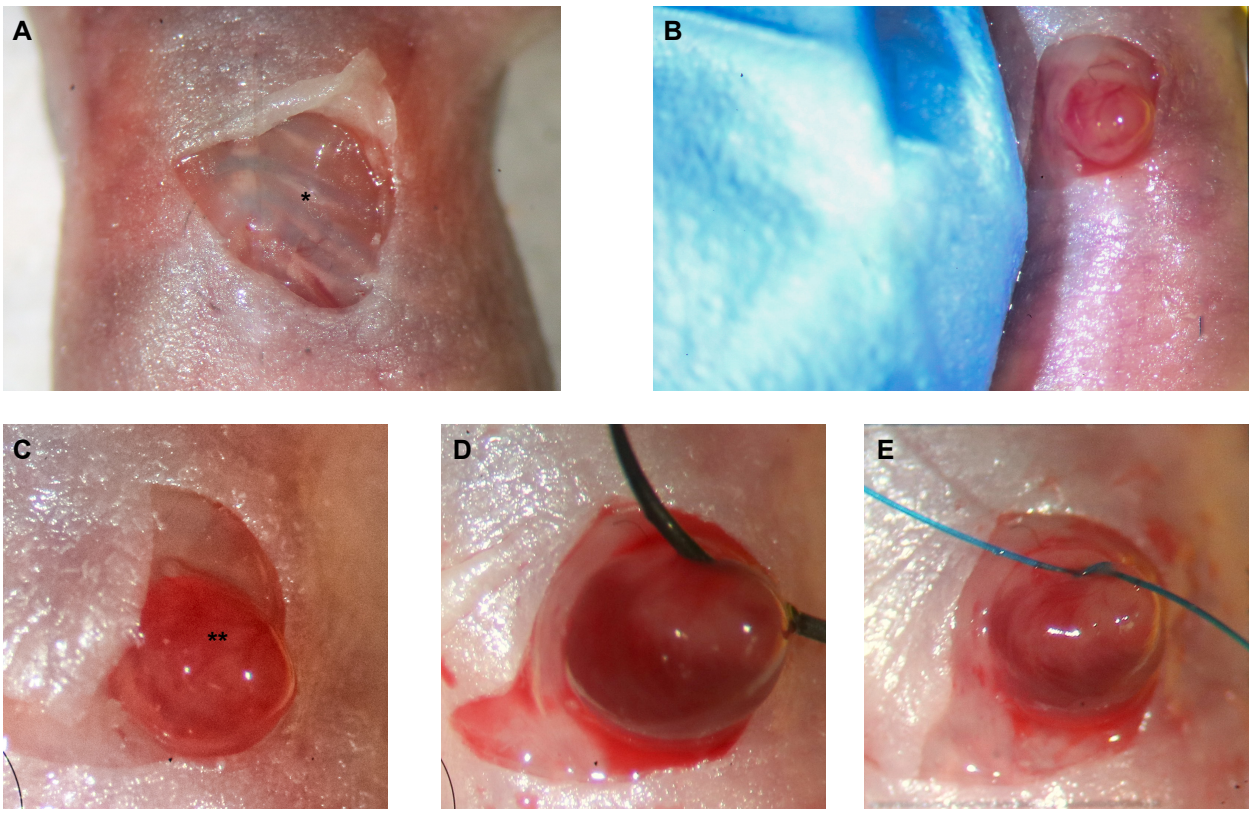

Figure 1: Induction of Myocardial Infarction in the Neonatal Mouse through Coronary Artery Occlusion of the Left Anterior Descending Artery (LAD). (**A**) The fourth intercostal space, indicated by a single asterisk (*), is located and a blunt dissection is performed. (**B**) Pressure is applied on the left abdomen to guide the heart out of the chest cavity. (**C**) The LAD, marked by a double asterisk (**), is identified as being the predominant artery and by anatomical position. (**D, E**) A suture is then passed behind the LAD and a square knot is tied around the LAD to induce a coronary artery occlusion and subsequent infarct. (**E**) Once complete, blanching can be seen below the suture, at the apex of the heart.

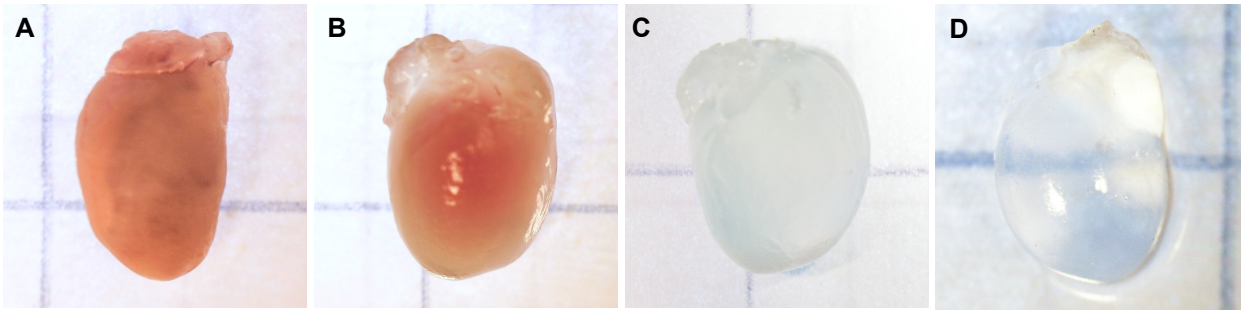

Figure 2: Progression of the Passive CLARITY Method on a P14 Mouse Heart. Hearts were harvested from P14 mice, (**A**) fixed, and (**B–D**) underwent the passive CLARITY protocol. For hearts taken at a P14 timepoint, Clearing Solution incubation step is (**B**) incomplete when discoloration at the center of the heart is apparent, seen after 6 days, and (**C**) complete when heart appears evenly opaque, seen after 10 days. (**D**) After the heart is stored in RIMS, the tissue is completely cleared.

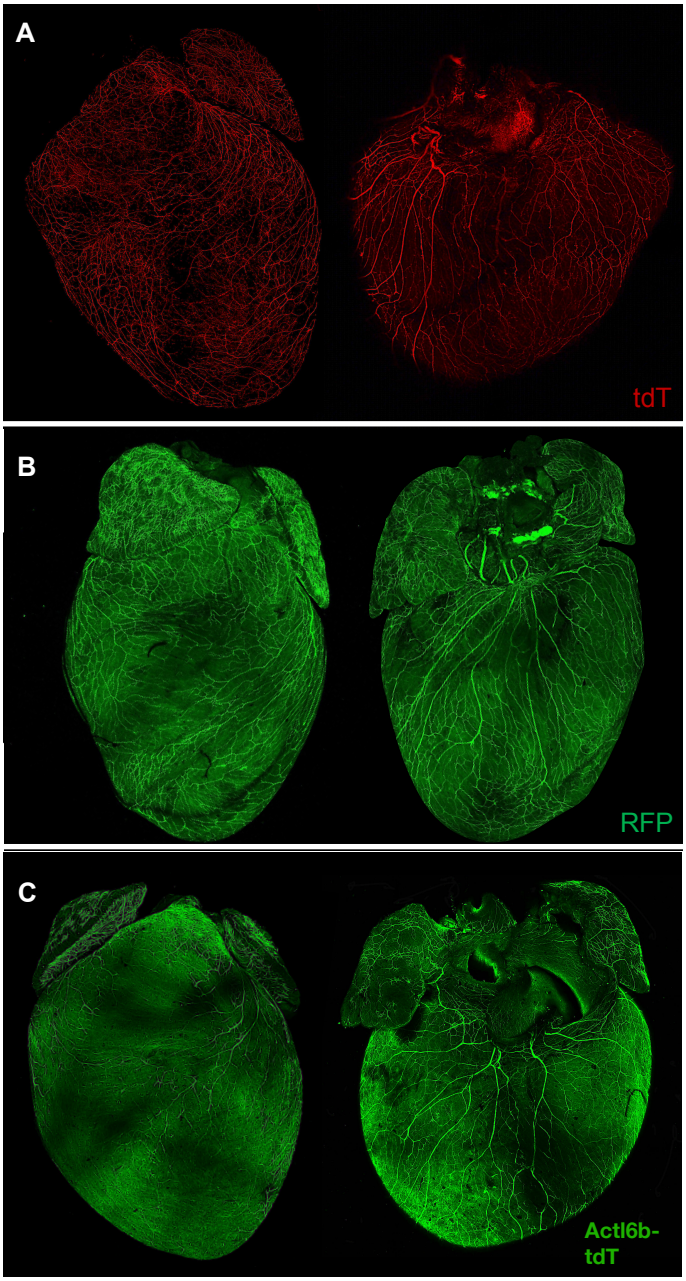

Figure 3: Whole-Mount 3D Imaging of P7 Mouse Hearts with Confocal Microscopy. Representative whole-mount 3D images from P7 Actl6b^{Cre};Rosa26^{tdT} transgenic mice hearts are shown as maximum intensity projections of z-stacked images. Hearts were imaged to show (**A**) endogenous tdTomato (tdT) fluorescence directly after harvesting (red) (**B**) immunostaining of tdT-positive nerves in an uncleared heart (Alexa Fluor 488; green) and (**C**) reproducible immunolabeling of tdT-positive nerves in a cleared heart (Alexa Fluor 488; green).

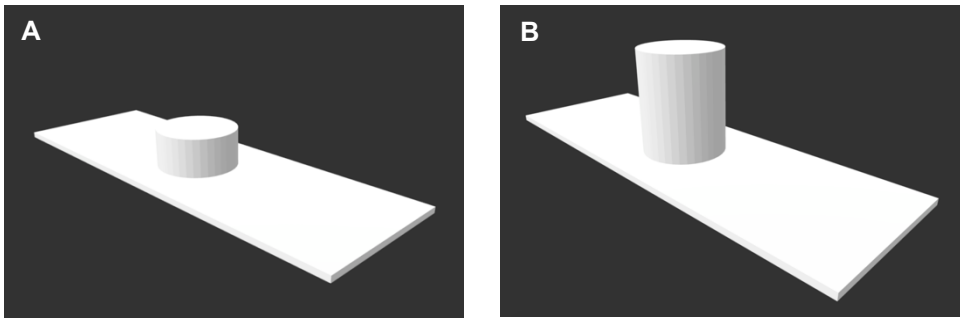

Figure 4. 3D Printed Polypropylene Depression Slides. To image the postnatal heart samples, custom depression slides were 3D printed on polypropylene. The slide dimensions are 25 mm x 75 mm x 1 mm, with a slide depression well 13 mm in diameter and either (**A**) 6.5 mm or (**B**) 17 mm in depth.

Equipment Type	Description	Company	Catalog Number
Glass Vial	12 x 35mm Vial with Cap	Fisherbrand	03-339-26A
6-0 Prolene Sutures	Polypropylene Sutures	Ethicon	8889H
Sharp Forceps	Fine Tip, Straight, 4.25 in	Sigma-Adrich	Z168777
Dressing Forceps	Dissecting, 4.5 in	Fisherbrand	13-812-39
Needle Holder	Mayo-Hegar, 6 in	Fisherbrand	08-966
Small Dissecting Scissor	30 mm Cutting Edge	Walter Stern Inc	25870-002
Tissue Forceps	Medium Tissue, 1X2 Teeth	Excelta	16050133
Large Dissecting Scissors	Straight, 6 in	Fisherbrand	08-951-20
Iridectomy Scissors	2 mm Cutting Edge	Fine Science Tools	15000-03
Curved Forceps	Half Curved, Serrated, 4 in	Excelta	16-050-146

Table 1. Surgical Equipment.

Clearing Solution			
Reagent	**Final**	**Amount**	**Notes**
Sodium Dodecyl Sulfate (SDS)	8.0% w/v	40 g	
Boric acid	1.25% w/v	6.25 g	
1-thioglycerol	0.5% w/v	5 µL/mL	Added as needed to solution
Add 400 ml of ultrapure H20 to 1 L beaker. Mix in SDS and Boric Acid with magnetic stirring.			
Adjust pH to 8.5 using 6M NaOH. Bring volume to 500 ml and Autoclave.			
Store solution at room temperature.			
Other CLARITY Reagents			
Reagent	**Final**	**Stock**	**Notes**
PFA	4.0%	16%	Diluted in PBS
Acrylamide	4.0%	40%	Diluted in PBS
VA-044	0.5%	10%	Added as needed to solution

Table 2. Clearing Solution and Other CLARITY Reagents

Reagent	Final	Amount
Phosphate Buffer	0.02 M	90 mL
Histodenz	133.3% w/v	120 g
Sodium Azide	0.05% w/v	45 mg
Add 90 mL of 0.02 M Phosphate Buffer to 250 mL glass media bottle wrapped in aluminum foil.		
Mix in reagents listed with magnetic stirring. Allow components to dissolve overnight.		
Vortex solution and filter purify with filtration system into a sterile 250 mL glass media bottle.		
Wrap bottle in aluminum foil and store solution at room temperature.		

Table 3. Refractive Index Matching Solution (RIMS)

DISCUSSION

Cell-cell interactions between cardiomyocytes and non-myocyte populations are a determining factor of whether the heart will undergo fibrosis or repair following injury. Discoveries have been made demonstrating that a variety of cell types, including nerves[14], epicardial cells[24], peritoneal macrophages[25], arterioles[12,13], and lymphatic endothelial cells[26], all play an essential role in mediating cardiac repair. These cell lineages and others of interest can be genetically traced during development, disease, and regeneration by applying Cre-lox and CRISPR-Cas9 technologies in mice. When coupled with organ clearing and advanced microscopy methods, the contributions of non-myocyte populations can be accurately assessed, opening the door to elucidate cellular and molecular targets of myocardial regeneration following injury.

The efficiency of the protocol is dependent on consistent and reproducible ligation of the LAD during coronary artery occlusion surgery. Neonatal mice are sensitive to extended exposure to hypothermia; thus, the surgery must not only be performed with accuracy but also within minutes. From start to finish, the myocardial infarction surgery should take less than 8 minutes. We recommend first practicing on several litters of the same background as the experimental mice until proficiency is achieved.

Progression of cardiac repair can be assessed by using echocardiography to measure cardiac function (i.e. fractional shortening, ejection fraction, systolic and diastolic volume) once within 3 to 7 days after surgery and again shortly before harvesting the heart, suggested between 21- and

28-days post injury. Hearts can be collected for clearing at multiple timepoints following myocardial infarction surgery.

The clearing step (step 2.18) is subject to variation in duration depending on age and strain of the mouse from which the heart was harvested, which can result in differences in heart size. For a B6 background mouse, clearing duration based on age is estimated as follows: P1 (7-10 days), P7 (14-17 days), P14 (21-24 days), P21 (28-31 days), P28 (35-38 days). Although the primary focus of our laboratory is heart clearing, our passive CLARITY method has been successful for clearing mice lungs (unpublished results) and we foresee no limit on broadly applying this to other organs. Overall, our expedited clearing process is highly valued for the ability to clear tissues rapidly and effectively.

It should be noted that complications can arise when applying tissue clearing techniques in organs with endogenous reporters in rare subpopulations. Reporter signal in dense cell populations (such as myocytes[23]) seem to be more resistant to the clearing process and thus the signal is typically retained; however, other more sensitive cell populations (such as cardiac nerves) are prone to having endogenous fluorescent protein signal quenched after prolonged fixation or clearing. This became apparent in the Actl6b^{Cre};Rosa26^{tdT} reporter mouse model, where P7 hearts fixed briefly for 15 minutes showed strong tdT signal (**Figure 3A**), however this fluorescent signal was quenched after fixation for 1 hour or overnight incubation in the Clearing Solution (data not shown). In the scenario of lost reporter signal, antibody staining targeting the reporter protein is compatible with tissue clearing to amplify the signal (**Figure 3**). The addition of an

immunolabeling step can be advantageous for tissues undergoing extensive imaging, as conjugated antibodies are bleach-resistant and produce stable, long-term expression. With the ability to track proteins endogenously and through immunostaining, our protocol uniquely allows for precise localization of rare cardiac cell populations that reside deep within the heart.

Cleared hearts can undergo lineage tracing or fluorescent protein expression analysis using whole-mount 3D confocal microscopy. The confocal microscope is equipped with laser lines optimized to excite florescent reporters (or conjugated secondary antibodies), for example: BFP (DAPI, Alexa Fluor 405), EGFP (FITC, Alexa Fluor 488), DsRed (TRITC, Alexa Fluor 546/555), and APC (Cy5, Alexa Fluor 647) at 405 nm, 488 nm, 561 nm, and 683 nm, respectively. For heart samples unable to fit in a depression slide – common if the heart harvested postnatally – a custom depression slide can be made by 3D printing on polypropylene. Custom slides followed dimensions of a microscope depression slide (25 mm x 75 mm x 1 mm), varying the well depth to either 6.5 mm or 17 mm (**Figure 4**).

In order to visualize the reporter cell lines in 3D, the confocal microscope is set to acquire z-stacked images throughout the heart. When imaging larger hearts, the entire heart may not be able to be captured in a single z-stacked image even with a low magnification objective. In this scenario, a series of multiple z-stacked images taken at different heart regions can be stitched together using a large image function. This is accomplished by calibrating the microscope to the appropriate objective lens and specifying the field for the large image scan area. Then, z-stacked images undergo 3D reconstruction using a volume rendering program and maximum intensity

projection (**Figure 3**). The high-resolution images acquired can be analyzed to determine precise 3D spatial cell patterning of targeted cell populations.

Collectively, this protocol provides a powerful molecular tool to understand the dynamic cellular changes that occur during cardiac repair and regeneration. This method describes the steps to induce a myocardial infarction, perform whole organ clearing, trace cell specific populations, and analyze 3D cell patterning. Together, these techniques provide access to trace cell populations that were previously inaccessible due to their sparse presence or location within the tissue. This will enable further investigation of questions paramount to advance therapeutic approaches in regenerative medicine, particularly those aimed at stimulating endogenous heart regeneration.

ACKNOWLEDGMENTS

Funding for this project was provided by the UW School of Medicine and Public Health from the Wisconsin Partnership Program (A.I.M.), and an American Heart Association Career Development Award 19CDA34660169 (A.I.M.).

DISCLOSURES

The authors declare that they have no competing financial interests.

REFERENCES

1 Lazar, E., Sadek, H. A., Bergmann, O. Cardiomyocyte renewal in the human heart: insights from the fall-out. *European Heart Journal.* **38** (30), 2333-2342 (2017).

2 Kikuchi, K., Poss, K. D. Cardiac regenerative capacity and mechanisms. *Annual Review of Cell and Developmental Biology.* **28**, 719-741 (2012).

3 Habecker, B. A. et al. Molecular and cellular neurocardiology: development, and cellular and molecular adaptations to heart disease. *The Journal of Physiology.* **594** (14), 3853-3875 (2016).

4 Savarese, G., Lund, L. H. Global Public Health Burden of Heart Failure. *Cardiac Failure Review.* **3** (1), 7-11 (2017).

5 Porrello, E. R. et al. Transient regenerative potential of the neonatal mouse heart. *Science.* **331** (6020), 1078-1080 (2011).

6 Mahmoud, A. I., Porrello, E. R., Kimura, W., Olson, E. N., Sadek, H. A. Surgical models for cardiac regeneration in neonatal mice. *Nature Protocols.* **9** (2), 305-311 (2014).

7 Karwowski, J. et al. Relationship between infarct artery location, acute total coronary occlusion, and mortality in STEMI and NSTEMI patients. *Polish Archives of Internal Medicine.* **127** (6), 401-411 (2017).

8 Lusis, A. J. Atherosclerosis. *Nature.* **407** (6801), 233-241 (2000).

9 The survival of patients with heart failure with preserved or reduced left ventricular ejection fraction: an individual patient data meta-analysis. *European Heart Journal.* **33** (14), 1750-1757 (2012).

10 Notari, M. et al. The local microenvironment limits the regenerative potential of the mouse neonatal heart. *Science Advances.* **4** (5), eaao5553 (2018).

11 Porrello, E. R. et al. Regulation of neonatal and adult mammalian heart regeneration by the miR-15 family. *Proceedings of the National Academy of Sciences of the United States of America.* **110** (1), 187-192 (2013).

12 Das, S. et al. A Unique Collateral Artery Development Program Promotes Neonatal Heart Regeneration. *Cell.* **176** (5), 1128-1142.e1118 (2019).

13 Wang, Z. et al. Decellularized neonatal cardiac extracellular matrix prevents widespread ventricular remodeling in adult mammals after myocardial infarction. *Acta Biomateria.* **87**, 140-151 (2019).

14 Mahmoud, A. I. et al. Nerves Regulate Cardiomyocyte Proliferation and Heart Regeneration. *Developmental Cell.* **34** (4), 387-399 (2015).

15 Yanai, H., Tanaka, T., Ueno, H. Multicolor lineage tracing methods and intestinal tumors. *Journal of Gastroenterology.* **48** (4), 423-433 (2013).

16 Ariel, P. A beginner's guide to tissue clearing. *The International Journal of Biochemistry & Cell Biology.* **84**, 35-39 (2017).

17 Chung, K. et al. Structural and molecular interrogation of intact biological systems. *Nature.* **497** (7449), 332-337 (2013).

18 Epp, J. R. et al. Optimization of CLARITY for Clearing Whole-Brain and Other Intact Organs. *eNeuro.* **2** (3) (2015).

19 Lee, H., Park, J. H., Seo, I., Park, S. H., Kim, S. Improved application of the electrophoretic tissue clearing technology, CLARITY, to intact solid organs including brain, pancreas, liver, kidney, lung, and intestine. *BMC Developmental Biol.* **14**, 48 (2014).

20 Wan, P. et al. Evaluation of seven optical clearing methods in mouse brain. *Neurophotonics.* **5** (3), 035007 (2018).

21 Phillips, J. et al. Development of passive CLARITY and immunofluorescent labelling of multiple proteins in human cerebellum: understanding mechanisms of neurodegeneration in mitochondrial disease. *Scientific Reports.* **6**, 26013 (2016).

22 Blom, J. N., Lu, X., Arnold, P., Feng, Q. Myocardial Infarction in Neonatal Mice, A Model of Cardiac Regeneration. *Journal of Visualized Experiments.* 10.3791/54100 (111) (2016).

23 Sereti, K. I. et al. Analysis of cardiomyocyte clonal expansion during mouse heart development and injury. *Nature Communications.* **9** (1), 754 (2018).

24 Lepilina, A. et al. A dynamic epicardial injury response supports progenitor cell activity during zebrafish heart regeneration. *Cell.* **127** (3), 607-619 (2006).

25 Wang, J., Kubes, P. A Reservoir of Mature Cavity Macrophages that Can Rapidly Invade Visceral Organs to Affect Tissue Repair. *Cell.* **165** (3), 668-678 (2016).

26 Vieira, J. M. et al. The cardiac lymphatic system stimulates resolution of inflammation following myocardial infarction. *Journal of Clinical Investigation.* **128** (8), 3402-3412 (2018).

CHAPTER III: PARASYMPATHETIC AND SYMPATHETIC AXONS ARE BUNDLED IN THE CARDIAC VENTRICLES AND UNDERGO PHYSIOLOGICAL REINNERVATION DURING HEART REGENERATION

Rebecca J. Salamon[1], Poorva Halbe[1], William Kasberg[2], Jiyoung Bae[3], Anjon Audhya[2], Ahmed I. Mahmoud[1*]

[1]Department of Cell and Regenerative Biology, [2]Department of Biomolecular Chemistry, University of Wisconsin School of Medicine and Public Health,
Madison, WI 53705, United States.
[3]Department of Nutritional Sciences, Oklahoma State University, Stillwater, OK 74078, United States.

*Corresponding author: Ahmed I. Mahmoud, Ph.D. Email: aimahmoud@wisc.edu

AUTHOR CONTRIBUTIONS

R.J.S., performed the experiments, imaging, and analyses. R.J.S. and J.B. performed the surgical procedures. R.J.S., P.H., W.K., and A.A. contributed to 3D reconstruction methods, analysis, and quantification. A.I.M. conceived the project. R.J.S. and A.I.M. designed the experiments, performed the analyses, and wrote the manuscript.

SUMMARY

Sympathetic innervation of cardiac ventricles has been shown to influence hemostasis, repair, and pathological functions; in contrast, the parasympathetic nerves are thought to primarily innervate the nodes of the heart and minimally impact ventricular physiology. However, our current understanding of cardiac nerve architecture has been limited to two-dimensional analysis. Here, we use genetic models, whole-mount imaging, and three-dimensional (3D) modeling tools to accurately define cardiac nerve architecture and neurovascular association during development, disease, and regeneration. Remarkably, our approach reveals for the first time that parasympathetic nerves extensively innervate the cardiac ventricles. Furthermore, we provide evidence that parasympathetic and sympathetic nerves develop synchronously and are bundled throughout the ventricles. Our results demonstrate that cardiac nerves sequentially associate with coronary veins and arteries during development. We expand this 3D modeling system to investigate cardiac nerve remodeling in the regenerative neonatal mouse and the non-regenerative postnatal heart. Our results show that the regenerating myocardium undergoes a unique process of physiological reinnervation, where proper nerve distribution and architecture is reestablished, in stark contrast to the non-regenerating heart. Mechanistically, we demonstrate that physiological reinnervation during regeneration is dependent on collateral artery formation via genetic ablation of collateral arteries. Our results reveal clinically significant insights into cardiac nerve remodeling during homeostasis, disease, and regeneration which can identify new therapies for cardiac disease.

GRAPHICAL ABSTRACT

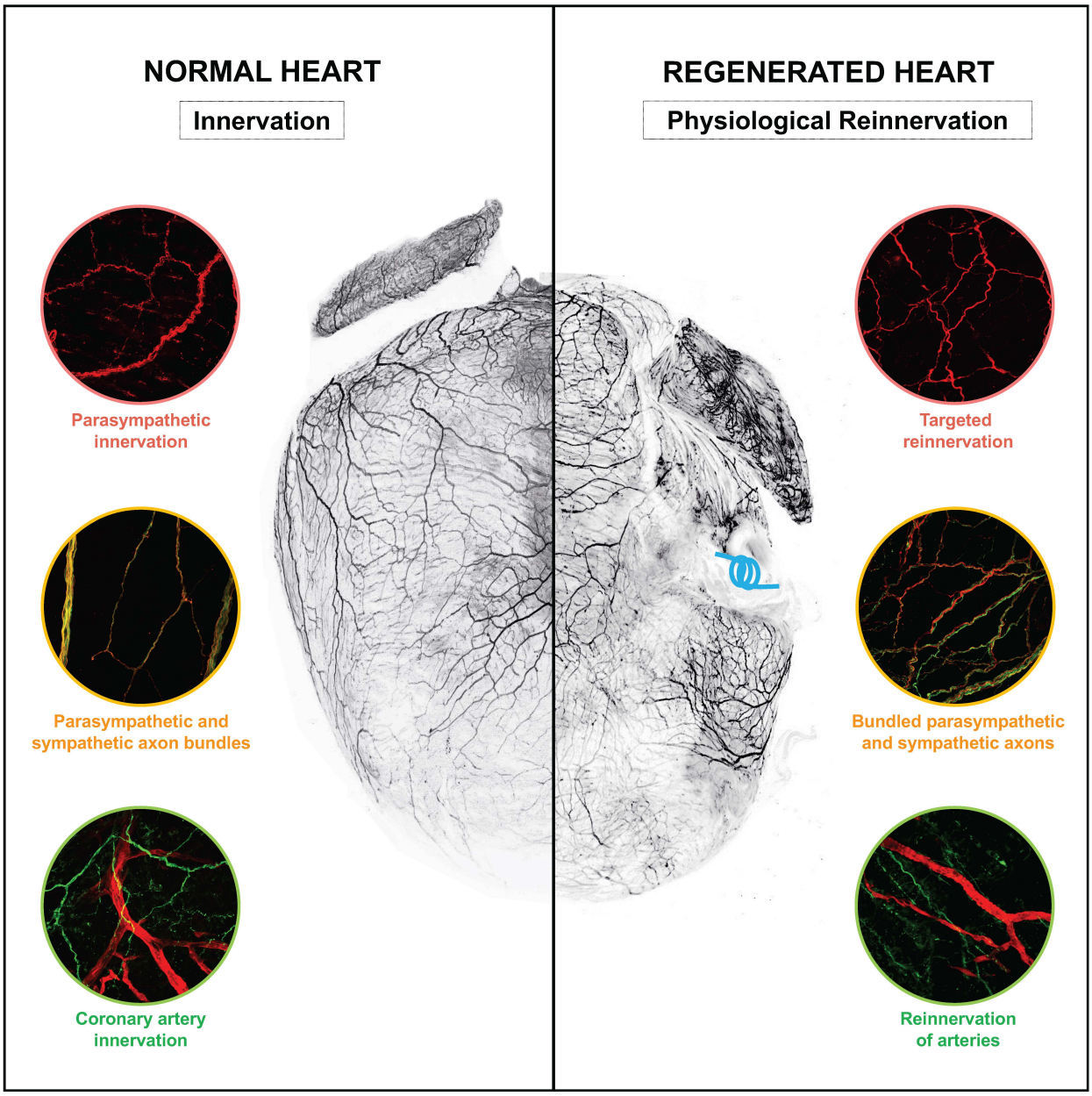

INTRODUCTION

The cardiac nervous system is a pillar of cardiac physiology, regulating conduction and contractility that is balanced by the two opposing branches of the sympathetic and parasympathetic inputs.[1] The peripheral nerves coalesce at the cardiac plexus and target innervation to the cardiac nodes, where contractile signals are relayed throughout the atria and the ventricles.[2,3] Recent studies have focused on defining the intrinsic cardiac nervous system, extensively mapping the innervation at the cardiac plexus and atrial nodes.[4,5] Yet, the cardiac nervous system also includes ventricular innervation, where the neuronal influence expands beyond autonomic regulation. Specifically, sympathetic nerves have been demonstrated to innervate the ventricles to regulate cardiac development and physiology.[6,7] The sympathetic nerve networks mediate communication across a variety of cell types, including myocytes and blood vessels.[8,9] These neural connections are established during late embryonic and early postnatal development by a co-maturation system,[10,11] where cell-cell interactions alter the physiology of the neuron and the innervated cell.[12-14] Interestingly, sympathetic nerves regulate the postnatal transition of cardiomyocytes from hyperplasia to hypertrophy[15] and cardiomyocyte size.[14,16]

In contrast, parasympathetic innervation has been less studied for its interactions within the cardiac ventricles, due to the widely-held belief that parasympathetic nerves do not significantly contribute to ventricular innervation.[17] This misconception has recently been challenged by molecular evidence of parasympathetic nerve function within the ventricles, including a high density of cells expressing muscarinic receptors,[18,19] protective functions against ventricular

arrythmias,[20] influence on contractility,[21] and sparse distribution of parasympathetic nerve fibers.[22-25] Furthermore, advances in viral tracing strategies and optogenetics have provided evidence that parasympathetic axons innervate the ventricles and impact cardiac physiology.[26] Yet, the anatomy, distribution, and cell-cell interactions of ventricular parasympathetic innervation remains unclear.

Autonomic nerve remodeling and dysfunction is a central cause of pathogenesis in cardiovascular disease.[10,27] The heterogeneity of nerve remodeling, including regions of denervation and sympathetic hyperinnervation, can trigger ventricular arrhythmias and sudden cardiac death.[27-31] Interestingly, nerves play an important role in promoting repair and regeneration across a variety of organs and species.[32] Importantly, parasympathetic nerve function regulates cardiomyocyte proliferation and regeneration of the neonatal mouse heart.[33] Remarkably, this regenerative response is accompanied with restoration of autonomic functions, suggesting physiological innervation of the regenerating mammalian heart.[34] However, how cardiac nerve patterning and distribution during regeneration compares to the uninjured or diseased heart has not been explored.

The wide role of the intrinsic cardiac nervous system in regulating heart development, homeostasis, and regeneration highlights the importance of defining the cardiac nerve architecture as a necessary step to promote physiological reinnervation in many cardiac diseases. Gaining insights into the patterns, density, and distribution of sympathetic and parasympathetic nerves during development is necessary to understand the normal circuitry of cardiac innervation.

Our current understanding of cardiac nerve architecture is largely based on two-dimensional (2D) histological analysis, where fixed tissues are labeled with different markers for visualization of neurons. This approach is inaccurate, as it inherently damages the nerves axons and is not reflective of the intact architecture. This has led to gross underestimation of the degree of ventricular innervation at an anatomical level. Additionally, histological analysis cannot reveal information about the developmental distribution of neurons in the heart. Thus, comprehensive lineage tracing of individual cardiac nerves while visualizing them in a three-dimensional (3D) manner is necessary to dissect the development, maturation, and lineage commitment of the cardiac autonomic nervous system.

Here we generate and analyze the first 3D neurovascular map of the mature, intact murine heart ventricles. We reconstruct nerve patterning with high-spatial accuracy by employing comprehensive lineage tracing, whole-mount immunostaining, confocal microscopy, and 3D reconstruction. We use this system to further explore neurovascular development and distribution of parasympathetic and sympathetic nerve subpopulations. We demonstrate that parasympathetic axons extensively innervate the heart and are bundled with sympathetic axons, highlighting that parasympathetic nerves contribute significantly to ventricular innervation and underscoring an underappreciated role for parasympathetic nerves in ventricular homeostasis. Furthermore, our results demonstrate a unique physiological nerve remodeling during neonatal heart regeneration, where sympathetic and parasympathetic axon bundles precisely reinnervate the arteries in the regenerating myocardium, a process distinct from the pathological remodeling of the non-regenerating heart. Mechanistically, we use genetic inhibition of collateral arteries to

demonstrate that physiological reinnervation during regeneration is dependent on collateral artery formation. Together, our findings define the 3D cardiac nerve architecture and identify a novel nerve remodeling process during heart regeneration.

RESULTS

Parasympathetic nerves extensively innervate the cardiac ventricles and closely localize with sympathetic nerves throughout embryonic and postnatal maturation

Recent evidence suggests that parasympathetic innervation and function has an underappreciated role in the cardiac ventricles. The patterning and distribution of the parasympathetic innervation has largely been based on 2D analysis; however, this approach is insufficient to reconstruct the intricate nerve networks and cell-cell interactions. To define the parasympathetic nerve patterning with respect to sympathetic innervation in the intact heart, we employed a pipeline of lineage tracing, whole-mount imaging, and 3D reconstruction in the intact heart. To capture each neuronal subtype, we used a parasympathetic reporter mouse line and immunostained for the sympathetic nerves. For parasympathetic nerve lineage labeling, we used the Choline Acetyltransferase (ChAT) Cre (*ChATCre)* knockin mouse and a *Rosa26*^{tdTomato} reporter (*ChATCre;Rosa26*^{tdTomato}). ChAT is an essential enzyme for acetylcholine biosynthesis and a reliable marker for cholinergic (parasympathetic) nerves.[35] For sympathetic nerve labeling, hearts underwent whole-mount immunostaining with the sympathetic nerve marker Tyrosine Hydroxylase (TH), a key enzyme for biosynthesis of catecholamines and a bona fide marker of adrenergic (sympathetic) nerves.[35] We then performed whole-mount confocal imaging on the

posterior and anterior heart, followed by image analysis using Imaris to reconstruct the 3D architecture of innervation in the ventricles (**Figure 1**).

Surprisingly, the P7 hearts of the *ChATCre;Rosa26^{tdTomato}* mice showed extensive parasympathetic innervation of the ventricles (**Figure 1A$_{i\text{-}iii}$**). The parasympathetic nerves branched extensively throughout the anterior and posterior regions of the ventricles (**Figure 1A, S1**). We then compared parasympathetic and sympathetic patterning and identified equal distribution throughout the heart. Moreover, both parasympathetic and sympathetic nerve fibers were intertwined in large bundles, as well as closely localized in smaller axon projections (**Figure 1A$_{ii}$-A$_{iv}$**). These results highlight that the parasympathetic nervous system extends into the cardiac ventricles, providing a means for parasympathetic ventricular influence and opening the possibility for undiscovered nerve-cell dynamics.

We then asked whether both parasympathetic and sympathetic nerve axons extend sequentially, with one guiding the other, or simultaneously, maintaining equal distribution. To investigate this, we used the *ChATCre;Rosa26^{tdTomato}* mice and harvested hearts during developmental stages of axon extension at embryonic day (E) 15.5 to E17.5 (**Figures 1B, S1, S2**). At E16.5, the axons first reach the apex and demonstrate that parasympathetic and sympathetic nerves are bundled (**Figure 1B$_{i\text{-}iii}$**). Both parasympathetic and sympathetic axons pattern in close localization during earlier (E15.5) and later stages (E17.5 and P1) of heart development (**Figure S2**). No differences between parasympathetic and sympathetic axon distribution were seen on the posterior or anterior side of the heart (**Figures 1A-B, S1, S2**).

To further quantify parasympathetic and sympathetic nerve patterning during embryonic and postnatal development, we used 3D reconstruction and analysis of individual branch trees, primary axons, and whole innervation networks (**Figures 1C-D, S3**). Branching level, density, volume, and patterning of parasympathetic and sympathetic nerves were investigated independently. No significant differences were found between the two nerve subtypes; therefore, we continue to describe the overall patterns identified. We analyzed branching level as a parameter of nerve development (**Figure 1C-D**). Primary axon bundles can branch into secondary-, tertiary-, and quintenary axons, and beyond, with each level assigned as branch level 1, 2, 3, and 4+, respectively. The branching level increased during embryonic and early postnatal development (**Figure 1C-D**). When axons first arise around E15.5, axons have minimal branching level (average branch level of 3) and mature by P7, with a significant increase in branching level (average branch level of ~11) (**Figure 1D**). The nerve networks also showed an increase in overall axon distances from origin, volume of primary axon bundles, and primary axon bundle length, with a consistent trend of significance between E17.5 and P7 hearts. (**Figure S3**). Interestingly, the mature heart showed primary and secondary axon bundles that were significantly higher in density compared to the tertiary branched axons and beyond (**Figures 1E, S3**). These patterns identify two phases of significant nerve growth that occurs between late embryonic and early postnatal development, marked by an increase in axon branch level, distance from origin, volume, and length.

Our results demonstrate that parasympathetic nerves extensively innervate the cardiac ventricles and share nearly identical patterning to sympathetic nerves. This architecture is a result of synchronous parasympathetic and sympathetic axon extension during late embryonic and early postnatal development, with axon subtypes maintaining similar increases in branching level, distribution, and density.

Cardiac nerves sequentially associate with the coronary veins and arteries during embryonic development

The development of cardiac innervation throughout the ventricles of the embryonic heart is not fully understood. Specifically, the coronary veins regulate sympathetic axon patterning;[13] however, how the coronary arteries influence the patterning of parasympathetic and sympathetic axon bundles is not well defined. Here, we sought to elucidate the dynamics between nerve-vein and nerve-artery association during embryonic heart development.

The main, large-diameter veins of the embryonic heart primarily reside on the posterior wall,[13] whereas the main coronary arteries are primarily located within the anterior wall.[13,36] Therefore, we divided the architectural regions into posterior and anterior sides of the heart, including right and left ventricles (LV, RV) (**Figure 2**). Coronary arteries were visualized with lineage labeling using the inducible Connexin 40 Cre (*Cx40CreER*) and a *Rosa26*^{tdTomato} reporter (*Cx40CreER;Rosa26*^{tdTomato}) (**Figure 2**). Neurovascular patterning was identified with additional markers for all nerves with beta tubulin III (Tuj1), and veins (along with capillaries) with endomucin (EMCN) (**Figure 2A-C**).

Sympathetic nerve axons are recruited to innervate the heart as early as E13.5 via secretion of Neuronal Growth Factor (NGF) from the coronary veins, establishing nerve-vein alignment.[13] We confirmed that our model accurately reflects coronary vascular architecture by identifying that the posterior axons aligned with large-diameter veins from E15.5-E17.5 (**Figure S4A-C**), verifying our use of EMCN to identify and trace large-diameter veins. Since coronary arteries primarily reside on the anterior side of the ventricle at these developmental stages,[36] we hypothesized that the anterior wall would have significant nerve-artery alignment. Supporting this, as early as E16.5, axons wrapped around from the posterior wall towards arteries in the anterior wall of the heart (**Figures S4E-G**). By E17.5, the nerve patterning was significantly associated with the anterior coronary arteries with limited association towards the anterior coronary veins (**Figure 2A-C**). These results demonstrate that nerve-artery association occurs within the anterior wall of the ventricle during late developmental stages.

We used 3D reconstruction to visualize and analyze the depth of innervation at E17.5 throughout multiple regions of the cardiac ventricles, where depth was defined as a function of z (**Figure 2B, Figure S4D**). The nerves showed similar depth to their closest vascular structure, with subepicardial nerves aligning closely with the coronary veins, and myocardial nerves aligning to the coronary arteries. Interestingly, the nerves in the base of the heart were more superficial than those in the periphery and apical regions; and this patterning was consistent on both posterior and anterior walls (**Figures 2B, S4D**). Proximity analysis supports the regional correlation of posterior nerve-vein alignment and anterior nerve-artery association at E17.5

(**Figure 2C**). Together, this demonstrates that the developing nerves show a programmed association with not only the coronary veins, but also the coronary arteries. Our results provide new insights into the developmental timeline and 3D architecture of embryonic coronary artery innervation.

Defining 3D cardiac nerve architecture of the postnatal mouse ventricle

Next, we sought to define typical nerve-vein and nerve-artery architecture in the postnatal heart. To rigorously define the 3D architecture of the postnatal heart ventricles, we considered that the spatial region of the heart is subject to natural biological variability of heart shape, size, and vascular patterning. To provide consistency between samples, we defined the architectural regions in two-fold. First, we again indicate posterior and anterior regions of the heart, including right and left ventricles (RV, LV). Second, we used the well-defined vascular system, composed of the coronary veins and arteries, to demonstrate association of the nerves with these vessels. The coronary vessels are defined as the main right, medial, and left coronary veins (RCV, MCV, LCV) and the right and left coronary arteries (RCA, LCA).

Hearts were collected at postnatal day (P) 7, a timepoint where co-maturation of the nerves and the myocardium takes place.[10] We utilized the *Cx40CreER;Rosa26*^{tdTomato} mice to label coronary arteries, in addition to whole-mount immunostaining for nerves with Tuj1 and veins with EMCN (**Figure 3**). Whole-mount imaging of the posterior wall demonstrates nerve-vein alignment, where large nerve bundles were localized near the left, medial, and right coronary veins (**Figure 3A**; LCV, RCV, MCV), in agreement with previous reports.[13] Interestingly, the anterior wall

demonstrates that innervation is highly localized to the right and left coronary arteries (**Figure 3B**; LCA, RCA). This close nerve-artery association allowed for axonal projections to directly innervate the arteries (**Figure 3B$_{v\text{-}vi}$**). Confocal images were reconstructed in 3D by Imaris and analyzed for neurovascular association (**Figure 3C-D**). This relationship between nerves, veins, and arteries is characterized and quantified to define the typical nerve patterning of the postnatal mouse heart. As expected, there was a significant nerve-vein association in the posterior wall compared to the anterior wall (**Figure 3D**). Contrastingly, the anterior wall showed a significant increase in the percent of nerves associated with the coronary arteries, in comparison to the posterior wall distribution (**Figure 3D**). Our results construct the 3D cardiac nerve architecture within the cardiovascular network in the postnatal heart, revealing a distinct innervation pattern with coronary veins and arteries in the cardiac ventricles.

Axon plasticity promotes reinnervation of the regenerating neonatal heart

Within a week after birth, the neonatal mouse heart transitions from being highly regenerative into a state of limited regenerative potential. A myocardial infarction (MI) in the non-regenerative adult heart causes pathological nerve remodeling, resulting in an arrythmia prone heart.[28,29] In contrast, the neonatal heart can fully regenerate by 21 days-post MI, through a process that is dependent on nerve function.[33,37] Furthermore, the regenerated heart fully restores contractile and autonomic function,[34] suggesting that physiological reinnervation may take place during regeneration. With this evidence, we hypothesized that the regenerating myocardium establishes physiological innervation patterns, whereas the diseased myocardium undergoes pathological nerve remodeling.

First, we investigated the level of axon plasticity in the regenerating neonatal heart. Injured peripheral axons are capable of undergoing a degree of axon regeneration, where axons are degraded through Wallerian degeneration followed by axon extension and reinnervation.[38] Yet, the degree of plasticity in neonatal cardiac axons after injury is not well defined. To explore this, MI surgery was performed on WT mice at the regenerative (P1) timepoint, and hearts were collected at 7-, 14-, and 21-days post MI, at early, middle and completed stages of regeneration, respectively (**Figure 4**). Nerves were marked with Tuj1 and imaged by whole-mount confocal microscopy. The degree of innervation was determined by quantifying the area of nerve coverage in the remote, border, and infarct zones. Nerve remodeling was compared to wild type uninjured, age-matched mice. P22 uninjured hearts show typical degree of innervation in regions similar to the remote, border, and infarct zones (**Figure 4A**). At 7 days post-MI, regenerating hearts were strikingly denervated in the border and infarction zones, with a compensatory hyperinnervation in the remote zone, in comparison to P8 uninjured hearts (**Figure 4B**). By 14 days post-MI, regenerating hearts restored innervation in the border zone, with a sustained decrease in degree of innervation in the infarct zone and hyperinnervation in the remote zone, in comparison to P15 uninjured hearts (**Figure 4C**). At 21 days post-MI, fully regenerated hearts showed restored levels of innervation in the remote, border, and infarct zones, in comparison to P22 uninjured hearts (**Figure 4D**).

The limited axon plasticity in the non-regenerated heart results in heterogenous reinnervation and denervation of the infarcted myocardium.[30,31,39] To distinguish the differences between

nerve remodeling in regenerating and non-regenerating hearts, we also performed MI surgery in WT mice at the non-regenerative (P7) timepoint and collected hearts at 21 days post-MI. Quantifying the degree of innervation revealed pathological nerve remodeling in the non-regenerative heart (**Figure 4E**). At 21 days post-MI, the non-regenerative hearts showed regions of denervation and hyperinnervation in the border zone, stark denervation in the infarct zone, and typical levels of innervation in the remote zone, in comparison to P22 uninjured hearts (**Figure 4E**). The heterogeneity of innervation in the border zone, as well as the denervation of the infarct zone, are well-established hallmarks of nerve pathology in the diseased heart after injury.[28,39]

Taken together, these findings indicates that a unique process of targeted reinnervation occurs in the regenerating neonatal heart. This dynamic process of denervation, transient hyperinnervation, and reinnervation highlights that the regenerating neonatal heart possesses a high degree of axon plasticity. Moreover, this suggests that the neonatal mouse heart may be a powerful model system to study axon regeneration and targeted reinnervation in the injured heart.

Reinnervation of the regenerating heart by parasympathetic and sympathetic axon bundles

Our results demonstrate that cardiac axons undergo distinct remodeling in diseased and regenerative settings (**Figure 4**). Interestingly, parasympathetic and sympathetic nerves are known to mediate both cardiac repair and pathology. Following adult infarction, sympathetic nerve remodeling by axon sprouting and hyperinnervation poses risk for ventricular

arrythmias.[28,39] Contrastingly, parasympathetic nerve activation can have cardioprotective effects by reducing ventricular arrythmias after MI.[40,41] Furthermore, neonatal heart regeneration is dependent on both parasympathetic and sympathetic nerve function.[33,37] Thus, we hypothesized that parasympathetic and sympathetic axons have distinct patterns of remodeling in the regenerative and non-regenerative hearts.

To distinguish between nerve remodeling in regenerating and non-regenerating hearts, we performed MI surgery in *ChATCre; Rosa26*^{tdTomato} mice at the regenerative (P1) and non-regenerative (P7) timepoints and collected hearts at 21 days post-MI. Collected hearts were further stained with tdTomato and TH to identify both parasympathetic and sympathetic nerve patterning, respectively. The control uninjured hearts at P22 demonstrate both parasympathetic and sympathetic nerve bundling and patterning, as expected (**Figure 5A**). In contrast, the infarct zone of the P7 non-regenerating heart at 21 days post-MI showed complete denervation (**Figure 5B$_{iii}$**). This is similar to the denervation seen in the infarcted adult human heart,[42] and interestingly, the degree of denervation rather than infarction size is an accurate predictor of ventricular arrhythmias.[43] Furthermore, the non-regenerating hearts demonstrate sympathetic axon sprouting at the border zone, a distinctive feature of pathological nerve remodeling (**Figure 5B$_{ii}$, white arrows**).[31] Remarkably, the regenerating myocardium at 21 days post-MI of the P1 heart shows restoration of both parasympathetic and sympathetic nerve architecture (**Figure 5C**), where the border zone shows large bundles of parasympathetic and sympathetic axons (**Figure 5C$_{ii}$**). This reinnervation of the parasympathetic and sympathetic nerves extends to cover the newly regenerated myocardium in the infarct zone (**Figure 5C$_{iii}$**).

Our results demonstrate that nerve remodeling that follows neonatal and adult heart injury vary widely. The diseased, non-regenerative heart shows hallmarks of nerve pathology including denervation, hyperinnervation, and a novel phenotype of disassociation between the parasympathetic and sympathetic nerves. Uniquely, the regenerating neonatal heart is precisely reinnervated, where the parasympathetic and sympathetic nerves are closely bundled throughout the regenerated myocardium. This reestablishment of physiological innervation patterning reveals that cardiac parasympathetic and sympathetic reinnervation occurs during neonatal heart regeneration, which may contribute to restoring normal autonomic function.[33,37]

Physiological reinnervation during heart regeneration is dependent on collateral artery formation

Nerve remodeling following cardiac injury in the adult mammalian heart is a prominent hallmark of the pathology of heart failure. In contrast, following a neonatal mouse heart injury, the heart regenerates normally and the regenerated myocardium is reinnervated, as we demonstrated (**Figure 4D, 5C**). Interestingly, neonatal heart regeneration is also dependent on collateral artery formation, where collateral arteries form at 4 days post-MI to bridge the occluded left coronary artery with the right coronary artery and mediate successful regeneration.[44] During development, artery formation precedes innervation and arterial cells recruit nerve axons to the myocardium.[13,36] Thus, we hypothesized that newly formed collateral arteries can recruit nerve axons during cardiac regeneration.

To determine whether reinnervated axons associate with arteries in the regenerating myocardium, we performed MI surgery in regenerative (P1) or non-regenerative (P7) *Cx40CreER;Rosa26*^{tdTomato} mice and collected hearts at 7- or 21 days-post MI. Hearts underwent tissue clearing (**Figure 6A**), followed by whole-mount immunostaining with the pan-neuronal marker Tuj1 (**Figure 6**). Artery innervation was compared to uninjured P22 control hearts, which showed regions of artery innervation, as expected (**Figure 6B**). First, we investigated innervation remodeling in the non-regenerating heart (**Figure 6C**). We show that the non-regenerating heart is starkly denervated in the infarct zone at 21 days post-MI, including regions where the infarcted tissue is vascularized (**Figure 6C**). We then explored how this compared to nerve remodeling in the regenerative heart. Since collateral arteries are formed by 4 days post-MI in the regenerating heart,[44] we began by investigating nerve remodeling first at 7 days post-MI (**Figure S5A**). Interestingly, whole-mount imaging demonstrates that although collateral arteries start to appear at 4 days post-MI, the infarct zone remains denervated at 7 days post-MI (**Figure S5A**). We then explored the remodeling of nerve-artery architecture in the fully regenerated myocardium at 21 days post-MI (**Figure 6D)**. Excitingly, the nerves show reestablishment of nerve-artery connection with the arteries in the infarct zone, suggesting targeted reinnervation takes place (**Figure 6D**).

To determine whether reinnervation is dependent on collateral artery formation, we impaired collateral artery formation using the *Cx40CreER;Cxcr4*$^{fl/fl}$ mouse[44] (**Figure 7**). Cxcr4 is a chemokine receptor expressed in arterial endothelial cells that responds to the chemotactic ligand Cxcl12.[45-47] The Cxcl12/Cxcr4 axis is important for arterial cell migration and artery formation during

development and regeneration, where deletion of *Cxcr*4 using the *Cx40CreER* mice impairs collateral artery formation during neonatal heart regeneration.[44] We injected *Cx40CreER;Cxcr4$^{fl/fl}$* pups at P0 with a single dose of tamoxifen and MI was performed within the regenerative window at P2 (**Figure 7A**). Hearts were collected at 21 days-post-MI and underwent immunostaining for Tuj1. Strikingly, the infarcted area was denervated in *Cx40CreER;Cxcr4$^{fl/fl}$* hearts, in contrast to the regenerated and reinnervated wild type controls (**Figure 7B-C**), demonstrating that reinnervation is dependent on collateral artery formation. This is the first evidence of targeted reinnervation of the regenerating myocardium, and that this reinnervation is dependent on collateral artery formation.

Collectively, the high degree of axon plasticity (**Figure 4B-D**), the reinnervation of parasympathetic and sympathetic axon bundles (**Figure 5C**), and the direct artery reinnervation (**Figures 6D, 7**), demonstrates that physiological reinnervation takes place during heart regeneration. This is in stark contrast to the non-regenerating heart, which shows denervation of the infarct zone and pathological reinnervation, including sympathetic axon sprouting at the border zone (**Figures 4E, 5B**).

DISCUSSION

Neural regulation of the cardiovascular system has long been recognized; however, the importance of neurocardiology in cardiovascular health and disease is only beginning to be appreciated. Recent studies aimed at identifying the cellular and molecular makeup of the

intrinsic cardiac nervous system underscore the importance of elucidating the innervation patterns and functions throughout cardiac nervous system.[4,5]

Sympathetic innervation of cardiac ventricles has been studied extensively,[6,13] however; parasympathetic innervation has been underappreciated due to misconceptions and technical limitations.[17] In our experience, whole-mount immunolabeling of ChAT is technically challenging, where ChAT antibodies have limited binding affinity in the peripheral nervous system. Furthermore, 2D analysis from histological sections is inaccurate and cannot reconstruct the complex patterns of nerves and networks with other cell types. Complications extend to endogenous labeling, where using a lineage reporter alone is prone to quenching (**Figure S6**). To overcome this limitation, we utilized the *ChATCre; Rosa26*^{tdTomato} model together with whole mount immunostaining for tdTomato and tissue clearing, which allowed for an intact view of the parasympathetic nervous system. We further validated that our data was highly accurate by imaging the endogenous reporter signal in the intact heart directly after harvesting before any additional preservation or tissue manipulation steps, which served as an internal reference (**Figure S6A**). One possible drawback is that the confocal imaging resolution can lead to size overestimation; therefore, closely localized structures such as sympathetic and parasympathetic axons can show regions of signal overlap. Alternatively, there could be a subset of biphenotypic axons that simultaneously express both ChAT and TH proteins.[23] Importantly, there are much wider regions of distinction between parasympathetic and sympathetic axons that supports our results. Higher spatial resolution imaging and single cell analysis can overcome these technical limitations.

Our findings demonstrating extensive parasympathetic innervation of the ventricles underscores the potential for intercellular dynamics and physiological influences between parasympathetic nerves and the surrounding heart tissue. However, the mechanisms that guide this innervation remain unclear. The synchroneity of parasympathetic and sympathetic axon growth suggests both are recruited by NGF signaling in the ventricles,[13] and are likely guided by other neurotrophic factors. Extensive analysis of NGF and other factors is necessary to define parasympathetic ventricular innervation. Furthermore, we demonstrate a spatiotemporal innervation pattern of cardiac ventricles with respect to coronary arteries, suggesting that targeted neuronal synapses may influence arterial cell physiology.

Cardiac injury results in denervation and pathological nerve remodeling, which leads to a disruption in the nerve circuity.[28,29,31] This pathological neural remodeling that occurs following injury can lead to fatal arrhythmias and heart failure.[27] Nerves have been therapeutically targeted using neuromodulation approaches, such as vagal nerve stimulation and sympathetic nerve denervation.[48-51] Some studies demonstrate promising outcomes; however, our lack of understanding of cardiac nerve development and remodeling hampers our understanding of the mechanisms by which these approaches modulate reinnervation and nerve function.[52]

Neonatal mice can regenerate their hearts following injury for a short window after birth.[34] Cardiac nerves have been demonstrated to regulate cardiomyocyte proliferation and neonatal heart regeneration.[33] Furthermore, autonomic heart functions are restored following

regeneration, suggesting that physiological reinnervation take place, which contrasts with the pathological innervation that occurs following adult cardiac injury. Additionally, from a clinical perspective, it has been well established that heart transplant recipients receive a completely de-innervated heart, which eventually becomes partially innervated by the host.[53-55] Thus, understanding the development and plasticity of cardiac innervation is a unique approach to stimulate physiological innervation and cardiac regeneration.

Remarkably, we demonstrate for the first time the reestablishment of physiological innervation of the regenerating myocardium. However, the physiological function of these nerves and their contribution to restoration of autonomic function in the regenerated heart is yet to be determined. Targeted methods like optogenetic stimulation or vagal nerve stimulation would be required to identify any functional variations in nerve physiology.[56] Furthermore, we demonstrate that physiological reinnervation is dependent on collateral artery formation, where inhibition of collateral arteries following injury blocks this reinnervation. These results suggest that promoting collateral artery formation can be targeted to promote both physiological reinnervation and cardiac regeneration following injury. Whether the neurotrophic factors that mediate innervation during development play a similar role during regeneration is unclear.

Our study reveals new insights into cardiac innervation during development, disease, and regeneration. However, it remains unclear whether a distinct gene regulatory network mediates physiological and pathological innervation. Furthermore, identifying the signals by which coronary arteries regulate reinnervation during regeneration can play an important role in

treatment of autonomic dysfunction, as well as promote cardiac repair following injury. Single cell analysis of wild type and *Cx40CreER;Cxcr4*$^{fl/fl}$ knockout mice can elucidate a distinct molecular and cellular signature that guides reinnervation, particularly in relation to collateral arteries. Our results provide a framework to start dissecting the intricate networks that guide cardiac innervation and regeneration.

LIMITATIONS OF THE STUDY

This study presents a comprehensive examination of parasympathetic innervation within the cardiac ventricles. Despite this extensive investigation of innervation, the precise impact of these nerves on cardiac physiology remains ambiguous. Additionally, we establish the occurrence of physiological reinnervation during the regeneration process; however, the functional significance of these reestablished nerves remains undefined. Moreover, our findings highlight the cellular reliance of reinnervation on collateral artery formation, yet the specific molecular mechanisms governing this reinnervation process remain unresolved. Further research is warranted to elucidate these intricate molecular pathways and better comprehend the role of ventricular innervation in cardiac physiology and regeneration.

ACKNOWLEDGMENTS

Funding for this project was provided by an AHA Predoctoral Fellowship 829586 (R.J.S.), NIH/NHLBI R56 HL155617 (A.I.M.), NIH/NHLBI R01 HL166256 (A.I.M.), DOD W81XWH2210094 (A.I.M.), and NIH/NIGMS R35 GM 134865 (A.A.). We thank Lucile Miquerol and Kristy Red-Horse

for generously sharing the *Cx40CreER* mice. We thank Lance Rodenkirch and the Optical Imaging Core (Grant 1S10OD025040-01) for imaging support.

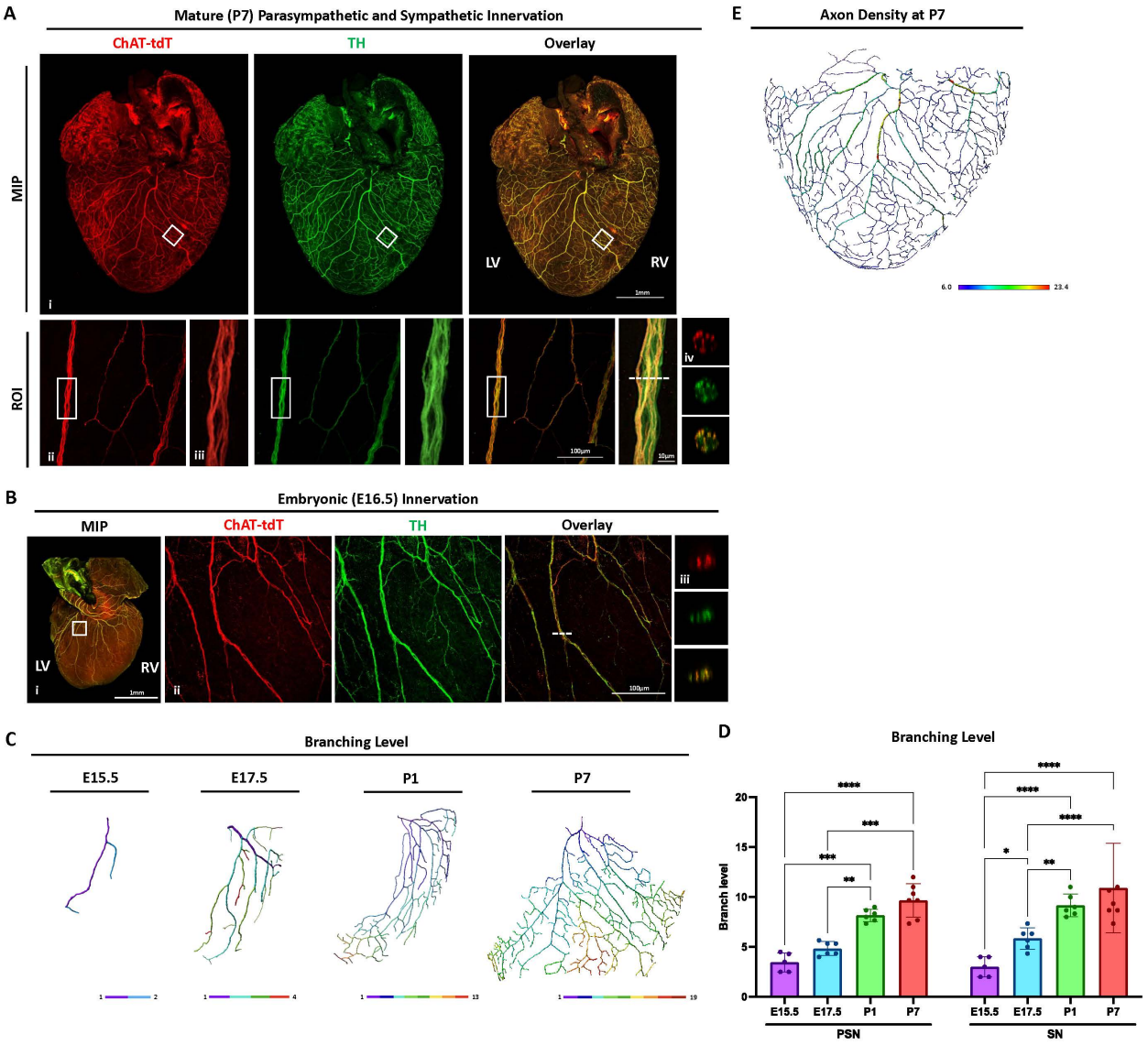

Figure 1. Parasympathetic and sympathetic axons are bundled and synchronous in development. Parasympathetic reporter hearts (*ChATCre;Rosa26*^{tdTomato}) were immunostained for sympathetic nerves with tyrosine hydroxylase (TH), imaged with confocal microscopy, and reconstructed with Imaris. (A) At postnatal day 7 (P7), (A_i) whole-heart max intensity projection (MIP) of the posterior mature nerve architecture shows close association between parasympathetic and sympathetic axons, with (A_{ii}) region of interest (ROI) demonstrating large and small nerve fibers closely aligned. (A_{iii}) ROI inset (white box in A_{ii}) and (**A_{iv}**) their cross-section

view (white dashed line in A_{iii} overlay) of axon bundles shows distinct parasympathetic and sympathetic axons (n=7). (B) At embryonic day 16.5 (E16.5), (B_i) both parasympathetic and sympathetic axons extend together in the posterior wall, with (B_{ii}) high-magnification and (B_{iii}) a cross-section view (white dashed line in B_{ii} overlay) demonstrating close localization and bundling of nerve subtypes (n=6). (C-D) 3D modeling and analysis shows increased branching level of parasympathetic and sympathetic nerves (PSN, SN) during embryonic and postnatal development (n=5-7). (E) Density analysis of the P7 heart shows axon bundles of primary and secondary axons are at higher density than tertiary and higher branched axons. Right and Left Ventricles (RV, LV) are indicated. Scale bars shown at 1mm for low magnification, 100μm for high magnification, and 10μm for insets. Significance shown as n.s. ($P > 0.05$), * ($P \leq 0.05$). **($P \leq 0.01$), ***($P \leq 0.001$), **** ($P \leq 0.0001$). Error bars presented as ± SEM.

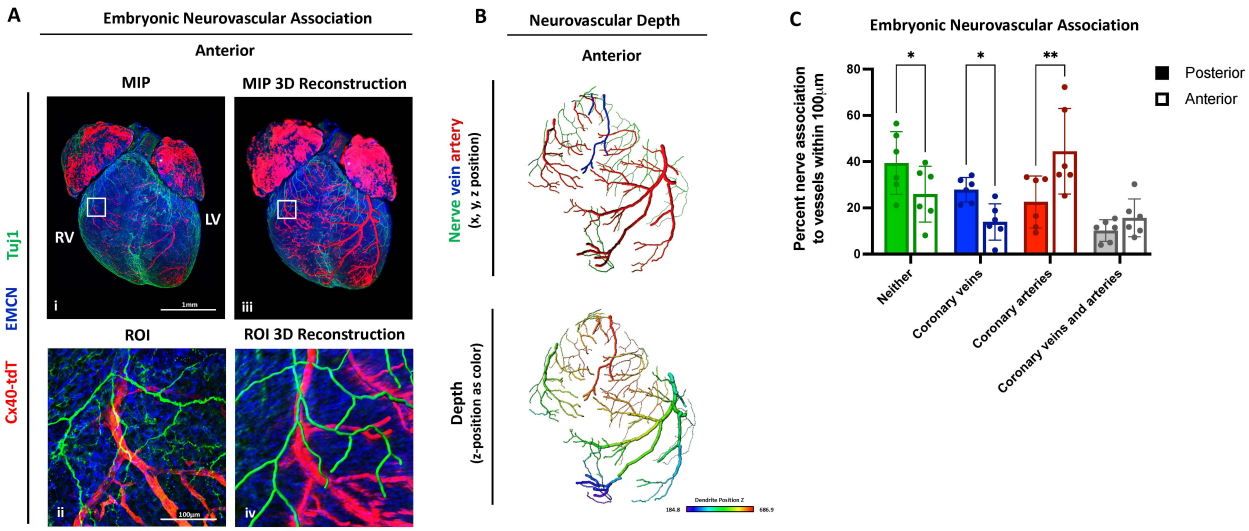

Figure 2. Neurovascular association shows cardiac axons align with the coronary arteries. Embryonic day 17.5 (E17.5) hearts of *Cx40CreER;Rosa26*^{tdTomato} coronary artery reporter mice were immunostained with the pan-neuronal marker Tuj1 and the endothelial cell marker endomucin (EMCN), followed by whole mount confocal imaging, and 3D reconstruction and modeling. (A) The neurovascular patterning is shown as (A_i) a whole-heart max intensity projection (MIP) of the anterior embryonic heart and (A_{ii}) a high-magnification in region of interest (ROI) (A_{iii}) 3D Imaris reconstruction of the whole embryonic heart, and (A_{iv}) a reconstruction of the ROI (n=6). (B) Neurovascular depth analysis shows that the anterior nerves are at similar depths to the coronary arteries (n=3). (C) Quantification of percentage of nerves associated within 100um of coronary veins (blue), arteries (red) both veins and arteries (grey) or neither vessel type (green) are shown, with an increased nerve artery association in the anterior wall (n=6). Right and Left Ventricles (RV, LV) are indicated. Scale bars shown at 1mm for low magnification and 100µm for high magnification. Significance shown as n.s. ($P > 0.05$), * ($P \leq 0.05$). **($P \leq 0.01$), ***($P \leq 0.001$), **** ($P \leq 0.0001$). Error bars presented as ± SEM.

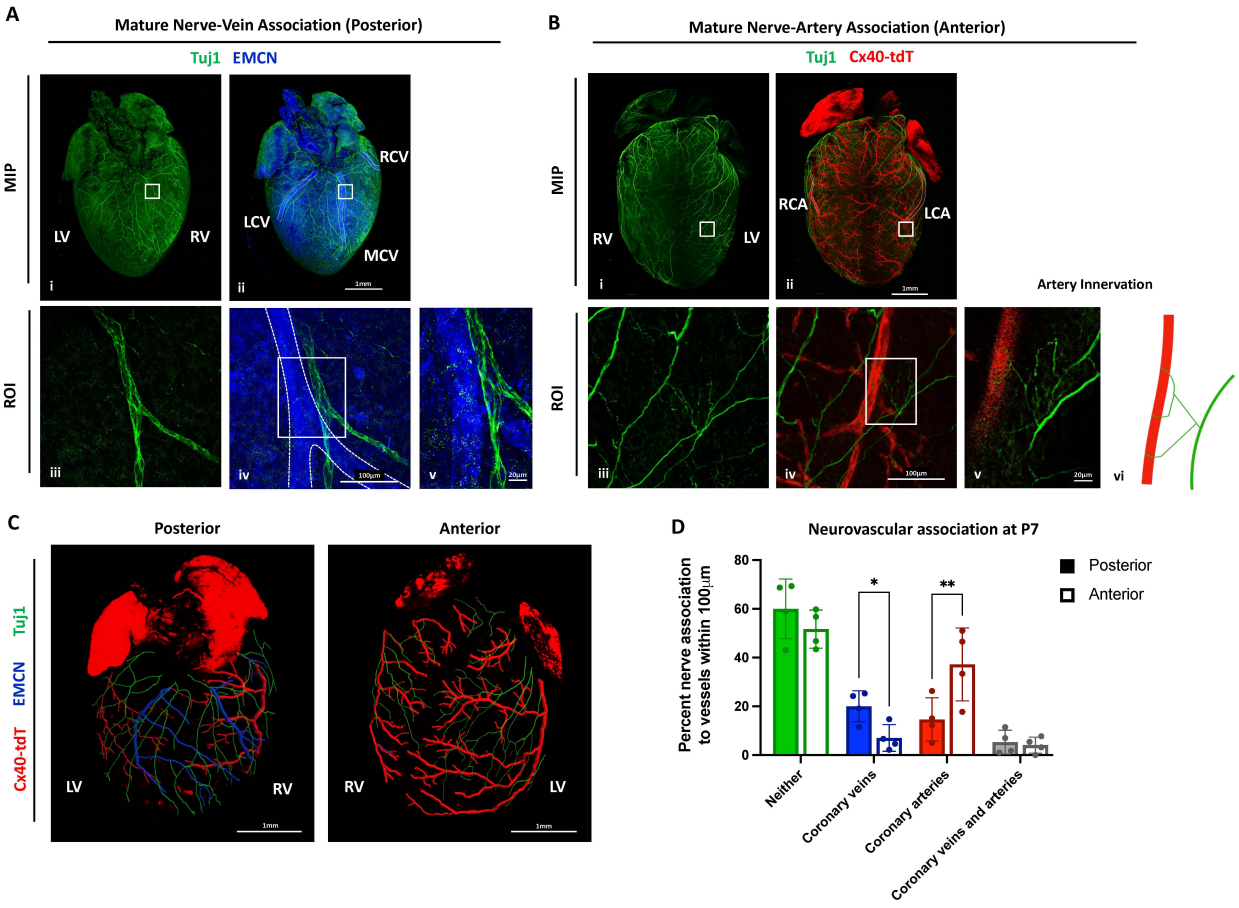

Figure 3. Mature 3D neurovascular architecture. P7 hearts of *Cx40CreER;Rosa26*^{tdTomato} coronary artery reporter mice were immunostained with the pan-neuronal marker Tuj1 and the endothelial cell marker endomucin (EMCN), followed by whole mount confocal imaging, and 3D reconstruction. (A) The posterior wall distribution of the mature cardiac nerves is shown as a whole-heart max intensity projection (MIP) of patterning of (A_i) posterior nerve patterning and (A_{ii}) nerve-vein association. (A_{iii-iv}) Region of interest (ROI) shows the nerves align without innervating the major left, medial, or right coronary veins (LCV, MCV, RCV), with (A_v) a representative magnified inset demonstrating lack of vein innervation (white box in A_{iv}) (n=4). (B) The anterior nerve architecture similarly is shown as MIP of the (B_i) anterior nerve patterning and (B_{ii}) nerve-artery association. (B_{iii-iv}) Nerves align and directly innervate the right and left coronary

arteries (RCA, LCA), with (B_v) a representative magnified z-plane inset (white box in B_{iv}) and (B_{vi}) a graphical representation demonstrating direct artery innervation (n=5). (C) Imaris 3D reconstruction highlights the neurovascular architecture of the posterior and anterior heart (n=3). (D) Quantification of percent of nerves associated within 100um of coronary veins (blue), arteries (red) both veins and arteries (grey) or neither vessel type (green) are shown, with an increased nerve artery association in the anterior wall (n=4). Scale bars shown at 1mm for low magnification, 100μm for high magnification, and 20μm for insets. Right and Left Ventricles (RV, LV) are indicated. Significance shown as n.s. ($P > 0.05$), * ($P \leq 0.05$). **($P \leq 0.01$), ***($P \leq 0.001$), **** ($P \leq 0.0001$). Error bars presented as ± SEM.

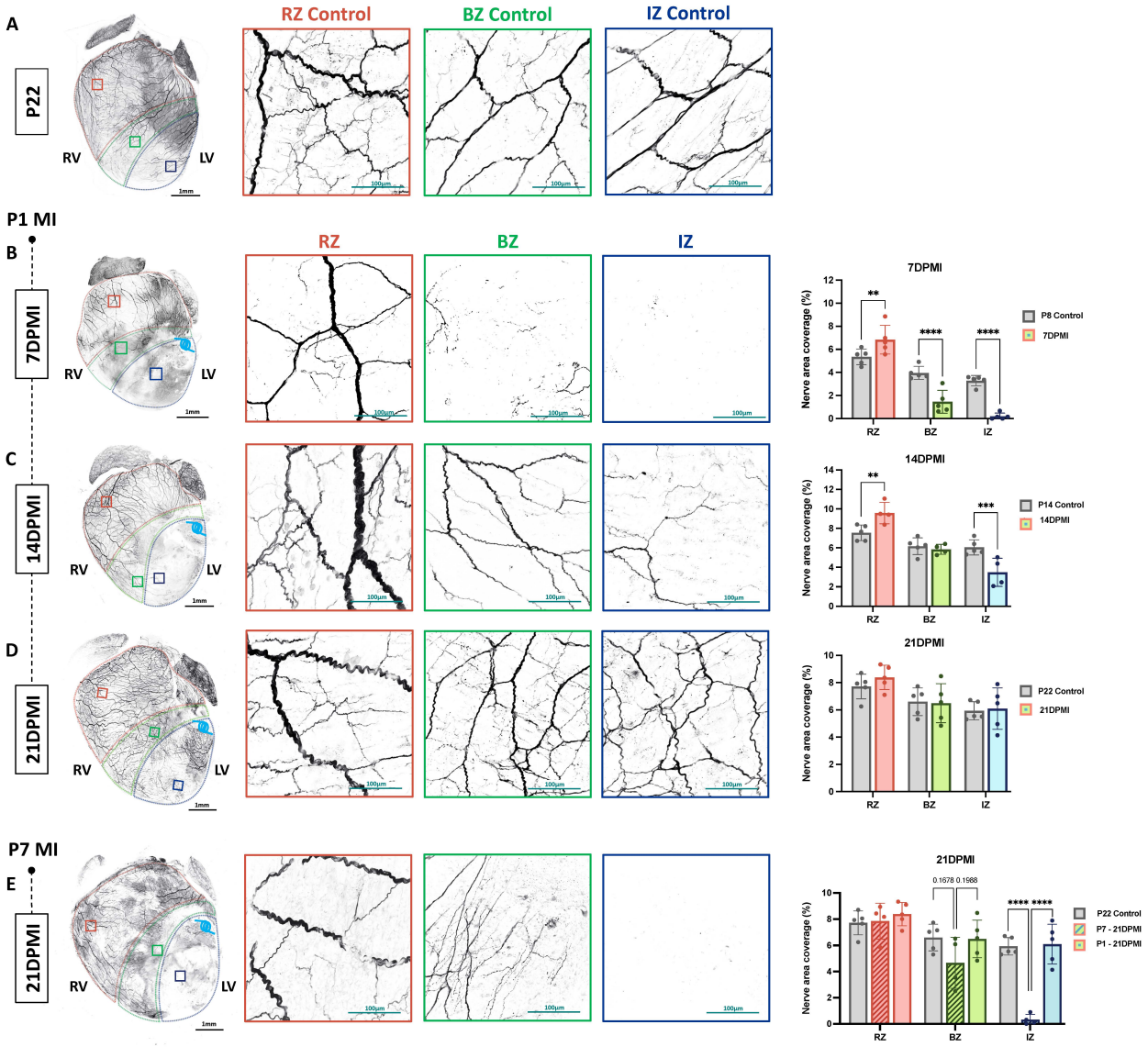

Figure 4. Cardiac axons show unique plasticity during neonatal heart regeneration. Myocardial Infarction (MI) was performed on WT mice at regenerative (P1) and non-regenerative (P7) timepoints. Nerve remodeling was compared to uninjured, age-matched control hearts. (A) P22 uninjured hearts show control innervation in regions similar to the remote zone (RZ, pink), border zone (BZ, green), and infarct zone (IZ, navy blue). (B-D) Regenerating hearts were collected following P1 MI at 7-, 14-, and 21-days post-MI (DPMI). (B) At 7DPMI, regenerative hearts were hyperinnervated in the RZ and denervated in the BZ and IZ (n=5), in comparison to P8 uninjured

hearts (n=5). (C) At 14DPMI, regenerative hearts were hyperinnervated in the RZ, with restored innervation in the BZ and decreased innervation in the IZ (n=4), in comparison to P15 uninjured hearts (n=5). (D) At 21DPMI, regenerated hearts show restored levels of innervation in the RZ, BZ, and IZ (n=5), in comparison to P22 uninjured hearts (n=5). (E) Non-regenerative hearts were collected following P7 MI at 21DPMI. Hearts showed no significant difference in RZ innervation, with heterogenous innervation in the BZ and denervation in the IZ, both indicators of nerve pathology (n=4). In whole-heart images, dashed borders outline the RZ (pink), BZ (green), and IZ (navy blue), and the light blue knot represents the suture site. Right and Left Ventricles (RV, LV) are indicated. Scale bars shown at 1mm for low magnification and 100μm for high magnification. Significance shown as n.s. ($P > 0.05$), * ($P \leq 0.05$). **($P \leq 0.01$), ***($P \leq 0.001$), **** ($P \leq 0.0001$). Error bars presented as ± SEM.

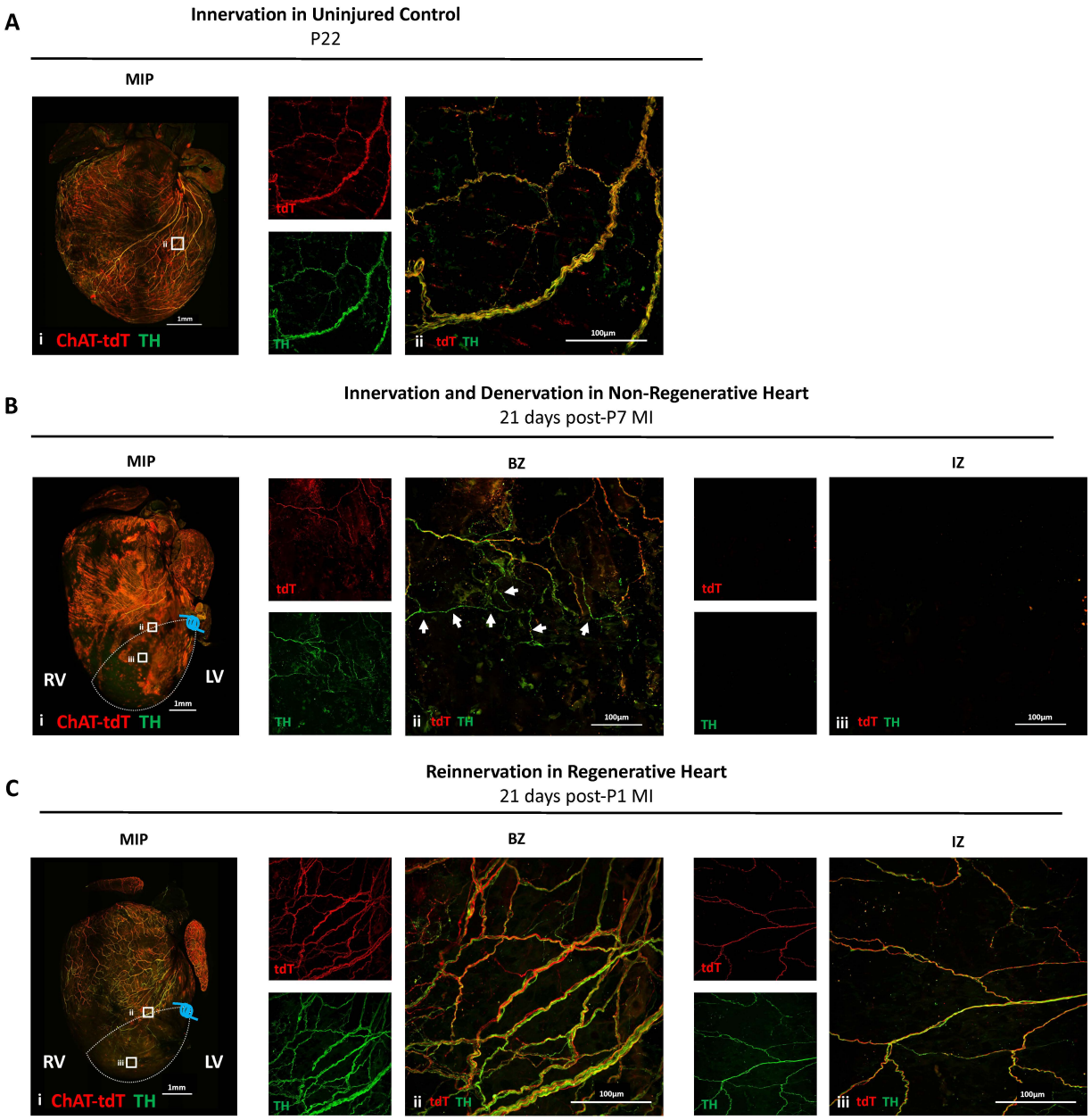

Figure 5. Parasympathetic and sympathetic nerves precisely reinnervate the regenerating myocardium. Myocardial Infarction (MI) was performed on *ChATCre;Rosa26*^{tdTomato} parasympathetic nerve reporter mice at regenerative (P1) and non-regenerative (P7) timepoints. Hearts were collected at 21 days post-MI, and immunostained for tyrosine hydroxylase (TH) and imaged with confocal microscopy. (A) Uninjured hearts in adult (P22) mice show parasympathetic and sympathetic nerve bundling in (A_i) whole-heart max intensity projection (MIP) of low

magnification and (A_{ii}) high magnification views of the ventricles (n=6). (B) Non-regenerating hearts show pathological remodeling of the nerves at 21 days post-P7 MI. (B_{ii}) The border zone (BZ) shows sympathetic axon sprouting (indicated by white arrows), independent of parasympathetic axons. (B_{iii}) The infarct zone (IZ) is denervated (n=6). (C) The regenerated heart shows reestablished parasympathetic and sympathetic axon bundling at 21 days post-P1 MI. (C_{ii}) The BZ shows dense nerve bundles of both nerve subtypes. (C_{iii}) The IZ also shows reinnervation of parasympathetic and sympathetic axons (n=5). In whole-heart MIP images, white dashed border indicates the IZ and the light blue knot represents the suture site. Right and Left Ventricles (RV, LV) are indicated. Scale bars shown at 1mm for low magnification and 100μm for high magnification. Significance shown as n.s. ($P > 0.05$), * ($P \leq 0.05$). **($P \leq 0.01$), ***($P \leq 0.001$), **** ($P \leq 0.0001$). Error bars presented as ± SEM.

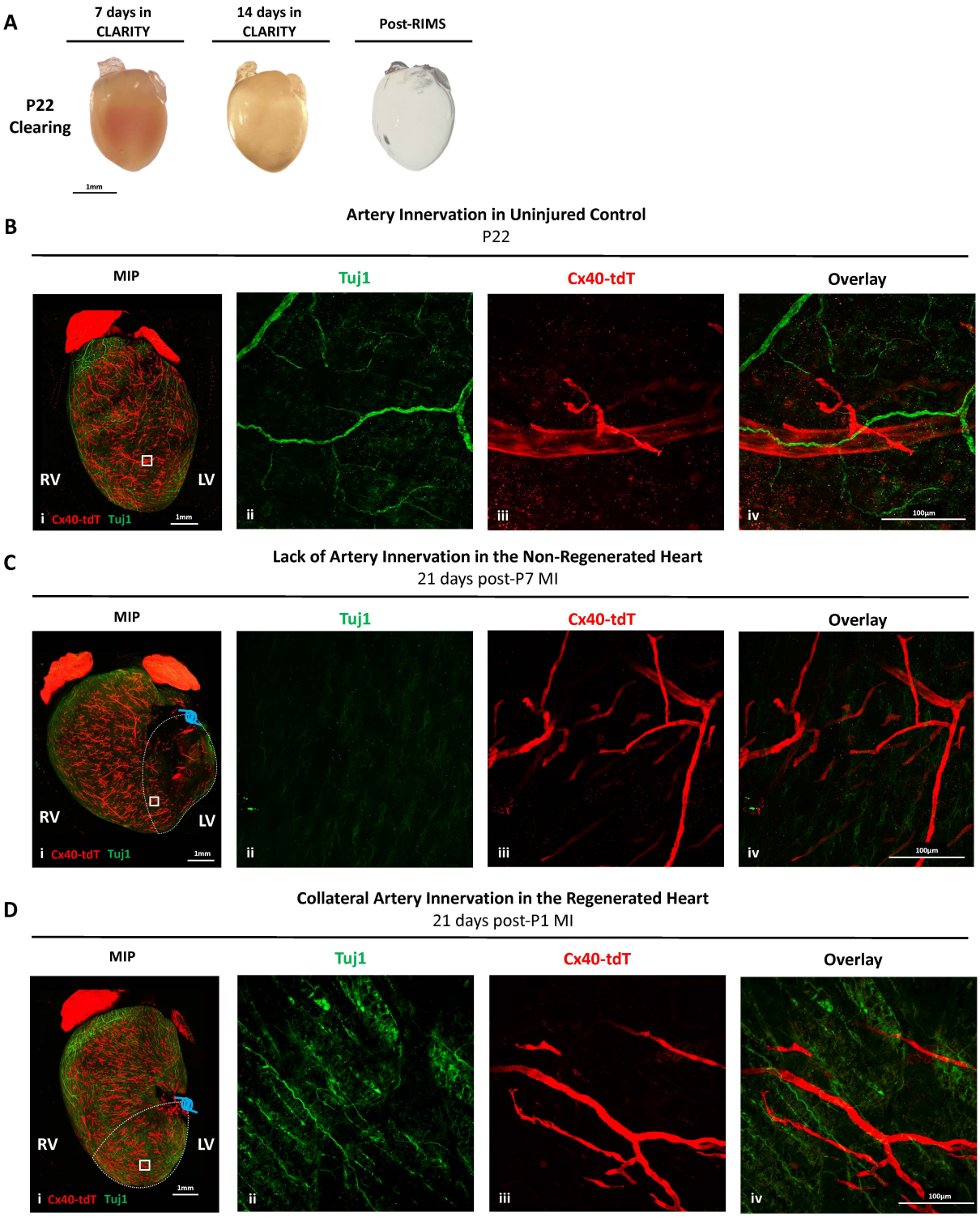
A
7 days in CLARITY
14 days in CLARITY
Post-RIMS
P22 Clearing
1mm
B
Artery Innervation in Uninjured Control
P22
MIP
Tuj1
Cx40-tdT
Overlay
RV
LV
i Cx40-tdT Tuj1
1mm
ii
iii
iv
100μm
C
Lack of Artery Innervation in the Non-Regenerated Heart
21 days post-P7 MI
MIP
Tuj1
Cx40-tdT
Overlay
RV
LV
i Cx40-tdT Tuj1
1mm
ii
iii
iv
100μm
D
Collateral Artery Innervation in the Regenerated Heart
21 days post-P1 MI
MIP
Tuj1
Cx40-tdT
Overlay
RV
LV
i Cx40-tdT Tuj1
1mm
ii
iii
iv
100μm

Figure 6. Nerve-artery association is reestablished in the regenerated heart. MI was performed in Cx40CreER;Rosa26tdTomato coronary artery reporter mice at regenerative (P1) or non-regenerative (P7) timepoints. (A) Hearts were collected at 21 dRebecca J. Salamon test.pdfays post-MI and underwent tissue clearing and nerve immunostaining with Tuj1. (B) Hearts were compared to uninjured P22 hearts, which showed (Bii) nerves, (Biii) arteries, and (Biv) artery innervation (n=4). (C) Non-regenerative hearts at 21 days post-P7 MI showed (C_{ii}) denervation in the infarct zone (IZ), (C_{iii-iv}) including areas with vascularization (n=6). (**D**) Regenerative hearts at 21 days post- P1 MI showed ($\mathbf{D_{ii}}$) innervation in the IZ, ($\mathbf{D_{iii-iv}}$) including reinnervation of arteries in the IZ (n=6). In whole-heart MIP images, dashed white lines indicate the IZ and the light blue knot represents the suture site. Right and Left Ventricles (RV, LV) are indicated. Scale bars shown at 1mm for low magnification and 100μm for high magnification. Significance shown as n.s. ($P > 0.05$), * ($P \leq 0.05$). **($P \leq 0.01$), ***($P \leq 0.001$), **** ($P \leq 0.0001$). Error bars presented as ± SEM.

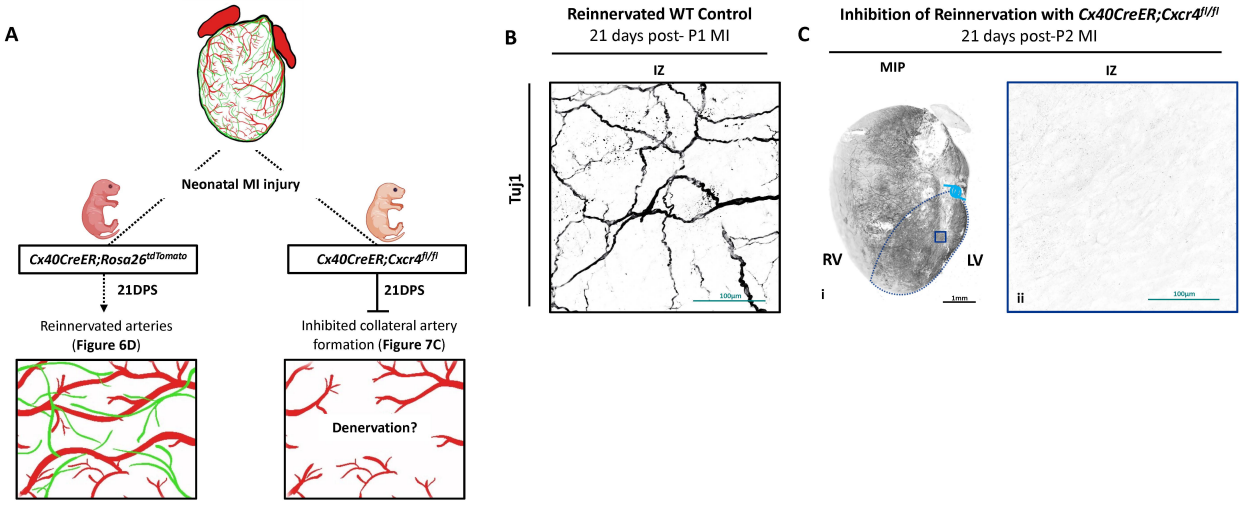

Figure 7. Reinnervation of the regenerating heart is dependent on collateral artery formation. MI was performed on *Cx40CreER;Rosa26*^{tdTomato} mice during the regenerative window (P2) and hearts were collected at 21-days post-MI. (A) We identify that the arteries in the infarct zone are reinnervated by 21-days post-MI. To determine whether reinnervation during regeneration is dependent on collateral artery formation, we used the *Cx40CreER;Cxcr4*$^{fl/fl}$ mouse to inhibit migration of arterial cells post-MI. At 21 days post-MI, Tuj1 immunostaining showed (B) innervation in the infarct zone (IZ) of wild type (WT) regenerated hearts (n=8), as expected. (C) In the *Cx40CreER;Cxcr4*$^{fl/fl}$ mice, the IZ remained denervated, shown by (C_i) whole-heart max intensity projection (MIP) and (C_{ii}) high-magnification of the IZ (n=4). In whole-heart images, navy blue dashed border indicates the IZ and the light blue knot represents the suture site. Right and Left Ventricles (RV, LV) are indicated. Scale bars shown at 1mm for low magnification and 100µm for high magnification. Significance shown as n.s. ($P > 0.05$), * ($P \leq 0.05$). **($P \leq 0.01$), ***($P \leq 0.001$), **** ($P \leq 0.0001$). Error bars presented as ± SEM.

SUPPLEMENTAL FIGURES

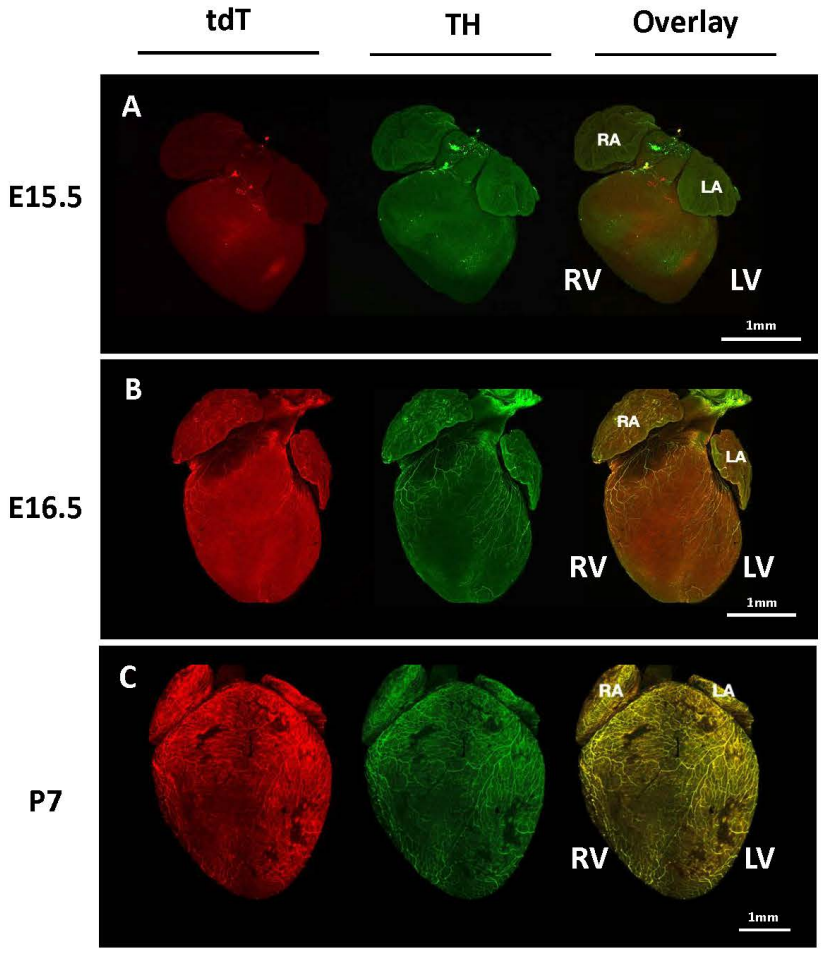

Figure S1. Anterior axon development. Parasympathetic reporter hearts, *ChATCre;Rosa26*^{tdTomato}, were harvested during embryonic and postnatal development and stained for sympathetic nerves with Tyrosine Hydroxylase (TH). The parasympathetic and sympathetic nerves in the anterior heart are (**A**) not present at E15.5 (n=7) (**B**) begin to innervate synchronously at E16.5 (n=6) and (**C**) are densely innervated by P7 (n=7). Right and left atria and ventricles are defined (RA, LA, RV, LV). Scale bars shown at 1mm.

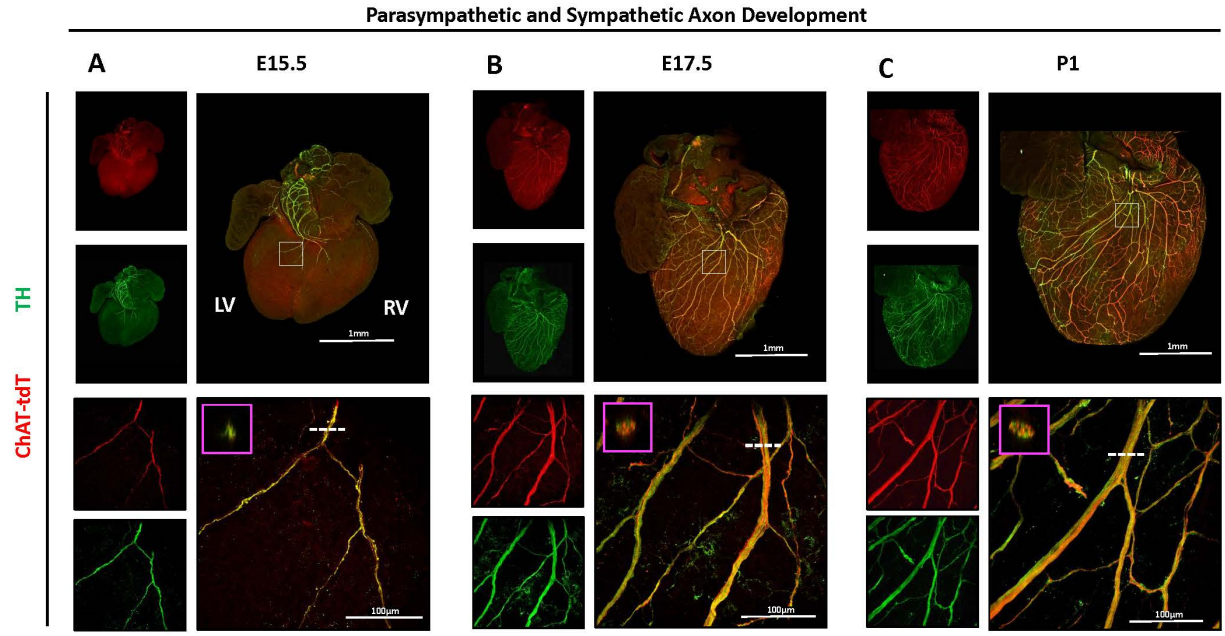

Figure S2. Embryonic development of parasympathetic and sympathetic nerves. Parasympathetic reporter hearts, *ChATCre;Rosa26*^{tdTomato}, were harvested during embryonic development and stained for sympathetic nerves with Tyrosine Hydroxylase (TH). Hearts are shown as whole-mount images and magnified regions of interest in the posterior. (A) At E15.5 nerves first appear in the ventricles, with parasympathetic and sympathetic axons showing close association and bundling (n=7); this trend continues throughout (B) at E17.5 in late embryonic development (n=6), and (C) at P1 in early postnatal development (n=6). Insets (magenta boxes) show cross-sections of nerve bundles, with white dashed lines indicating the region of optical cross-section. Scale bars shown at 1mm for whole-heart overlay images and 100µm for magnified overlay images.

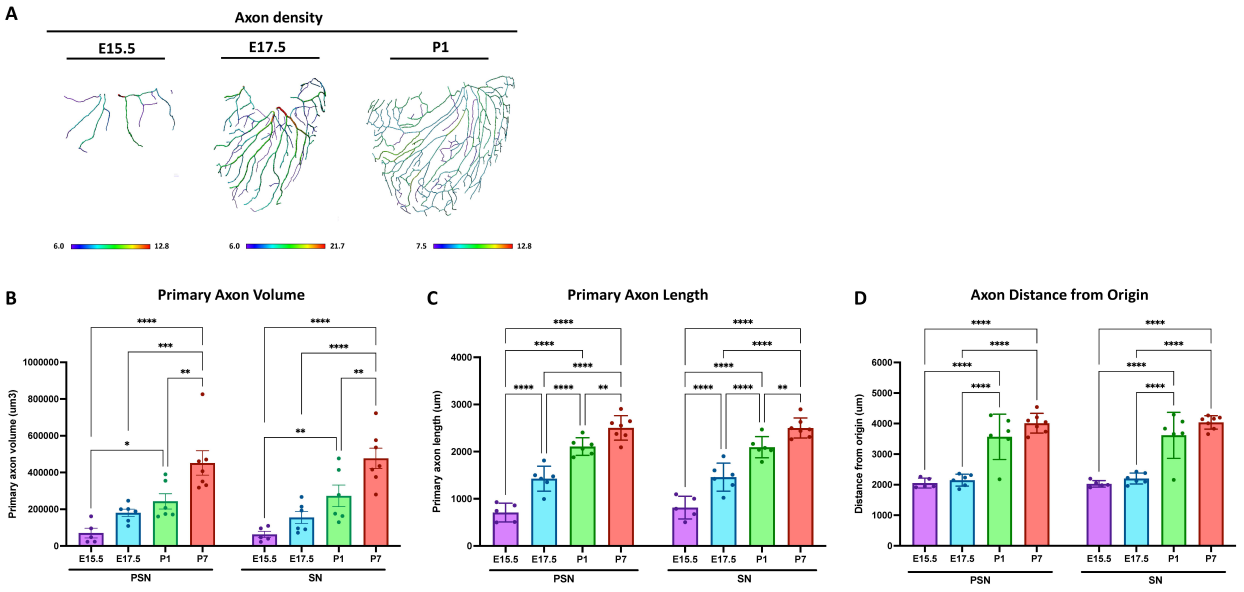

Figure S3. Analysis of embryonic and postnatal axon development. (A) Density distribution in developing nerve networks. Axon density is shown at E15.5, E17.5 and P1 for the entire parasympathetic nerve networks. Quantification of (B) primary axon volume (C) primary axon length and (D) distance from origin for parasympathetic (PSN) and sympathetic (SN) nerves during embryonic and postnatal development (n=5-7).

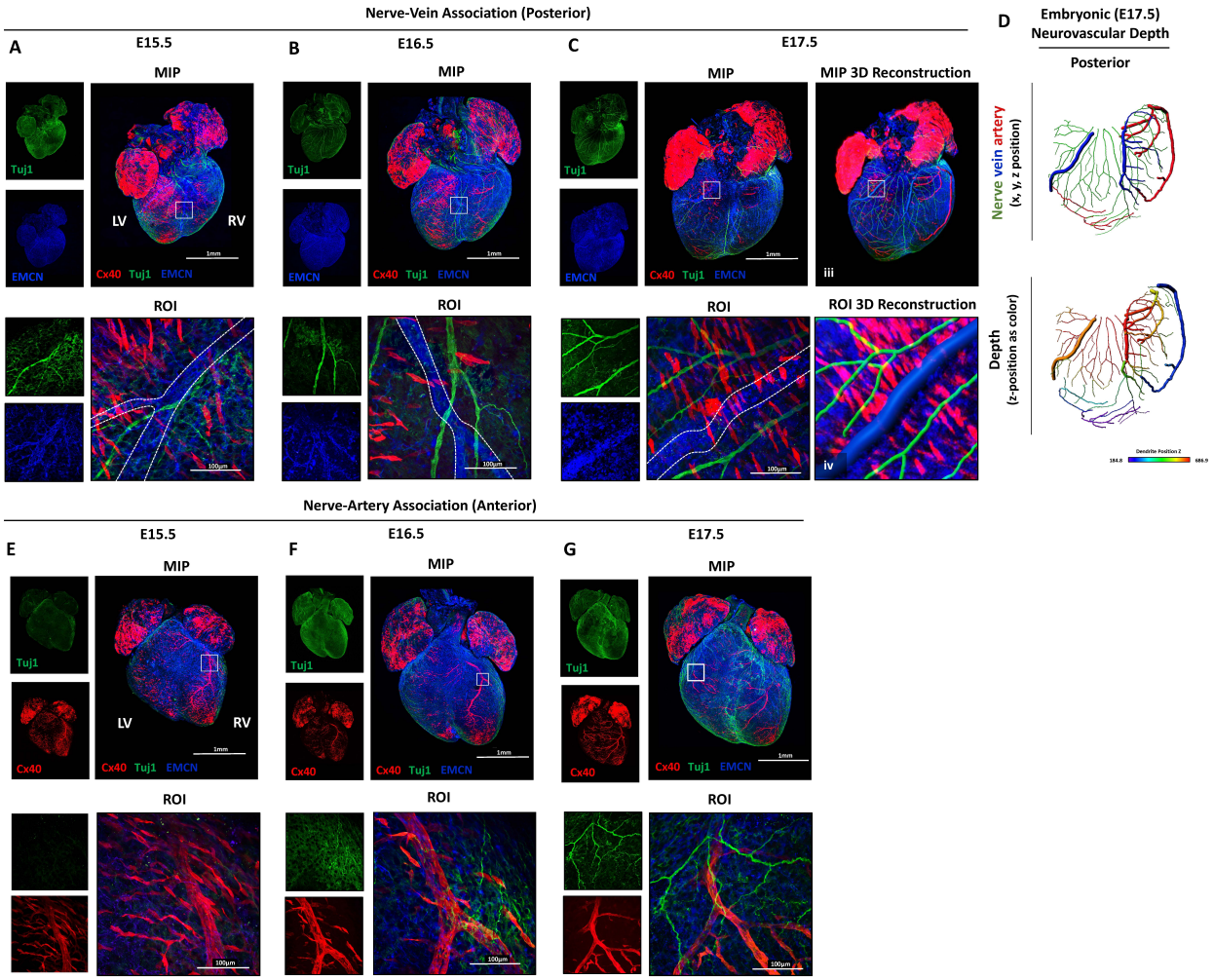

Figure S4. Embryonic nerve-vein and nerve-artery association. Embryonic hearts were immunostained for nerves (Tuj1), veins (EMCN) and arteries (Cx40-tdTomato) and imaged using confocal microscopy. The embryonic nerve development shows axon extension occurs from E15.5-E17.5. (A-C) The nerves first appear on the posterior heart at E15.5 and show association with the veins at (A) E15.5, (B) 16.5) and (C) 17.5. (D) Neurovascular depth analysis shows that the posterior nerves are at similar depths to the veins (n=4-6). (E-G) The anterior portion of the heart the begins to be innervated at E16.5 and axons associate with the coronary arteries by E17.5 (n=4-6). Scale bars shown at 1mm for whole-heart overlay images and 100µm for magnified overlay images.

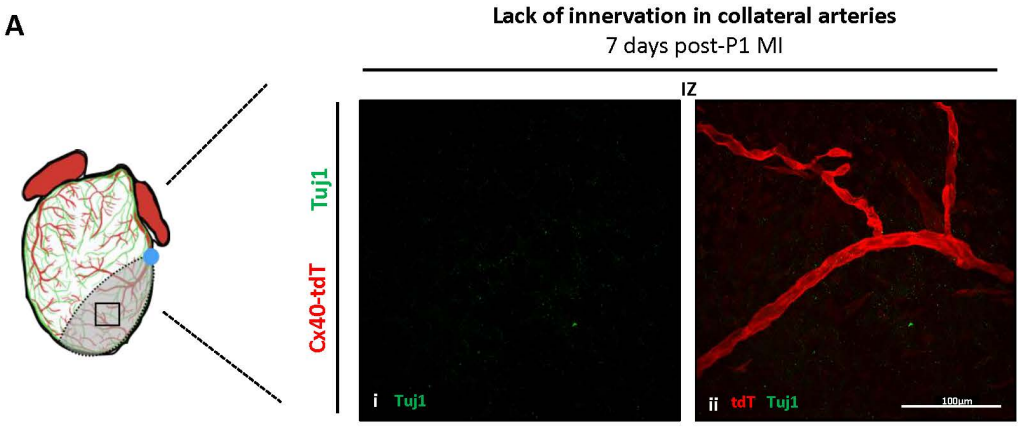

Figure S5. Lack of innervation in collateral arteries at 7 days-post MI. MI was performed in *Cx40CreER;Rosa26*^{tdTomato} in regenerative (P1) mice. Hearts were collected at 7-days post-MI and underwent tissue clearing and nerve immunostaining with Tuj1. (A) Regenerative hearts at 7 days after P1 MI showed (A_i) the IZ is denervated, (A_{ii}) including the newly formed collateral arteries (n=6). Scale bar shown at 100um.

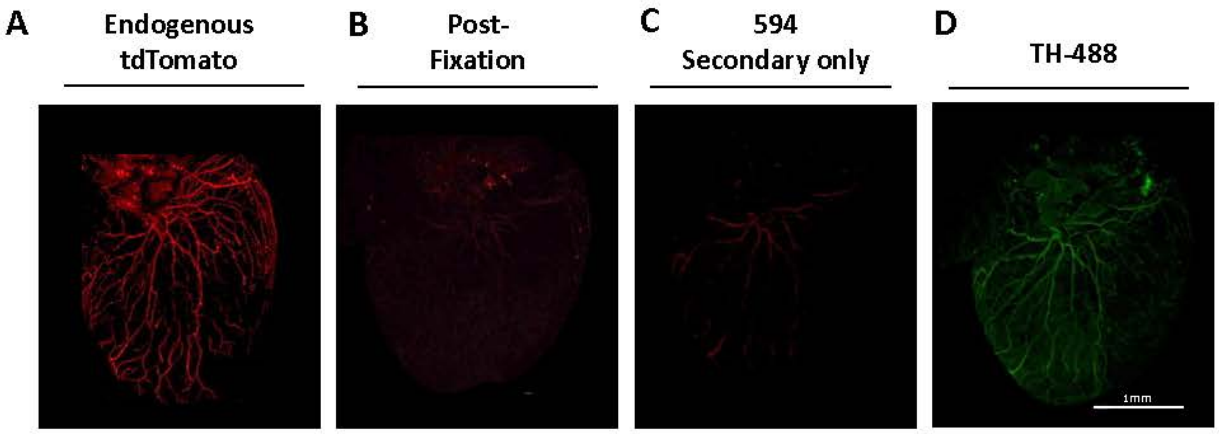

Figure S6. ChAT-Tdtomato signal is quenched post-fixation. ChAT-Tdtomato staining control to show secondary is specifically binding to tdTomato, shown by whole-mount of P1 hearts. (A) Endogenous TdTomato expression is fluorescent. (B) Post-fixation in PFA, this endogenous signal is quenched. (C) Adding in 594 secondary only without tdTomato primary produces no off-target binding. (D) Staining with Tyrosine Hydroxylase (TH) primary and matching 488 secondary shows the 488 specific to the TH epitope binds specifically. Scale bar shown at 1mm.

STAR★METHODS

Key Resources Table

REAGENT or RESOURCE	SOURCE	IDENTIFIER
Antibodies		
RFP/tdTomato (Rabbit)	Rockland	Cat# RL600-401-379
Tuj1 (Mouse)	Sigma	Cat# T8453
Tuj1 (Rabbit)	Abcam	Cat# ab18207
TH (Sheep)	Chemicon	Cat# AB1542
Endomucin (Rat)	Santa Cruz	Cat# SC65494
Alexa Fluor Plus 594 (anti-rabbit)	Invitrogen	Cat# A32740
Alexa Fluor Plus 488 (anti-mouse)	Invitrogen	Cat# A32723
Alexa Fluor 488 (anti-sheep)	Invitrogen	Cat# A-11015
Alexa Fluor Plus 405 (anti-rat)	Invitrogen	Cat# A48261
Chemicals		
Tamoxifen	Sigma	Cat# T5648-5G
PFA	Electron Microscopy Sciences	Cat# 15710
Triton X-100	Sigma	Cat# X100
Acrylamide	Bio-Rad	Cat# 1610140
VA-044	Wako Chemicals	Cat# NC0632395
SDS	VWR	Cat# 470302-616
Boric Acid	Dot Scientific	Cat# DSB32050-500
1-Thioglycerol	Sigma	Cat# M6145-25ML
Experimental models: Organisms/strains		
ChATCre	The Jackson Laboratory	Stock# 006410
Rosa26^{tdTomato}	The Jackson Laboratory	Stock# 007905
Cx40CreER	Miquerol et al., 2015	N/A
Cxcr4$^{fl/fl}$	The Jackson laboratory	Stock# 008767
Software and algorithms		
Imaris (with Filament Tracer)	Bitplane (https://imaris.oxinst.com)	N/A
ImageJ	NIH (http://imagej.net/ij/index.html)	N/A
GraphPad Prism 9	GraphPad Software (https://www.graphpad.com/features)	N/A
Microscope and Imaging	Nikon (https://www.microscope.healthcare.nikon.com/products/software)	N/A
Adobe Photoshop and Lightroom	https://www.adobe.com/products/photoshop.html	N/A
Other		
6-0 Polypropylene Sutures	Covidien	VP706X

Mice

All animal experimental procedures were approved by the Institutional Animal Care and Use Committee of the University of Wisconsin-Madison. All experiments were performed on age and sex matched mice, with an equal ratio of male to female mice. Mouse lines used in this study

are: *ChATCre* (The Jackson Laboratory, Stock# 006410), *Rosa26*^{tdTomato} (The Jackson laboratory, Stock# 007905), *Cx40CreER,*[57] *Cxcr4*$^{fl/fl}$ (The Jackson laboratory, Stock# 008767).

Tamoxifen administration

Tamoxifen was prepared at 100 mg/ml, dissolved in a 9:1 solution of corn oil to 100% ethanol, and incubated at 37ºC overnight with rotation. Solution was vortex as needed. Tamoxifen stock was kept at 4ºC for up to one month and incubated at 37ºC overnight before use. For *Cx40CreER* postnatal Cre induction, tamoxifen (1mg per pup) was administered by a subcutaneous (SubQ) injection directly to pup at P4 [44]. For *Cx40CreER* embryonic Cre induction, tamoxifen (0.1mg/g BW) was administered to the intraperitoneal (IP) cavity of the pregnant dam 24 hours before harvest.

Myocardial infarction surgery

Myocardial Infarction surgery (MI) was performed at P1 or P7, as described.[58] Pups were separated from dam and placed into a new cage with bedding. Pup was anesthetized on ice for 3 minutes. Working under a dissecting scope, a small incision was made in the skin, area under the skin was loosened, the 4th intercostal muscle was located, and incision was made, and the heart was gently guided out of the chest cavity with blunt forceps. The LAD was located at ligated with a 6-0 polypropylene suture by two simple knots, and apical blanching was visualized. Heart was gently guided back into the chest cavity, ribs were sutured together, and skin was glued. Pup was placed into a heating pad until lively. Once surgery was complete, pups were rubbed with original bedding to transfer scent and placed back to dam. Hearts were collected at 7- or 21-days post-MI.

Tissue clearing of intact postnatal hearts

Our passive CLARITY technique was performed with minimal modifications[59] in hearts that required imaging of structures deep within the tissue (i.e. coronary arteries). Briefly, hearts were harvested, washed in PBS, and placed into 4% PFA, incubating overnight at 4ºC with rotation. Following, hearts were washed with PBS for 30min at room temperature (RT), repeated three times, and placed into a polymerization solution (4% acrylamide and 0.5% VA-044) overnight at 4ºC. The next day, polymerization was activated with a 3-hour incubation at 37ºC. Hearts were again washed at RT in PBS for 30 min, repeated three times. Hearts were placed into clearing solution (8.0% w/v SDS, 1.25% w/v Boric acid, 0.5% w/v 1-thioglycerol dissolved in purified H2O, pH 8.5) and incubated at 37ºC, changing the solution every two days until tissue was fully cleared. Typically, P7 and P22 hearts were cleared for 3-5 or 10-14 days, respectively. In some tissues, a dark, green colored pigment persists even after clearing; regardless tissues were moved onto next steps, as it will be cleared out during washing. After clearing, tissues were washed in a conical tube with 10ml of PBS for 3 days, changing PBS solution 2-3 times daily.

Whole-mount immunohistochemistry

For uncleared tissues, hearts were harvested, blood removed, fixed for 1-2 hours in 4% PFA at 4ºC. Hearts were washed in PBS for 15 min, repeated 3 times. Cleared and uncleared hearts underwent the same immunohistochemistry staining protocol described. Hearts were blocked in 20% blocking buffer (BB, matching serum from secondary host) made in PBS with 0.2% triton (PBST) for 1 hour at RT. Primary antibodies were diluted in 0.2% PSBT with 2% BB and at the following concentrations: rabbit RFP/tdTomato (Rockland, Cat# RL600-401-379) at [1:200], mouse Tuj1 (Sigma, Cat# T8453) at [1:200], rabbit Tuj1 (Abcam, Cat# ab18207) at [1:500], sheep

TH (Chemicon, Cat# AB1542) at [1:200], endomucin (Santa Cruz, Cat# SC65494) at [1:100]. Primary concentrations for hearts at P21 or older were doubled. Primary incubation was performed overnight at RT, then transferred to 4ºC for an additional overnight incubation. Following, hearts were washed with PBS for 30min at RT, repeated three times. Secondary antibodies were diluted in 0.2% PBST + BB at [1:250], using the following Alexa Fluor antibodies from Invitrogen: 594 anti-rabbit (Cat# A32740), 488 anti-mouse (Cat# A32723), 488 anti-sheep (Cat# A-11015), 405 anti-rat (Cat# A48261). Secondary incubation was performed for 3 hours at RT then moved to 4ºC overnight. When using a combination of mouse and rat primary antibodies, the staining was performed sequentially to limit cross-reaction of secondary antibodies.[60]

Analysis of Nerve Area Coverage

Nerve area coverage was measured in the remote, border, and infarction zones. Each region was defined by the anatomical landscape of the injured hearts, where the infarction zone was defined as the area directly impacted by the ligation, the border zone as the region beside the infarction where tissue composition appeared impacted, and the remote zone as the region furthest away from the ligation and appeared unaltered. For quantification, 3-4 field of view replicate images were taken at 40x magnification per region. Image J software was used to quantify nerve coverage per each image, measuring the percent of nerve area coverage within the field of view. Graph points are displayed as the average nerve coverage per region (remote, border, infarct zone) in each heart.

Microscopy and 3D reconstruction

Confocal imaging was performed on a Nikon Upright FN1 microscope equipped with high sensitivity GaAsP detectors. Hearts were placed into a 3D-printed well, filled with water, and

positioned for anatomical view. Whole heart images were taken using a 4x air objective (0.2 NA), with 5 um spacing between z-planes, and tiles stitched with Nikon pic-stitching function, and scale bars shown as 1 mm. Higher magnification images were taken using a 40x water immersion objective (0.8 NA), with 1 um steps between z-planes, and scale bars shown as 100 um. Imaris microscopy image analysis software in filaments mode was used to segment hearts generate statistics. Representative images are shown as max intensity projections (MIP) and were edited using Adobe Lightroom and Photoshop for clarity. Since Endomucin (EMCN) stains veins and capillaries, EMCN signal in large-diameter veins was artificially highlighted in Photoshop. Confocal images were deconvolved using iterative classic maximum likelihood estimation in Huygens Profession before Imaris 3D reconstruction.

Statistical analysis

Data generated via Imaris, with 2-3 replicates averaged per sample and 4-7 samples per group. Nerve area coverage was generated with Image J analysis, with 3-4 replicates imaged per region and 4-6 hearts per group. Graphs generated in GraphPad Prism 9, with individual points representing the average per sample. Groups with one variable were compared using ordinary one-way ANOVA with Tukey post hoc test to determine significance. Groups with multiple variables were compared by an ordinary two-way ANOVA, with uncorrected Fisher's LSD, with a single pooled variance. Significance shown as n.s. ($P > 0.05$), * ($P \leq 0.05$). **($P \leq 0.01$), ***($P \leq 0.001$), **** ($P \leq 0.0001$). Error bars presented as ± SEM.

REFERENCES

1. Hasan, W. (2013). Autonomic cardiac innervation: development and adult plasticity. Organogenesis *9*, 176-193. 10.4161/org.24892.
2. Randall, W.C. (1984). Nervous control of cardiovascular function (Oxford University Press, USA).
3. Randall, W.C. (1965). Nervous control of the heart (Williams and Wilkins Company).
4. Achanta, S., Gorky, J., Leung, C., Moss, A., Robbins, S., Eisenman, L., Chen, J., Tappan, S., Heal, M., Farahani, N., et al. (2020). A Comprehensive Integrated Anatomical and Molecular Atlas of Rat Intrinsic Cardiac Nervous System. iScience *23*, 101140. 10.1016/j.isci.2020.101140.
5. Hanna, P., Dacey, M.J., Brennan, J., Moss, A., Robbins, S., Achanta, S., Biscola, N.P., Swid, M.A., Rajendran, P.S., Mori, S., et al. (2021). Innervation and Neuronal Control of the Mammalian Sinoatrial Node a Comprehensive Atlas. Circ Res *128*, 1279-1296. 10.1161/CIRCRESAHA.120.318458.
6. Vegh, A.M.D., Duim, S.N., Smits, A.M., Poelmann, R.E., Ten Harkel, A.D.J., DeRuiter, M.C., Goumans, M.J., and Jongbloed, M.R.M. (2016). Part and Parcel of the Cardiac Autonomic Nerve System: Unravelling Its Cellular Building Blocks during Development. J Cardiovasc Dev Dis *3*. 10.3390/jcdd3030028.
7. Zaglia, T., and Mongillo, M. (2017). Cardiac sympathetic innervation, from a different point of (re)view. J Physiol *595*, 3919-3930. 10.1113/JP273120.
8. Dokshokova, L., Franzoso, M., Di Bona, A., Moro, N., Sanchez Alonso, J.L., Prando, V., Sandre, M., Basso, C., Faggian, G., Abriel, H., et al. (2022). Nerve growth factor transfer from cardiomyocytes to innervating sympathetic neurons activates TrkA receptors at the neuro-cardiac junction. J Physiol *600*, 2853-2875. 10.1113/jp282828.
9. Larrivée, B., Freitas, C., Suchting, S., Brunet, I., and Eichmann, A. (2009). Guidance of vascular development: lessons from the nervous system. Circ Res *104*, 428-441. 10.1161/circresaha.108.188144.
10. Habecker, B.A., Anderson, M.E., Birren, S.J., Fukuda, K., Herring, N., Hoover, D.B., Kanazawa, H., Paterson, D.J., and Ripplinger, C.M. (2016). Molecular and cellular neurocardiology: development, and cellular and molecular adaptations to heart disease. J Physiol *594*, 3853-3875. 10.1113/JP271840.
11. Hildreth, V., Anderson, R.H., and Henderson, D.J. (2009). Autonomic innervation of the developing heart: origins and function. Clin Anat *22*, 36-46. 10.1002/ca.20695.
12. Moon, J.I., and Birren, S.J. (2008). Target-dependent inhibition of sympathetic neuron growth via modulation of a BMP signaling pathway. Dev Biol *315*, 404-417. 10.1016/j.ydbio.2007.12.041.
13. Nam, J., Onitsuka, I., Hatch, J., Uchida, Y., Ray, S., Huang, S., Li, W., Zang, H., Ruiz-Lozano, P., and Mukouyama, Y.S. (2013). Coronary veins determine the pattern of sympathetic innervation in the developing heart. Development *140*, 1475-1485. 10.1242/dev.087601.
14. Pianca, N., Di Bona, A., Lazzeri, E., Costantini, I., Franzoso, M., Prando, V., Armani, A., Rizzo, S., Fedrigo, M., Angelini, A., et al. (2019). Cardiac sympathetic innervation

network shapes the myocardium by locally controlling cardiomyocyte size through the cellular proteolytic machinery. J Physiol *597*, 3639-3656. 10.1113/JP276200.

15. Tampakakis, E., Gangrade, H., Glavaris, S., Htet, M., Murphy, S., Lin, B.L., Liu, T., Saberi, A., Miyamoto, M., Kowalski, W., et al. (2021). Heart neurons use clock genes to control myocyte proliferation. Sci Adv *7*, eabh4181. 10.1126/sciadv.abh4181.
16. Zaglia, T., Milan, G., Franzoso, M., Bertaggia, E., Pianca, N., Piasentini, E., Voltarelli, V.A., Chiavegato, D., Brum, P.C., Glass, D.J., et al. (2013). Cardiac sympathetic neurons provide trophic signal to the heart via beta2-adrenoceptor-dependent regulation of proteolysis. Cardiovasc Res *97*, 240-250. 10.1093/cvr/cvs320.
17. Coote, J.H. (2013). Myths and realities of the cardiac vagus. J Physiol *591*, 4073-4085. 10.1113/jphysiol.2013.257758.
18. Dunlap, M.E., Bibevski, S., Rosenberry, T.L., and Ernsberger, P. (2003). Mechanisms of altered vagal control in heart failure: influence of muscarinic receptors and acetylcholinesterase activity. Am J Physiol Heart Circ Physiol *285*, H1632-1640. 10.1152/ajpheart.01051.2002.
19. Mittmann, C., Pinkepank, G., Stamatelopoulou, S., Wieland, T., Nürnberg, B., Hirt, S., and Eschenhagen, T. (2003). Differential coupling of m-cholinoceptors to Gi/Go-proteins in failing human myocardium. J Mol Cell Cardiol *35*, 1241-1249. 10.1016/s0022-2828(03)00235-9.
20. Brack, K.E., Winter, J., and Ng, G.A. (2013). Mechanisms underlying the autonomic modulation of ventricular fibrillation initiation--tentative prophylactic properties of vagus nerve stimulation on malignant arrhythmias in heart failure. Heart Fail Rev *18*, 389-408. 10.1007/s10741-012-9314-2.
21. Nalivaiko, E., Antunes, V.R., and Paton, J.F. (2010). Control of cardiac contractility in the rat working heart-brainstem preparation. Exp Physiol *95*, 107-119. 10.1113/expphysiol.2009.048710.
22. Johnson, T.A., Gray, A.L., Lauenstein, J.M., Newton, S.S., and Massari, V.J. (2004). Parasympathetic control of the heart. I. An interventriculo-septal ganglion is the major source of the vagal intracardiac innervation of the ventricles. J Appl Physiol (1985) *96*, 2265-2272. 10.1152/japplphysiol.00620.2003.
23. Rysevaite, K., Saburkina, I., Pauziene, N., Vaitkevicius, R., Noujaim, S.F., Jalife, J., and Pauza, D.H. (2011). Immunohistochemical characterization of the intrinsic cardiac neural plexus in whole-mount mouse heart preparations. Heart Rhythm *8*, 731-738. 10.1016/j.hrthm.2011.01.013.
24. Pauza, D.H., Saburkina, I., Rysevaite, K., Inokaitis, H., Jokubauskas, M., Jalife, J., and Pauziene, N. (2013). Neuroanatomy of the murine cardiac conduction system: a combined stereomicroscopic and fluorescence immunohistochemical study. Auton Neurosci *176*, 32-47. 10.1016/j.autneu.2013.01.006.
25. Yasuhara, O., Matsuo, A., Bellier, J.P., and Aimi, Y. (2007). Demonstration of choline acetyltransferase of a peripheral type in the rat heart. J Histochem Cytochem *55*, 287-299. 10.1369/jhc.6A7092.2006.
26. Rajendran, P.S., Challis, R.C., Fowlkes, C.C., Hanna, P., Tompkins, J.D., Jordan, M.C., Hiyari, S., Gabris-Weber, B.A., Greenbaum, A., Chan, K.Y., et al. (2019). Identification of

peripheral neural circuits that regulate heart rate using optogenetic and viral vector strategies. Nat Commun *10*, 1944. 10.1038/s41467-019-09770-1.

27. Fukuda, K., Kanazawa, H., Aizawa, Y., Ardell, J.L., and Shivkumar, K. (2015). Cardiac innervation and sudden cardiac death. Circ Res *116*, 2005-2019. 10.1161/CIRCRESAHA.116.304679.
28. Cao, J.M., Chen, L.S., KenKnight, B.H., Ohara, T., Lee, M.H., Tsai, J., Lai, W.W., Karagueuzian, H.S., Wolf, P.L., Fishbein, M.C., and Chen, P.S. (2000). Nerve sprouting and sudden cardiac death. Circ Res *86*, 816-821. 10.1161/01.res.86.7.816.
29. Cao, J.-M., Fishbein, M.C., Han, J.B., Lai, W.W., Lai, A.C., Wu, T.-J., Czer, L., Wolf, P.L., Denton, T.A., Shintaku, I.P., et al. (2000). Relationship Between Regional Cardiac Hyperinnervation and Ventricular Arrhythmia. Circulation *101*, 1960-1969. doi:10.1161/01.CIR.101.16.1960.
30. Li, W., Knowlton, D., Van Winkle, D.M., and Habecker, B.A. (2004). Infarction alters both the distribution and noradrenergic properties of cardiac sympathetic neurons. Am J Physiol Heart Circ Physiol *286*, H2229-2236. 10.1152/ajpheart.00768.2003.
31. Yokoyama, T., Lee, J.K., Miwa, K., Opthof, T., Tomoyama, S., Nakanishi, H., Yoshida, A., Yasui, H., Iida, T., Miyagawa, S., et al. (2017). Quantification of sympathetic hyperinnervation and denervation after myocardial infarction by three-dimensional assessment of the cardiac sympathetic network in cleared transparent murine hearts. PLoS One *12*, e0182072. 10.1371/journal.pone.0182072.
32. Kumar, A., and Brockes, J.P. (2012). Nerve dependence in tissue, organ, and appendage regeneration. Trends Neurosci *35*, 691-699. 10.1016/j.tins.2012.08.003.
33. Mahmoud, A.I., O'Meara, C.C., Gemberling, M., Zhao, L., Bryant, D.M., Zheng, R., Gannon, J.B., Cai, L., Choi, W.Y., Egnaczyk, G.F., et al. (2015). Nerves Regulate Cardiomyocyte Proliferation and Heart Regeneration. Dev Cell *34*, 387-399. 10.1016/j.devcel.2015.06.017.
34. Porrello, E.R., Mahmoud, A.I., Simpson, E., Hill, J.A., Richardson, J.A., Olson, E.N., and Sadek, H.A. (2011). Transient regenerative potential of the neonatal mouse heart. Science *331*, 1078-1080. 10.1126/science.1200708.
35. Liu, D.S., and Xu, T.L. (2019). Cell-Type Identification in the Autonomic Nervous System. Neurosci Bull *35*, 145-155. 10.1007/s12264-018-0284-9.
36. Su, T., Stanley, G., Sinha, R., D'Amato, G., Das, S., Rhee, S., Chang, A.H., Poduri, A., Raftrey, B., Dinh, T.T., et al. (2018). Single-cell analysis of early progenitor cells that build coronary arteries. Nature *559*, 356-362. 10.1038/s41586-018-0288-7.
37. White, I.A., Gordon, J., Balkan, W., and Hare, J.M. (2015). Sympathetic Reinnervation Is Required for Mammalian Cardiac Regeneration. Circ Res *117*, 990-994. 10.1161/CIRCRESAHA.115.307465.
38. Huebner, E.A., and Strittmatter, S.M. (2009). Axon regeneration in the peripheral and central nervous systems. Results Probl Cell Differ *48*, 339-351. 10.1007/400_2009_19.
39. Cao, J.M., Fishbein, M.C., Han, J.B., Lai, W.W., Lai, A.C., Wu, T.J., Czer, L., Wolf, P.L., Denton, T.A., Shintaku, I.P., et al. (2000). Relationship between regional cardiac hyperinnervation and ventricular arrhythmia. Circulation *101*, 1960-1969. 10.1161/01.cir.101.16.1960.

40. Beaumont, E., Southerland, E.M., Hardwick, J.C., Wright, G.L., Ryan, S., Li, Y., KenKnight, B.H., Armour, J.A., and Ardell, J.L. (2015). Vagus nerve stimulation mitigates intrinsic cardiac neuronal and adverse myocyte remodeling postmyocardial infarction. Am J Physiol Heart Circ Physiol *309*, H1198-1206. 10.1152/ajpheart.00393.2015.
41. Vaseghi, M., Salavatian, S., Rajendran, P.S., Yagishita, D., Woodward, W.R., Hamon, D., Yamakawa, K., Irie, T., Habecker, B.A., and Shivkumar, K. (2017). Parasympathetic dysfunction and antiarrhythmic effect of vagal nerve stimulation following myocardial infarction. JCI Insight *2*. 10.1172/jci.insight.86715.
42. Ripplinger, C.M., Noujaim, S.F., and Linz, D. (2016). The nervous heart. Prog Biophys Mol Biol *120*, 199-209. 10.1016/j.pbiomolbio.2015.12.015.
43. Fallavollita, J.A., Heavey, B.M., Luisi, A.J., Jr., Michalek, S.M., Baldwa, S., Mashtare, T.L., Jr., Hutson, A.D., Dekemp, R.A., Haka, M.S., Sajjad, M., et al. (2014). Regional myocardial sympathetic denervation predicts the risk of sudden cardiac arrest in ischemic cardiomyopathy. J Am Coll Cardiol *63*, 141-149. 10.1016/j.jacc.2013.07.096.
44. Das, S., Goldstone, A.B., Wang, H., Farry, J., D'Amato, G., Paulsen, M.J., Eskandari, A., Hironaka, C.E., Phansalkar, R., Sharma, B., et al. (2019). A Unique Collateral Artery Development Program Promotes Neonatal Heart Regeneration. Cell *176*, 1128-1142 e1118. 10.1016/j.cell.2018.12.023.
45. Ivins, S., Chappell, J., Vernay, B., Suntharalingham, J., Martineau, A., Mohun, T.J., and Scambler, P.J. (2015). The CXCL12/CXCR4 Axis Plays a Critical Role in Coronary Artery Development. Dev Cell *33*, 455-468. 10.1016/j.devcel.2015.03.026.
46. Chang, A.H., Raftrey, B.C., D'Amato, G., Surya, V.N., Poduri, A., Chen, H.I., Goldstone, A.B., Woo, J., Fuller, G.G., and Dunn, A.R. (2017). DACH1 stimulates shear stress-guided endothelial cell migration and coronary artery growth through the CXCL12–CXCR4 signaling axis. Genes & development *31*, 1308-1324.
47. Cavallero, S., Shen, H., Yi, C., Lien, C.-L., Kumar, S.R., and Sucov, H.M. (2015). CXCL12 signaling is essential for maturation of the ventricular coronary endothelial plexus and establishment of functional coronary circulation. Developmental cell *33*, 469-477.
48. Vaseghi, M., Gima, J., Kanaan, C., Ajijola, O.A., Marmureanu, A., Mahajan, A., and Shivkumar, K. (2014). Cardiac sympathetic denervation in patients with refractory ventricular arrhythmias or electrical storm: intermediate and long-term follow-up. Heart Rhythm *11*, 360-366. 10.1016/j.hrthm.2013.11.028.
49. Sharma, K., Premchand, R.K., Mittal, S., Monteiro, R., Libbus, I., DiCarlo, L.A., Ardell, J.L., Amurthur, B., KenKnight, B.H., and Anand, I.S. (2021). Long-term Follow-Up of Patients with Heart Failure and Reduced Ejection Fraction Receiving Autonomic Regulation Therapy in the ANTHEM-HF Pilot Study. Int J Cardiol *323*, 175-178. 10.1016/j.ijcard.2020.09.072.
50. Bourke, T., Vaseghi, M., Michowitz, Y., Sankhla, V., Shah, M., Swapna, N., Boyle, N.G., Mahajan, A., Narasimhan, C., Lokhandwala, Y., and Shivkumar, K. (2010). Neuraxial modulation for refractory ventricular arrhythmias: value of thoracic epidural anesthesia and surgical left cardiac sympathetic denervation. Circulation *121*, 2255-2262. 10.1161/circulationaha.109.929703.
51. Hadaya, J., and Ardell, J.L. (2020). Autonomic Modulation for Cardiovascular Disease. Front Physiol *11*, 617459. 10.3389/fphys.2020.617459.

52. Brandt, E.B., Bashar, S.J., and Mahmoud, A.I. (2019). Stimulating ideas for heart regeneration: the future of nerve-directed heart therapy. Bioelectron Med *5*, 8. 10.1186/s42234-019-0024-0.
53. Bravo, P.E., Lautamaki, R., Carter, D., Holt, D.P., Nekolla, S.G., Dannals, R.F., Russell, S.D., and Bengel, F.M. (2015). Mechanistic Insights into Sympathetic Neuronal Regeneration: Multitracer Molecular Imaging of Catecholamine Handling After Cardiac Transplantation. Circ Cardiovasc Imaging *8*, e003507. 10.1161/CIRCIMAGING.115.003507.
54. Awad, M., Czer, L.S., Hou, M., Golshani, S.S., Goltche, M., De Robertis, M., Kittleson, M., Patel, J., Azarbal, B., Kransdorf, E., et al. (2016). Early Denervation and Later Reinnervation of the Heart Following Cardiac Transplantation: A Review. J Am Heart Assoc *5*. 10.1161/JAHA.116.004070.
55. Schwaiblmair, M., von Scheidt, W., Uberfuhr, P., Ziegler, S., Schwaiger, M., Reichart, B., and Vogelmeier, C. (1999). Functional significance of cardiac reinnervation in heart transplant recipients. J Heart Lung Transplant *18*, 838-845. 10.1016/s1053-2498(99)00048-0.
56. Chapleau, M.W., and Sabharwal, R. (2011). Methods of assessing vagus nerve activity and reflexes. Heart Fail Rev *16*, 109-127. 10.1007/s10741-010-9174-6.
57. Miquerol, L., Thireau, J., Bideaux, P., Sturny, R., Richard, S., and Kelly, R.G. (2015). Endothelial plasticity drives arterial remodeling within the endocardium after myocardial infarction. Circ Res *116*, 1765-1771. 10.1161/CIRCRESAHA.116.306476.
58. Mahmoud, A.I., Porrello, E.R., Kimura, W., Olson, E.N., and Sadek, H.A. (2014). Surgical models for cardiac regeneration in neonatal mice. Nat Protoc *9*, 305-311. 10.1038/nprot.2014.021.
59. Salamon, R.J., Zhang, Z., and Mahmoud, A.I. (2020). Capturing the Cardiac Injury Response of Targeted Cell Populations via Cleared Heart Three-Dimensional Imaging. JoVE, e60482. doi:10.3791/60482.
60. Mao, S., Xiong, G., Johnson, B.N., Cohen, N.A., and Cohen, A.S. (2021). Blocking Cross-Species Secondary Binding When Performing Double Immunostaining With Mouse and Rat Primary Antibodies. Front Neurosci *15*, 579859. 10.3389/fnins.2021.579859.

CHAPTER IV: LRRC10 REGULATES MAMMALIAN CARDIOMYOCYTE CELL CYCLE EXIT AND HEART REGENERATION

Rebecca J. Salamon[1], Megan C. McKeon[2], Jiyoung Bae[5], Xiaoya Zhang[1], Wyatt G. Paltzer[1], Kayla N. Wanless[1], Alyssa R. Schuett[1], Dakota J. Nuttall[1], Stephen A. Nemr[1], Rupa Sridharan[1], Youngsook Lee[1], Timothy J. Kamp[1,3,4], Ahmed I. Mahmoud[1*]

[1]Department of Cell and Regenerative Biology, [2]Department of Biomolecular Chemistry, [3]Department of Medicine, [4]Stem Cell and Regenerative Medicine Center, University of Wisconsin-Madison School of Medicine and Public Health, Madison, WI 53705, United States.

[5]Department of Nutritional Sciences, Oklahoma State University, Stillwater, OK 74078, United States.

*Corresponding author: Ahmed I. Mahmoud, Ph.D. Email: aimahmoud@wisc.edu

Salamon RJ, McKeon MC, Bae J, Zhang X, Paltzer WG, Wanless KN, Schuett AR, Nuttall DJ, Nemr SA, Sridharan R, Lee Y, Kamp TJ, Mahmoud AI. LRRC10 regulates mammalian cardiomyocyte cell cycle during heart regeneration. NPJ Regen Med. 2023 Jul 28;8(1):39. doi: 10.1038/s41536-023-00316-0. PMID: 37507410; PMCID: PMC10382521.

AUTHOR CONTRIBUTIONS

R.J.S., J.B. performed the experiments and performed data analysis. R.J.S., M.C.M., X.Z., R.S. contributed to RNA-seq analysis. R.J.S., J.B., W.G.P., K.N.W., A.R.S., D.J.N., S.A.N. performed data acquisition and analysis. Y.L., T.J.K., A.I.M. conceived the project, designed the experiments, and contributed to data analysis. R.J.S., A.I.M. wrote the manuscript.

ABSTRACT

Leucine-rich repeat containing 10 (LRRC10) is a cardiomyocyte-specific protein, but its role in cardiac biology is little understood. Recently Lrrc10 was identified as required for endogenous cardiac regeneration in zebrafish; however, whether LRRC10 plays a role in mammalian heart regeneration remains unclear. In this study, we demonstrate that LRRC10 specifically regulates cardiomyocyte cytokinesis, which is the final stage of cardiomyocyte cell division, during neonatal mouse heart regeneration. *Lrrc10*$^{-/-}$ knockout mice exhibit a loss of the neonatal mouse regenerative response marked by reduced cardiomyocyte cytokinesis and increased cardiomyocyte nucleation. Interestingly, LRRC10 deletion disrupts the regenerative transcriptional landscape of the regenerating neonatal mouse heart. Remarkably, cardiac overexpression of LRRC10 restores cardiomyocyte cytokinesis and the cardiac regenerative capacity of *Lrrc10*$^{-/-}$ mice. Our results reveal a novel role for LRRC10 in regulating postnatal cardiomyocyte cytokinesis as well as the transcriptional landscape during mammalian heart regeneration.

INTRODUCTION

The adult human heart shows little regenerative capacity following an ischemic injury, such as a myocardial infarction (MI), in which contractile cardiac muscle is replaced with a fibrotic scar[1]. In contrast, some species of fish and amphibians exhibit the capability of adult heart regeneration in response to injury[2-4]. In addition, neonatal mice and neonatal pigs exhibit a transient potential to undergo heart regeneration after an induced MI[5-7]. New understanding of the mechanisms underlying cardiac regeneration provides opportunities for innovative cardiac regenerative therapies following MI to prevent the progression to heart failure and increased risk of early death[8].

A recent example of the delicate balance between cardiac regeneration and scar formation following myocardial injury is a study comparing cardiac regeneration in the Pachón cave-dwelling and surface populations of the teleost fish, *Astyanax mexicanus*[9]. Remarkably, this species of fish diverged into cave-dwelling and surface populations 1.5 million years ago and evolved different responses to cardiac injury. The surface fish show robust cardiac regeneration, but little regeneration occurs in the Pachón cave-dwelling fish. Comparison of gene expression profiles following injury revealed that Lrrc10 is more highly expressed in regenerating surface fish. LRRC10 is a cardiomyocyte-specific member of the leucine-rich repeat (LRR) motif family of proteins that mediate protein-protein interactions[10]. Furthermore, *lrrc10* deletion in zebrafish results in loss of cardiac regeneration capacity. In both the Pachón and *lrrc10* knockout zebrafish, there is no difference in the burst in DNA synthesis following injury compared to wild type controls, but regeneration does not occur, suggesting some impairment of proliferation or cell

survival. These results suggest that LRRC10 is essential for cardiac regeneration in fish models; however, the mechanisms remain unclear. In addition, whether LRRC10 is necessary for cardiac regeneration in a mammalian model remains to be understood.

LRRC10 knockout (*Lrrc10*$^{-/-}$) mice exhibit mild systolic dysfunction, first detected at embryonic day (E)17.5 without changes in cardiac structure or evidence of fibrosis, and postnatally, the *Lrrc10*$^{-/-}$ mice gradually develop a dilated cardiomyopathy but exhibit normal survival[11]. Interestingly, LRRC10 has been recently demonstrated to regulate $Ca_V1.2$ channel function and contribute to homeostasis of intracellular Ca^{2+} cycling[12]. In this study, we demonstrate that *Lrrc10* deletion blocks neonatal heart regeneration. Remarkably, *Lrrc10* deletion did not disrupt nuclear division (karyokinesis) during the early stages of M-phase of cardiomyocyte cell cycle, but specifically reduces cardiomyocyte cytoplasmic division (cytokinesis), which results in increased cardiomyocyte nucleation. Transcriptional analysis revealed a unique signature following *Lrrc10* deletion compared to the regenerating control hearts. Importantly, LRRC10 overexpression during neonatal MI rescued the cardiac regenerative capacity of *Lrrc10*$^{-/-}$ mice, demonstrating an important role for LRRC10 in regulating cardiomyocyte cytokinesis and cardiac regeneration. Our results reveal a novel role for LRRC10 in postnatal cardiomyocyte cell cycle exit and mammalian cardiac regenerative potential.

RESULTS

***Lrrc10* knockout inhibits neonatal mouse heart regeneration**

The role of LRRC10 in mammalian heart regeneration has not been explored. *Lrrc10*$^{-/-}$ mice postnatally develop a slowly progressive dilated cardiomyopathy[11], an indication that LRRC10 is critical for cardiac homeostasis. To determine whether LRRC10 plays a role in mammalian heart regeneration, we evaluated the regenerative capacity of the *Lrrc10*$^{-/-}$ mouse heart following an MI in postnatal-day 1 (P1) mice[13]. We utilized the whole-body *Lrrc10* knockout mouse model, *Lrrc10*$^{-/-}$, as LRRC10 is a cardiomyocyte-specific protein[14-16]. To determine the effect of *Lrrc10* deletion on myocardial regeneration, we performed Masson's trichrome staining at 21 days post-MI in wild type (WT) control and *Lrrc10*$^{-/-}$ mice. Remarkably, *Lrrc10*$^{-/-}$ mice showed increased scar size and incomplete myocardial regeneration in comparison to control hearts (**Fig. 1A, Supplementary Fig. 1**). Since LRRC10 is a cardiomyocyte-specific protein, this increase in fibrosis is likely due to disruption of the cardiac regenerative response at the cardiomyocyte level rather than an impact on fibroblasts. In addition, we quantified a significant increase in heart weight to body weight ratio in *Lrrc10*$^{-/-}$ mice post-MI (**Fig. 1B**). At 21-days post-sham surgery, no difference in heart weight: body weight was identified between WT and *Lrrc10*$^{-/-}$ mice (**Fig. 1A-B, Supplementary Fig. 1**), indicating there has been no significant remodeling in *Lrrc10*$^{-/-}$ hearts by this developmental timepoint. These results demonstrate an evolutionarily conserved role for LRRC10 in regulating cardiac regeneration.

Heart regeneration is mediated by the proliferation of the pre-existing cardiomyocytes[5]. Here, we analyze two stages of M-phase during cardiomyocyte cell cycle. We use phospho-Histone3

(pH3) as a marker for early G2-M phase to measure karyokinesis. In addition, we use Aurora B as a marker of cytokinesis, which is symmetrically localized at the cleavage furrow to measure cytoplasmic division. During mammalian heart regeneration, cardiomyocyte proliferation peaks around 7 days post-MI[5,17]. To establish the impact of Lrrc10 deletion on cardiomyocyte proliferation and division, we performed immunostaining for the early M-phase marker pH3 and the cardiomyocyte marker cardiac troponin T (cTnT) at 7 days following MI at P1. We found no significant difference in levels of pH3 positive cardiomyocytes between WT control and *Lrrc10*$^{-/-}$ mice (**Fig. 1C, Supplementary Fig. 2A-B**). Our results are similar to the prior cavefish and zebrafish study, which showed comparable levels of induced DNA synthesis in both controls and *lrrc10*$^{-/-}$ zebrafish at the same timepoint [9]. However, mammalian cardiomyocytes are prone to multinucleation and increased ploidy following DNA synthesis, a phenomenon that contributes to the loss of regenerative capacity in mice[18]. Localization of the cytokinesis marker Aurora B can distinguish between events of complete cytokinesis and binucleation in cardiomyocytes. Symmetrical localization of Aurora B between two nuclei is indicative of cytokinesis, whereas asymmetrical localization of Aurora B can indicate binucleation[19,20]. To determine whether LRRC10 regulates later stages of cardiomyocyte cell cycle, we measured levels of the symmetric and asymmetric Aurora B localization in cardiomyocytes at 7 days post-MI. Interestingly, we detected a significant decrease in number of symmetrically localized Aurora B cardiomyocytes in *Lrrc10*$^{-/-}$ mice compared to control mice following MI (**Fig. 1D, Supplementary Fig. 2C-D**). There was no significant difference in the number of cardiomyocytes with asymmetric Aurora B localization between WT and *Lrrc10*$^{-/-}$ mice (**Supplementary Fig. 2E**). At 7 days-post sham surgery, WT and *Lrrc10*$^{-/-}$ mice had comparable levels of cardiomyocytes positive for pH3 (**Fig. 1C**), as well

as symmetrical and asymmetrical Aurora B localization (**Fig. 1D, Supplementary Fig. 2E**). These results suggest that LRRC10 specifically regulates cardiomyocyte cytokinesis during cardiomyocyte proliferation and heart regeneration.

To further establish the impact of *Lrrc10* deletion on cardiomyocyte nucleation, we isolated cardiomyocytes from control and *Lrrc10*$^{-/-}$ mice at 14-days post-injury and quantified nucleation with the DNA dye Hoechst. We measured a significant decrease in mononucleated cardiomyocytes, as well as a significant increase in binucleated and multinucleated cardiomyocytes in *Lrrc10*$^{-/-}$ mice post-MI compared to control mice (**Fig. 1E**). No significant difference in nucleation levels were identified between sham control and *Lrrc10*$^{-/-}$ mice (**Supplementary Fig. 2F**). Furthermore, we quantified a significant increase in cardiomyocyte size in *Lrrc10*$^{-/-}$ mice compared to controls post-MI by Wheat Germ Agglutinin (WGA) staining, without significant changes in cardiomyocyte area post-sham surgery (**Fig. 1F**).

Collectively, our results demonstrate that *Lrrc10* deletion specifically impedes cardiomyocyte cytokinesis but not karyokinesis following injury, which results in increased cardiomyocyte nucleation and blockade of the neonatal cardiac regenerative response. Thus, LRRC10 plays a conserved role in heart regeneration across permissive species in controlling the late stages of cardiomyocyte proliferation prior to completion of cell division.

***Lrrc10* deletion results in a unique transcriptional signature following injury**

Our results demonstrate that LRRC10 regulates cardiomyocyte cytokinesis and mammalian heart regeneration post-MI. The endogenous heart regenerative response of the neonatal mouse heart is regulated by a unique transcriptional landscape[21-23]. To identify how LRRC10 mediates cardiomyocyte cytokinesis and cardiac regeneration at the transcriptional level, we analyzed the global transcriptome in control and *Lrrc10*$^{-/-}$ hearts. We performed bulk RNA sequencing on the ventricles from WT control and *Lrrc10*$^{-/-}$ mice that underwent a sham or MI surgery at P1 (**Fig. 1G-I**). Hearts were collected at 7 days post-injury from equal numbers of male and female mice. Analysis of the transcriptomic landscape by Principal Component Analysis (PCA) and Pearson correlation demonstrates distinct clustering between control and *Lrrc10*$^{-/-}$ sham and MI groups (**Supplementary Fig. 3A-B**), indicative of a unique transcriptional signature in *Lrrc10*$^{-/-}$ mice following injury.

To further dissect the transcriptional signature related to the regenerative defects following *Lrrc10* deletion, we defined the differentially expressed genes (DEGs) and performed K-means clustering and Gene Ontology (GO) analysis of the DEGs. We identified 8 total clusters with distinct transcriptomic patterns (**Fig. 1G**). Most interestingly, Cluster 1 shows a transcriptomic signature only upregulated in the *Lrrc10*$^{-/-}$ mice post-MI (**Fig. 1G, Cluster 1**). The clustered genes encode for myofilament proteins, such as myosins (*Myh1, Myh3, Myh8*), troponins (*Tnnt3, Tnnc2, Tnni2*), and actin (*Actn3*) proteins (**Fig. 1H**). Furthermore, GO analysis identified cell processes related to regulation of muscle contraction and development (**Fig. 1G-I**). This increased

expression of myofilament proteins maybe a compensatory effect, as recent evidence demonstrates that LRRC10 modulates $Ca_v1.2$ calcium channels and cardiomyocyte contraction[12], while LRRC10 deletion results in development of dilated cardiomyopathy later in life[11].

Cluster 3 shows a distinct transcriptome in both sham and MI *Lrrc10*$^{-/-}$ mice compared to controls, which includes genes encoding for major ion channels, such as a voltage-gated T-type Ca^{2+} channel (*Cacna1g*), sodium channels (*Scna10a, Scn3b*), and a potassium channel (*Kcnaj5*) (**Fig. 1G-H, Cluster 3**). GO analysis related these channel-encoding genes to regulation of cardiac contraction, membrane potential, and depolarization (**Fig. 1H**). Changes in ion channel expression can be linked to a variety of cardiac pathologies. For example, mutations in sodium channels can lead to ventricular arrythmias in humans, and expression of T-type Ca^{2+} channel genes are associated with cardiac hypertrophy[24,25].

The transcriptome in Cluster 4 reveals a specific gene expression in *Lrrc10*$^{-/-}$ samples post-MI compared to controls (**Fig. 1G, Cluster 4**), suggesting this cluster contained a distinct transcriptomic profile linked to the injury response of *Lrrc10*$^{-/-}$ hearts. Further analysis identified genes associated with cell cycle such as *Cdc20, Ccnb1*, and the related GO pathways involved in cell cycle regulation (**Fig. 1H-I**). Interestingly, one of the downregulated genes in the cluster, *Aurkb*, encodes for the cytokinesis regulator Aurora B kinase, supporting our earlier evidence that *Lrrc10*$^{-/-}$ inhibits the completion of cardiomyocyte division (**Fig. 1D**).

Lastly, we investigated the transcriptome in Cluster 7, as the overall gene expression was downregulated in *Lrrc10*$^{-/-}$ sham and MI mice compared to controls. Genes and related GO terms highlight an association to cell metabolism, such as fatty acid oxidation and mitochondrial metabolism (*Sdhaf1, Ndufs5, Slc25a33*) (**Fig. 1G-H, Cluster 7**). The cardiac metabolic state plays an important role in mediating endogenous heart regeneration, where altering the balance between glucose and fatty acid oxidation metabolism can promote or inhibit regeneration, respectively[26]. This transcriptional signature demonstrates that *Lrrc10* deletion may drive metabolic dysregulation and result in the impaired regenerative response to injury.

Our analysis highlights novel roles for LRRC10 in transcriptional regulation of key cell processes related to muscle contraction, ion-channel function, cell cycle activity, and metabolism. Together, this demonstrates that *Lrrc10*$^{-/-}$ mice have a unique transcriptional signature underpinning the loss of the cardiac regenerative capacity.

LRRC10 overexpression restores the cardiac regenerative capacity in *Lrrc10*$^{-/-}$ mice

Our results demonstrate that loss of LRRC10 blocks neonatal heart regeneration. However, whether lack of LRRC10 is primarily responsible for the defect in neonatal heart regeneration rather than secondary effects on the heart remains unclear. Thus, we wanted to determine whether restoration of LRRC10 protein levels can rescue the blockade of the cardiac regenerative response in post-natal *Lrrc10*$^{-/-}$ hearts. (**Fig. 2A**). To address this question, we injected WT and *Lrrc10*$^{-/-}$ mice at P0 with a single dose of AAV9-cTnT-GFP control vector or AAV9-cTnT-LRRC10 rescue vector, for cardiac-specific overexpression of LRRC10, followed by an MI surgery at P1 (**Fig.**

2A). This dosing strategy was sufficient to target the heart, as evident by GFP expression throughout the heart by 7 days post-injection (**Fig. 2B, Supplementary Fig. 4**). We first investigated if the overexpression of LRRC10 in *Lrrc10*$^{-/-}$ hearts was sufficient to rescue the defect of symmetrical Aurora B localization in cardiomyocytes. Interestingly, at 7 days post-MI we measured a significant increase in cytokinesis in *Lrrc10*$^{-/-}$ mice treated with AAV9-cTnT-LRRC10 rescue vector compared to the AAV9-cTnT-GFP control vector (**Fig. 2C**). There was no significant difference in asymmetrical Aurora B localization between the same groups (**Supplementary Fig. 5)**, in line with our earlier results demonstrating comparable levels of asymmetrical Aurora B between WT and *Lrrc10*$^{-/-}$ hearts post-MI (**Fig. 1D**).

We further investigated the effect of LRRC10 overexpression on cardiomyocyte cytokinesis by quantifying cardiomyocyte nucleation as a readout of cardiomyocyte division across control and rescue groups. At 14 days post-MI, LRRC10 rescue hearts restored the increase in mononucleated cardiomyocytes compared to the LRRC10 KO controls (**Fig. 2D**). Furthermore, the number of binucleated and multinucleated cardiomyocytes in LRRC10 rescue hearts were restored to the levels of WT control hearts, whereas LRRC10 KO controls show a significant elevation in binucleated cardiomyocytes (**Fig. 2D**). This demonstrates that overexpression of LRRC10 in *Lrrc10*$^{-/-}$ mice restores the increase in mononucleated cardiomyocytes post-MI.

To determine whether LRRC10 overexpression restores myocardial regeneration and scar size reduction in *Lrrc10*$^{-/-}$ mice, we performed trichrome staining at 28 days post-MI. LRRC10 KO control mice show incomplete regeneration, persistent scar tissue, and thinning of the left

ventricle, as expected (**Fig. 2E, Supplementary Fig. 6)**. Strikingly, the LRRC10 rescue mice show structural regeneration, with little to no scarring present and increased wall thickness in the left ventricle similar to WT controls. In addition, LRRC10 rescue mice also demonstrate a reduction of heart weight to body weight ratio, restoring heart size to similar levels as WT controls (**Fig. 2F**). To identify if this repair translated to improved cardiac function, we used echocardiography to measure ejection fraction (EF) and fractional shortening. Hearts of LRRC10 rescue mice showed trending improvements in EF and FS compared to LRRC10 KO control hearts (**Fig. 2G**). The restoration of myocardial structure and scar resolution demonstrate that LRRC10 overexpression can promote heart regeneration in *Lrrc10*$^{-/-}$ hearts (**Fig. 2E-G**). Together, these results demonstrate that the inhibition of regeneration in *Lrrc10*$^{-/-}$ mice is driven by reduced levels of LRRC10 and that LRRC10 overexpression postnatally is sufficient to restore myocardial regeneration following neonatal MI.

DISCUSSION

Heart failure with reduced ejection fraction following myocardial infarction remains a major health and economic burden given the inability of the adult mammalian heart to regenerate following injury. Defining the mechanisms that control endogenous heart regeneration can identify new therapeutic approaches to promote adult human heart regeneration. Our results demonstrate an evolutionarily conserved role for LRRC10 in heart regeneration, from the *Astyanax mexicanus* surface fish and zebrafish to the neonatal mouse. More importantly, we demonstrate that LRRC10 regulates later stages of cardiomyocyte cell cycle activity that impacts cardiomyocyte division and nucleation during neonatal mouse heart regeneration. Loss of

LRRC10 results in transcriptional dysregulation of muscle, ion channel, cell cycle, and metabolic genes, which may play a role in impeding heart regeneration. Remarkably, restoration of LRRC10 levels in *Lrrc10*$^{-/-}$ hearts is sufficient to rescue the endogenous regenerative response. Our results reveal a novel role for LRRC10 in regulating cardiomyocyte cytokinesis but not karyokinesis, demonstrating a stage-specific regulation of cardiomyocyte cell cycle.

Owing to the identified role of LRRC10 in regulating L-type Ca^{2+} channels in adult cardiomyocyte, future studies are warranted to further define the impact of calcium handling on cardiomyocyte proliferation and heart regeneration. Furthermore, the impact of LRRC10 deletion on cardiac metabolism needs to be further investigated, which might reveal a novel link between calcium homeostasis and cardiomyocyte cell cycle. In addition, whether overexpression of LRRC10 in the adult heart can promote adult cardiomyocyte cell cycle re-entry and regeneration remains to be determined. This study provides an important new target to modulate cardiomyocyte cell cycle activity and heart regeneration.

METHODS

Animal Models

Wild type C57BL/6J (Stock #000664) mice were obtained from Jackson Laboratories. *Lrrc10*$^{-/-}$ mice were generated in C57BL/6 background and genotyped as described previously[11,27]. All animal experimental procedures were approved by the Institutional Animal Care and Use Committee of the University of Wisconsin-Madison. All experiments were performed on age and sex matched mice, and RNA-seq analysis was performed with an equal ratio of male to female mice.

Neonatal Myocardial Infarction Surgery

Neonatal mice underwent myocardial infarction (MI) surgery at postnatal day 1, as previously described [28]. Briefly, neonates were anesthetized by hypothermia on ice. A blunt dissection was performed in the fourth intercostal space. The heart was gently guided to rest on the chest cavity and the LAD was located. Using a C-1 tapered needle with a 6-0 Prolene suture (Ethicon Inc., Bridgewater, NJ), the LAD was ligated and blanching at the apex was visualized. The heart was guided back into the chest, the ribs were sutured closed, and skin was joined using adhesive glue (3M). The mice recovered on a warmed heating pad until mobile. The sham operation consisted of hypothermic anesthesia, blunt dissection in the fourth intercostal space, and closing of the chest cavity, without heart exposure or LAD ligation.

Histology

For paraffin embedding, hearts were fixed in 4% paraformaldehyde (PFA) in PBS at 4°C overnight. Samples were embedded in a paraffin block and sectioned below the ligation at 5um thickness. Masson's trichrome stain was run according to the manufacturer's protocol (Newcomer Supply, Middleton, WI). Scar area quantified in ImageJ and averaged across 3 sections per heart.

For cryosections, hearts were fixed in 4% PFA in PBS at RT for 1hr. Tissues were soaked in 30% sucrose overnight before being submerged into cryomold with OTC and frozen at -80°C. Hearts were sectioned at 8um thickness.

Immunostaining on Cardiac Sections

Paraffin sections underwent deparaffinization and rehydration by sequential 3min incubations in xylene and ethanol (100%, 90%, 70%) solutions. Samples were placed into IHC antigen retrieval solution (Invitrogen, Carlsbad, CA) and microwaved for 10 min. Sections were blocked in 10%

blocking serum (matching secondary) and incubated in primary antibodies overnight incubation at 4°C. Primary antibodies were used against phospho-Histone3 Ser10 (Millipore, catalog # 06-570) at [1:200] dilution, Aurora B (Sigma, catalog # A5102) at [1:100] dilution, and Cardiac Troponin T (cTnt Abcam, catalog # AB8295) at [1:200] dilution. Sections were washed with PBS and incubated with secondary antibodies (Invitrogen) at [1:400] dilution with DAPI for 1 hour at room temperature. Slides were mounted in antifade mounting medium and stored at 4°C. Representative images were taken on a Nikon A1RS HD confocal microscope.

Cardiomyocyte cross-sectional area was measured by Wheat Germ Agglutinin (WGA) staining. Paraffin sections were processed as described above, incubating with WGA-488 conjugated antibody (Thermo Fisher, catalog # W11261) at [1:50] dilution and cTnT. Cardiomyocyte area was quantified by measuring cross-sectional area of cardiomyocytes dual-positive for WGA+ and cTnT in Image J, measuring approximately 200 cardiomyocytes across 4-6 replicate sections.

For GFP staining in AAV9-injected mice, cryosections were placed into a humidifying chamber and incubated with 10% blocking buffer, diluted in PBS with 0.2% Triton X-100 (PBST) at RT for 1 hr. Slides were incubated with primary GFP-488 conjugated antibody (Thermo Fisher, catalog #A21331) and cTnT diluted in PBST with 5% blocking buffer at 4°C overnight. Sections were washed, mounted, and stored at -20°C. Representative images were taken on a Nikon A1RS HD confocal microscope. For whole-mount staining, the whole heart was harvested, washed in PBS and immediately imaged for endogenous GFP expression. Representative images were acquired on a Nikon Upright FN1 confocal microscope.

AAV9 injection strategy

Adenovirus vector constructs, AAV9-cTnT-EGFP-WPRE (catalog # VB5428) and AAV9-cTnT-mLRRC10-WPRE were designed and produced by Vector Biolabs (Malvern, PA). Mice were injected subcutaneously at P0 with AAV9 constructs at a viral titer of $5x10^{13}$vg/kg BW (diluted in saline to a total volume of 10ul). MI was performed at P1, as described above, and hearts were collected at 7 days-post MI for cytokinesis analysis, 14 days post-MI for nucleation analysis, and 21 days post-MI for histological analysis.

Cardiomyocyte isolation and nucleation

Mice hearts were harvested at 14 days post-surgery and fixed in 4% PFA in PBS at RT for 2hrs. Hearts were washed for three, 15min incubations in PBS. Hearts were mined into 1mm pieces and transferred into Eppendorf tubes containing collagenase solution with collagenase D (2.4mg/ml, Cat #11088866001) and collagenase B (1.8mg/ml, Cat #: #110088807007) diluted in Hank's Balanced Salt Solution (Santa Cruz, #sc-391061A) and incubated on a rocker at 37°C overnight. Collagenase solution was replaced every two days by centrifugation at 500g for 1min at RT and removing supernatant. After cells were dissociated, cell pellets were collected by centrifugation at 500g for 2min at RT, resuspended in PBS, and passed through a 100µm cell filter to purify cardiomyocyte populations and remove clumps. Cells were stored at 4°C until ready for staining.

Nucleation staining and quantification was performed on isolated cardiomyocytes. Cells were mixed gently to resuspend and 200ul of cardiomyocytes were transferred to a 1.5ml Eppendorf tube with 300ul of PBST (PBS with 0.2% Triton X-100). DAPI was added to solution and incubated for 10min at RT. After, 1ml of 10% blocking buffer was added to reduce cell clumping. Cells were

collected by centrifugation at 800g for 2min and supernatant was discarded, leaving approximately 100ul of solution. For nucleation quantification, around 300-500 cardiomyocytes were aliquoted onto a coverslip and sealed with nail polish. Approximately 1000 intact cardiomyocytes were counted per heart, with 4-9 replicate hearts per sample group. Nucleation distribution was presented as percent nucleation of total cardiomyocytes per sample.

RNA sequencing and analysis

Sex-matched heart ventricles were collected at 7 days post-surgery (Sham or MI) and immediately homogenized in Trizol (Invitrogen) according to the manufacturer's protocol. Mouse tissue samples suspended in TRIzol were submitted to the University of Wisconsin Biotechnology Center (UWBC) Gene Expression Center (*Research Resource Identifier - RRID:SCR_017757)* for RNA extraction. Total RNA was purified following the recommendations of the Qiagen RNeasy Mini (Qiagen, Hilden, Germany) procedure, which included on-column DNase treatment. RNA quality and integrity (RINe > 8.4) were verified on a NanoDrop One Spectrophotometer (Thermo Fisher Scientific, Waltham, MA, USA) and Agilent 4200Tapestation (Santa Clara, CA, USA), respectively.

Total RNA was used as input material and libraries were prepared by following the SMARTer Stranded Total RNA Sample Prep Kit – HI Mammalian user manual (Takara Bio USA, Mountain View, CA, USA). In brief, 900ng total RNA were hybridized to RiboGone™ oligos for depletion of rRNA sequences by RNase H-mediated digestion followed by SPRI bead cleanup. Reduced rRNA templates were fragmented at 94 °C for 3 min prior to first-strand synthesis. Takara adaptors and indexes were added to single-stranded cDNA via 12 cycles of PCR. Quality and quantity of the finished libraries were assessed on the Agilent 4200 Tapestation (Agilent, Santa Clara, CA,

USA) and Qubit Fluorometer (Invitrogen, Carlsbad, CA, USA), respectively. Paired end 150bp sequencing was performed by Illumina Sequencing by UWBC DNA Sequencing Facility *(RRID:SCR_017759)* on an Illumina NovaSeq6000, with libraries multiplexed for an approximate 50 million reads per library. Sequencing was done using standard 300 cycle TruSeq v1.5 SBS kits and SCS 2.8 software. Images were analyzed using the standard Illumina Pipeline, version 1.8. Bioinformatic analysis of transcriptomic data adhere to recommended ENCODE guidelines and best practices for RNA-Seq (Encode Consortium, 2016). Alignment of adapter-trimmed[29] (Skewer v0.1.123) 2x150 (paired-end; PE) bp strand-specific Illumina reads to the *Mus musculus Mus musculus* GRCm39 mouse genome (assembly accession NCBI: GCA_000001635.9) was achieved with the Spliced Transcripts Alignment to a Reference (STAR v2.5.3a) software[30], a splice-junction aware aligner. Expression estimation was performed with RSEM[31] (RNASeq by Expectation Maximization, v1.3.0), generating overall RSEM gene counts. Counts were normalized by TPM. To test for differential gene expression among individual group contrasts, expected read counts obtained from RSEM were used as input into DESeq2 [32] (Version 1. 36.0). Statistical significance of Differentially Expressed genes (DEGs) was defined by a log2fold change of $\pm(0.5)$, with statistical significance of the negative-binomial regression test adjusted with a Benjamini-Hochberg FDR correction at the 10% level[33] and independent filtering requiring genes to have a minimum read count (10 reads) in each group. Heatmap was generated using pheatmap [V.1.0.12] from K-means clustering of all DEGs in the 4-way comparison, with cell value is TPM row-normalized. DOT plots for GO analysis were generated with enrichGO in Clusterprofiler using p-value <0.05. These raw and processed data sets have been deposited in NCBI's Gene Expression

Omnibus and are accessible through GEO accession number GSE221539. Groups for RNA-seq were sex matched and independently analyzed, with no sex-specific differences identified.

Statistical analysis

Graphs were generated using Prism 9 (GraphPad Software). Statistical analysis between two groups was run using a student's unpaired t-test. Multiple groups were compared using ordinary one-way ANOVA with Tukey post hoc test to determine significant comparisons. Statistical significance described as a $p < 0.05$. P-values shown as n.s. ($P > 0.05$), * ($P \leq 0.05$). **($P \leq 0.01$), ***($P \leq 0.001$), **** ($P \leq 0.0001$). Error bars presented as SEM.

DATA AVAILABILITY

RNA-seq data from WT and *Lrrc10*$^{-/-}$ mice are available at the NCBI's Gene Expression Omnibus (GSE221539). All data are available from the corresponding author upon request.

ACKNOWLEDGEMENTS

Funding for this project was provided by an AHA Predoctoral Fellowship 829586 (R.J.S.), NIH/NHLBI R56 HL155617 (A.I.M.), NIH/NHLBI R01 HL166256 (A.I.M.), DOD W81XWH2210094 (A.I.M.), NIH/NHLBI under Ruth L. Kirschstein NRSA T32 HL007936 to the UW Cardiovascular Research Center (W.G.P.), NIH/NIGMS Training Program in Genetics T32 GM713348 (D.J.N.), NIH U01HL134764 (T.J.K), NSF EEC-1648035 (TJK), University of Wisconsin Graduate School AAI8129 (Y.L.), X.Y.Z. was supported on 2R01GM113033 (R.S).

FIGURES

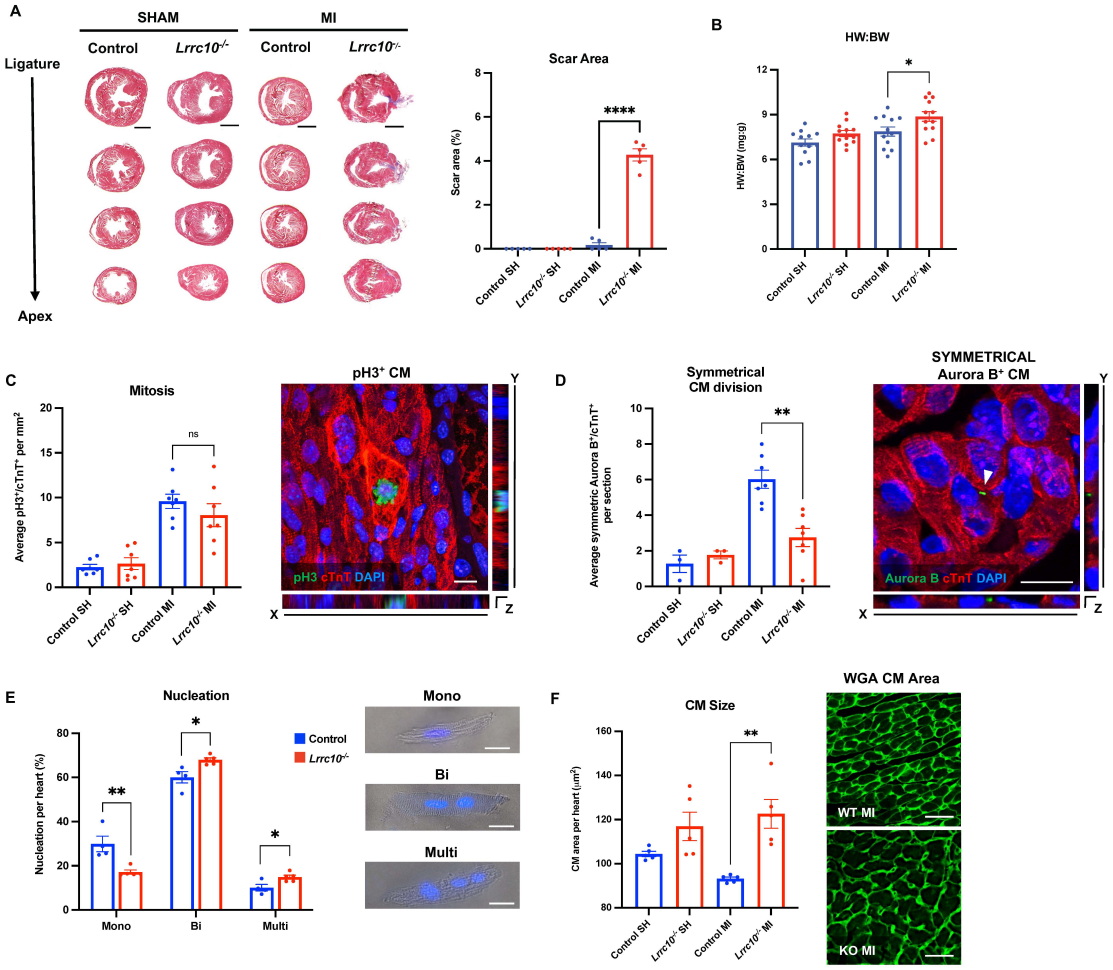
A
SHAM
MI
Control
Lrrc10-/-
Control
Lrrc10-/-
Ligature
Apex
Scar Area
Scar area (%)
****
Control SH
Lrrc10-/- SH
Control MI
Lrrc10-/- MI
B
HW:BW
HW:BW (mg/g)
*
C
Mitosis
Average pH3+/cTnT+ per mm2
ns
pH3+ CM
pH3 cTnT DAPI
D
Symmetrical CM division
Average symmetric Aurora B+/cTnT+ per section
**
SYMMETRICAL Aurora B+ CM
Aurora B cTnT DAPI
E
Nucleation
Nucleation per heart (%)
Control
Lrrc10-/-
Mono
Bi
Multi
F
CM Size
CM area per heart (um2)
WGA CM Area
WT MI
KO MI
G
Group
WT SH
KO SH
WT MI
KO MI
Cluster
Z-score
H
Cluster 1
Cluster Genes:
Myh8 Myh3 Ryr1 Tnni2 Tnnt3 Tnnc2 Actn3 Mybpc1 Kcnma1 Tpm3
GO Terms:
Muscle system process
Muscle contraction
Regulation of muscle contraction
Skeletal muscle tissue development
Cluster 3
Cluster Genes:
Avpr1a Kcnj5 Cacna1g Chrm3 Atp1b2 Scn10a Scna3a Scn3b Hey2 Gabra1
GO Terms:
Membrane potential
Heart contraction
Membrane depolarization during action potential
Musculoskeletal movement
Cluster 4
Cluster Genes:
Aurkb Aurka Cdc20 Ccnb1 E2f7 Cenpf Pbk Ska3 Mcm3 Plk4
GO Terms:
Nuclear division
Chromosome segregation
Positive regulation of cell cycle
Spindle organization
Cluster 7
Cluster Genes:
Sdhaf1 Ndufs5 Slc25a33 C1qtnf2 Ppara Pil6 Hand2 Rgr2 Pak1 Mrpl55
GO Terms:
Generation of precursor metabolites and energy
Regulation of fatty acid oxidation
Regulation of cardiac cell growth in development
I
Cluster 1
muscle system process
muscle contraction
regulation of muscle system process
regulation of muscle contraction
neuromuscular process
striated muscle contraction
skeletal muscle tissue development
skeletal muscle contraction
multicellular organismal movement
musculoskeletal movement
GeneRatio
Count
p.adjust
Cluster 4
nuclear division
organelle fission
chromosome segregation
mitotic nuclear division
nuclear chromosome segregation
positive regulation of cell cycle
sister chromatid segregation
positive regulation of cell cycle process
mitotic sister chromatid segregation
spindle organization
GeneRatio
Count
p.adjust

Figure 1. Cardiac regeneration is inhibited in the neonatal Lrrc10-/- mouse with disruption of the transcriptional landscape following injury. Control and *Lrrc10*$^{-/-}$ neonatal mice underwent a sham (SH) or myocardial infarction (MI) surgery at P1 and were analyzed at 7-, 14-, or 21 days post-surgery (DPS). (A) Mason's trichrome staining (viable tissue in red; scar tissue in blue) at 21DPS (n=5); scale=1mm. (B) Analysis of Heart Weight (HW) to Body Weight (BW) ratio (n=12). (C) Analysis of cardiomyocyte mitosis with pH3 and cTnT at 7DPS (n=7); scale=10uM. (D) Analysis of cytokinesis by symmetrical localization of Aurora B with cTnT at 7DPS (SH n=3; MI n=7); arrowhead indicates Aurora B localization between cardiomyocytes; scale=10uM. (E) Percentage of mononucleated (Mono), binucleated (Bi), and multinucleated (Multi) cardiomyocytes per heart at 14DPS (WT n=4; KO n=5); scale=20uM. (F) Quantification of cardiomyocyte size by Wheat Germ Agglutinin (WGA) at 21DPS (n=5); scale=25uM. Hearts were collected from WT and *Lrrc10*$^{-/-}$ mice at 7 days after sham or MI surgery, processed for bulk-tissue RNA-sequencing (n=4 per group), and the transcriptome of differentially expressed genes (DEGs) was identified. (G) Heatmap generated by k-means clustering of DEGs and divided into 8 clusters; colored scale is related to z-score. (H) Clusters 1, 3, 4, and 7 show a unique transcriptome in *Lrrc10*$^{-/-}$ hearts. (I) Gene Ontology (GO) analysis highlights LRRC10 dysregulated pathways related to muscle contraction (Cluster 1) and cell metabolism (Cluster 4).

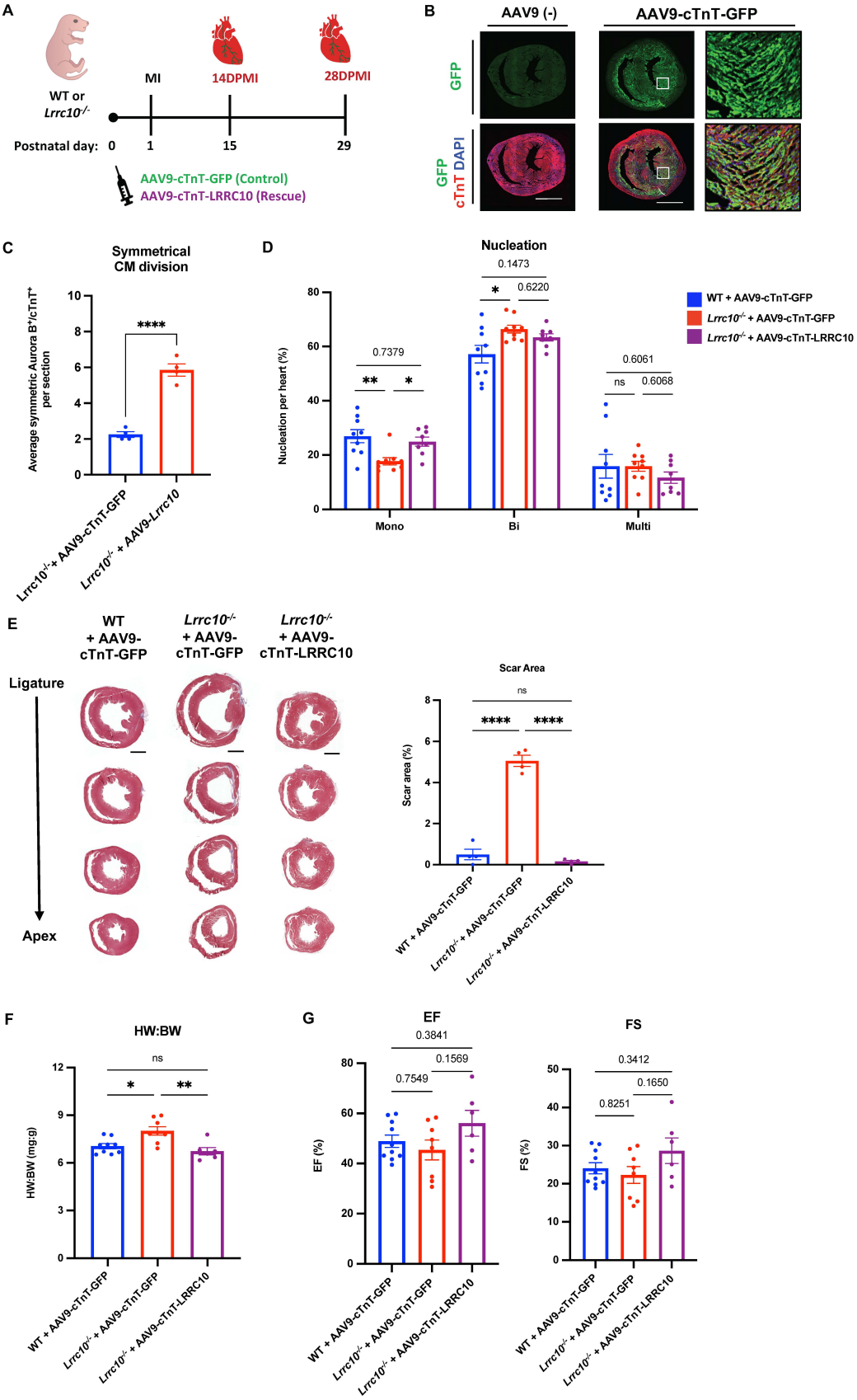
A
WT or Lrrc10-/-
MI
14DPMI
28DPMI
Postnatal day: 0 1 15 29
AAV9-cTnT-GFP (Control)
AAV9-cTnT-LRRC10 (Rescue)
B
AAV9 (-)
AAV9-cTnT-GFP
GFP
GFP cTnT DAPI
C
Symmetrical CM division
Average symmetric Aurora B+/cTnT+ per section
****
Lrrc10-/- + AAV9-cTnT-GFP
Lrrc10-/- + AAV9-Lrrc10
D
Nucleation
Nucleation per heart (%)
0.1473
0.6220
0.7379
0.6061
ns
0.6068
Mono
Bi
Multi
WT + AAV9-cTnT-GFP
Lrrc10-/- + AAV9-cTnT-GFP
Lrrc10-/- + AAV9-cTnT-LRRC10
E
WT + AAV9-cTnT-GFP
Lrrc10-/- + AAV9-cTnT-GFP
Lrrc10-/- + AAV9-cTnT-LRRC10
Ligature
Apex
Scar Area
Scar area (%)
ns
****
****
F
HW:BW
HW:BW (mg:g)
ns
G
EF
EF (%)
0.3841
0.1569
0.7549
FS
FS (%)
0.3412
0.1650
0.8251

Figure 2. Lrrc10 overexpression rescues heart regeneration in Lrrc10-/- mice. (A) Control and *Lrrc10*$^{-/-}$ neonatal mice were treated with a single-dose of AAV9-cTnT-GFP control or AAV9-cTnT-LRRC10 rescue viral vector before undergoing sham or MI surgery at P1. (B) Efficient transfection shown by GFP expression in WT P8 mice treated with or without AAV9-cTnT-GFP at P0 (n=3). Hearts were analyzed for regeneration hallmarks at 7-, 14- and 28-days post-MI (DPMI). (C) Cytokinesis measured by symmetrical Aurora B within cardiomyocytes, marked by cTnT at 7DPMI (n=4). (D) Nucleation percentages of mononucleated (Mono), binucleated (Bi), and multinucleated (Multi) cardiomyocytes (WT and KO controls n=9; KO rescue n=8) at 14DPMI. (E) Masson's trichrome analysis at 28DPMI (n=4); trichrome scale 1mm. (F) Heart Weight (HW) to Body Weight (BW) ratios at 28DPMI (WT control n=9; KO control n=8; KO rescue n=6). (G) Echocardiography of ejection fraction (EF) and fractional shortening (FS) at 28DPMI (WT control n=9; KO control n=8; KO rescue n=6).

SUPPLEMENTAL FIGURES

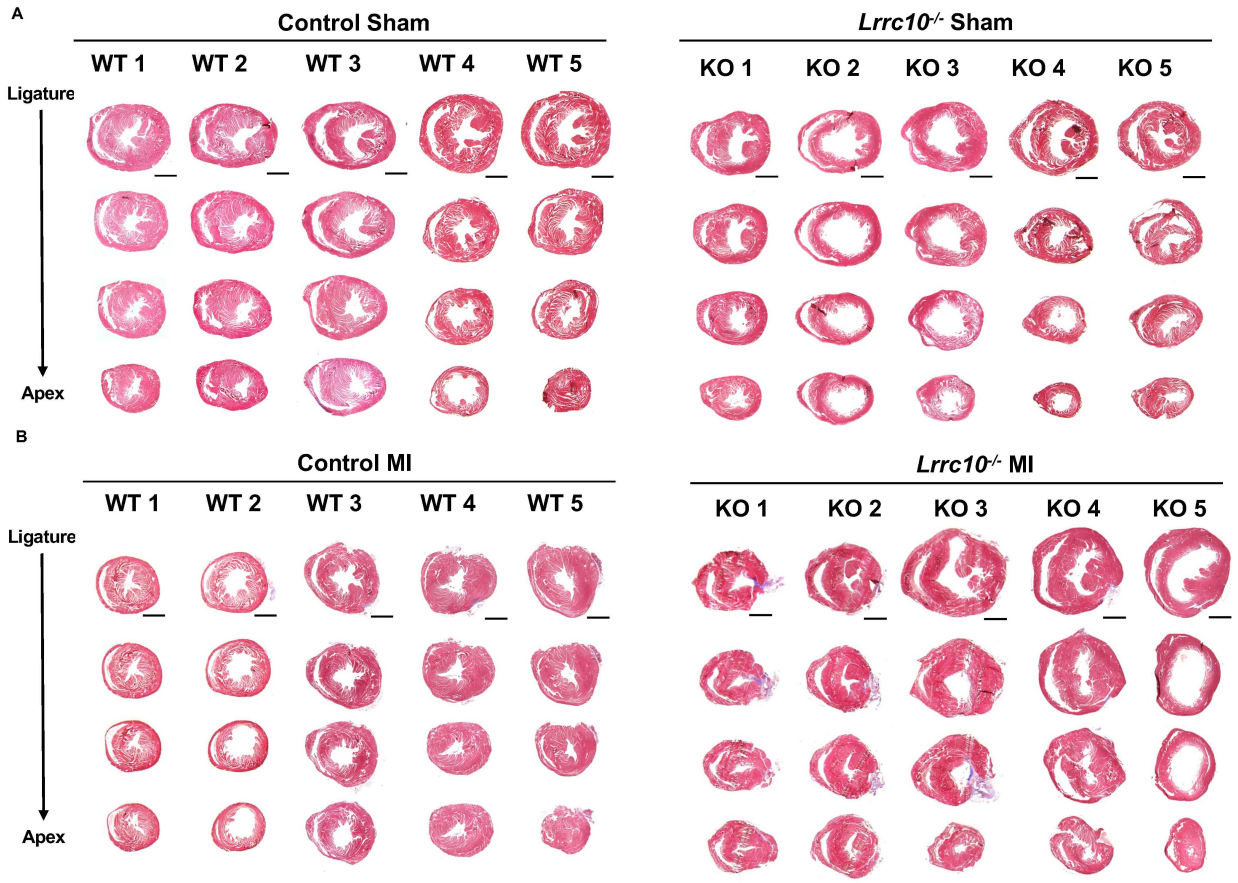

Supplemental Figure 1. Lrrc10-/- hearts show increased scar tissue post-MI. Masson's Trichrome was performed on control (WT) and Lrrc10-/- heart sections at 21 days post (A) sham (SH) and (B) MI surgery (n=5).

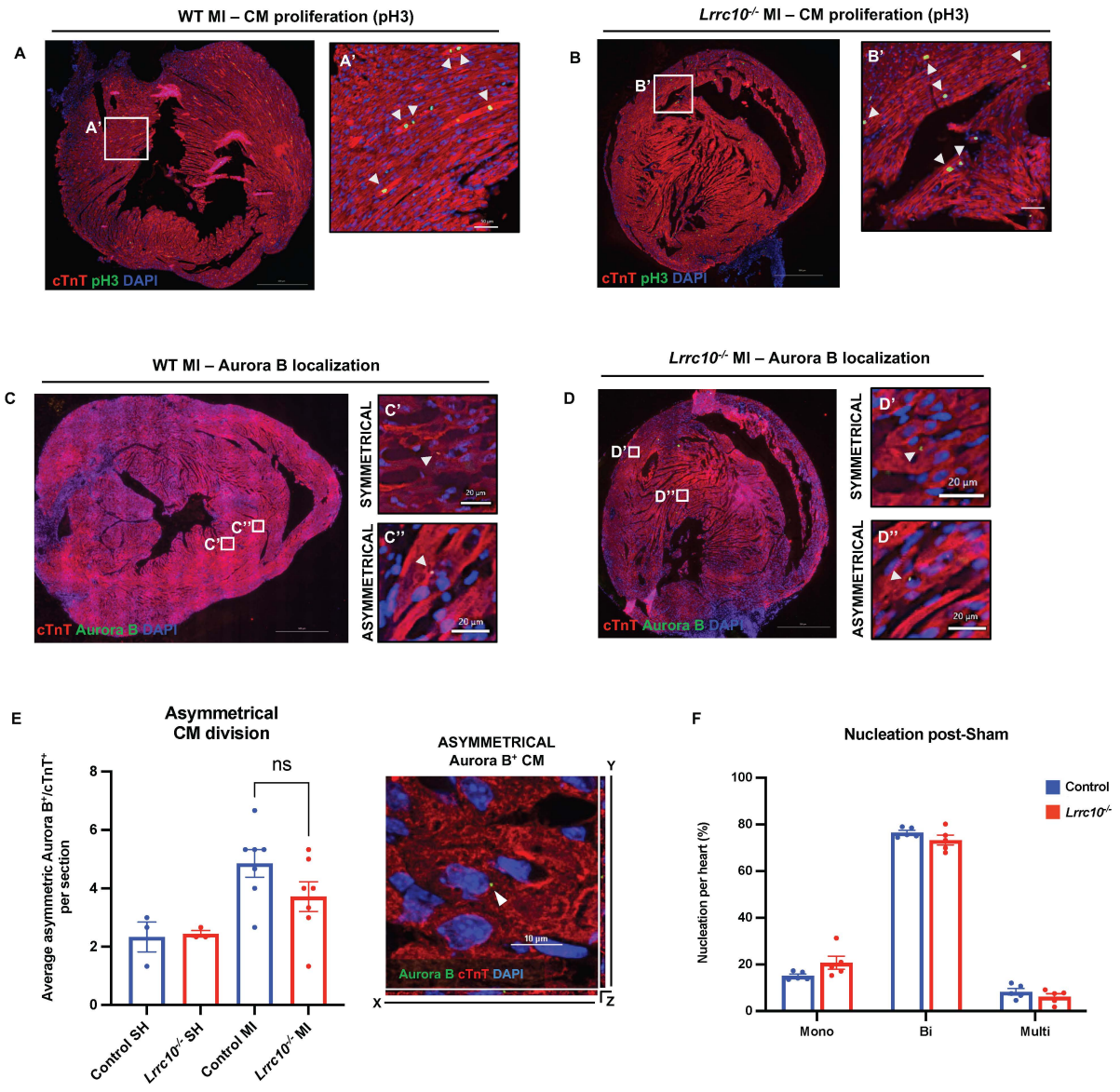

Supplemental Figure 2. Lrrc10-/- hearts show no change in proliferation, asymmetrical cell division, or sham nucleation counts. At 7 days post-sham or post-MI surgery, there was no difference in cardiomyocyte (CM) proliferation between (A) WT and (B) Lrrc10-/- groups, shown as representative sections and (A', B') insets; arrowheads indicate pH3+ cardiomyocytes. (C) WT and (D) Lrrc10-/- hearts showed no difference in the Aurora B localization, shown as representative sections and insets of (C', D') symmetrical or (C'', D'') asymmetrical CM division; arrowhead indicates Aurora B localization between cardiomyocytes (E) Post-MI or post-sham

surgery, Lrrc10-/- hearts showed no difference in asymmetrical CM division in comparison to WT hearts. (F) At 14 days post-sham surgery, nucleation counts for mono-, bi-, and multinucleated CMs did not differ between WT and Lrrc10-/- groups.

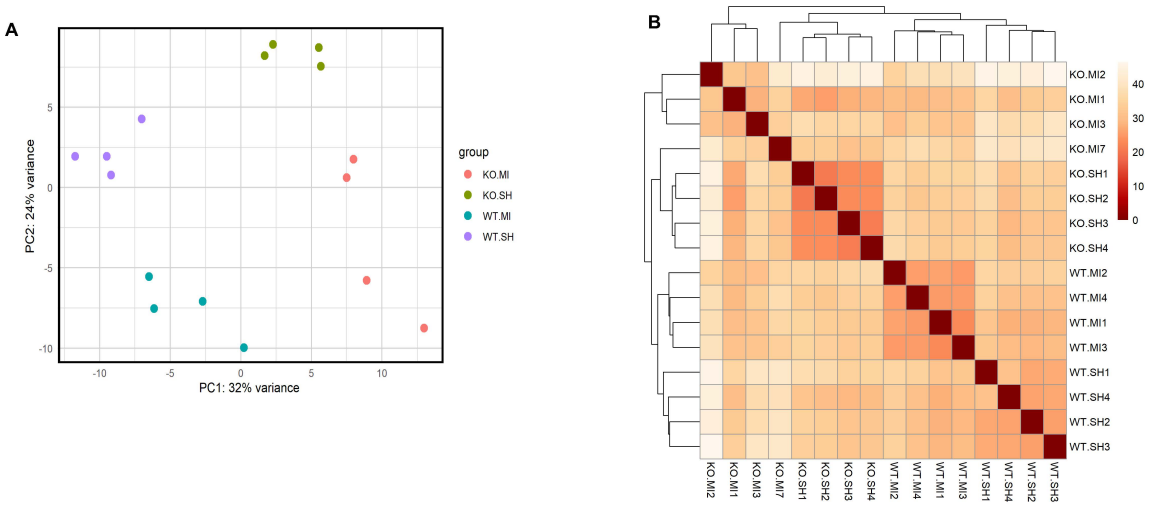

Supplemental Figure 3. Transcriptomic analysis shows unique signature between control and Lrrc10-/- hearts post-injury. Bulk RNA sequencing of control and Lrrc10-/- mice that underwent a sham (SH) or MI surgery at P1. (A) Principal Component Analysis (PCA) shows gene expression patterning. (B) Pearson correlation shows clustering of transcriptomic profiles.

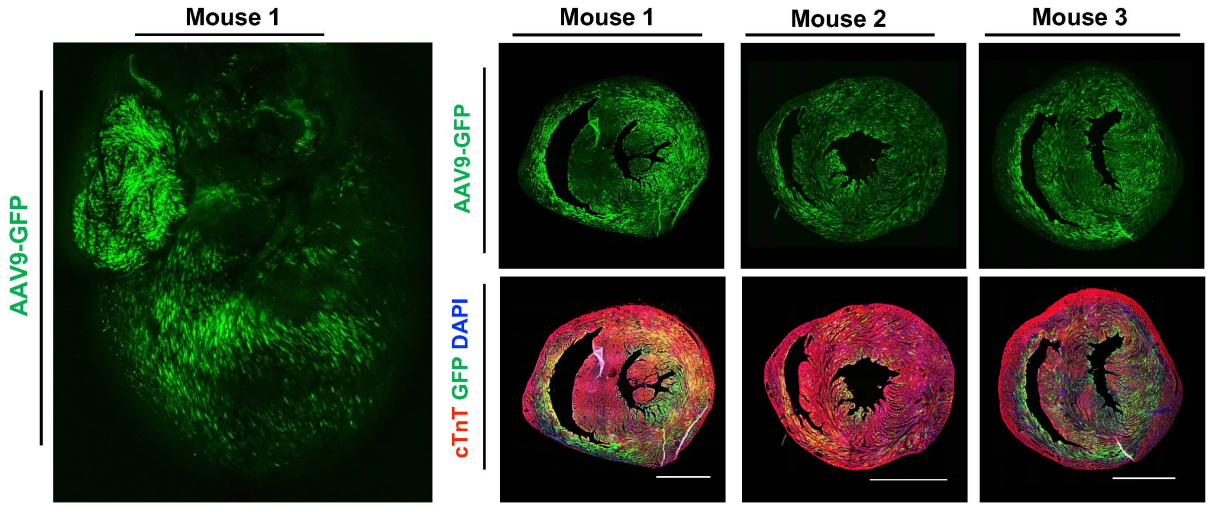

Supplemental Figure 4. Viral control shows successful reporter expression in the postnatal heart. AAV9-cTnT-GFP control vector was injected into P0 mice and hearts were collected at 7 days post-injections. Images were captured of the (A) whole-mount and (B) sectioned hearts (n=3). Scale bar=1mm.

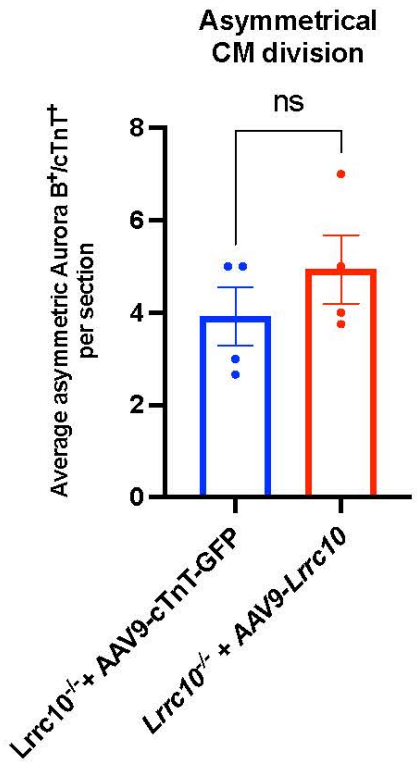

Supplemental Figure 5. Asymmetrical cytokinesis is unchanged between *Lrrc10*$^{-/-}$ treated with AAV9-GFP or AAV9-Lrrc10 virus. AAV9-cTnT-GFP (control) or AAV9-cTnT-LRRC10 (rescue) vector was injected into P0 mice, MI surgery was performed at P1, and asymmetrical cytokinesis was measured by Aurora B at 7 days post-MI. No difference in asymmetric cardiomyocyte (CM) division was identified between Lrrc10-/- hearts treated with control or rescue vector.

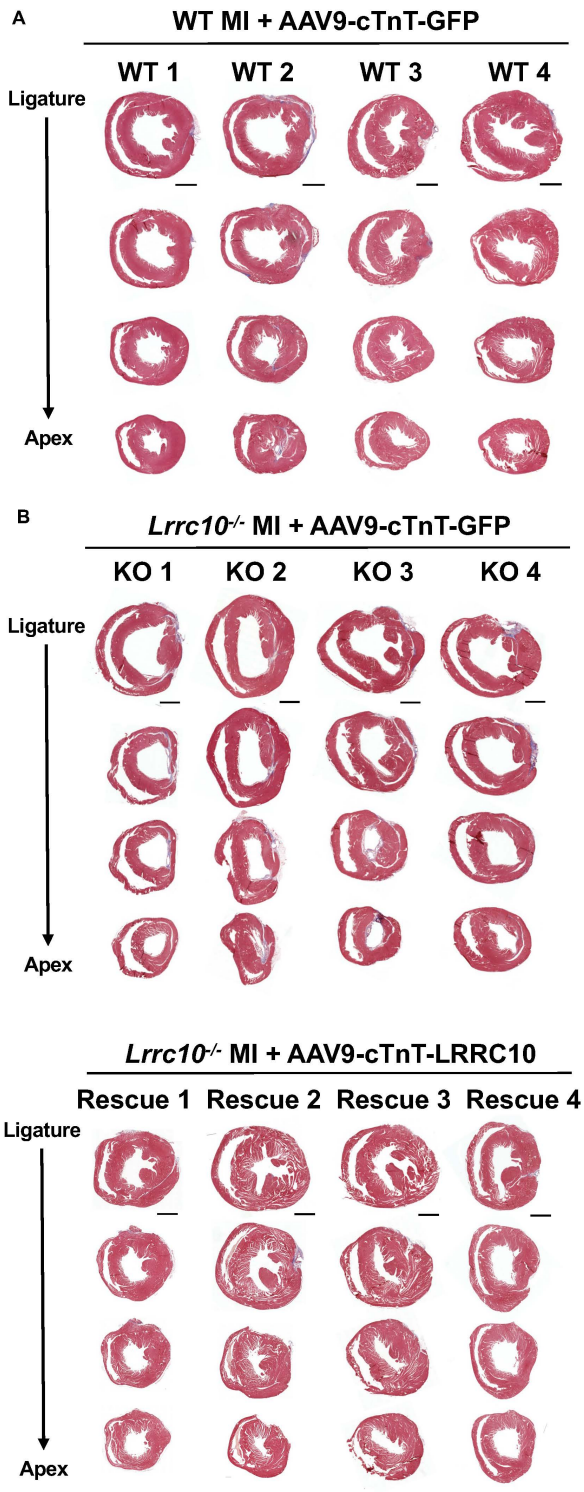

Supplemental Figure 6. Lrrc10-/- treated with AAV9-Lrrc10 virus promotes regeneration post-MI. Masson's Trichrome of heart sections from WT and *Lrrc10*$^{-/-}$ (KO) mice treated with (A-B) control AAV9-cTnT-GFP or (C) rescue AAV9-cTnT-LRRC10 rescue virus at 21 days post-MI (n=4).

REFERENCES

1 Murphy, S. P., Ibrahim, N. E. & Januzzi, J. L., Jr. Heart Failure With Reduced Ejection Fraction: A Review. *JAMA* **324**, 488-504, doi:10.1001/jama.2020.10262 (2020).

2 Becker, R. O., Chapin, S. & Sherry, R. Regeneration of the ventricular myocardium in amphibians. *Nature* **248**, 145-147, doi:10.1038/248145a0 (1974).

3 Cano-Martinez, A. *et al.* Functional and structural regeneration in the axolotl heart (Ambystoma mexicanum) after partial ventricular amputation. *Arch Cardiol Mex* **80**, 79-86 (2010).

4 Poss, K. D., Wilson, L. G. & Keating, M. T. Heart regeneration in zebrafish. *Science* **298**, 2188-2190, doi:10.1126/science.1077857 (2002).

5 Porrello, E. R. *et al.* Transient regenerative potential of the neonatal mouse heart. *Science* **331**, 1078-1080, doi:10.1126/science.1200708 (2011).

6 Zhu, W. *et al.* Regenerative Potential of Neonatal Porcine Hearts. *Circulation* **138**, 2809-2816, doi:10.1161/CIRCULATIONAHA.118.034886 (2018).

7 Ye, L. *et al.* Early Regenerative Capacity in the Porcine Heart. *Circulation* **138**, 2798-2808, doi:10.1161/CIRCULATIONAHA.117.031542 (2018).

8 Sadek, H. & Olson, E. N. Toward the Goal of Human Heart Regeneration. *Cell Stem Cell* **26**, 7-16, doi:10.1016/j.stem.2019.12.004 (2020).

9 Stockdale, W. T. *et al.* Heart Regeneration in the Mexican Cavefish. *Cell Rep* **25**, 1997-2007 e1997, doi:10.1016/j.celrep.2018.10.072 (2018).

10 Kobe, B. & Deisenhofer, J. The leucine-rich repeat: a versatile binding motif. *Trends Biochem Sci* **19**, 415-421, doi:10.1016/0968-0004(94)90090-6 (1994).

11 Brody, M. J. *et al.* Ablation of the cardiac-specific gene leucine-rich repeat containing 10 (Lrrc10) results in dilated cardiomyopathy. *PLoS One* **7**, e51621, doi:10.1371/journal.pone.0051621 (2012).

12 Woon, M. T. *et al.* Pediatric Dilated Cardiomyopathy-Associated LRRC10 (Leucine-Rich Repeat-Containing 10) Variant Reveals LRRC10 as an Auxiliary Subunit of Cardiac L-Type Ca(2+) Channels. *J Am Heart Assoc* **7**, doi:10.1161/JAHA.117.006428 (2018).

13 Mahmoud, A. I., Porrello, E. R., Kimura, W., Olson, E. N. & Sadek, H. A. Surgical models for cardiac regeneration in neonatal mice. *Nat Protoc* **9**, 305-311, doi:10.1038/nprot.2014.021 (2014).

14 Adameyko, II *et al.* Expression and regulation of mouse SERDIN1, a highly conserved cardiac-specific leucine-rich repeat protein. *Dev Dyn* **233**, 540-552, doi:10.1002/dvdy.20368 (2005).

15 Kim, K. H. *et al.* Lrrc10 is required for early heart development and function in zebrafish. *Dev Biol* **308**, 494-506, doi:10.1016/j.ydbio.2007.06.005 (2007).

16 Kim, K. H., Kim, T. G., Micales, B. K., Lyons, G. E. & Lee, Y. Dynamic expression patterns of leucine-rich repeat containing protein 10 in the heart. *Dev Dyn* **236**, 2225-2234, doi:10.1002/dvdy.21225 (2007).

17 Porrello, E. R. *et al.* Regulation of neonatal and adult mammalian heart regeneration by the miR-15 family. *Proc Natl Acad Sci U S A* **110**, 187-192, doi:10.1073/pnas.1208863110 (2013).

18 Patterson, M. *et al.* Frequency of mononuclear diploid cardiomyocytes underlies natural variation in heart regeneration. *Nat Genet* **49**, 1346-1353, doi:10.1038/ng.3929 (2017).
19 Hesse, M. *et al.* Midbody Positioning and Distance Between Daughter Nuclei Enable Unequivocal Identification of Cardiomyocyte Cell Division in Mice. *Circ Res* **123**, 1039-1052, doi:10.1161/CIRCRESAHA.118.312792 (2018).
20 Leone, M., Magadum, A. & Engel, F. B. Cardiomyocyte proliferation in cardiac development and regeneration: a guide to methodologies and interpretations. *Am J Physiol Heart Circ Physiol* **309**, H1237-1250, doi:10.1152/ajpheart.00559.2015 (2015).
21 Cui, M. *et al.* Dynamic Transcriptional Responses to Injury of Regenerative and Non-regenerative Cardiomyocytes Revealed by Single-Nucleus RNA Sequencing. *Dev Cell* **53**, 102-116 e108, doi:10.1016/j.devcel.2020.02.019 (2020).
22 Quaife-Ryan, G. A. *et al.* Multicellular Transcriptional Analysis of Mammalian Heart Regeneration. *Circulation* **136**, 1123-1139, doi:10.1161/CIRCULATIONAHA.117.028252 (2017).
23 O'Meara, C. C. *et al.* Transcriptional reversion of cardiac myocyte fate during mammalian cardiac regeneration. *Circ Res* **116**, 804-815, doi:10.1161/CIRCRESAHA.116.304269 (2015).
24 Houser, S. R., Piacentino, V., 3rd & Weisser, J. Abnormalities of calcium cycling in the hypertrophied and failing heart. *J Mol Cell Cardiol* **32**, 1595-1607, doi:10.1006/jmcc.2000.1206 (2000).
25 Valdivia, C. R. *et al.* Loss-of-function mutation of the SCN3B-encoded sodium channel beta3 subunit associated with a case of idiopathic ventricular fibrillation. *Cardiovasc Res* **86**, 392-400, doi:10.1093/cvr/cvp417 (2010).
26 Bae, J. *et al.* Malonate Promotes Adult Cardiomyocyte Proliferation and Heart Regeneration. *Circulation* **143**, 1973-1986, doi:10.1161/circulationaha.120.049952 (2021).
27 Manuylov, N. L., Manuylova, E., Avdoshina, V. & Tevosian, S. Serdin1/Lrrc10 is dispensable for mouse development. *Genesis* **46**, 441-446, doi:10.1002/dvg.20422 (2008).
28 Mahmoud, A. I., Porrello, E. R., Kimura, W., Olson, E. N. & Sadek, H. A. Surgical models for cardiac regeneration in neonatal mice. *Nature Protocols* **9**, 305-311, doi:10.1038/nprot.2014.021 (2014).
29 Jiang, H., Lei, R., Ding, S.-W. & Zhu, S. Skewer: a fast and accurate adapter trimmer for next-generation sequencing paired-end reads. *BMC Bioinformatics* **15**, 182, doi:10.1186/1471-2105-15-182 (2014).
30 Dobin, A. *et al.* STAR: ultrafast universal RNA-seq aligner. *Bioinformatics* **29**, 15-21, doi:10.1093/bioinformatics/bts635 (2013).
31 Li, B. & Dewey, C. N. RSEM: accurate transcript quantification from RNA-Seq data with or without a reference genome. *BMC Bioinformatics* **12**, 323, doi:10.1186/1471-2105-12-323 (2011).
32 Love, M. I., Huber, W. & Anders, S. Moderated estimation of fold change and dispersion for RNA-seq data with DESeq2. *Genome Biology* **15**, 550, doi:10.1186/s13059-014-0550-8 (2014).

33 Reiner, A., Yekutieli, D. & Benjamini, Y. Identifying differentially expressed genes using false discovery rate controlling procedures. *Bioinformatics* **19**, 368-375, doi:10.1093/bioinformatics/btf877 (2003).

CHAPTER V: MALONATE PROMOTES ADULT CARDIOMYOCYTE PROLIFERATION AND HEART REGENERATION

Jiyoung Bae, PhD[1]; Rebecca J. Salamon, BS[1]; Emma B. Brandt, PhD[1]; Wyatt G. Paltzer, BS[1]; Ziheng Zhang, BS[1]; Emily C. Britt, BS[2]; Timothy A. Hacker, PhD[3]; Jing Fan, PhD[2]; Ahmed I. Mahmoud, PhD[1]

[1]Department of Cell and Regenerative Biology, University of Wisconsin-Madison School of Medicine and Public Health, Madison, WI 53705, USA (J.B., R.J.S., E.B.B., W.G.P., Z.Z., A.I.M.).
[2]Morgridge Institute for Research, Madison, WI 53715, USA; Department of Nutritional Sciences, University of Wisconsin-Madison, Madison, WI 53706, USA (E.C.B, J.F.)
[3]Cardiovascular Research Center, University of Wisconsin-Madison School of Medicine and Public Health, Madison, WI 53705, USA (T.A.H.)

*Correspondence: Ahmed I. Mahmoud, Ph.D. Email: aimahmoud@wisc.edu

Bae J, Salamon RJ, Brandt EB, Paltzer WG, Zhang Z, Britt EC, Hacker TA, Fan J, Mahmoud AI. Malonate Promotes Adult Cardiomyocyte Proliferation and Heart Regeneration. Circulation. 2021 May 18;143(20):1973-1986. doi: 10.1161/CIRCULATIONAHA.120.049952. Epub 2021 Mar 5. PMID: 33666092; PMCID: PMC8131241.

AUTHOR CONTRIBUTIONS

J.B. and R.J.S. performed the experiments. J.B., R.J.S., E.B.B., W.G.P. analyzed the data. Z.Z. captured representative images for cardiomyocyte division. E.C.B. and T.A.H. performed adult mouse surgeries and echocardiography. J.F. performed metabolic analysis. J.B., R.J.S., and A.I.M. designed the experiments. A.I.M. conceived the project and contributed to preparation of the manuscript.

ABSTRACT:

BACKGROUND: Neonatal mouse cardiomyocytes undergo a metabolic switch from glycolysis to oxidative phosphorylation, which results in a significant increase in reactive oxygen species (ROS) production that induces DNA damage. These cellular changes contribute to cardiomyocyte cell cycle exit and loss of the capacity for cardiac regeneration. The mechanisms that regulate this metabolic switch and the increase in ROS production have been relatively unexplored. Current evidence suggests that elevated ROS production in ischemic tissues occurs due to accumulation of the mitochondrial metabolite succinate during ischemia via succinate dehydrogenase (SDH), and this succinate is rapidly oxidized at reperfusion. Interestingly, mutations in SDH in familial cancer syndromes have been demonstrated to promote a metabolic shift into glycolytic metabolism, suggesting a potential role for SDH in regulating cellular metabolism. Whether succinate and SDH regulate cardiomyocyte cell cycle activity and the cardiac metabolic state remains unclear.

METHODS: Here, we investigated the role of succinate and succinate dehydrogenase (SDH) inhibition in regulation of postnatal cardiomyocyte cell cycle activity and heart regeneration.

RESULTS: Our results demonstrate that injection of succinate in neonatal mice results in inhibition of cardiomyocyte proliferation and regeneration. Our evidence also shows that inhibition of SDH by malonate treatment after birth extends the window of cardiomyocyte proliferation and regeneration in juvenile mice. Remarkably, extending malonate treatment to the adult mouse heart following myocardial infarction injury results in a robust regenerative response within 4 weeks following injury via promoting adult cardiomyocyte proliferation and

revascularization. Our metabolite analysis following SDH inhibition by malonate induces dynamic changes in adult cardiac metabolism.

CONCLUSIONS: Inhibition of SDH by malonate promotes adult cardiomyocyte proliferation, revascularization, and heart regeneration via metabolic reprogramming. These findings support a potentially important new therapeutic approach for human heart failure.

CLINICAL PERSPECTIVE

What Is New?

- We found that malonate, a competitive inhibitor of succinate dehydrogenase (SDH), promotes adult cardiomyocyte proliferation, revascularization of the infarct zone, and myocardial regeneration following infarction.
- We also found that SDH inhibition by malonate induces a metabolic shift from oxidative phosphorylation to glucose metabolism in the adult heart.

What Are the Clinical Implications?

- Transient inhibition of SDH represents an important metabolic target to promote adult heart regeneration following infarction.
- The long-term effects of systemic SDH inhibition needs to be closely evaluated owing to its role as a tumor suppressor.

INTRODUCTION

Cardiovascular disease remains the leading cause of death in the world[1]. Both vascular and myocardial damage arise from acute cardiovascular events such as myocardial infarction (MI).

The limited capacity of the adult heart to repair itself represents a major barrier in cardiovascular medicine and often leads to heart failure. In contrast, the neonatal mouse heart has the ability to regenerate following MI, with the newly formed cardiac tissue being derived primarily from the proliferation of the pre-existing cardiomyocytes[2-4]. During postnatal development, exposure to high levels of atmospheric oxygen following birth results in a metabolic switch in energy utilization from glycolysis to oxidative phosphorylation[5]. This metabolic switch results in increased mitochondrial reactive oxygen species (ROS) production, causing cardiomyocyte DNA damage and contributing to the postnatal cardiomyocyte cell cycle arrest in mice[6]. Thus, understanding the metabolic state of the mammalian heart following birth can lead to important insights towards restoring adult cardiomyocyte cell cycle activity and subsequent regenerative abilities following injury.

Recent studies have demonstrated that the metabolite succinate accumulates during ischemia, which is a conserved phenomenon across vertebrates[7-9]. Different models suggest that succinate accumulation occurs either through reverse activity of the enzyme complex succinate dehydrogenase (SDH, also known as complex II), or via canonical tricarboxylic acid (TCA) cycle[7, 9]. SDH activity plays a central role in succinate accumulation in the proposed models owing to its involvement in both the TCA cycle and the electron transport chain (ETC)[10]. Subsequently upon reperfusion, the high levels of accumulated succinate are rapidly metabolized into fumarate, which results in a burst of ROS production via reverse activity of mitochondrial complex I[7, 11]. More importantly, administration of the SDH competitive inhibitor, malonate, prevents the

accumulation of succinate and the subsequent metabolization that increases ROS levels during ischemia/reperfusion injury, emphasizing the link between SDH and ROS production[7, 11, 12].

SDH plays an important role in metabolism and cell cycle activity, as it is the first mitochondrial protein to be identified as a tumor suppressor[13]. Mutations in SDH in familial cancer syndromes promote a metabolic shift into glycolysis that drives cell division[13-15]. Interestingly, metabolic reprogramming to glycolysis is essential during zebrafish heart regeneration, which is concomitant with a significant reduction in SDH activity as well[16]. However, whether succinate and SDH activity directly contribute to the limited regenerative capability of the heart after injury is unknown. In this study, we aim to determine the role of succinate and SDH in regulation of postnatal cardiomyocyte cell cycle activity and heart regeneration.

METHODS

Animals

CD-1 mice were obtained from Charles River Laboratories. All animal experimental procedures were approved by the Institutional Animal Care and Use Committee of the University of Wisconsin-Madison. All experiments were performed on age and sex matched mice, with an equal ratio of male to female mice for neonatal experiments and only male mice for adult experiments.

Neonatal Myocardial Infarction

Neonatal mice at postnatal day 1 (P1) or day 7 (P7) were used for myocardial infarction (MI) surgery. Neonatal mice were subjected to MI surgeries as previously described[2]. Briefly, neonates

were anesthetized by hypothermia on ice. Lateral thoracotomy at the fourth intercostal space was performed by blunt dissection of the intercostal muscles after skin incision. A C-1 tapered needle attached to a 6-0 prolene suture (Ethicon Inc., Bridgewater, NJ) was passed through the mid-ventricle below the left anterior descending coronary artery (LAD) and tied off to induce MI. The prolene suture was used to suture the ribs together and seal the chest wall incisions, and the skin was closed using adhesive glue (3M). The mice then were warmed on a heating pad until recovery. Sham-operated mice underwent the same procedure including hypothermic anesthesia, but not LAD ligation.

Adult Myocardial Infarction

Adult male mice (8-week-old) were subjected to MI by ligation of the proximal aspect of the LAD coronary artery. In brief, mice were anaesthetized using 3% isoflurane, then mice were intubated with PE50 tubing and placed on a mouse ventilator at 120-130 breaths per minute with a stroke volume of 150 microliters and maintained on 2% isoflurane. A left lateral incision through the fourth intercostal space was made to expose the heart. After visualizing the left coronary artery, 7-0 suture was placed through the myocardium in the anterolateral wall and secured as previously described[17, 18]. Coronary artery entrapment was confirmed by observing blanching of the distal circulation (ventricular apex). ECG was used to confirm MI by noting ST segment changes. The lungs were over inflated, and the ribs and muscle layers were closed by absorbable sutures. The skin is closed by additional suturing using 6-0 nylon. The mouse was recovered from the anesthesia and extubated.

Drug Administration

Neonatal mice were weighed and injected daily with either saline, 100 mg/kg dimethyl succinate (Sigma), 100 mg/kg dimethyl malonate (Sigma), or 10 μg/kg Atpenin A5 (Enzo Life Sciences). Dimethyl succinate and dimethyl malonate were dissolved in saline. Stock solution of Atpenin A5 at 0.1mg/ml was initially prepared by dissolving in DMSO (Sigma) and then further diluted with saline before injection. Saline was used as a vehicle control for all experiments. Neonatal mice were given intravenous injections for the first 5 days after birth, followed by intraperitoneal injections until completion of the injection time course. Adult mice were injected intraperitoneally daily with either saline or 100 mg/kg dimethyl malonate post-MI for 2 or 4 weeks. To track cardiomyocyte proliferation, we added 0.25 mg/ml 5-bromodeoxyuridine (BrdU, Sigma) to the drinking water for 2 weeks post-MI. Fresh BrdU-containing water was changed every 2 days.

Histology

Hearts were harvested and fixed in 4% paraformaldehyde (PFA) in PBS solution overnight at 4 °C, processed for paraffin embedding, and sectioned in intervals. Masson's trichrome staining was performed according to the manufacture's protocol (Newcomer Supply, Middleton, WI). Scar size measurements were quantified from at least 3 sections of the heart from ligature to apex. ImageJ was used to quantify the fibrotic scar, and the average scar area for each heart was plotted.

Metabolite analysis

Metabolites were extracted with cold liquid chromatography–mass spectrometry (LC–MS) grade 3/1 butanol/methanol (v/v) following previously established method[19]. Tissue extracts containing polar metabolites were dried under nitrogen flow and subsequently dissolved in LC–

MS grade water for analysis. Protein pellets were removed by centrifugation. Samples were analyzed using a Thermo Q-Exactive mass spectrometer coupled to a Vanquish Horizon Ultra-High Performance Liquid Chromatograph (UHPLC). Metabolites were separated on a 2.1 × 100 mm, 1.7 µM Acquity UPLC BEH C18 Column (Waters) at a 0.2 ml per min flow rate and 30 °C column temperature, with a gradient of solvent A (97/3 H2O/methanol, 10 mM TBA, 9 mM acetate, pH 8.2) and solvent B (100% methanol). The gradient was: 0 min, 5% B; 2.5 min, 5% B; 17 min, 95% B; 21 min, 95% B; 21.5 min, 5% B. Data were collected on a full scan negative mode. The identification of metabolites reported was based on exact m/z and retention times, which were determined with chemical standards. Data were analyzed with Maven. Relative metabolite levels were normalized to internal standard Tryptophan (^{13}C11) and expressed relative to levels measured in the control group.

Echocardiography

Transthoracic echocardiography was performed by using a Visual Sonics 770 ultrasonograph with a 25-MHz transducer (Visual Sonics, Toronto) as described previously[20]. Mice were lightly anesthetized with 1% isoflurane and maintained on a heated platform. Two-dimensionally guided M-mode images from a parasternal long axis (PLAX) of the LV were acquired at the tip of the papillary muscles. Wall thickness and chamber diameters were measured in both diastole and systole. Fractional shortening was calculated as (LVDd-LVDs)/LVDd x 100, where LVDd is LV diameter in diastole and LVDs is LV diameter in systole. Ejection fraction was calculated as $[(7.0/(2.4 + LVDd)(LVDd)^3 – (7.0/(2.4 + LVDs)(LVDs)^3/(7.0/(2.4 + LVDd)(LVDd)^3$ x 100 and LV mass was calculated by using the formula $[1.05 \times ((\text{Posterior Wall}_{\text{diastole}} + \text{Anterior Wall}_{\text{diastole}} + LVDd)^3 – (LVDd)^3)]$. All parameters were measured over at least three consecutive cycles.

Statistical Analysis

All graphs are presented as means ± SE. Statistical analysis was performed using Prism 9 (GraphPad Software). Two-tailed Student's *t-test* was performed to determine the difference between the treatment group and control group. One-way ANOVA was performed by Tukey's multiple comparison test to determine the differences of group mean among treatment groups. The level of significance was set at $P < 0.05$.

RESULTS

Succinate Reduces Cardiomyocyte Proliferation and Heart Regeneration in Neonatal Mice

To determine whether an increase in succinate levels impacts cardiomyocyte cell cycle activity and neonatal mouse heart regeneration, neonatal mice were injected with dimethyl succinate (100 mg/kg) daily for 7 days following myocardial infarction at postnatal day1 (P1) (Figure 1A). We tested multiple doses (50, 100, 150 mg/kg) and we found that 100 mg/kg was the minimum effective dose that reduces cardiomyocyte proliferation (data not shown). To determine whether succinate reduces cardiomyocyte proliferation, we performed immunostaining of the mitosis marker pH3 at 7 days post-MI. Our results revealed a reduction in cardiomyocyte mitosis in succinate injected MI hearts compared to controls (Figure 1B & C).

Loss of cardiomyocyte cell cycle activity occurs due to increase in cardiomyocyte DNA damage as a consequence of the metabolic switch to oxidative phosphorylation and the subsequent rise in ROS levels. To determine whether succinate induces cardiomyocyte DNA damage, we performed immunostaining of γH2AX, which is a marker for DNA double-strand breaks. We quantified a

significant increase in cardiomyocytes with γH2AX foci in succinate-treated mice (Figure 1D & E). Our results demonstrate that in neonatal mice high levels of succinate can induce cardiomyocyte DNA damage and reduce the proliferative potential of pre-existing cardiomyocytes, which is the main source of the newly formed cardiomyocytes during cardiac regeneration[3, 21].

To further establish the effects of succinate on neonatal heart regeneration, we performed trichrome staining at 21 days post-MI to assess regeneration and fibrosis in control and dimethyl succinate injected mice. As expected, saline-injected control mice demonstrated complete heart regeneration. In contrast, dimethyl succinate-injected mice showed lack of regeneration with persistence of a fibrotic scar (Figure 1F). This lack of regeneration was also evident in the significant reduction in cardiac function of dimethyl succinate-injected mice compared to saline-injected controls, as measured by ejection fraction (EF), fractional shortening (FS), left ventricle internal diameter diastole (LVIDD), and left ventricle internal diameter systole (LVIDS) (Figure 1G & Table I in the Data Supplement). Together, these results reveal that succinate injection during the first week of life can result in premature cardiomyocyte cell cycle exit, which inhibits the neonatal cardiac regenerative response.

Malonate Extends the Cardiac Regenerative Window in Postnatal Hearts

Although our results demonstrate that exogenous administration of succinate can inhibit cardiomyocyte proliferation and regeneration, it remains unclear whether succinate dehydrogenase (SDH) activity contributes to cardiomyocyte cell cycle exit in the postnatal heart. Thus, we wanted to determine whether the SDH complex competitive inhibitor, malonate, could

extend the cardiomyocyte proliferative window and improve the cardiac regeneration capacity of the juvenile, normally non-regenerative 7-day-old mice. We injected dimethyl malonate (100 mg/kg, daily) in neonatal mice directly after birth for 2 weeks with an MI performed once the mice reached P7. We then analyzed the hearts following injury to determine whether malonate results in prolongation of the neonatal regenerative window (Figure 2A).

To examine whether malonate stimulates cardiomyocyte proliferation, we performed MI in 7-day-old mice and analyzed their hearts at 7 days post-MI (14-day-old) by immunostaining for markers of proliferation. We measured a significant increase in the number of cardiomyocytes undergoing mitosis as evident by pH3 staining in the dimethyl malonate-injected mice compared to saline injected controls (Figure 2B & C). We also quantified a significant increase in the number of cardiomyocytes undergoing cytokinesis by Aurora B staining, suggesting that a significantly higher number of cardiomyocytes are undergoing complete cell division (Figure 2D & E). Furthermore, there was a significant reduction in cardiomyocyte cell size at 21 days post-MI in the dimethyl malonate injected mice as quantified by wheat germ agglutinin staining (WGA), suggestive of newly formed cardiomyocytes and a reduction in cardiomyocyte hypertrophy (Figure 2F & G).

To determine whether this increase in cardiomyocyte proliferation results in improved regeneration in the P7 mouse heart, we performed trichrome staining at 21 days post-MI to quantify structural regeneration and fibrosis. As expected, lack of myocardium regeneration and persistence of fibrotic scarring was detected below the ligature plane of the saline-injected

controls. In contrast, mice that were injected with dimethyl malonate demonstrated complete heart regeneration (Figure 2H & Figure I in the Data Supplement). More importantly, cardiac function assessed by EF, FS, LVIDD, and LVIDS in the dimethyl malonate injected hearts was restored to normal levels (Figure 2I & Table II in the Data Supplement). These data indicate that SDH inhibition by malonate can promote cardiomyocyte proliferation and extend the regenerative capacity of the neonatal mouse heart beyond 1 week after birth, resulting in a complete regenerative response following MI in P7 juvenile mice.

SDH Inhibition by Atpenin A5 Recapitulates the Regenerative Effect of Malonate

To establish that malonate promotes cardiomyocyte proliferation and heart regeneration via SDH inhibition, we used a similar treatment strategy using Atpenin A5, which is a potent inhibitor of SDH (Figure 3A)[22]. To determine whether Atpenin A5 treatment can stimulate cardiomyocyte proliferation in the non-regenerative heart, we performed MI in P7 mice and analyzed their hearts at 7 days post-MI for markers of proliferation. We quantified a significant increase in the percentage of cardiomyocytes undergoing mitosis and cytokinesis as evident by pH3 and Aurora B staining, respectively, in the Atpenin A5 injected mice compared to controls (Figure 3B-E).

To determine whether SDH inhibition by Atpenin A5 regenerates the non-regenerating P7 mouse heart similar to malonate, we performed trichrome staining at 21 days post-MI to quantify fibrosis and myocardial regeneration. Atpenin A5-injected mice demonstrated myocardial thickness at the infarct zone and a significant reduction in scar size compared to controls (Figure 3F & G). This was concomitant with restoration of cardiac function in Atpenin A5-injected mice

(Figure 3H & Table III in the Data Supplement). Our results demonstrate that Atpenin A5 restores cardiac structure and function similar to malonate, suggesting that SDH inhibition is a central mechanism by which malonate promotes heart regeneration.

Malonate Promotes Cardiomyocyte Proliferation and Heart Regeneration in Adult Mice Following Myocardial Infarction

The ability of malonate to promote cardiomyocyte proliferation and heart regeneration beyond the 1-week postnatal regenerative window in mice raises the question of whether malonate can metabolically reprogram the adult heart to a regenerative state following injury. To address this question, we performed MI in 8-week-old mice and injected either saline or dimethyl malonate (100 mg/kg) within an hour following MI and continued this treatment daily for two weeks (Figure 4A). Although SDH inhibition by malonate results in cardioprotection from reperfusion injury, whether malonate can protect the myocardium following infarction remains undetermined.

To determine whether malonate protects against infarction similar to reperfusion injury, we performed a viability stain using triphenyltetrazolium chloride (TTC) at 3 days post-MI. Quantification of the non-viable myocardium (white) in heart sections below the ligature showed no significant difference in both saline and malonate injected mice, suggesting that malonate did not protect against myocardial necrosis following infarction (Figure 4B, Figure II in the Data Supplement). In addition, there was no difference in the number of apoptotic cardiomyocytes at 3- or 7-days post-MI in saline- and dimethyl malonate-injected hearts as quantified by TdT-mediated dUTP nick-end labelling (TUNEL) staining (Figure 4C, Figure III A in the Data

Supplement). These results demonstrate that malonate did not protect against infarction and cardiomyocyte death following adult MI.

To determine whether malonate stimulates adult cardiomyocyte proliferation, we performed immunostaining for the mitosis marker pH3 at 7- and 14 days post-MI. We quantified a significant increase in the number of cardiomyocytes undergoing mitosis in dimethyl malonate-injected hearts compared to saline-injected controls at both 7- and 14-days post-MI (Figure 4D, Figure III B&D in the Data Supplement). In addition, there was a significant increase in the number of cardiomyocytes undergoing cytokinesis in dimethyl malonate-injected hearts as demonstrated by Aurora B staining at 7- and 14 days post-MI (Figure 4E, Figure III C&E in the Data Supplement). Furthermore, there was a significant increase in 5-bromodeoxyuridine (BrdU) incorporation in cardiomyocytes in malonate-treated mice at 14 days post-MI (Figure 4F). This was concomitant with a remarkable increase in the number of mononucleated cardiomyocytes and a significant decrease in the number of binucleated cardiomyocytes in the malonate-treated mice (Figure 4G). Additionally, we quantified a significant decrease in the number of cardiomyocytes with γH2AX foci in malonate-treated mice indicating a significant reduction in cardiomyocyte DNA damage (Figure 4H). These results suggest that malonate can promote adult cardiomyocyte cell cycle activity following MI.

To determine whether SDH inhibition regulates cardiomyocyte cell cycle activity by modulating succinate levels, we measured the levels of intracellular succinate by liquid chromatography–mass spectrometry (LC–MS). Interestingly, there was a significant increase in succinate levels in

the hearts of malonate-treated mice at 14 days post-MI (Figure 4I). This is in line with multiple studies showing that SDH inhibition and subsequent blockade of oxidative phosphorylation is accompanied by an increase in succinate levels, which promotes metabolic reprogramming to aerobic glycolysis[23-25]. This is distinct from the cardioprotective role of malonate in reperfusion injury, which confers cardioprotection by inhibiting reverse activity of SDH that prevents succinate accumulation[7]. This suggests that malonate might promote cardiomyocyte cell cycle activity via metabolic reprogramming of the adult heart to a regenerative state, rather than preventing succinate accumulation.

We then collected the hearts of both saline and dimethyl malonate-treated adult mice at 14- and 28-days post-MI and quantified structural regeneration by trichrome staining. By 14 days, fibrotic scarring in heart sections was evident in both dimethyl malonate-treated mice and saline-treated control (Figure 5A, Figure IV in the Data Supplement). Quantification showed a trend for reduction in fibrosis in the dimethyl malonate-treated samples compared to controls at 14 days post-MI, but the difference was not significant (Figure 5A). By 28 days post-MI, trichrome staining from the dimethyl malonate-injected hearts showed remarkable restoration of the myocardium with minimal fibrosis compared to the saline-injected controls that showed ventricle dilation and significant fibrotic scarring, as expected from an adult MI (Figure 5A, Figure V in the Data Supplement). Quantification of fibrosis demonstrated a significant reduction of scar size in the dimethyl malonate-treated mice at 28 days post-MI. Notably, there was incomplete regeneration in one mouse heart that was subjected to a large infarct (Figure V in the Data Supplement), indicating that the size of infarction can impact the regenerative response, similar to neonatal

mouse heart regeneration[26]. Whether longer duration of malonate treatment can regenerate larger infarcts is yet to be determined.

To determine whether this restoration of cardiac structure was accompanied by improvement in cardiac function, we performed echocardiographic measurements of both saline and dimethyl malonate-injected mice at 14- and 28-days post-MI. Our echocardiographic measurements demonstrated a reduction in cardiac function at 14 days post-MI (Figure 5B & Table IV in the Data Supplement). There was a trending improvement in cardiac function of dimethyl malonate injected hearts compared to controls by 14 days post-MI, but the difference was not significant (Figure 5B). Remarkably, there was a significant improvement of cardiac function in dimethyl malonate-injected mice as measured by EF and FS at 28 days post-MI (Figure 5B). Interestingly, there was a significant reduction in cardiomyocyte size in dimethyl malonate-injected mice compared to controls at 28 days post-MI as quantified by WGA staining (Figure 5C). No significant differences in heart weight to body weight ratios were detected (Figure 5D). Our results reveal that malonate is capable of restoring cardiac structure and function following adult MI. Collectively, these results demonstrate that malonate promotes adult cardiomyocyte proliferation and heart regeneration following adult MI.

Malonate Induces a Metabolic Shift in the Adult Heart and Promotes Revascularization Following Infarction

The metabolic switch from glycolysis to oxidative phosphorylation results in loss of the endogenous cardiac regenerative ability in mammals[6]. Furthermore, a metabolic switch to

glycolysis promotes cardiomyocyte proliferation during zebrafish heart regeneration[16]. Interestingly, mutations in SDH have been demonstrated to induce a metabolic shift into glycolysis in familial cancer syndromes that promotes cell division and angiogenesis[13-15]. These studies together with our comprehensive results strongly suggest that SDH inhibition may promote a cardiac regenerative response by modulating the cardiac metabolic state. To determine whether inhibition of SDH promotes metabolic reprogramming in the adult heart, we treated adult mice for 2 weeks with dimethyl malonate and performed metabolomics using LC-MS (Figure 6A). Several metabolites in the TCA cycle, such as α-ketoglutarate, were downregulated following SDH inhibition by malonate, except for succinate, which was increased as expected (Figure 6B). This is consistent with previous studies showing inhibition of aerobic respiration in response to SDH inhibition, since SDH participates in both the TCA cycle and the electron transport chain (ETC)[10]. More importantly, this was accompanied by a dynamic shift in metabolites in other pathways of glucose metabolism (Figure 6C). These results are consistent with previous studies demonstrating that SDH inhibition stimulates a metabolic shift to glycolysis, which is a metabolic state that can promote heart regeneration.

Cardiomyocyte proliferation is key to replenishing the lost myocardium following injury; however, complete regeneration following infarction requires coronary artery formation and revascularization to supply the newly formed myocardium with oxygenated blood. This response has been demonstrated to be activated during neonatal mouse regeneration and is a hallmark for complete regeneration following infarction[27]. Interestingly, glycolysis plays in important role in angiogenesis[28, 29]. Since malonate treatment induces a cardiac metabolic shift in the adult heart,

we wanted to determine whether malonate promotes heart regeneration by inducing coronary artery formation and revascularization following injury. To address this question, we performed coronary casting of saline and dimethyl malonate injected hearts at 28 days post-MI. There was a remarkable formation of coronary arteries below the ligature site in the dimethyl malonate injected mice compared to controls (Figure 6D). In addition, there was a significant increase in capillary density and vascular smooth muscle cells in the infarct zone, suggesting an increase in newly synthesized vessels ranging in size from small capillaries to large-diameter vessels (Figure 6E & F). These results reveal that malonate can induce myocardial regeneration by stimulating adult cardiomyocyte proliferation as well as revascularization post-MI.

Malonate Treatment at 1-Week Following Infarction Promotes Heart Regeneration

To determine whether malonate can promote a regenerative response following the establishment of infarction, we performed MI in 8-week-old mice and started malonate treatment at 1-week post-MI (Figure 7A). The reduction of cardiac function was confirmed at 1-week post-MI by echocardiography (Figure 7D). Mice were then randomized and treated with saline or malonate for a period of 4 weeks, and hearts were harvested at 6 weeks post-MI (Figure 7A). Trichrome staining at 6 weeks post-MI showed a remarkable increase in myocardial thickness with minimal fibrosis in malonate-treated mice (Figure 7B & Figure VI in the Data Supplement). Fibrosis quantification demonstrated a significant reduction in scar size in the malonate-treated mice at 6 weeks post-MI (Figure 7C). Remarkably, there was a significant increase in cardiac function in malonate-treated mice at 4-weeks and 6-weeks post-MI (Figure 7D & Table V in the Data Supplement). Our results demonstrate that injection of malonate in

adult mice at 1-week post-MI promoted myocardial regeneration and functional improvement over time. Together, these results demonstrate that SDH inhibition by malonate can stimulate a cardiac regenerative response following the establishment of infarction in the adult heart.

DISCUSSION

Systolic heart failure often occurs as a consequence of the inability of the adult mammalian heart to regenerate following injury such as MI. Models of mammalian endogenous heart regeneration provide an opportunity to identify new approaches to restore adult human heart regeneration[30]. Lineage tracing studies demonstrated that proliferation of the pre-existing cardiomyocytes is the main source of the newly formed functional myocardium during endogenous regeneration. Thus, stimulating adult cardiomyocyte proliferation represents an important target towards regenerating the adult human heart following injury.

The metabolic switch in energy utilization of the postnatal heart and the subsequent increase in ROS production has emerged as an important factor in loss of this regenerative response[6]. The mechanisms that regulate this metabolic switch remain unclear. In this study, our results demonstrate a powerful link in succinate metabolism and succinate dehydrogenase (SDH) activity to the regenerative response of the mammalian heart. We demonstrate that high levels of succinate can induce cardiomyocyte DNA damage and inhibit cardiomyocyte proliferation and regeneration. More importantly, we demonstrate that inhibition of SDH activity by malonate can also restore a cardiac regenerative response in the adult heart by stimulating adult cardiomyocyte cell cycle re-entry and revascularization, important hallmarks of endogenous

heart regeneration. This regenerative effect is largely due to SDH inhibition, since Atpenin A5, a potent inhibitor of SDH, can recapitulate the regenerative effect of malonate. Furthermore, our analysis demonstrates that SDH inhibition induces metabolite level changes that are consistent with a metabolic shift from oxidative phosphorylation to glycolysis in the adult heart. Although we did not detect an increase in lactate levels, serial metabolite analysis at multiple timepoints can reveal the extent of the dynamic cardiac metabolic shift following SDH inhibition. The metabolic switch from aerobic respiration to glycolysis is implicated by previous studies defining SDH as a tumor suppressor, where SDH mutations result in a metabolic reprogramming to glycolysis that promotes cancer growth[13-15].

Malonate has been demonstrated to play a cardioprotective role in reperfusion injury by inhibiting reverse activity of SDH, which prevents succinate accumulation and the subsequent redox insult and cardiac damage[7]. Interestingly, SDH inhibition by malonate for 2 weeks increased succinate levels, a consequence of inhibition of oxidative phosphorylation[23-25]. In contrast to reperfusion injury, our results demonstrate that malonate does not exhibit a cardioprotective role following myocardial infarction. The progression in restoration of cardiac structure and function over time strongly suggests a stimulation of a regenerative response by malonate following infarction, rather than protection. Furthermore, we demonstrate that malonate treatment starting 1-week post-MI promotes myocardial regeneration and functional improvement over time. Collectively, these results reveal a novel role for SDH in its ability to metabolically reprogram the adult heart to a regenerative state. This underscores the

translational potential of SDH inhibition as a powerful metabolic target for promoting adult heart regeneration.

There is an emerging appreciation for the role of metabolism in controlling cell state. Adult neural stem cell activity changes from a quiescent to a proliferative state via a metabolic shift by a single metabolite[31]. Similarly, metabolic reprogramming regulates macrophage function in response to different stimuli[32, 33]. Interestingly, a recent study demonstrated that metabolic reprogramming is required for cardiomyocyte proliferation during zebrafish heart regeneration[16]. The potential metabolic targeting of multiple cell types by systemic administration of malonate explains the striking regenerative effect following adult myocardial infarction. In this study, we demonstrate that SDH inhibition promotes adult cardiomyocyte proliferation and revascularization following injury. The overall impact of malonate on other cell types will need to be further investigated. For example, SDH inhibition by malonate has been shown to promote an anti-inflammatory state of macrophages following lipopolysaccharide stimulation[34]. Thus, whether SDH inhibition regulates the inflammatory response following infarction remains unclear. In addition, mutations in SDH have been shown to promote DNA methylation, demonstrating an interplay between epigenetics and metabolism[14, 23, 35]. Whether SDH inhibition by malonate can modulate the epigenetic landscape and the transcriptional activity of multiple cardiac cell types needs to be determined.

Understanding the effect of malonate on the heart as well as other tissues will be an essential step prior to translating our findings to the clinic for treatment of heart failure. Targeted delivery

to the heart would avoid any off-target effects from systemic SDH inhibition. Furthermore, additional safety and pharmacokinetic studies are warranted owing to the role of SDH inhibition in multiple cancers, which will pave the way to harnessing the regenerative effect of malonate due to its simplicity and efficacy. Malonate provides an opportunity for transient SDH inhibition, but the long-term effects need to be determined as well. Promoting adult heart regeneration by SDH inhibition has enormous implications for treatment of systolic heart failure patients.

FIGURES

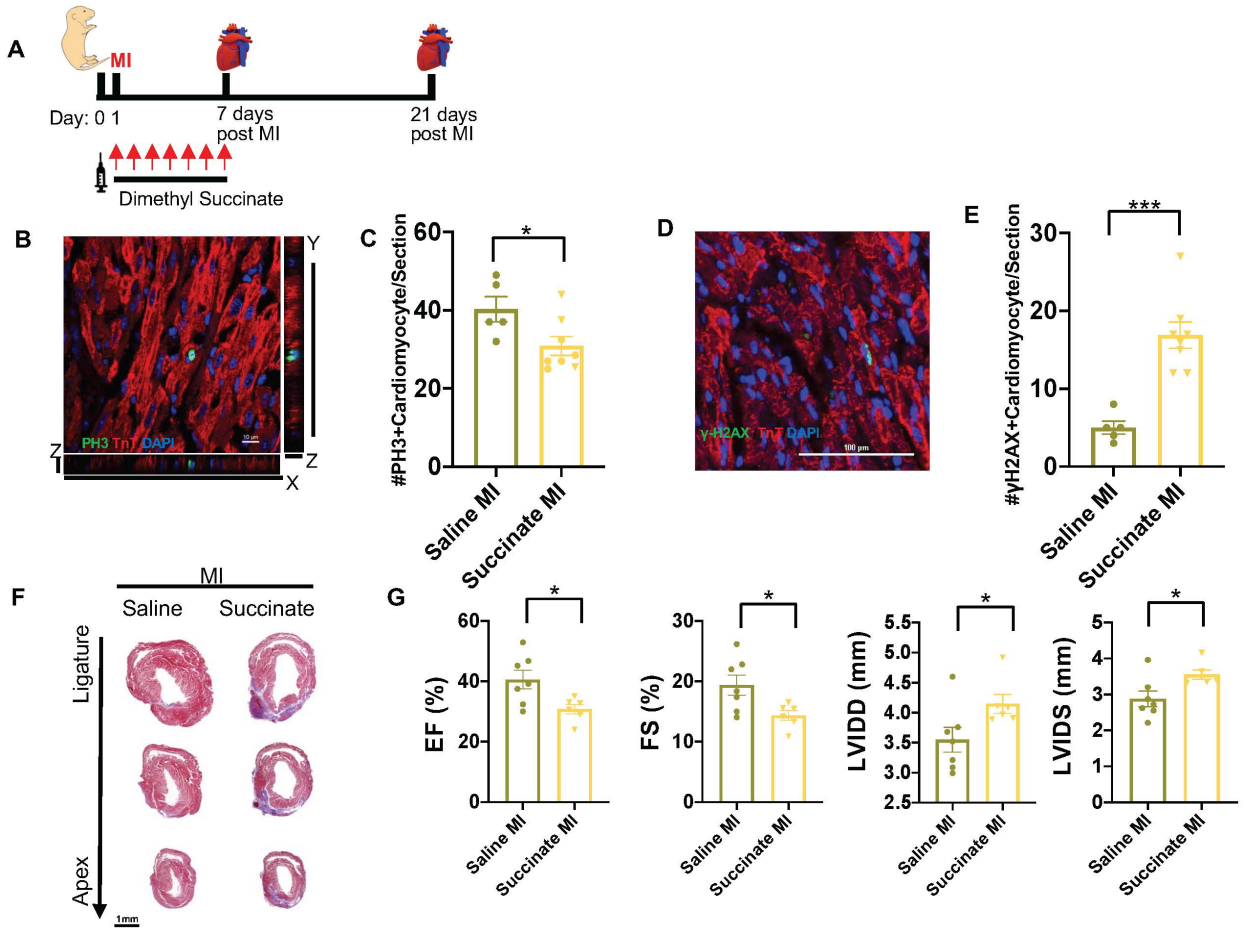

Figure 1. Succinate reduces cardiomyocyte proliferation and blocks heart regeneration in neonatal mice following myocardial infarction (MI). (A) Schematic of injection period and myocardial infarction strategy in neonatal mice. (B) High magnification Z-stack image of a mitotic cardiomyocyte following immunostaining of pH3 and cTnT at 7 days post-MI. Scale bar, 10 µm. (C) Quantification of the number of mitotic cardiomyocytes per section showing a significant decrease in cardiomyocyte mitosis following dimethyl succinate injection. (D) Immunostaining of the DNA double-strand breaks marker γH2AX. Scale bar, 100 µm. (E) Quantification of cardiomyocytes with increased γH2AX foci demonstrating a significant increase in DNA damage

in succinate-treated mice compared to controls. (F) Trichrome staining demonstrating persistence of the fibrotic scar following MI in the dimethyl succinate-injected mice compared to saline-injected controls. Scale bar, 1 mm. (G) Echocardiography at 21 days post-MI showing a significant reduction in the cardiac function of dimethyl succinate-injected mice following MI compared to saline-injected controls as measured by ejection fraction (EF), fractional shortening (FS), left ventricle internal diameter diastole (LVIDD) and left ventricle internal diameter systole (LVIDS). (n=5-8 mice per group). *P< 0.05, ***P<0.0001 by Student's t-test.

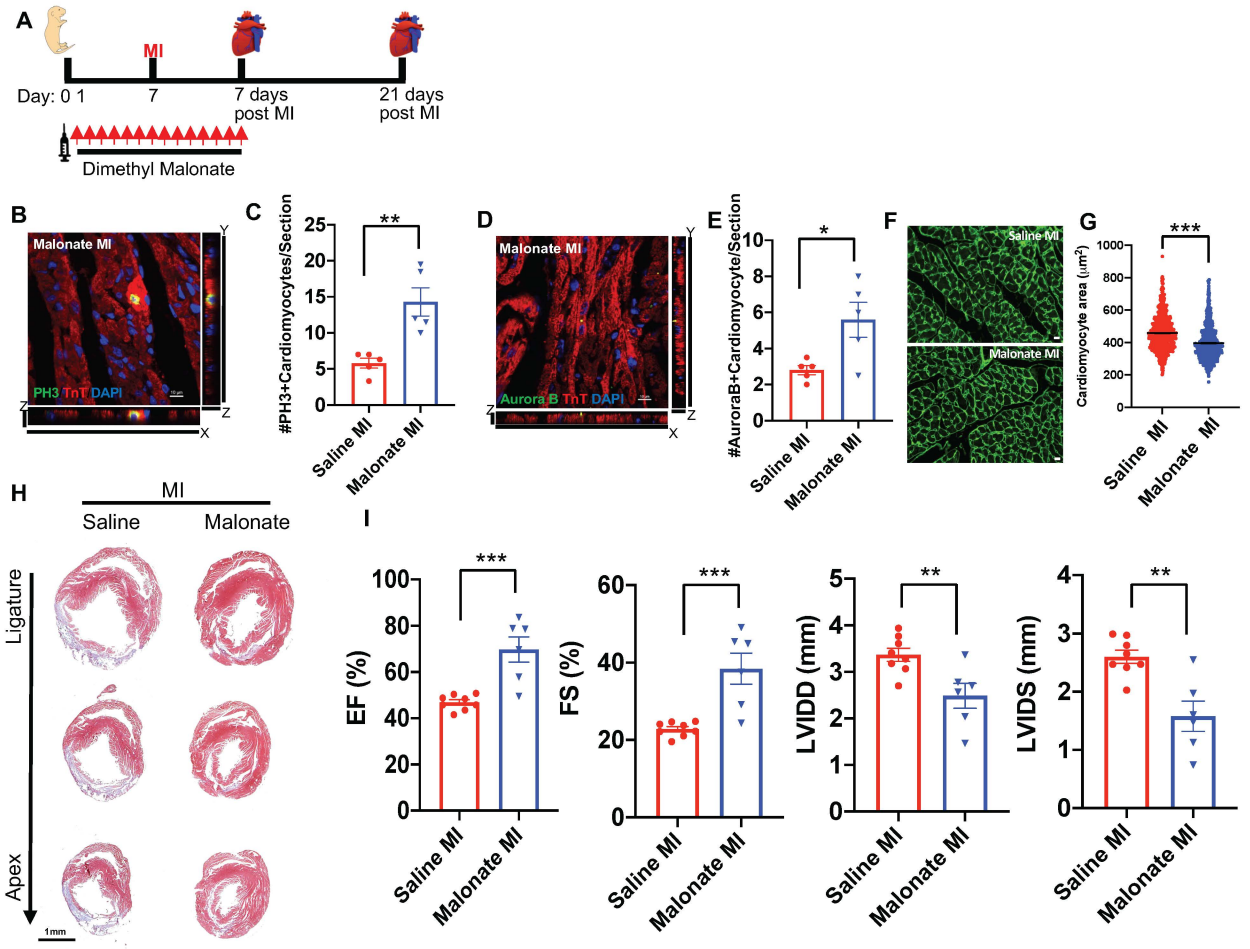

Figure 2. Malonate promotes cardiomyocyte proliferation and heart regeneration in the postnatal heart following MI. (A) Schematic of dimethyl malonate injection and MI strategy. (B, C) Immunostaining and quantification of pH3 positive cardiomyocytes showing a significant increase in the levels of mitotic myocytes in dimethyl malonate injected hearts at 7 days post-MI compared to controls. Scale bar, 10 µm. (D, E) Immunostaining and quantification of Aurora B positive cardiomyocytes demonstrating a significant increase in myocyte cytokinesis in the dimethyl malonate injected mice. Scale bar, 10 µm. (F, G) Wheat germ agglutinin (WGA) staining and cell size quantification showing decrease in the cardiomyocyte size in malonate injected hearts at 21 days post-MI. Quantitative analyses represent counting of multiple fields from

independent samples per group (~ 700 cells per group). Scale bar, 10 μm. (H) Trichrome staining of malonate injected hearts at 21 days post-MI at P7, showing complete regeneration in dimethyl malonate injected mice compared to control. Scale bar, 1 mm. (I) Left ventricular systolic function quantified by EF, FS, LVIDD and LVIDS at 3 weeks post-MI demonstrating functional recovery in dimethyl malonate injected MI hearts compared to the saline injected controls. (n=5-8 mice per group). *P< 0.05, **P<0.005, ***P<0.0001 by Student's t-test.

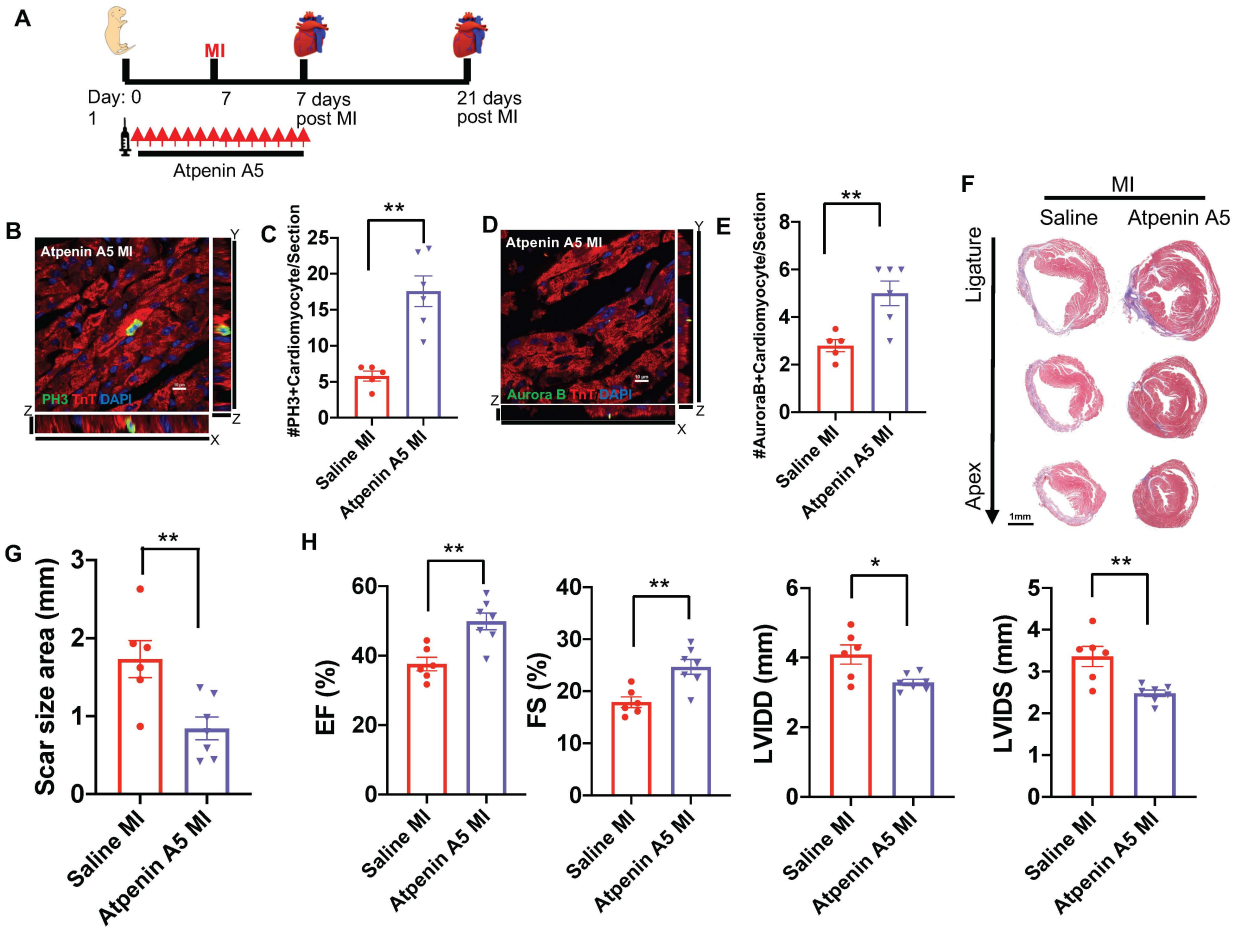

Figure 3. SDH inhibition by Atpenin A5 promotes cardiomyocyte mitosis and regeneration in the postnatal heart following MI. (A) Schematic of Atpenin A5 injection and MI strategy. (B) Z-stack confocal image of a mitotic cardiomyocyte stained with pH3 and cTnT. Scale bar, 10 µm. (C) Quantification of mitotic cardiomyocytes showing a significant increase in the number of mitotic cardiomyocytes in Atpenin A5 injected mice at 7 days post-MI compared to controls. (D) Z-stack confocal image of an Aurora B positive cardiomyocyte. Scale bar, 10 µm. (E) Quantification of cardiomyocytes undergoing cytokinesis showing a significant increase in the number of cardiomyocytes in cytokinesis in Atpenin A5 injected mice at 7 days post-MI compared to controls. (F) Trichrome staining of Atpenin A5 injected mice at 3 weeks post-MI at P7

demonstrating myocardial regeneration and a significant reduction in scar size in Atpenin A5 injected mice compared to controls. Scale bar, 1 mm. (G) Quantification of scar size by ImageJ software from serial sections from ligature to apex. (H) Echocardiography measurements of EF, FS, LVIDD and LVIDS at 3 weeks post-MI showing restoration of cardiac function in Atpenin A5 injected mice compared to controls. (n=6-8 mice per group). *P< 0.05, **P<0.005 by Student's t-test.

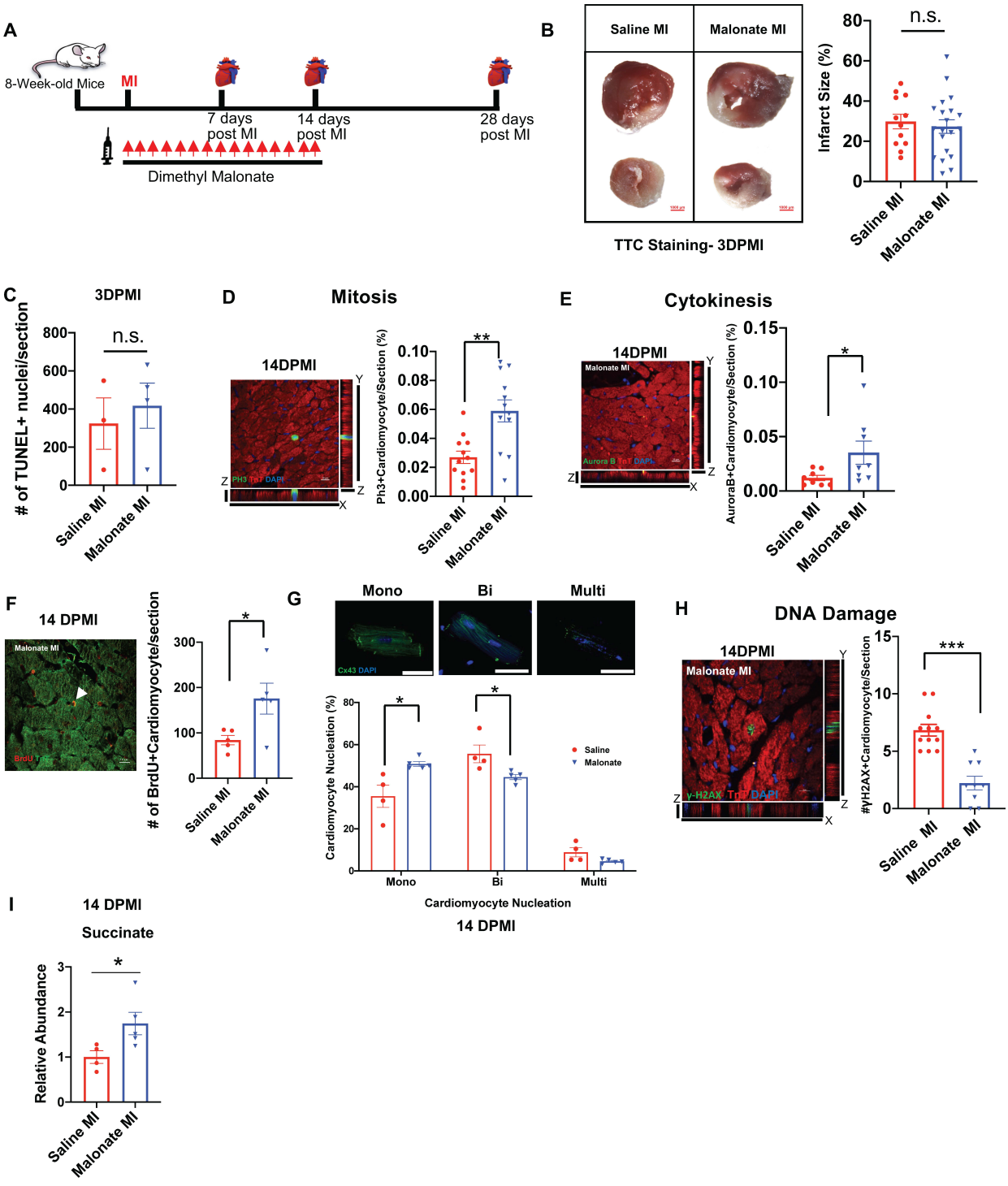

Figure 4. Malonate promotes adult cardiomyocyte proliferation following MI. (A) Schematic of dimethyl malonate injection following adult MI. (B) TTC viability stain and quantification showing no significant difference in myocardial necrosis (white) in both saline and dimethyl malonate

injected mice at 3 days post-MI (DPMI). Scale bar, 1 mm. (C) Quantification of TUNEL positive cardiomyocytes demonstrating no significant difference between TUNEL positive myocytes in saline and malonate injected mice at 3 days post-MI. (D) Z-stack confocal image of a pH3 positive cardiomyocyte at 14-days post-MI. Scale bar, 10 μm. Quantification of the percentage of pH3 positive cardiomyocytes showing a significant increase in the numbers of mitotic cardiomyocytes in dimethyl malonate injected hearts at 14-days post-MI compared to controls. (E) Z-stack confocal image of an Aurora B positive cardiomyocyte at 14-days post-MI. Scale bar, 10 μm. Quantification of the percentage of Aurora B positive cardiomyocytes demonstrating a significant increase in the numbers of cardiomyocytes undergoing cytokinesis in dimethyl malonate injected hearts at 14-days post-MI compared to controls. (F) Representative image and quantification of BrdU positive cardiomyocytes demonstrating a significant increase in BrdU positive cardiomyocytes at 14 days post-MI in malonate-treated mice. Scale bar, 10 μm. (G) Cardiomyocyte nucleation staining with connexin 43 (Cx43) and DAPI and quantification at 14 days post-MI demonstrating a significant increase in mononucleated cardiomyocytes as well as a significant decrease in binucleated cardiomyocytes following malonate treatment. Scale bar, 50 μm. (H) Immunostaining and quantification of the DNA double-strand breaks marker γH2AX demonstrating a significant decrease in DNA damage in malonate-treated mice compared to controls. Scale bar, 10 μm. (I) Relative intracellular abundance of succinate showing a significant increase in succinate levels in malonate-treated mice at 14 days post-MI (n=3-6 mice per group). *P< 0.05, ***P<0.0001 by Student's t-test. N.s. indicates not significant.

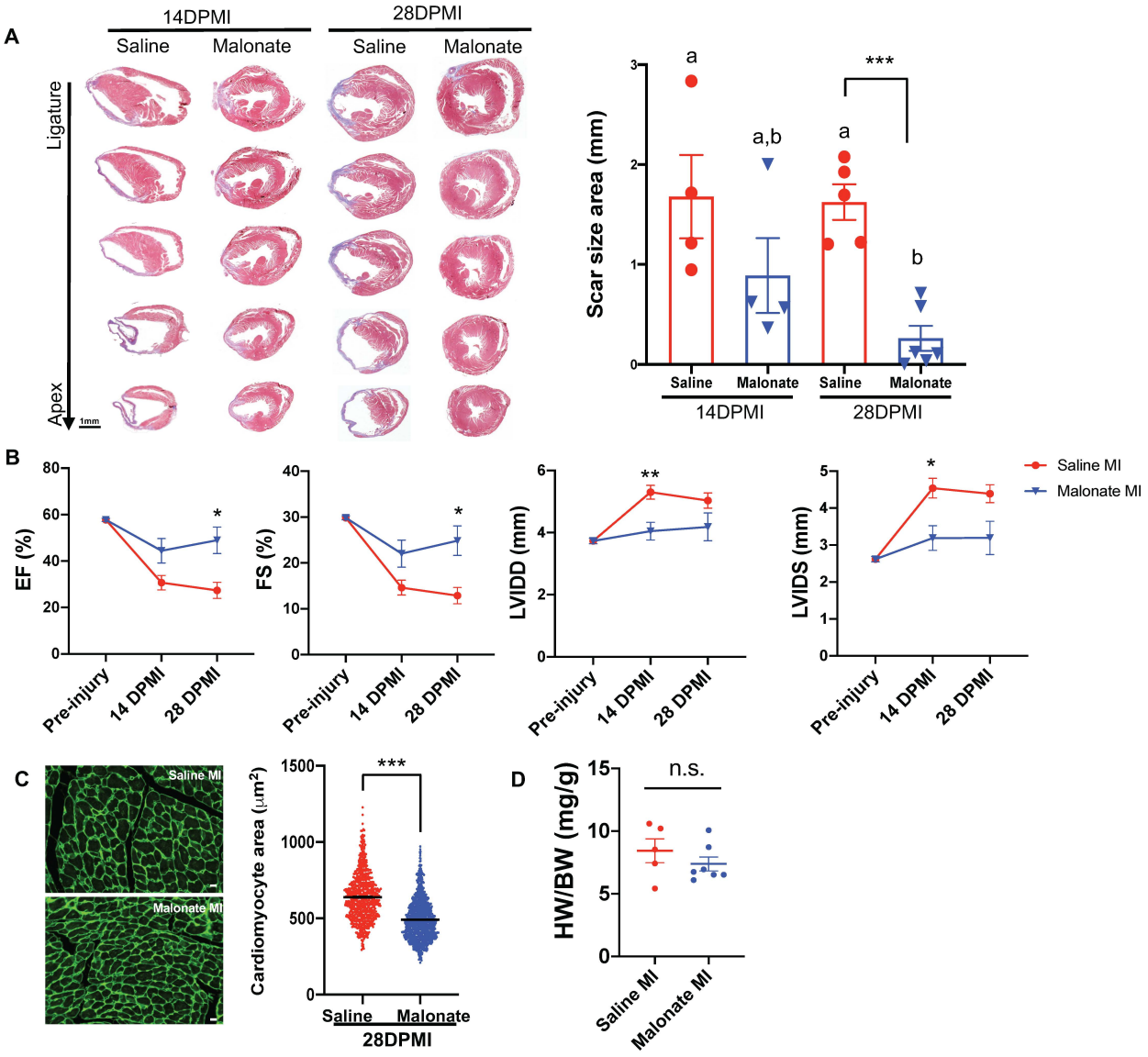

Figure 5. Malonate restores cardiac structure and function following adult MI. (A) Trichrome staining of heart sections from saline and dimethyl malonate-injected mice at 14 and 28 days following adult MI, showing restoration of cardiac structure and no fibrotic scarring by 28 days post-MI in dimethyl malonate injected mice. Quantification of scar size demonstrating a significant reduction in fibrosis in dimethyl malonate treated mice at 28 days post-MI. (B) Echocardiography of cardiac function measured by EF, FS, LVIDD and LVIDS at 14- and 28-days post-MI showing a significant functional recovery in dimethyl malonate injected hearts compared

to saline injected controls at 28 days post-MI. (C) Wheat germ agglutinin (WGA) staining and cell size quantification showing decrease in cardiomyocyte size in dimethyl malonate injected hearts at 4 weeks post-MI. Quantitative analyses represent counting of multiple fields from 5-6 independent samples per group (750 ~ 1000 cells per group). Scale bar, 10 μm. (D) Heart weight-to-body weight ratios at 28 days post-MI showing no significant difference between saline and malonate injected mice. (n=5-6 mice per group). *P< 0.05, **P< 0.005, ***P<0.0001 by Student's *t*-test. One-way ANOVA was performed by Tukey's multiple comparison test to determine the differences of group mean among treatment groups. Different letters indicate significant differences among groups. N.s. indicates not significant.

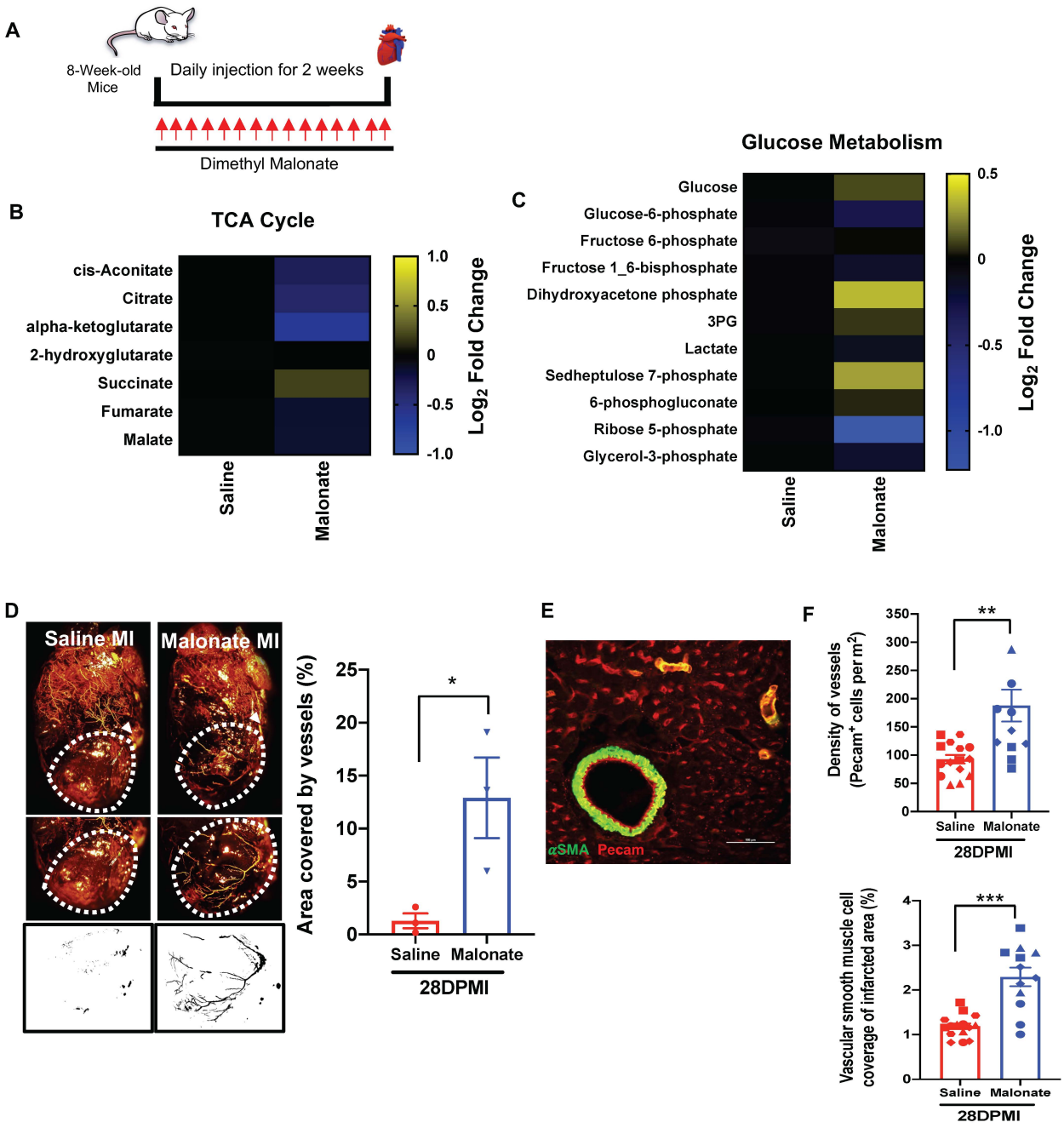

Figure 6. Malonate induces a dynamic metabolic shift in the adult heart and promotes revascularization following MI. (A) Schematic of malonate administration for metabolomics. (B & C) Metabolomic changes of tricarboxylic acid (TCA) cycle and glucose metabolism in saline and malonate treated mice at 14 days following treatment. Relative abundance of metabolites in malonate-treated mice is compared to saline-treated mice and presented as a heatmap on a $\log_2$

scale demonstrating a dynamic metabolic shift from oxidative phosphorylation to glucose metabolism in malonate-treated mice. (D) Coronary vessel casting by MICROFIL injection at 28 days post-MI showing a significant increase in revascularization of the infarct zone in malonate-treated mice compared to controls. Quantification of vasculature in region of interest (ROI) by analyzing binarized images for grey level intensity by ImageJ demonstrating a significant increase in vascular density in the infarct zone. (E) Immunostaining with the endothelial marker PECAM and vascular smooth muscle cell marker α-SMA. Scale bar, 100 μm. (F) Quantification of vascular lineages demonstrating a significant increase in endothelial capillary density and vascular smooth muscle cells in the infarct zone at 28 days post-MI. (n=3-4 mice per group). *P< 0.05, **P<0.005, ***P<0.0001 by Student's t-test.

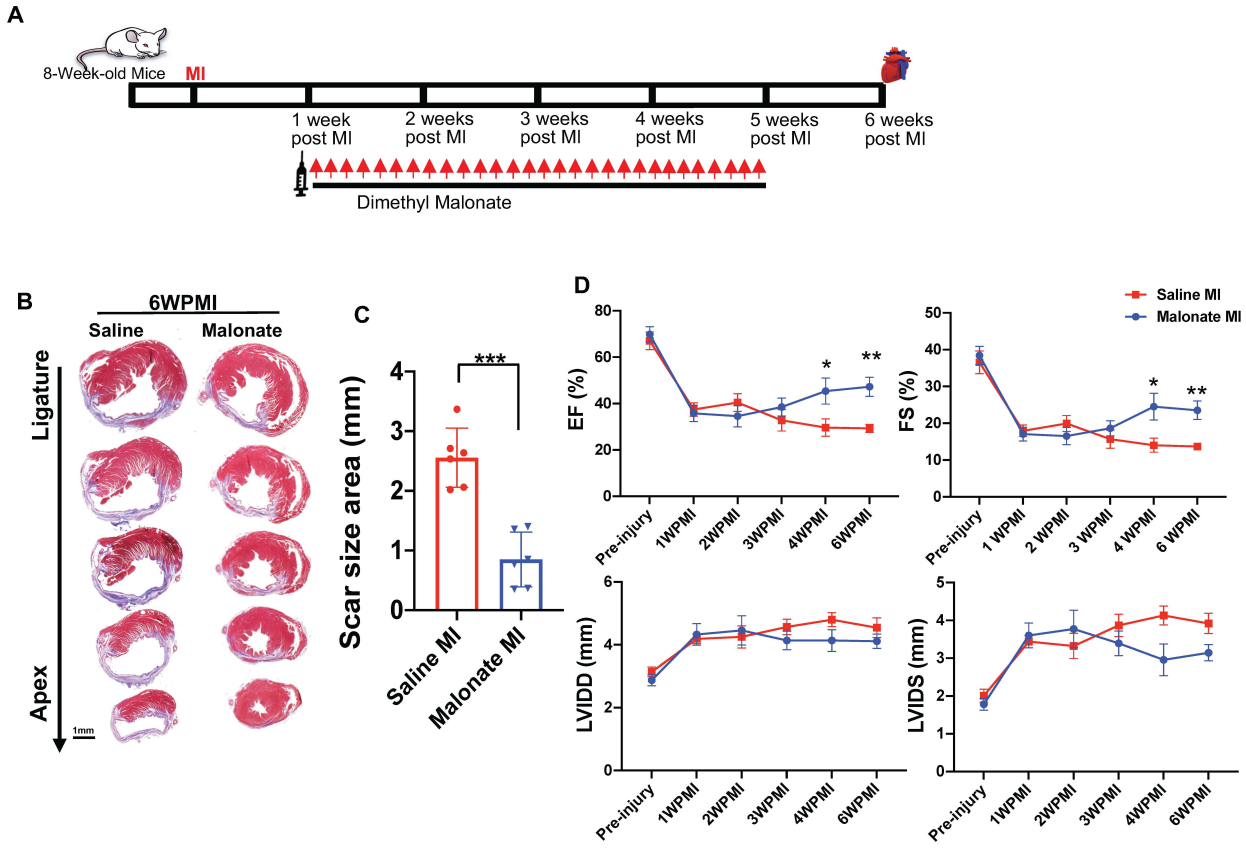

Figure 7. Malonate treatment starting 1-week post-MI promotes myocardial regeneration. (A) Schematic of malonate injection and MI strategy. (B) Trichrome staining of heart sections from saline and malonate-injected mice at 6 weeks post-MI. (C) Scar size quantification by ImageJ from serial sections per heart showing a significant reduction in scar size in malonate treated mice at 6 weeks post-MI. (D) Serial echocardiography measurements of EF, FS, LVID, LVIDS showing significant functional recovery in malonate-injected mice over time compared to controls. (n=6 mice per group). *P< 0.05, **P<0.005, ***P<0.0001 by Student's t-test.

SUPPLEMENTAL MATERIALS

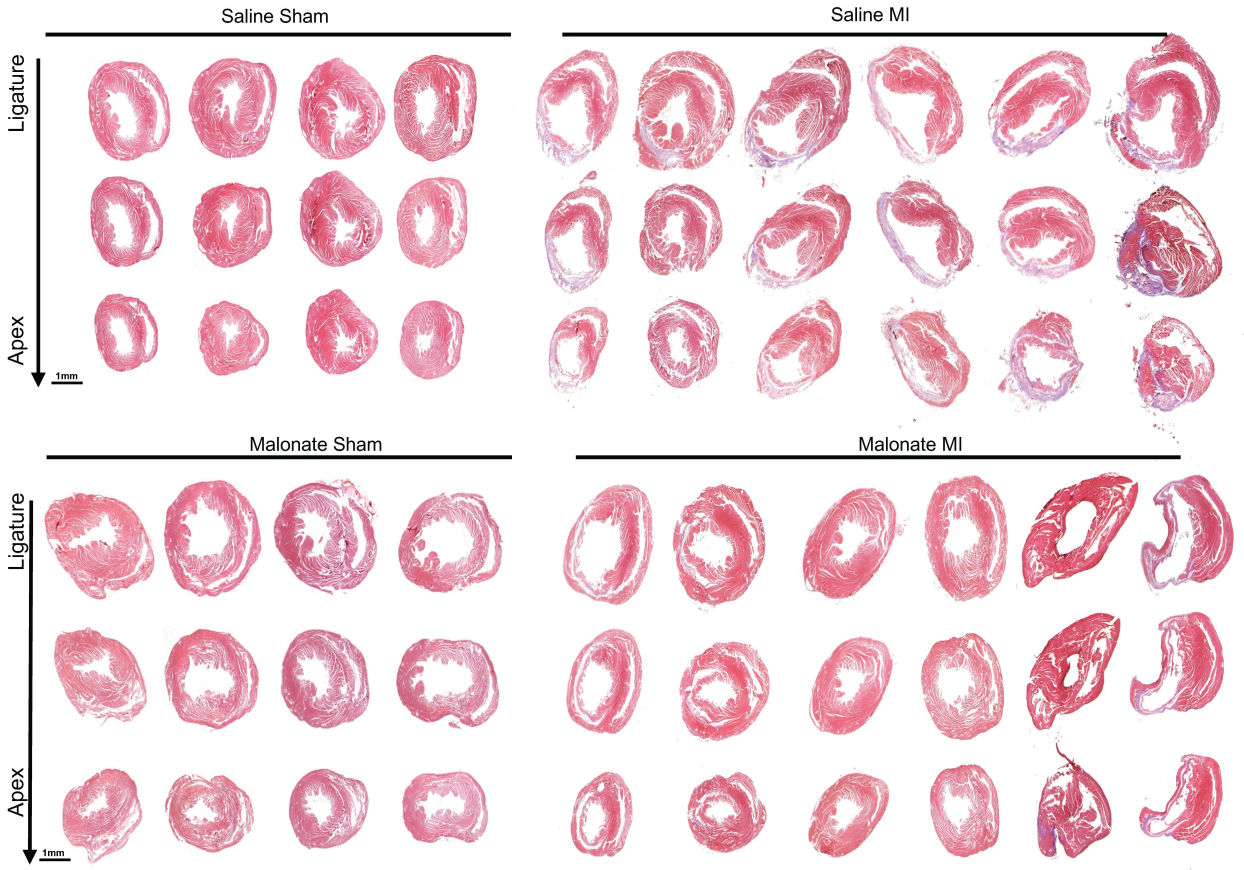

Supplemental Figure I. Masson's trichrome-stained heart sections of saline or malonate injected mice at 21 days post sham or MI surgery performed at P7. Serial sections were cut from the site of the ligature to the apex. All hearts are shown.

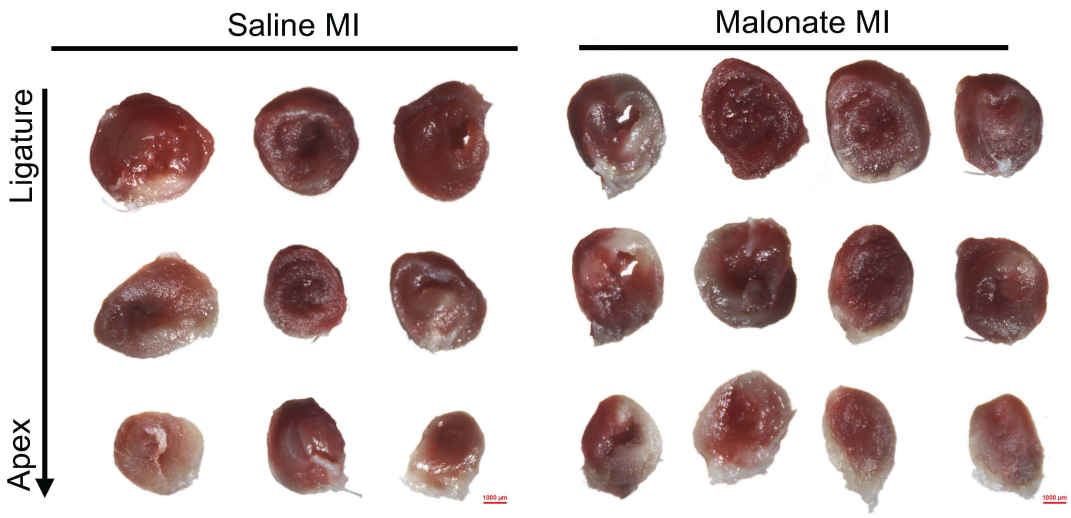

Supplemental Figure II. Triphenyl tetrazolium chloride (TTC) of fresh hearts from saline or malonate injected adult mice at 3 days post MI. All hearts are shown.

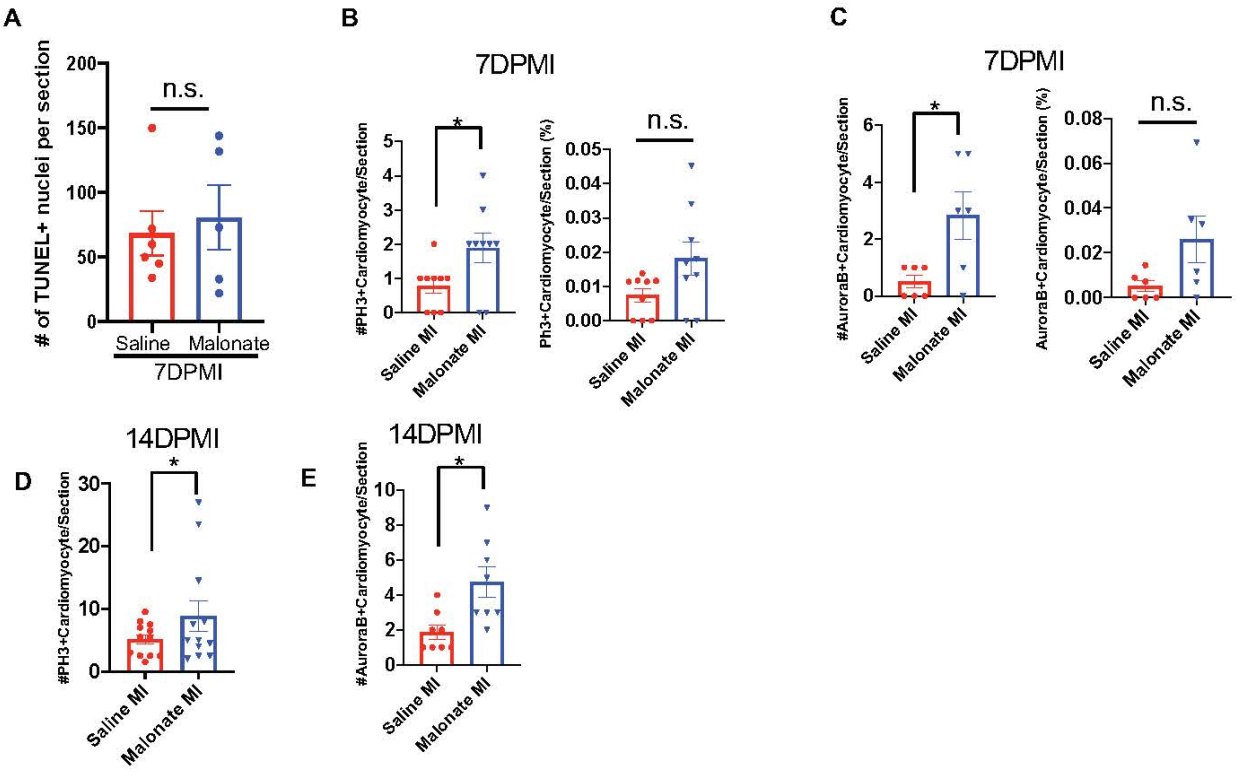

Supplemental Figure III. Quantification of immunostaining of paraffin heart sections from saline and malonate injected mice at 7 and 14 days post adult MI. Quantification of (A) TUNEL positive nuclei (B) PH3 positive cardiomyocyte (C) Aurora B positive cardiomyocyte at 7 days post MI. Quantification of number of (D) PH3 and (E) Aurora B positive cardiomyocyte at 14 days post MI per section.

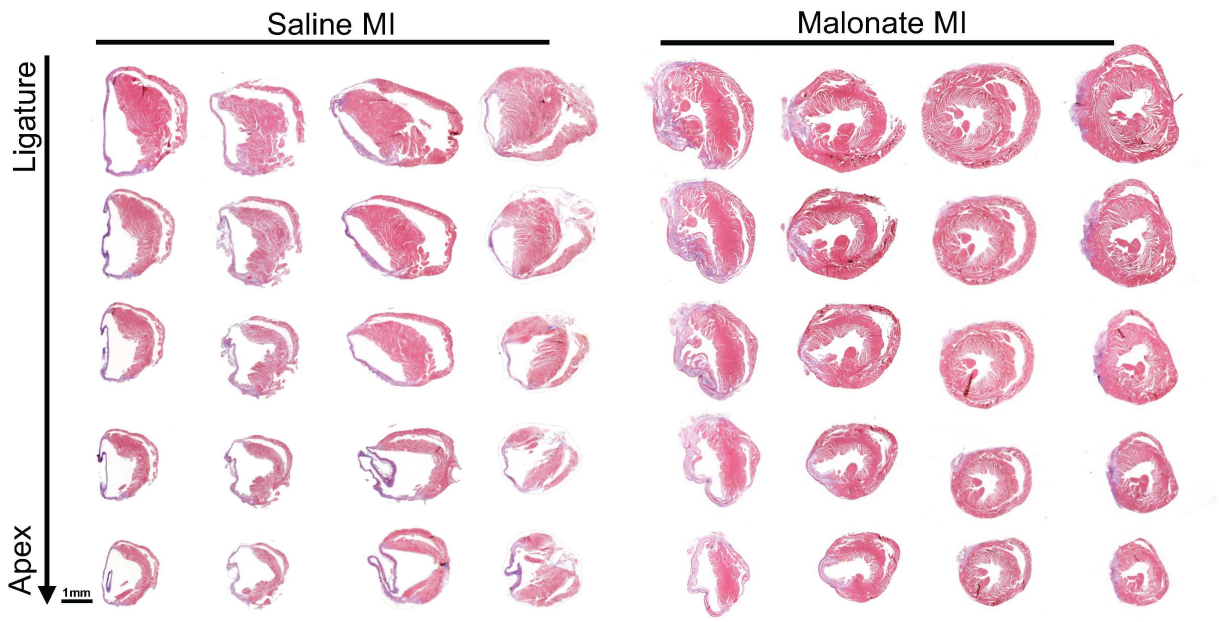

Supplemental Figure IV. Masson's trichrome-stained heart sections of saline or malonate injected mice at 14 days post MI performed at 8 weeks old. Serial sections were cut from the site of the ligature to the apex. All hearts are shown.

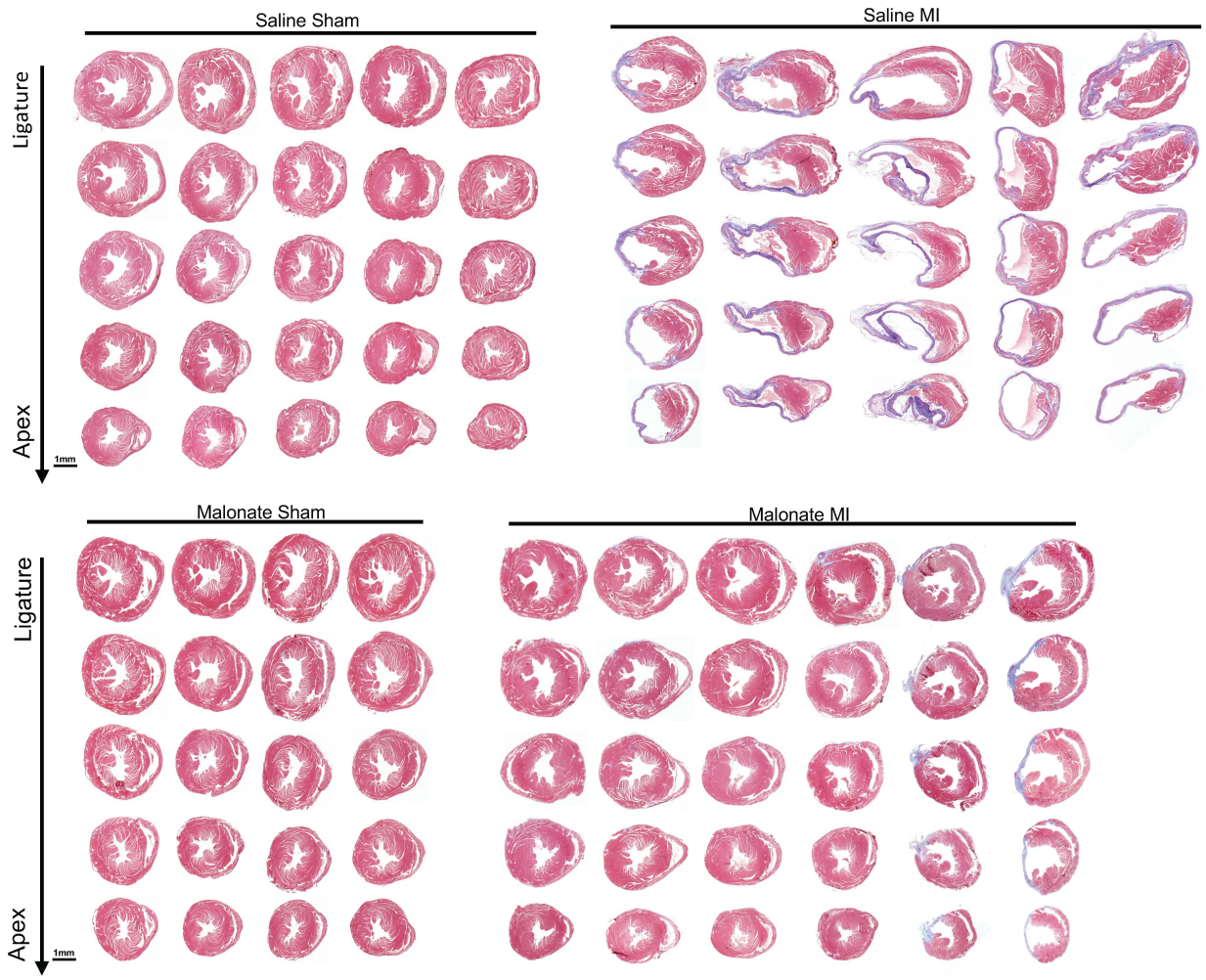

Supplemental Figure V. Masson's trichrome-stained heart sections of saline or malonate injected mice for 14 days post-MI, harvested at 28 days post MI. Serial sections were cut from the site of the ligature to the apex. All hearts are shown.

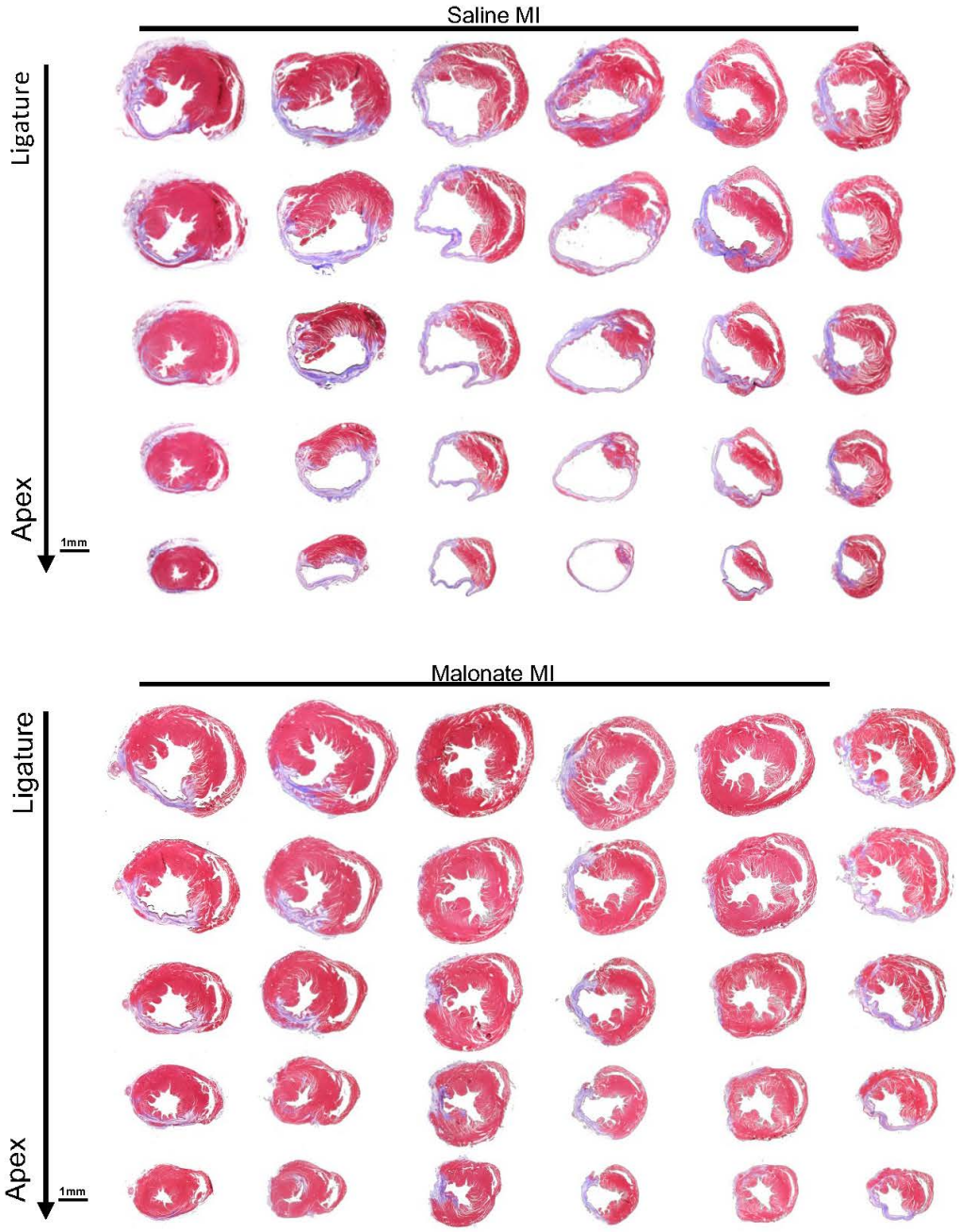

Supplemental Figure VI. Masson's trichrome-stained heart sections of saline or malonate injected mice at 1-week post-MI, hearts harvested at 6 weeks post-MI. Serial sections were cut from the site of the ligature to the apex. All hearts are shown.

REFERENCES

1. Virani SS, Alonso A, Benjamin EJ, Bittencourt MS, Callaway CW, Carson AP, Chamberlain AM, Chang AR, Cheng S, Delling FN, Djousse L, Elkind MSV, Ferguson JF, Fornage M, Khan SS, Kissela BM, Knutson KL, Kwan TW, Lackland DT, Lewis TT, Lichtman JH, Longenecker CT, Loop MS, Lutsey PL, Martin SS, Matsushita K, Moran AE, Mussolino ME, Perak AM, Rosamond WD, Roth GA, Sampson UKA, Satou GM, Schroeder EB, Shah SH, Shay CM, Spartano NL, Stokes A, Tirschwell DL, VanWagner LB, Tsao CW, American Heart Association Council on E, Prevention Statistics C and Stroke Statistics S. Heart Disease and Stroke Statistics-2020 Update: A Report From the American Heart Association. *Circulation*. 2020;141:e139-e596.
2. Mahmoud AI, Porrello ER, Kimura W, Olson EN and Sadek HA. Surgical models for cardiac regeneration in neonatal mice. *Nature protocols*. 2014;9:305-11.
3. Porrello ER, Mahmoud AI, Simpson E, Hill JA, Richardson JA, Olson EN and Sadek HA. Transient regenerative potential of the neonatal mouse heart. *Science*. 2011;331:1078-80.
4. Porrello ER, Mahmoud AI, Simpson E, Johnson BA, Grinsfelder D, Canseco D, Mammen PP, Rothermel BA, Olson EN and Sadek HA. Regulation of neonatal and adult mammalian heart regeneration by the miR-15 family. *Proceedings of the National Academy of Sciences of the United States of America*. 2013;110:187-92.
5. Webster WS and Abela D. The effect of hypoxia in development. *Birth Defects Res C Embryo Today*. 2007;81:215-28.
6. Puente BN, Kimura W, Muralidhar SA, Moon J, Amatruda JF, Phelps KL, Grinsfelder D, Rothermel BA, Chen R, Garcia JA, Santos CX, Thet S, Mori E, Kinter MT, Rindler PM, Zacchigna S, Mukherjee S, Chen DJ, Mahmoud AI, Giacca M, Rabinovitch PS, Aroumougame A, Shah AM, Szweda LI and Sadek HA. The oxygen-rich postnatal environment induces cardiomyocyte cell-cycle arrest through DNA damage response. *Cell*. 2014;157:565-79.
7. Chouchani ET, Pell VR, Gaude E, Aksentijevic D, Sundier SY, Robb EL, Logan A, Nadtochiy SM, Ord ENJ, Smith AC, Eyassu F, Shirley R, Hu CH, Dare AJ, James AM, Rogatti S, Hartley RC, Eaton S, Costa ASH, Brookes PS, Davidson SM, Duchen MR, Saeb-Parsy K, Shattock MJ, Robinson AJ, Work LM, Frezza C, Krieg T and Murphy MP. Ischaemic accumulation of succinate controls reperfusion injury through mitochondrial ROS. *Nature*. 2014;515:431-435.
8. Hochachka PW and Dressendorfer RH. Succinate accumulation in man during exercise. *Eur J Appl Physiol Occup Physiol*. 1976;35:235-42.
9. Zhang J, Wang YT, Miller JH, Day MM, Munger JC and Brookes PS. Accumulation of Succinate in Cardiac Ischemia Primarily Occurs via Canonical Krebs Cycle Activity. *Cell Rep*. 2018;23:2617-2628.
10. King A, Selak MA and Gottlieb E. Succinate dehydrogenase and fumarate hydratase: linking mitochondrial dysfunction and cancer. *Oncogene*. 2006;25:4675-82.
11. Kula-Alwar D, Prag HA and Krieg T. Targeting Succinate Metabolism in Ischemia/Reperfusion Injury. *Circulation*. 2019;140:1968-1970.
12. Valls-Lacalle L, Barba I, Miro-Casas E, Ruiz-Meana M, Rodriguez-Sinovas A and Garcia-Dorado D. Selective Inhibition of Succinate Dehydrogenase in Reperfused Myocardium with Intracoronary Malonate Reduces Infarct Size. *Sci Rep*. 2018;8:2442.
13. Gottlieb E and Tomlinson IP. Mitochondrial tumour suppressors: a genetic and biochemical update. *Nat Rev Cancer*. 2005;5:857-66.

14. Her YF and Maher LJ, 3rd. Succinate Dehydrogenase Loss in Familial Paraganglioma: Biochemistry, Genetics, and Epigenetics. *Int J Endocrinol*. 2015;2015:296167.
15. Tseng PL, Wu WH, Hu TH, Chen CW, Cheng HC, Li CF, Tsai WH, Tsai HJ, Hsieh MC, Chuang JH and Chang WT. Decreased succinate dehydrogenase B in human hepatocellular carcinoma accelerates tumor malignancy by inducing the Warburg effect. *Sci Rep*. 2018;8:3081.
16. Honkoop H, de Bakker DE, Aharonov A, Kruse F, Shakked A, Nguyen PD, de Heus C, Garric L, Muraro MJ, Shoffner A, Tessadori F, Peterson JC, Noort W, Bertozzi A, Weidinger G, Posthuma G, Grun D, van der Laarse WJ, Klumperman J, Jaspers RT, Poss KD, van Oudenaarden A, Tzahor E and Bakkers J. Single-cell analysis uncovers that metabolic reprogramming by ErbB2 signaling is essential for cardiomyocyte proliferation in the regenerating heart. *Elife*. 2019;8.
17. Kumar D, Hacker TA, Buck J, Whitesell LF, Kaji EH, Douglas PS and Kamp TJ. Distinct mouse coronary anatomy and myocardial infarction consequent to ligation. *Coron Artery Dis*. 2005;16:41-4.
18. Singla DK, Hacker TA, Ma L, Douglas PS, Sullivan R, Lyons GE and Kamp TJ. Transplantation of embryonic stem cells into the infarcted mouse heart: formation of multiple cell types. *J Mol Cell Cardiol*. 2006;40:195-200.
19. Seim GL, John SV and Fan J. Metabolomic and Lipidomic Analysis of Bone Marrow Derived Macrophages. *Bio-protocol*. 2020;10:e3693.
20. Harris SP, Bartley CR, Hacker TA, McDonald KS, Douglas PS, Greaser ML, Powers PA and Moss RL. Hypertrophic cardiomyopathy in cardiac myosin binding protein-C knockout mice. *Circ Res*. 2002;90:594-601.
21. Mahmoud AI, Kocabas F, Muralidhar SA, Kimura W, Koura AS, Thet S, Porrello ER and Sadek HA. Meis1 regulates postnatal cardiomyocyte cell cycle arrest. *Nature*. 2013;497:249-253.
22. Miyadera H, Shiomi K, Ui H, Yamaguchi Y, Masuma R, Tomoda H, Miyoshi H, Osanai A, Kita K and Omura S. Atpenins, potent and specific inhibitors of mitochondrial complex II (succinate-ubiquinone oxidoreductase). *Proceedings of the National Academy of Sciences of the United States of America*. 2003;100:473-7.
23. Letouze E, Martinelli C, Loriot C, Burnichon N, Abermil N, Ottolenghi C, Janin M, Menara M, Nguyen AT, Benit P, Buffet A, Marcaillou C, Bertherat J, Amar L, Rustin P, De Reynies A, Gimenez-Roqueplo AP and Favier J. SDH mutations establish a hypermethylator phenotype in paraganglioma. *Cancer Cell*. 2013;23:739-52.
24. Pollard PJ, Briere JJ, Alam NA, Barwell J, Barclay E, Wortham NC, Hunt T, Mitchell M, Olpin S, Moat SJ, Hargreaves IP, Heales SJ, Chung YL, Griffiths JR, Dalgleish A, McGrath JA, Gleeson MJ, Hodgson SV, Poulsom R, Rustin P and Tomlinson IP. Accumulation of Krebs cycle intermediates and over-expression of HIF1alpha in tumours which result from germline FH and SDH mutations. *Hum Mol Genet*. 2005;14:2231-9.
25. Sciacovelli M, Guzzo G, Morello V, Frezza C, Zheng L, Nannini N, Calabrese F, Laudiero G, Esposito F, Landriscina M, Defilippi P, Bernardi P and Rasola A. The mitochondrial chaperone TRAP1 promotes neoplastic growth by inhibiting succinate dehydrogenase. *Cell Metab*. 2013;17:988-999.
26. Bryant DM, O'Meara CC, Ho NN, Gannon J, Cai L and Lee RT. A systematic analysis of neonatal mouse heart regeneration after apical resection. *J Mol Cell Cardiol*. 2015;79:315-8.

27. Das S, Goldstone AB, Wang H, Farry J, D'Amato G, Paulsen MJ, Eskandari A, Hironaka CE, Phansalkar R, Sharma B, Rhee S, Shamskhou EA, Agalliu D, de Jesus Perez V, Woo YJ and Red-Horse K. A Unique Collateral Artery Development Program Promotes Neonatal Heart Regeneration. *Cell*. 2019;176:1128-1142 e18.
28. De Bock K, Georgiadou M, Schoors S, Kuchnio A, Wong BW, Cantelmo AR, Quaegebeur A, Ghesquiere B, Cauwenberghs S, Eelen G, Phng LK, Betz I, Tembuyser B, Brepoels K, Welti J, Geudens I, Segura I, Cruys B, Bifari F, Decimo I, Blanco R, Wyns S, Vangindertael J, Rocha S, Collins RT, Munck S, Daelemans D, Imamura H, Devlieger R, Rider M, Van Veldhoven PP, Schuit F, Bartrons R, Hofkens J, Fraisl P, Telang S, Deberardinis RJ, Schoonjans L, Vinckier S, Chesney J, Gerhardt H, Dewerchin M and Carmeliet P. Role of PFKFB3-driven glycolysis in vessel sprouting. *Cell*. 2013;154:651-63.
29. Eelen G, de Zeeuw P, Simons M and Carmeliet P. Endothelial cell metabolism in normal and diseased vasculature. *Circ Res*. 2015;116:1231-44.
30. Sadek H and Olson EN. Toward the Goal of Human Heart Regeneration. *Cell Stem Cell*. 2020;26:7-16.
31. Knobloch M, Pilz GA, Ghesquiere B, Kovacs WJ, Wegleiter T, Moore DL, Hruzova M, Zamboni N, Carmeliet P and Jessberger S. A Fatty Acid Oxidation-Dependent Metabolic Shift Regulates Adult Neural Stem Cell Activity. *Cell Rep*. 2017;20:2144-2155.
32. Kelly B and O'Neill LA. Metabolic reprogramming in macrophages and dendritic cells in innate immunity. *Cell Res*. 2015;25:771-84.
33. Seim GL, Britt EC, John SV, Yeo FJ, Johnson AR, Eisenstein RS, Pagliarini DJ and Fan J. Two-stage metabolic remodelling in macrophages in response to lipopolysaccharide and interferon-γ stimulation. *Nature Metabolism*. 2019;1:731-742.
34. Mills EL, Kelly B, Logan A, Costa ASH, Varma M, Bryant CE, Tourlomousis P, Dabritz JHM, Gottlieb E, Latorre I, Corr SC, McManus G, Ryan D, Jacobs HT, Szibor M, Xavier RJ, Braun T, Frezza C, Murphy MP and O'Neill LA. Succinate Dehydrogenase Supports Metabolic Repurposing of Mitochondria to Drive Inflammatory Macrophages. *Cell*. 2016;167:457-470 e13.
35. Kaelin WG, Jr. and McKnight SL. Influence of metabolism on epigenetics and disease. *Cell*. 2013;153:56-69.

FUNDING

Funding for this project was provided by the UW School of Medicine and Public Health from the Wisconsin Partnership Program (A.I.M.), an American Heart Association Career Development Award 19CDA34660169 (A.I.M.), NIH/NCATS through CTSA award UL1TR002373 to the UW Institute for Clinical and Translational Research, a postdoctoral training award from the Stem Cell & Regenerative Medicine Center at UW-Madison (J.B.) and NIH/NHLBI under Ruth L. Kirschstein NRSA T32 HL007936 to the UW Cardiovascular Research Center (J.B.).

CHAPTER VI: CONCLUSIONS AND FUTURE DIRECTIONS

Rebecca J. Salamon[1]

[1]Department of Cell and Regenerative Biology, School of Medicine and Public Health, University of Wisconsin-Madison, Madison, Wisconsin, USA

Summary of Findings

The work outlined in this thesis highlights important findings about the pathways and patterns regulating cardiac development, disease, and regeneration. Our technological advances set the stage to investigate the architecture and remodeling of the intact cardiovascular system at high resolution. Our additional studies focused on identifying mechanisms underpinning cardiac regeneration. These advances and findings have direct clinical implications for understanding proper heart development, as well as promoting endogenous cardiac regeneration after injury.

In Chapter II, we detailed the generation of our methodology to analyze the heart in 3D. Our pipeline utilized lineage tracing, tissue clearing, and whole-mount imaging to analyze the intact heart. This involved the modification of a tissue clearing protocol (passive CLARITY) that was compatible with the mouse heart, ranging from postnatal to adult stages. Furthermore, our tissue clearing method is compatible with endogenous reporters and immunostaining techniques, permitting multiple cell types to be labeled within the same intact tissue. This expanded our ability to explore cell-cell patterning and interactions occurring *in vivo*.

In Chapter III, we analyzed the intact, mammalian cardiac nervous system and neurovascular network in high resolution using our tissue clearing, whole-mount staining, and 3D analysis pipeline. Parasympathetic nerves are known to innervate the cardiac ventricles[1-3], but to what degree and their architecture remained largely unknown. Our results identified extensive parasympathetic innervation in the murine cardiac ventricles. We further detailed a novel phenotype where parasympathetic and sympathetic axons are intertwined throughout the

ventricles. The cardiac axons also showed a close association to the coronary arteries during embryonic development. We used this knowledge as a basis to identify nerve remodeling in diseased and regenerative settings. In the regenerating neonatal mouse heart, we demonstrated that precise reinnervation occurs following injury, in stark contrast to the non-regenerating heart. Remarkably, the regenerated ventricles had reestablished parasympathetic and sympathetic axon bundling. Mechanistically, we demonstrated that this neuroplasticity is dependent on collateral artery formation, which precedes reinnervation during regeneration. These discoveries provided evidence that the process of physiological reinnervation occurs uniquely during neonatal mouse heart regeneration.

In Chapter IV, we demonstrated the power of leveraging the cellular metabolic state to promote adult mammalian cardiac regeneration. During development, neonatal mouse cardiomyocytes undergo a metabolic shift from glycolysis to oxidative phosphorylation. This metabolic shift directly contributes to cardiomyocyte cell cycle arrest and the loss of regenerative capacity in the heart[4]. We explored the role of the mitochondrial metabolite succinate and its enzyme, succinate dehydrogenase (SDH), in regulating cardiomyocyte metabolism and cell cycle activity. We showed that succinate injection inhibits cardiomyocyte proliferation and regeneration in neonatal mice. Inversely and importantly, SDH inhibition by malonate treatment promotes a robust regenerative response in the adult mouse heart following myocardial infarction injury. Malonate treatment results in dynamic changes in adult cardiac metabolism, suggesting that SDH inhibition promotes metabolic reprogramming that ultimately enhances cardiac regeneration. These findings offer a potential therapeutic strategy for treating heart failure.

In Chapter V, we explored a role for the cardiac-specific protein, Leucine-rich repeat containing 10 (LRRC10) in neonatal mouse heart regeneration. Recent discoveries indicated that LRRC10 is crucial for cardiac regeneration in fish models. However, it was unclear whether this finding extends to a mammalian model. Our research found that *Lrrc10* knockout mice lack the regenerative response of neonatal mice, marked by decreased cardiomyocyte cytokinesis and increased cardiomyocyte nucleation. We also demonstrated that this is due to LRRC10's unique capacity to regulate cardiomyocyte cytokinesis, rather than mitosis, throughout neonatal mouse heart regeneration. Our discoveries highlight LRRC10's new role in regulating cardiomyocyte cytokinesis after birth and reshaping the transcriptional landscape during mammalian heart regeneration.

Taken together, these findings provide insight into the patterns and processes underpinning heart development, disease, and repair. Identifying mechanisms unique to neonatal heart regeneration has an enormous therapeutic potential for the treatment of heart failure. Clinical translation will require a detailed understanding of proper heart development, as well as the processes facilitating physiological repair in the regenerating neonatal mouse heart. These studies provide important findings that serve as a basis to identify pathways and molecular targets that can reawaken the regenerative response in the adult heart after injury.

Future Directions

We identified several aspects of heart development and repair, opening a variety of avenues for future research. Two seminal findings, first the identification of dense parasympathetic innervation of the cardiac ventricles, and second the process of physiological reinnervation in the regenerated heart (see Chapter III), elicits a wealth of exciting questions for future studies that will be discussed here. Continued investigation of these elements will provide insight into the development, maintenance, and repair of parasympathetic innervation in the cardiac ventricles.

The recruitment of parasympathetic axons into the developing ventricles.

Our research showed that the parasympathetic and sympathetic axons are intertwined within the ventricles. This patterning is the result of synchronous axon extension during cardiac development. The mechanism of coordinated parasympathetic and sympathetic axon extension during development remains to be elucidated. The synchroneity of axon extension is interesting, as the axon subtypes are thought to be attracted or repelled by different neurotrophic factors (see Chapter I). This opens two non-mutually exclusive possibilities: (1) identical neurotrophic factors can influence both parasympathetic and sympathetic axon extension or (2) there is coordination/reflective expression patterns between parasympathetic-targeting and sympathetic-targeting neurotrophic factors.

There is data supporting the notion that neurotrophic factors known to guide parasympathetic axon extension may also influence sympathetic axon extension, and vice-versa. Neuronal growth factor (NGF) has largely been associated with the guidance of sympathetic innervation in the

cardiac ventricles[5-8]. During embryonic development, NGF is secreted by the vascular smooth muscle cells surrounding the coronary vessels, promoting sympathetic nerve-vessel alignment[9]. Evidence also suggests that NGF has the potential to promote parasympathetic ganglia outgrowth in the heart[10]. Thus, it remains a possibility that NGF secretion may also guide parasympathetic axon extension in the ventricles. Parasympathetic axon guidance in the cardiac ventricles is primarily associated glial line-derived neurotrophic factor (GDNF) expression[11, 12]. Yet, conclusions that detail normal sympathetic innervation in the context of GDNF inactivation are based on two-dimensional histological quantification of nerve fibers[11, 13, 14]; therefore, this does not exclude the possibility of disrupted sympathetic axon patterning without a reduction in nerve density. Other evidence suggests that GDNF could influence sympathetic axon recruitment in the ventricles. Indeed, GDNF expression by neonatal rat cardiomyocytes promotes sympathetic nerve growth *in vitro*[15]. Nevertheless, these results need further support by in animal models to verify this mechanism is recapitulated *in vivo*. Taken together, these findings suggests that both NGF and GDNF may play roles in co-regulating both parasympathetic and sympathetic axon patterning.

Interestingly, Sema3A has been identified as a repulsive cue that inhibits growth of both parasympathetic and sympathetic axons[16]. In in rat pelvic neurons, Sema3A targets specific pathways to each nerve subtype, causing the collapse of their neural growth cones[16]. In sympathetic neurons, Sema3A targets the soluble guanylylcyclase–cGMP pathway, whereas in parasympathetic neurons it targets the adenylyl cyclase–cAMP pathway[16]. Specifically in the cardiac ventricles, the role of Sema3A has been primarily investigated in relation to sympathetic

innervation[17, 18], but this opens the possibility that Sema3A expression may regulate parasympathetic innervation, too. Furthermore, this unique process of Sema3A having parallel effects by distinct mechanisms of action in sympathetic and parasympathetic nerves raises the question of whether other guidance molecules can function via similar processes.

The development of cardiac innervation requires the expression of a variety of neurotrophic factors in a cell-specific manner[9], creating the possibility for coordinated expression. Yet, the level of expression and coordination of neurotrophic signaling during the development of the cardiac ventricles are not well understood. Is there a balance between the neurotrophic factors expressed during heart development? What is the cell type-specific neurotrophic expression profile at different stages in heart development? Does knockdown or inhibition of one neurotrophic factor cause a compensatory increase in another? These are all interesting questions that remain largely outstanding in the cardiac field.

To expand on these questions, further research is needed to identify the neurotrophic factors that guide parasympathetic axon patterning in the ventricles. There are several approaches that may be used to identify the level and types of neurotrophic factors secreted during axon growth in the cardiac ventricles. Single-cell sequencing and pseudotime cell trajectory mapping of the developing embryonic ventricles (during the growth and targeting of axons at E13.5-E17.5) would provide insights to both. Single-cell sequencing can identify the expression of neurotrophic factors in a cell type-specific manner. Pseudotime trajectory mapping would identify how the

levels of neurotrophic factors dynamically change in each cell type during development. These insights would begin to uncover the regulation and targeting of parasympathetic innervation.

Further experiments can use conditional knockout of neurotrophins (i.e. with inducible Cre-lox mouse models) to conclusively determine its influence on parasympathetic axon development. It would be interesting to use these transgenic models to identify if disruption of parasympathetic innervation also impacts sympathetic nerve pattering, which can be analyzed by applying our immunostaining and whole-mount imaging methods (see Chapter II). If sympathetic nerves pattern normally without proper parasympathetic innervation, this provides support that independent neurotrophic factors regulate the patterning of each neuron subtype. Conversely, if sympathetic innervation is disrupted, this suggests that neurotrophic factors may influence axon growth in broad manner. These models could also demonstrate how inhibition of a single neurotrophic factor may affect the expression of other neurotrophins, as determined by RNA (transcriptomic, qPCR, RNA-scope) or protein (proteomic, immunostaining, Western blot) analysis. Together, these experiments can provide mechanistic insight into the signaling cascades regulating parasympathetic axon extension and targeting in the cardiac ventricles.

Identifying the cassette of neurotrophic factors that guide cardiac innervation is an essential first step to understand how parasympathetic innervation is patterned and maintained in the ventricles. Further discovering the cell type-specific transcriptomic profiles will provide insight into the molecular mechanisms of parasympathetic axon extension and development of neuron-

target cell contacts. These findings can reveal innervation targets and nerve-specific signaling cascades and that regulate parasympathetic nerve patterning, function, and crosstalk.

Remodeling of cardiac axons in the diseased and regenerating ventricles.

Our findings showed that the diseased and regenerating heart undergo two distinct processes of cardiac nerve remodeling. Interestingly, during neonatal heart regeneration, the heart is reinnervated by axons with a similar architecture to those in the uninjured heart. The cardiac axons in the regenerated myocardium reestablish parasympathetic and sympathetic axon bundling, as well as nerve-artery association. Moreover, the process of reinnervation is dependent on collateral artery formation. Taken together, our findings demonstrated that physiological reinnervation occurs the regenerated mammalian heart, creating a novel model to study the mechanistic basis for physiological reinnervation after cardiac injury.

In the diseased, non-regenerative heart, nerves undergo pathological remodeling after myocardial infarction (MI), which are associated with ventricular arrythmias and sudden cardiac death[19-23] (see Chapter I). We demonstrated the non-regenerated, infarcted myocardium undergoes heterogenous nerve remodeling, with regions of sympathetic axon sprouting and regions of full denervation. The heterogenous remodeling of sympathetic nerves is linked to the pathology after an MI[27-29]. In the infarcted heart, regions of sympathetic hyperinnervation and denervation can lead to disordered responses in β-adrenergic receptor signaling[27 26, 30, 31]. Thus, sympathetic nerve remodeling can contribute to the pro-arrhythmic environment of the infarcted myocardium[27-29].

One potential driver of sympathetic hyperinnervation is an increase in NGF at the border zone, which has been demonstrated in mouse and canine MI models[32, 33]. Disrupted NGF signaling after MI may be at the crux for causing aberrant sympathetic nerve patterning and function, ultimately causing arrhythmogenesis[34]. In support of this, knockdown of NGF expression following MI inhibits sympathetic nerve sprouting and improves cardiac function in rats[35]. Interestingly, NGF secretion can also provide beneficial remodeling in the infarcted heart[34]. Promoting NGF expression can stimulate angiogenesis and supports cardiomyocyte survival in adult mouse MI models[34, 36]. Furthermore, NGF promotes cardiomyocyte division and cardiac regeneration in the neonatal mouse heart [36-38].

The ability of NGF regulate both physiological and pathological remodeling in the infarcted myocardium highlights the need to dissect the molecular mechanisms in either condition. Several factors may contribute to the variable effects of NGF expression after an MI, including the timing of NGF expression, the amount of NGF secreted, and the cell type(s) expressing NGF. To address these questions, comparison between the regenerative neonatal and non-regenerative juvenile mouse heart can provide insight into mechanisms of physiological and pathological nerve remodeling, respectively. Ideal timepoints for analysis can be determined by monitoring the changes in NGF expression (measured by transcriptomic, qPCR, or RNA-scope analysis) in correlation with the timeline of nerve remodeling after injury defined in our study. Once key timepoints are defined, spatial transcriptomic analysis can be used to identify the cell type(s), their relative location (i.e. remote, border, or infarct zone), and gene expression profiles. The use

of spatial transcriptomics would also provide a wealth of knowledge to explore other neurotrophic factors known to regulate ventricular innervation. These findings would begin unraveling the differing mechanism by which neurotrophic factors can regulate physiological and pathological nerve remodeling.

Identifying the cellular and molecular pathways underpinning physiological reinnervation of the regenerated mammalian heart has therapeutic potential for the treatment of heart failure. Identifying the level and cell type-specific expression can provide information for cell targeting, dosage, and localization of treatment to fully harness the beneficial effects and promote physiological reinnervation. Contrasting this expression profile to the non-regenerated heart would further reveal the cellular pathophysiology contributing to sympathetic hyperinnervation and the pro-arrhythmic environment. Modulating neurotrophic factor expression is an exciting therapeutic strategy post-MI, as it could aid not only to elicit physiological reinnervation, but also repair the myocardium, promote revascularization, and limit arrhythmogenesis[34, 36].

REFERENCES

1. Kawano H, Okada R and Yano K. Histological study on the distribution of autonomic nerves in the human heart. *Heart and vessels*. 2003;18:32.
2. Rajendran PS, Challis RC, Fowlkes CC, Hanna P, Tompkins JD, Jordan MC, Hiyari S, Gabris-Weber BA, Greenbaum A, Chan KY, Deverman BE, Münzberg H, Ardell JL, Salama G, Gradinaru V and Shivkumar K. Identification of peripheral neural circuits that regulate heart rate using optogenetic and viral vector strategies. *Nature Communications*. 2019;10:1944.
3. Ulphani JS, Cain JH, Inderyas F, Gordon D, Gikas PV, Shade G, Mayor D, Arora R, Kadish AH and Goldberger JJ. Quantitative analysis of parasympathetic innervation of the porcine heart. *Heart rhythm*. 2010;7:1113-1119.
4. Puente BN, Kimura W, Muralidhar SA, Moon J, Amatruda JF, Phelps KL, Grinsfelder D, Rothermel BA, Chen R and Garcia JA. The oxygen-rich postnatal environment induces cardiomyocyte cell-cycle arrest through DNA damage response. *Cell*. 2014;157:565-579.
5. Nam J, Onitsuka I, Hatch J, Uchida Y, Ray S, Huang S, Li W, Zang H, Ruiz-Lozano P and Mukouyama YS. Coronary veins determine the pattern of sympathetic innervation in the developing heart. *Development*. 2013;140:1475-85.
6. Korsching S and Thoenen H. Developmental changes of nerve growth factor levels in sympathetic ganglia and their target organs. *Dev Biol*. 1988;126:40-6.
7. Ieda M, Fukuda K, Hisaka Y, Kimura K, Kawaguchi H, Fujita J, Shimoda K, Takeshita E, Okano H, Kurihara Y, Kurihara H, Ishida J, Fukamizu A, Federoff HJ and Ogawa S. Endothelin-1 regulates cardiac sympathetic innervation in the rodent heart by controlling nerve growth factor expression. *J Clin Invest*. 2004;113:876-84.
8. Crowley C, Spencer SD, Nishimura MC, Chen KS, Pitts-Meek S, Armaninl MP, Ling LH, McMahon SB, Shelton DL and Levinson AD. Mice lacking nerve growth factor display perinatal loss of sensory and sympathetic neurons yet develop basal forebrain cholinergic neurons. *Cell*. 1994;76:1001-1011.
9. Nam J, Onitsuka I, Hatch J, Uchida Y, Ray S, Huang S, Li W, Zang H, Ruiz-Lozano P and Mukouyama Y-s. Coronary veins determine the pattern of sympathetic innervation in the developing heart. *Development*. 2013;140:1475.
10. Rana OR, Saygili E, Gemein C, Zink MD, Buhr A, Saygili E, Mischke K, Nolte KW, Weis J and Weber C. Chronic electrical neuronal stimulation increases cardiac parasympathetic tone by eliciting neurotrophic effects. *Circulation research*. 2011;108:1209-1219.
11. Hiltunen JO, Laurikainen A, Airaksinen MS and Saarma M. GDNF family receptors in the embryonic and postnatal rat heart and reduced cholinergic innervation in mice hearts lacking Ret or GFRα2. *Developmental Dynamics*. 2000;219:28-39.
12. Végh AMD, Duim SN, Smits AM, Poelmann RE, Ten Harkel ADJ, DeRuiter MC, Goumans MJ and Jongbloed MRM. Part and Parcel of the Cardiac Autonomic Nerve System: Unravelling Its Cellular Building Blocks during Development. *Journal of cardiovascular development and disease*. 2016;3:28.
13. Heuckeroth RO, Enomoto H, Grider JR, Golden JP, Hanke JA, Jackman A, Molliver DC, Bardgett ME, Snider WD, Johnson EM, Jr. and Milbrandt J. Gene targeting reveals a critical role for neurturin in the development and maintenance of enteric, sensory, and parasympathetic neurons. *Neuron*. 1999;22:253-63.

14. Rossi J, Luukko K, Poteryaev D, Laurikainen A, Sun YF, Laakso T, Eerikäinen S, Tuominen R, Lakso M, Rauvala H, Arumäe U, Pasternack M, Saarma M and Airaksinen MS. Retarded growth and deficits in the enteric and parasympathetic nervous system in mice lacking GFR alpha2, a functional neurturin receptor. *Neuron*. 1999;22:243-52.
15. Miwa K, Lee JK, Takagishi Y, Opthof T, Fu X and Kodama I. Glial cell line-derived neurotrophic factor (GDNF) enhances sympathetic neurite growth in rat hearts at early developmental stages. *Biomed Res*. 2010;31:353-61.
16. Nangle MR and Keast JR. Semaphorin 3A inhibits growth of adult sympathetic and parasympathetic neurones via distinct cyclic nucleotide signalling pathways. *Br J Pharmacol*. 2011;162:1083-95.
17. Ieda M, Kanazawa H, Kimura K, Hattori F, Ieda Y, Taniguchi M, Lee J-K, Matsumura K, Tomita Y, Miyoshi S, Shimoda K, Makino S, Sano M, Kodama I, Ogawa S and Fukuda K. Sema3a maintains normal heart rhythm through sympathetic innervation patterning. *Nature Medicine*. 2007;13:604-612.
18. Behar O, Golden JA, Mashimo H, Schoen FJ and Fishman MC. Semaphorin III is needed for normal patterning and growth of nerves, bones and heart. *Nature*. 1996;383:525-8.
19. Zipes DP and Rubart M. Neural modulation of cardiac arrhythmias and sudden cardiac death. *Heart Rhythm*. 2006;3:108-13.
20. Vaseghi M and Shivkumar K. The role of the autonomic nervous system in sudden cardiac death. *Prog Cardiovasc Dis*. 2008;50:404-19.
21. Fukuda K, Kanazawa H, Aizawa Y, Ardell JL and Shivkumar K. Cardiac innervation and sudden cardiac death. *Circ Res*. 2015;116:2005-19.
22. Cao JM, Chen LS, KenKnight BH, Ohara T, Lee MH, Tsai J, Lai WW, Karagueuzian HS, Wolf PL, Fishbein MC and Chen PS. Nerve sprouting and sudden cardiac death. *Circ Res*. 2000;86:816-21.
23. Cao J-M, Fishbein MC, Han JB, Lai WW, Lai AC, Wu T-J, Czer L, Wolf PL, Denton TA, Shintaku IP, Chen P-S and Chen LS. Relationship Between Regional Cardiac Hyperinnervation and Ventricular Arrhythmia. *Circulation*. 2000;101:1960-1969.
24. Sahoglu SG, Kazci YE, Karadogan B, Aydin MS, Nebol A, Turhan MU, Ozturk G and Cagavi E. High-resolution mapping of sensory fibers at the healthy and post-myocardial infarct whole transgenic hearts. *Journal of Neuroscience Research*. 2023;101:338-353.
25. Vaseghi M, Salavatian S, Rajendran PS, Yagishita D, Woodward WR, Hamon D, Yamakawa K, Irie T, Habecker BA and Shivkumar K. Parasympathetic dysfunction and antiarrhythmic effect of vagal nerve stimulation following myocardial infarction. *JCI Insight*. 2017;2.
26. Inoue H and Zipes DP. Time course of denervation of efferent sympathetic and vagal nerves after occlusion of the coronary artery in the canine heart. *Circulation Research*. 1988;62:1111-1120.
27. Gardner RT, Ripplinger CM, Myles RC and Habecker BA. Molecular Mechanisms of Sympathetic Remodeling and Arrhythmias. *Circ Arrhythm Electrophysiol*. 2016;9:e001359.
28. Chen P-S, Chen LS, Cao J-M, Sharifi B, Karagueuzian HS and Fishbein MC. Sympathetic nerve sprouting, electrical remodeling and the mechanisms of sudden cardiac death. *Cardiovascular Research*. 2001;50:409-416.

29. Zekios KC, Mouchtouri ET, Lekkas P, Nikas DN and Kolettis TM. Sympathetic Activation and Arrhythmogenesis after Myocardial Infarction: Where Do We Stand? *J Cardiovasc Dev Dis*. 2021;8.
30. Stanton MS, Tuli MM, Radtke NL, Heger JJ, Miles WM, Mock BH, Burt RW, Wellman HN and Zipes DP. Regional sympathetic denervation after myocardial infarction in humans detected noninvasively using I-123-metaiodobenzylguanidine. *Journal of the American College of Cardiology*. 1989;14:1519-1526.
31. Yokoyama T, Lee JK, Miwa K, Opthof T, Tomoyama S, Nakanishi H, Yoshida A, Yasui H, Iida T, Miyagawa S, Okabe S, Sawa Y, Sakata Y and Komuro I. Quantification of sympathetic hyperinnervation and denervation after myocardial infarction by three-dimensional assessment of the cardiac sympathetic network in cleared transparent murine hearts. *PLoS One*. 2017;12:e0182072.
32. Oh YS, Jong AY, Kim DT, Li H, Wang C, Zemljic-Harpf A, Ross RS, Fishbein MC, Chen PS and Chen LS. Spatial distribution of nerve sprouting after myocardial infarction in mice. *Heart Rhythm*. 2006;3:728-36.
33. Zhou S, Chen LS, Miyauchi Y, Miyauchi M, Kar S, Kangavari S, Fishbein MC, Sharifi B and Chen P-S. Mechanisms of cardiac nerve sprouting after myocardial infarction in dogs. *Circulation research*. 2004;95:76-83.
34. Pius-Sadowska E and Machaliński B. Pleiotropic activity of nerve growth factor in regulating cardiac functions and counteracting pathogenesis. *ESC Heart Fail*. 2021;8:974-987.
35. Hu H, Xuan Y, Wang Y, Xue M, Suo F, Li X, Cheng W, Li X, Yin J, Liu J and Yan S. Targeted NGF siRNA delivery attenuates sympathetic nerve sprouting and deteriorates cardiac dysfunction in rats with myocardial infarction. *PLoS One*. 2014;9:e95106.
36. Meloni M, Caporali A, Graiani G, Lagrasta C, Katare R, Van Linthout S, Spillmann F, Campesi I, Madeddu P, Quaini F and Emanueli C. Nerve growth factor promotes cardiac repair following myocardial infarction. *Circulation research*. 2010;106:1275-1284.
37. Mahmoud AI, O'Meara CC, Gemberling M, Zhao L, Bryant DM, Zheng R, Gannon JB, Cai L, Choi W-Y, Egnaczyk GF, Burns CE, Burns CG, MacRae CA, Poss KD and Lee RT. Nerves Regulate Cardiomyocyte Proliferation and Heart Regeneration. *Dev Cell*. 2015;34:387-399.
38. Lam NT, Currie PD, Lieschke GJ, Rosenthal NA and Kaye DM. Nerve growth factor stimulates cardiac regeneration via cardiomyocyte proliferation in experimental heart failure. *PLoS One*. 2012;7:e53210-e53210.

APPENDIX

PERSPECTIVE: BRIDGING THE COMMUNICATION GAP: CARDIOMYOCYTES RECIPROCATE SYMPATHETIC NERVE SIGNALLING

Rebecca J. Salamon [1], Ahmed I. Mahmoud [1*]

[1]Department of Cell and Regenerative Biology, University of Wisconsin-Madison School of Medicine and Public Health, Madison, WI 53705, United States.

*Corresponding author: Ahmed I. Mahmoud, Ph.D. Email: aimahmoud@wisc.edu

Salamon RJ, Mahmoud AI. Bridging the communication gap: cardiomyocytes reciprocate sympathetic nerve signalling. J Physiol. 2022 Jun;600(12):2827-2828. doi: 10.1113/JP283173. Epub 2022 May 25. PMID: 35614020; PMCID: PMC9204971.

AUTHOR CONTRIBUTIONS

R.J.S. wrote and edited the manuscript. A.I.M. conceived, wrote, and edited the manuscript.

Sympathetic nerves (SNs) innervate the mammalian heart and regulate cardiac function by increasing contraction and rhythm. The precise spatial patterning of cardiac sympathetic innervation during development is the result of tightly regulated events including neurotrophic and neuro-repellant factors from cardiomyocytes (CMs) (Ieda et al. 2007). Importantly, the distinct innervation patterns of SNs allow for precise anterograde neuro-cardiac 'SNs to CMs' communication via the synaptic release of norepinephrine that governs cardiac function at the Neuro-Cardiac Junction (NCJ), which is analogous in name and structure to the Neuro-Muscular Junction (Prando et al. 2018). Interestingly, several cardiovascular diseases are accompanied with secondary myocardial sympathetic denervation, providing evidence that maintenance of SN innervation is dependent on CMs (Gardner et al. 2016). Collectively, these findings demonstrate a significant link between CMs and SNs during homeostasis, and that disruption of this signaling can exacerbate cardiovascular disease. However, whether retrograde signaling from CMs to SNs at the NCJ is required to maintain adult heart SN innervation under homeostasis was unknown. Defining the mechanisms by which CMs and SNs communicate can provide novel avenues to maintain physiological innervation in cardiovascular diseases.

In this issue of *Journal of Physiology*, Dokshokova et al. explore whether a reverse CM to SN communication at the NCJ is required for maintaining adult heart sympathetic innervation and function (Dokshokova et al. 2022). Immunofluorescence staining of rat ventricular sections showed the expression of nerve growth factor (NGF) vesicles in CMs at the NCJ, which is the main neurotrophin required for SN innervation and maturation (Clegg et al. 1989). Furthermore, the high-affinity NGF receptor, TrkA, was present on SN neuronal processes. Interestingly, this expression pattern was also detected in myocardial samples from human hearts as well. These findings supported the hypothesis that retrograde communication from CMs to SNs takes place via NGF at the NCJ in the mammalian heart.

To further establish this retrograde communication, the authors performed co-culture experiments with SNs and CMs. Typically, SN survival and maturation in culture requires the addition of exogenous NGF, however; the co-culture of SNs with CMs alone was sufficient to promote survival and maturation of SNs without exogenous NGF. These results demonstrate that CMs provide NGF for SN survival and maturation. To further define whether cell-specific interactions between CMs and SNs mediate this signaling, the authors co-cultured SNs with cardiac fibroblasts (CFs), which synthesizes high levels of NGF, but lack an NCJ. Remarkably, the co-culture of SNs with CFs demonstrated significantly lower levels of NGF in the SN processes in contact with CFs in comparison to the CMs co-culture. These results reveal that CMs are the source of NGF for the innervating SNs, and this retrograde signaling occurs specifically at the NCJ.

Since sympathetic denervation occurs following CM injury, the authors wanted to determine whether specific inhibition of NGF in CMs can induce degeneration of SNs. The authors treated CMs with an siRNA against NGF, which reduced NGF expression without disrupting the expression of other neurotrophins or impacting CM viability. Interestingly, NGF knockdown in CMs resulted in fragmentation and reduction of the innervating SNs, which was restored by exogenous addition of NGF. To explore if the NGF release from CMs is diffused or localized at the NCJ, the authors measured NGF levels in the conditioned medium from CMs and quantified very low levels

of NGF. In addition, treatment of SN and CM co-culture with a TrkA receptor antagonist reduced neuronal viability. Together, these results demonstrate that specific retrograde release of NGF from CMs is required to maintain survival of the innervating SNs by binding to the TrkA receptor at the NCJ.

Collectively, the findings of Dokshokova et al. demonstrate that CMs and SNs participate in bidirectional cellular communication, specifically via NGF release at the NCJ. This study provides mechanistic evidence to the sympathetic denervation that takes place in the context of cardiovascular diseases. The identification of the bidirectional communication between CMs and SNs provides new avenues towards maintaining physiological innervation that can ameliorate the extent of cardiac diseases. The precise nature of nerve topology and intracellular connections highlights a structural and physiological component of neuro-cardiology that is beginning to be appreciated. Heart disease, such as myocardial infarction, as well as several cardiomyopathies, results in abnormalities in synaptic transmission and reception. In the failing heart, the myocardial response to synaptic signaling is desensitized, resulting in a pathological, non-compensatory upregulation of synaptic transmission (Gardner et al. 2016). Following ischemic injury, CM loss results in mass denervation of synaptic nerves. Understanding the mechanisms that regulate homeostatic innervation and interconnectivity between the two cell types lends a new perspective on pathological denervation that takes place during cardiac disease. Moreover, identifying how myocardial injury can impair nerve viability may reveal new molecular underpinnings for cardiac dysautonomia. Identifying the mechanisms of the bidirectional signaling between CMs and SNs will be applicable for future investigations of cardiac pathologies and the development of targeted therapeutics.

Recent studies have led to a deeper recognition of sympathetic physiology, where the role of SN's extend beyond the fight-or-flight response and towards directly influencing intracellular signaling. In contrast, the level of parasympathetic innervation of the ventricular myocardium remains poorly defined. Thus, future studies are needed to map parasympathetic innervation of the ventricles and determine whether similar communication between CMs and other cell types takes place. Collectively, these findings identify a mechanistic basis for neurogenic regulation of the heart and provide novel insights into the physiology of cardiac homeostasis and disease.

REFERENCES

Clegg, D. O., T. H. Large, S. C. Bodary, and L. F. Reichardt. 1989. 'Regulation of nerve growth factor mRNA levels in developing rat heart ventricle is not altered by sympathectomy', *Dev Biol*, 134: 30-7.

Dokshokova, L., M. Franzoso, A. D. Bona, N. Moro, J. Sanchez-Alonso-Mardones, V. Prando, M. Sandre, C. Basso, G. Faggian, H. Abriel, O. Marin, J. Gorelik, T. Zaglia, and M. Mongillo. 2022. 'Nerve Growth Factor transfer from cardiomyocytes to innervating sympathetic neurons activates TrkA receptors at the neuro-cardiac junction', *J Physiol*.

Gardner, R. T., C. M. Ripplinger, R. C. Myles, and B. A. Habecker. 2016. 'Molecular Mechanisms of Sympathetic Remodeling and Arrhythmias', *Circ Arrhythm Electrophysiol*, 9: e001359.

Ieda, M., H. Kanazawa, K. Kimura, F. Hattori, Y. Ieda, M. Taniguchi, J. K. Lee, K. Matsumura, Y. Tomita, S. Miyoshi, K. Shimoda, S. Makino, M. Sano, I. Kodama, S. Ogawa, and K. Fukuda. 2007. 'Sema3a maintains normal heart rhythm through sympathetic innervation patterning', *Nat Med*, 13: 604-12.

Prando, V., F. Da Broi, M. Franzoso, A. P. Plazzo, N. Pianca, M. Francolini, C. Basso, M. W. Kay, T. Zaglia, and M. Mongillo. 2018. 'Dynamics of neuroeffector coupling at cardiac sympathetic synapses', *J Physiol*, 596: 2055-75.

FUNDING

This work was supported by an AHA Predoctoral Training Award 829586 (R.J.S.), an NIH/NHLBI grant HL155617-01A1 (A.I.M.), and a DOD grant PR210594 (A.I.M.).